A THEORETICAL STUDY OF NON-EQUILIBRIUM

PHOTOEXCITED CARRIERS IN SEMICONDUCTORS
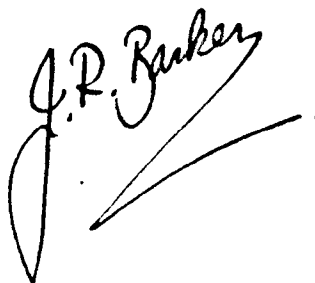
by

John Reginald Barker

A dissertation submitted

to the University of Warwick for

admission to the degree of

Doctor of Philosophy

BEST COPY

AVAILABLE

Poor quality text in the original thesis.

MEMORANDUM

This dissertation is submitted to the University
of Warwick in support of my application for admission to
the degree of Doctor of Philosophy.   It contains an account
of my own work performed at the School of Physics of the
University of Warwick in the period October 1967 to October
1969 under the general supervision of Doctor C. J. Hearn.
No part of this dissertation has been used previously in a
degree thesis submitted to this or any other university.
The work described in this thesis is the result of my own
independent research except where specifically acknowledged
in the text.

October, 1969.   J. R. BARKER

ACKNOWLEDGEMENTS

ABSTRACT

A theoretical study is made of the physics of photoexcited carriers in one of the bands of a semiconductor. The emphasis is on pnotoexcited hot carrier phenomena, for which the mean carrier energy deviates significantly from the thermal equilibrium value in the steady state. Very little previous theoretical work in this area has been reported.

Two situations are analysed. The first is an investigation of hot photo-excited carriers in germanium and silicon at low temperatures. The carriers are excited into the band by a model black-body excitation spectrum having a mean energy in excess of the thermal energy. Full account is taken of the interaction of the carriers with impurities and phonons, and recombination is assumed to occur via a cascade mechanism. Significant carrier heating is found for trapping densities of the order 10^{16} cm^{-3} at lattice temperatures below about 30°K. The steady-state carrier distribution functions are derived numerically from the Boltzmann equation in the absence of external fields. The low field transport and trapping parameters are then derived by a perturbation theory. The assumption of a linear response to applied fields is checked by an adaptation of the Monte Carlo technique first employed by Kurosawa (1966) and Boardman et al (1968) in high field studies of semiconductors. The technique is extensively modified to suit our problem; in particular the concept of the self-scattering device is enlarged.

The theory shows good agreement with the experimentally measured (Rollin and Rowell 1960) temperature variation of the Hall mobility of photoexcited holes in germanium. Agreement is also obtained with an experimental curve for the temperature dependence of the capture cross section for electrons in silicon.

Experimentally a 'cut-off' is found in the temperature dependence below about 30°K. The hot carrier model explains this phenomenon in terms of an anomalous temperature dependent Hall number which arises from the severe non-Maxwellian heating of the carriers. However, not all the experimental results can be explained this way and a tentative alternative mechanism is suggested.

The second situation analysed involves monochromatic photoexcitation leading to the oscillatory photoconductivity effect in many polar semiconductors. Considerable controversy has existed previously as to the origin of this effect. The distribution functions and photoconductivity are studied as a function of photon frequency and electric field strength on the basis of an analytical model and detailed Monte Carlo calculations. Good agreement is found with experiment as regards the field dependence of the overall spectral response, confirming the assumptions of an earlier approximate analytical approach (Stocker and Kaplan 1966).

For certain photon frequencies the photoexcited carriers can theoretically exhibit both total and differential negative mobility for certain ranges of applied electric field, confirming a previous approximate theory (Stocker 1967), although the effect has not been observed experimentally. This leads to a non-uniform field distribution in the semiconductor and the possibility of space-charge instabilities. The possibility of steady-state negative photoconductivity is investigated with particular reference to the spatial distribution of electric field and the stability of the carrier system. The evolution and form of the instabilities and steady-states are evaluated numerically. Full account is taken of the electron and trap dynamics. It is shown that the total negative resistance state is unstable in the presence of injecting contacts. Instead either a non-uniform field distribution showing bulk positive resistance is established or there occur propagating instabilities leading to positive current oscillations.

PUBLICATIONS

Various aspects of the work described in this thesis have been published, or are in the course of publication, in the scientific literature. The papers involved are published jointly with Dr. C. J. Hearn and are as follows:-

(1) "The observed trapping parameters of photoexcited carriers in germanium and silicon." Physics Letters, 26A, 148 (1968).

(2) "Monte Carlo simulation of oscillatory photoconductivity." Physics Letters, 29A, 215 (1969).

(3) "Field effects in oscillatory photoconductivity." Journal of Physics (Proc.Phys.Soc.) C, 2, 2128, (1969).

(4) "Monte Carlo methods in electron transport theory." Proceedings of the first Conference on Computational Physics, Culham (1969), Culham report, in the press.

Further parts of this thesis will be shortly submitted for publication in the journal ' Journal of Physics (Proc.Phys.Soc.) C.'

CONTENTS

CHAPTER I

INTRODUCTION

1.1 Objectives

The basic theme of this thesis is a theoretical study of non-equilibrium carrier distributions and their consequences appropriate to non-degenerate photoexcited carriers in one of the bands of a semiconductor. The objective is to relate measurements of phototransport and trapping parameters to our existing knowledge of recombination processes and the interaction of carriers with phonons and impurities. Particular emphasis is placed on hot carrier phenomena. The extensive literature on hot carriers deals almost entirely with their production by high electric fields: very little theoretical work has been reported on the optically excited case. Our work has direct relevance to a series of experiments conducted over the past ten years and was initiated to provide a theoretical understanding of the physics of photoexcited hot carriers.

1.2 Hot electrons

The key to understanding many of the transport and trapping properties of semiconductors is the steady-state momentum distribution of carriers. In thermal equilibrium this is well known: degenerate carrier assemblies are described by the Fermi-Dirac distribution function, whilst Maxwell-Boltzmann statistics apply to non-degenerate systems. Conventional transport theory (c.f. Ziman 1960) describes the linear response of equilibrium carrier distributions to weak external agencies such as applied electric and magnetic fields or temperature gradients. In these circumstances the steady-state distribution function bears a simple relation to the equilibrium distribution. There are, however, many physical situations in which the steady-state distribution

function can become severely distorted from the equilibrium form. The most familiar case occurs under conditions of high applied electric fields (Conwell 1967) which give rise to 'hot' carriers having a mean energy far greater than the equilibrium value appropriate to the lattice temperature. The mean carrier energy rises until in the steady-state the rates at which momentum and energy are gained from the field balance the corresponding loss rates to the lattice and impurities. Whereas small departures from thermal equilibrium are adequately described by the momentum relaxation processes, hot electron problems involve both energy and momentum relaxation. High field hot electron problems are generally characterized by a breakdown of Ohm's law and involve a non-linear response to the applied field. In some circumstances, for example in the Gunn effect (Butcher 1967), this leads to a decrease of the mean carrier drift velocity with increased applied field. Instabilities may then develop which give rise to current oscillations under constant applied bias voltages.

Another situation in which hot carriers may be produced, the subject of this thesis, arises when the carriers are only maintained in the band by constant photoexcitation from states exterior to the band, subsequent recombination occurring into these states. If the photoexcited carriers enter the band with a mean energy in excess of the thermal equilibrium value they will require a finite thermalisation time to lose this excess energy. When the recombination lifetime of the carriers is large compared to the thermalisation time an approximate quasi-equilibrium can be achieved (Shockley 1949, Mattis 1960). The steady-state distribution function then closely resembles the equilibrium distribution with a quasi-Fermi level determined by the steady-state carrier concentration. However for sufficiently short lifetimes the steady-state distribution will show significant heating and quasi-equilibrium cannot be achieved. Instead the distribution will reflect the detailed nature of the excitation spectrum, recombination processes and energy relaxation processes within the band. Evidence for the occurrence of this form of carrier heating may be inferred from the low temperature phototransport measure-

ments made by Rollin and Rowell (1960), Habeggar and Fan (1964), Stocker et al (1966). Discrepancies between the theoretical and experimental work on the cascade capture of carriers into shallow traps in germanium and silicon have also been attributed to such carriers (Mattis 1960, Levitt and Honig 1961, Loewenstein and Honig 1966). The lack of any quantitative theory to describe these experiments provided the original motivation for the present work.

The first theoretical investigation of photoexcited hot carriers was made by Mattis (1960) who discussed the problem of calculating the photoexcited carrier distribution function within the framework of a variational principle. This study was based on a simple model involving acoustic deformation scattering of non-degenerate carriers in the band in the presence of cascade capture into shallow impurities. Distribution functions were not derived but Mattis showed that significant departures from quasi-equilibrium could occur at very low temperatures. These were to be associated with the rapid decrease of carrier lifetime with lattice temperature.

A series of papers (Hearn et al 1962, Hearn 1965, 1966) have considered the criteria for the use of an effective temperature to describe a heated photoexcited carrier distribution. These studies were concerned with carrier concentrations sufficiently large for intercarrier collisions to be important, (but without degeneracy). The present work deals entirely with carrier concentrations below the critical concentrations for which intercarrier collisions have importance. Other theoretical work of interest is the study of the oscillatory photoconductivity effect made by Stocker and Kaplan (1966). This was a qualitative investigation of the monoenergetic excitation of carriers into the valence and conduction bands of the III-V semiconductors at low temperatures. This problem has some relation to the present work and is discussed further in section 1.3. Apart from the above studies, no detailed theory of optically excited hot electrons

has been forthcoming.   In this thesis a quantitative treatment is attempted of specific aspects of the photoexcited hot carrier problem, a brief survey of which is given in the following sections.

1.3 Scope and plan of thesis

Two situations are analysed in detail.   The first described in Chapter II is a study of the physics of carriers which are photoexcited by a broad spectrum radiation field with a high effective temperature into the valence or conduction bands of germanium and silicon at lattice temperatures below 30°K.   Whilst in the band the carriers suffer collisions with impurities and phonons, and are subject to the influence of external electric and magnetic fields.   Recombination is considered to occur at shallow traps by the phonon cascade mechanism (Lax 1960). A preliminary investigation of this problem was made by the author as the basis of an M.Sc. dissertation (Barker 1967) but no quantitative comparison with experiment was possible.   The analysis of Chapter II shows that significant non-Maxwellian carrier heating occurs below about 30°K for trapping densities of the order $10^{16} cm^{-3}$.   The effects of heating are most effectively displayed in the low field transport properties (linear response regime).   Good agreement is found with experiment for the lattice temperature variation of the Hall mobility, of holes in germanium.   Agreement is also obtained with an experimental curve for the temperature dependence of the capture cross section for electrons in silicon. Extensive experimental work over the past few years (a complete list of references is given by Loewenstein and Honig, 1966) has shown that a 'cut-off' is present in the temperature dependence of the capture cross section below about 20°K.   Our hot carrier model interprets this phenomenon in terms of an anomalous temperature dependent Hall number which arises from the severe non-Maxwellian heating of the carriers.   However, not all the experimental results can be explained this way and reasons why the simple model could break down for these cases are suggested at the end of Chapter II.

The carrier distribution functions for this problem are obtained numerically from the steady-state Boltzmann equation in the absence of external fields. Additional terms enter the Boltzmann equation to incorporate the effects of carrier generation and recombination. This is a relatively simple problem since the distribution functions are isotropic. The low field transport properties are then derived by a perturbation theory. This involves a linear response to weak fields, where the presence of the fields does not appreciably alter the isotropic part of the distribution function. An important problem here is to know how large the external fields may be before this simple theory breaks down. For thermalized carriers fields of the order of 10 V/cm set the limit. However, for photoexcited carriers, as will be shown in Chapter IV, much smaller fields may severely distort the isotropic part of the distribution function. One approach to this problem is to solve the Boltzmann equation with the field terms included. This leads to severe computational difficulties: the distribution function is anisotropic and both energy and momentum relaxation processes must be included. Drastic approximations must be made if conventional numerical techniques are employed.

To overcome thse difficulties we have resorted to a Monte Carlo method, essentially a computer simulation of the motion of carriers in momentum space. The technique has considerable flexibility and is not restricted to low field problems. It was first introduced into high field transport theory by Kurosawa (1966) and Boardman et al (1968). We have extensively modified the technique to suit our problem and introduced several features which have more general application (Barker and Hearn, 1969a, b). In particular the concept of the self scattering device (Boardman et al 1968) has been enlarged and the first proof of its validity offered. In view of the potential importance of this technique we devote a whole Chapter (Chapter III) to the Monte Carlo method as applied to electron transport theory. The Monte Carlo calculations confirm

the solutions obtained from the Boltzmann equation and verify the assumption of Ohmic conduction up to fields of 1V/cm which are typical of the field strengths used in relevant experimental work. Recent experimental findings (Yariv et al 1968) support this analysis but show the occurrence of non-linear effects for fields in excess of 10 V/cm. These more recent developments are discussed in Chapter VI.

The second problem to be analysed is the oscillatory photoconductivity effect. For this problem a narrow spectrum radiation field (essentially monochromatic) is used so that carriers enter the band with a well defined energy. The relevant semiconductors are the III-V compounds which have a strong interaction between the optical phonons and the electrons. If the interaction is sufficiently strong the photoconductivity becomes an oscillatory function of injection energy with a period equal to the longitudinal optical phonon energy. The effect appears at lattice temperatures below $30^{\circ}K$ and is most certainly a hot carrier phenomenon. It was first observed by Blunt (1957) and has since received considerable experimental attention. The present work was initiated to investigate the reported strong field dependence of the oscillatory structure (Habeggar and Fan 1964) and to provide a quantitative theory of the basic spectral response. Considerable controversey as to the origins of the effect has existed prior to 1966. A theory of oscillatory photoconductivity was given by Stocker and Kaplan (1966) using certain approximations regarding the form of the carrier distribution function but no quantitative comparison with experiment was possible. In view of the strong field dependence of the effect, even for very low fields, we have performed Monte Carlo calculations for the distribution function on the basis of a detailed model. This work is described in Chapter IV. Good agreement has been found with experiment except for injection energies very close to a multiple optical phonon energy (Barker and Hearn 1969a). The distribution functions are highly non-equilibrium and show considerable heating. The electric

field produces severe distortion in the distributions and under certain circumstances can act to reduce the mean carrier energy; carrier cooling occurs.

An interesting result which arises from our calculations is the prediction of total negative conductivity, for a certain range of electric fields, if the carriers are excited into the band with an energy of just less than a multiple number of optical phonon energies. A simple physical argument which explains this effect has also been given by Stocker (1967). Detailed calculations, made on the basis of an exact analytical model and the Monte Carlo technique, confirm that the negative conductivity is a real effect and not a consequence of approximations made in determining the carrier distribution function. The derived drift velocity-field characteristics for this problem are highly non-linear with regions of negative differential and total negative mobility.

The velocity-field characteristics describe the carrier drift velocity attained in the steady-state for a spatially homogeneous carrier distribution subjected to a constant uniform electric field. It is well known, however, (c.f. Butcher 1967) that if a region of negative differential mobility occurs we can expect the system to be unstable with respect to space-charge formation. The field and carrier concentration will no longer be spatially or temporally homo-geneous. The static velocity-field characteristic is no longer a good indication of the current-voltage relation. This problem is investigated in some detail in Chapter V (see also Barker and Hearn 1969b). Ideally we would solve the problem from the standpoint of the full time and space dependent Boltzmann equation coupled to Maxwell's equations (which reduce to Poisson's equation for this problem). This is a problem of formidable complexity, however, and is not attempted. Instead we adopt a more phenomenological approach.

In Chapter V we investigate the occurrence of negative conductivity with particular reference to the spatial distribution of electric field and the stability of the carrier system. This work is of general interest to the understanding of the physics of instabilities in semiconductors and to negative resistance devices. A phenomenological model is used, based on Poisson's euqation, the continuity equations for carriers and ionized impurities and the static velocity-field characteristic. Spatial dependence is taken care of by including diffusion terms. Small signal perturbation theory is used to derive the linear response of the system to small fluctuations. The qualitative form of static field distributions which could arise are obtained by topological methods (phase-plane analysis) applied to the system of non-linear differential equations deduced from the model. Consideration of the problem of contacts and the external circuits is essential to the analysis. Diffusion processes are found to play a crucial role. Detailed numerical calculations are also given for the time evolution of the steady-state, where it exists, and the non-linear growth of instabilities in the system. A variety of instabilities are found which are analysed by phase-plane methods. These give new insight into the general problem of instabilities in negative resistance materials and bear strong resemblances to instabilities occurring in gallium arsenide at room temperature under high electric field. We give a comparison between these instabilities which lead to the Gunn effect and the instabilities predicted for the oscillatory photoconductivity problem. The major result is that for ordinary contacts a total negative resistance state does not occur. Instead a non-uniform steady static field distribution leading to positive conductivity is set up in the sample, or small amplitude positive current oscillations occur which arise from the cyclic uniform propagation of weak field domains through the sample. Under certain conditions of recombination and excitation these domains are suppressed and the cyclic non-uniform propagation of accumulation layer instabilities may occur.

Chapter VI discusses some of the problems raised by our work and suggest areas for future research at both the theoretical and experimental level. More recent experimental work is discussed in the light of our analysis.

The Appendices contain information of a more mathematical nature, such as the detailed forms of the scattering processes used in our calculations, Monte Carlo subroutines and elements of phase-plane analysis.

CHAPTER II

HOT PHOTOEXCITED CARRIERS IN GERMANIUM AND SILICON AT LOW

TEMPERATURES

2.1 Introduction

In this chapter we describe the first of two separate investigations
of optically excited hot carriers in semiconductors. The situation considered
is that in which the carrier excitation spectrum has an approximately black
body character with a radiation temperature greater than the lattice temperature.
Recombination is considered to take place via the cascade capture process
into shallow ionized traps originally proposed by Lax (1960). The details
of the theoretical model are given in section 2.2. The essential approach
is to derive the Boltzmann equation on the basis of a simple model to include
the processes of carrier generation and recombination. A Monte Carlo technique
(to be described in detail in Chapter 3) is utilized to check the validity of
the solutions obtained from the Boltzmann equation approach. In section 2.3
we describe the methods used to determine the resultant distribution functions
in the absence of external electric and magnetic fields. The salient features
of the numerically computed distribution functions are discussed in section 2.4.

The problem described here has direct relevance to a series of experiments
performed on germanium and silicon made in the last few years (Levitt and
Honig 1960, Rollin and Rowell 1960, Betjemann 1965, Loewenstein and Honig 1966).
Accounts of our results have been given in the literature (Barker and Hearn,
1968; 1969d). The Lax model predicts that the carrier recombination lifetimes
decrease very rapidly with decreasing lattice temperature so that at

temperatures below about 30°K, depending on the detailed parameters considered, the carrier distribution can become significantly heated. One of the simplest and most direct methods of detecting this heating is to measure the Hall mobility as a function of lattice temperature. One experiment of this type has been reported by Rollin and Rowell (1960) for photoexcited holes in germanium. The theoretical work indicates that the carrier distributions have an ohmic (linear) response to small electric fields. Consequently, we can show by perturbation theory that the Hall mobility involves suitable moments of the zero field distribution functions (section 2.5). If all the important energy and momentum relaxation processes are taken into account the present model gives results which are in good agreement with those of Rollin and Rowell (section 2.7). Similar measurements have been reported by Betjemann (1965) for electrons in silicon. Betjemann interprets the observed anomalies in the measured Hall mobility as due to carrier heating. However, the present model suggests that the carrier lifetimes are much too long for this to be a valid explanation of the results.

In section 2.6 we report a more subtle, and rather more difficult application of the model to situations in which photoexcited carriers are used to measure the mean capture cross sections of shallow impurities. Such experiments have been described by Levitt and Honig (1961), and Loewenstein and Honig (1966) using electrons in douple doped silicon. Their results indicate that the measured capture cross sections are roughly of the correct order of magnitude as required for thermalised electrons on the Lax model but show a serious discrepancy with regard to the lattice temperature dependence. The present model predicts carrier heating in some of these experiments. There are two aspects of heating effects which are important in this context. The first, which was originally pointed out by Mattis (1960), is that heating decreases the average capture cross-section because the capture probability decreases with carrier energy. This has

rather a weak effect on the observed temperature dependence of the cross

sections. Secondly, our model predicts that the heating is non-Maxwellian.

Consequently the Hall number, which is the "constant" of proportionality

between the Hall coefficient and reciprocal carrier concentration, shows a

strong temperature dependence through the energy dependence of the momentum

relaxation processes. The Hall effect is used experimentally to calculate

the concentration of photoexcited carriers, from which the mean cross-section

is determined. Except at the lowest temperatures investigated this second

effect is found to be the more important. Good agreement is obtained with

the measured temperature dependence of the cross section for one of the samples

used by Levitt and Honig (1961); this gives further support to our model

for carrier heating. However, the majority of samples show a temperature

independent mean recombination lifetime which is at variance with both the

Lax model and the hot carrier model. This represents a considerable problem

and a qualitative attempt to understand these results is given in section 8.

2.2 The basic model

This section describes the basic equation which leads to the steady state

carrier distribution $f_o(\underline{k})$ in $\underline{k}$-space, in the absence of any applied fields.

We consider a simple energy band characterised by a scalar effective mass m^*.

In terms of an energy band with a multivalley structure the analysis applies

to a single valley. At this stage we do not consider the effects of

anisotropic effective masses. However, these are included in the calculation

of transport parameters. Photoexcited carriers are assumed to be generated

by an applied external radiation field which gives rise to a spatially uniform

excitation rate into the band. The excitation rate is considered to be a

function of carrier energy $\epsilon(\underline{k})$ only. The distribution function $f_o(\underline{k})$ is then

only a function of carrier energy. In which case only the inelastic scattering

processes, that is electron-phonon interaction, are effective in determining the form of f_o. Low carrier concentrations, typically of the order 10^8cm^{-3}, are considered so that intercarrier scattering may be neglected. This condition also allows us to neglect the effects of non equilibrium phonon distributions.

The steady state rate equation describing the photoexcitation of carriers into a single band is

$$W\left\{\omega_e(\underline{k}) - \omega_r(\underline{k})\right\} = J(\underline{k}) \qquad\qquad 2.2.1$$

where W is the total excitation rate into the band (equal to the total recombination rate). The normalised quantities $\omega_e(\underline{k})$, $\omega_r(\underline{k})$ are the fractional rates of excitation and recombination for entering and leaving state $\underline{k}$ respectively. The term $J(\underline{k})$ is the total rate of intra-band electron-phonon scattering out of the state $\underline{k}$. Summing over all the states $\underline{k}$ in the band leads to the sum rule

$$\sum_{\underline{k}} J(\underline{k}) = 0 \qquad\qquad 2.2.2$$

which is a consequence of carrier conservation in collisions. The re-combination and scattering terms are functionals of $f_o(\underline{k})$ so that $f_o(\underline{k})$ can be determined if the independent function $\omega_e(\underline{k})$ is known.

The scattering rate is based on acoustic deformation and non-polar optical phonon scattering since the model is to be applied to germanium and silicon; inter equivalent valley scattering, for the case of electrons, is formally included in the optical phonon term. The detailed form for J applicable to these processes are discussed considerably in the literature (for example Paige 1964, Conwell 1967). For completeness the form of J is given in Appendix 2.1. We note that in general J has the structure
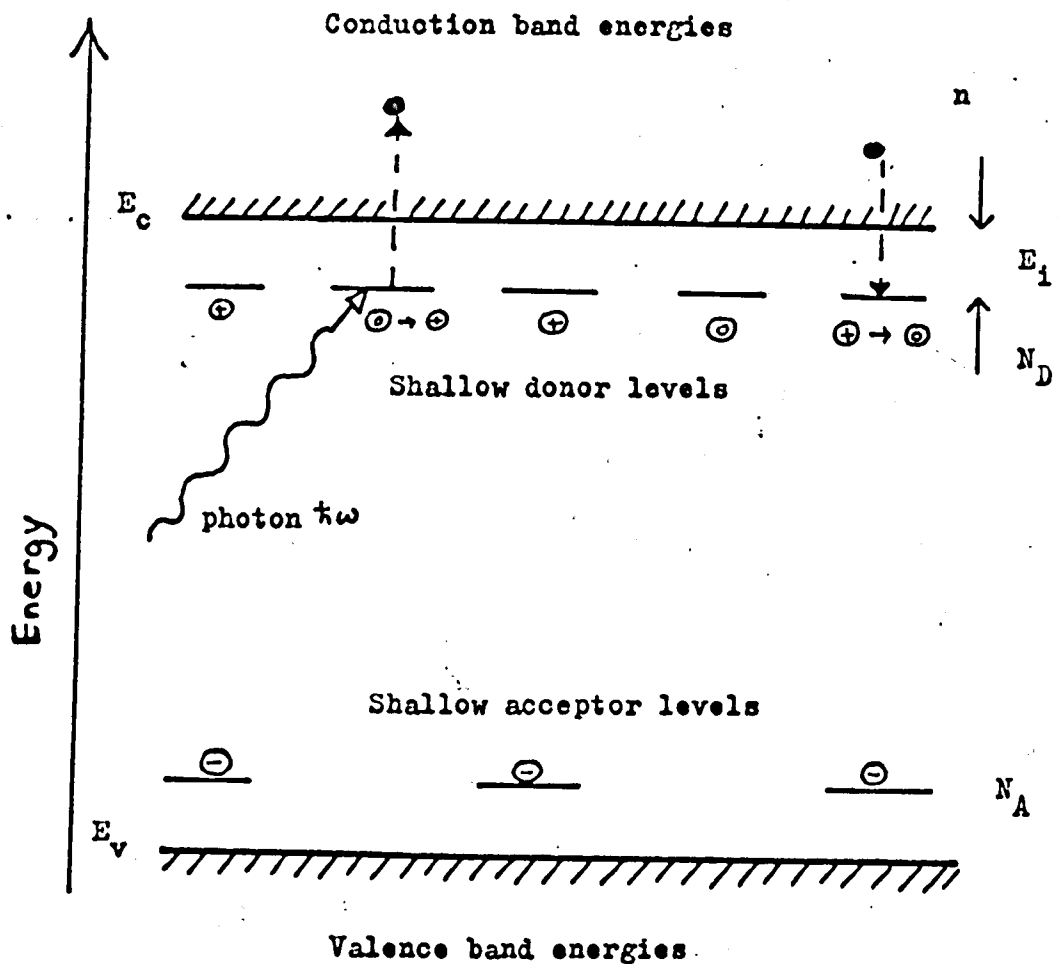
$$J(\underline{k}) = \sum_{\underline{k}'} G(\underline{k},\underline{k}') \left\{ f_o(\underline{k}')e^{\varepsilon'/k_BT} - f_o(\underline{k})e^{\varepsilon/k_BT} \right\} \qquad 2.2.3$$

where $G(\underline{k},\underline{k}')$ is a symmetric function in $\underline{k},\underline{k}'$. It is clear that J vanishes in thermal equilibrium since $f_o(k)$ is then proportional to $\exp(-\varepsilon/k_BT)$. We also point out that our numerical calculations do not involve any approximations for J.

For clarity we now specialise to the case of photoexcited electrons, a similar analysis applies for holes in p type material. We consider the semiconductor to be doped with a concentration N_D of shallow donors, and partially compensated with acceptors of density N_A (where $N_A < N_D$). The acceptors are assumed to be fully ionised so that there are N_A ionised donors and $N_D^o = N_D - N_A$ neutral donors. This is a good approximation at very low temperatures. Electrons are excited from the neutral donors into the band and subsequently recombine with the ionised donors. The general scheme is sketched in Figure 2.1. Relevant experiments have employed very low carrier concentrations which enables us to neglect any change in the fractional ionization of the donors due to the applied radiation. The rate of generation of carriers by a flux of photons incident on the neutral donors is proportional to the neutral donor concentration, the photoionization cross section and the intensity of radiation. We consider shallow donors for which the ionization energy is of the order 0.05eV. The quantity of interest as regards the excitation process is ω_e and this is poorly known experimentally. We therefore adopt a model excitation spectrum

$$\omega_e(\underline{k}) \propto \varepsilon^\ell \exp(-\varepsilon/k_BT_r) \qquad 2.2.4$$

based on a black body radiation field with temperature T_r, where k_B is Boltzmann's constant. We recall that the energy ε is the energy of state $\underline{k}$

Conduction band energies

E_c //

n

E_i

Shallow donor levels

$\oplus$ $\odot \rightarrow \oplus$ $\oplus$ $\odot$ $\oplus \rightarrow \odot$

N_D

photon $\hbar\omega$

Shallow acceptor levels

$\ominus$ $\ominus$ $\ominus$

N_A

E_v ////////////////////////////////////

Valence band energies

FIG 2.1   ILLUSTRATION OF THE DYNAMICS OF EXTRINSIC
           PHOTOEXCITATION NEAR THE BAND EXTREMA OF
           A SIMPLE N-TYPE COMPENSATED SEMICONDUCTOR

relative to the band edge. The exponent ℓ is a positive constant, the shape parameter, which in fact characterizes the selection rules and matrix elements for the electron-photon interaction. Fortunately, the detailed form of ω_e does not seem to be very important in the application of the model; the main requirement is that the spectrum is peaked at some small multiple of $k_B T_r$. Appendix 2.2 contains a brief derivation of the model spectrum. Intrinsic black body radiation from the lattice exists at all temperatures and gives rise to an equilibrium concentration of carriers. However, at very low temperatures, for which $k_B T \sim 0.0025$ eV, this component may be neglected in comparison with high temperature extrinsic radiation (for which $k_B T_r \sim$ 0.025 eV).

The recombination rate into the ionised donors is written

$$
\begin{aligned}
W\omega_r(\underline{k}) &= V(\epsilon)\sigma(\epsilon)N_A f_o(\underline{k}) \\
&= f_o(\underline{k})/\tau(\epsilon)
\end{aligned}
\qquad\qquad 2.2.5
$$

where $\sigma(\epsilon)$ is the capture cross section, $V(\epsilon)$ the carrier velocity, and τ the carrier recombination lifetime. We assume that the recombination takes place via the attractive cascade mechanism (Lax 1960) and we neglect the capture into neutral donors. This latter approximation is generally valid in our applications since the neutral donor concentration is of the same order experimentally as N_A whilst the cross section is considerably smaller. We recall that on the cascade theory, the charged attractive donor centres are considered to possess a set of excited states whose radii increase indefinitely in real space (in fact one should really consider a limit to the size of such "orbital" states because of screening effects and the possible overlap between states associated with different centres). Initial capture of a conduction electron into a highly excited state of large radius may be followed by cascade into more tightly bound states with the emission of

acoustic phonons, or the electron may be thermally reionized back into the band. If the electron reaches an excited state of binding energy greater than $k_B T$ (where T is the lattice temperature) it is effectively trapped and may eventually enter the ground state. Consequently not all the excited states are effective in the capture of electrons, only those with binding energies in excess of $k_B T$ give a large contribution. This leads to a capture cross section which increases rapidly with decreasing temperature as more states become available for firm capture.

Following Lax (1960) we use the cross section

$$\sigma(\epsilon) = (4^5/6)\sigma_1(\tfrac{1}{2} m^* s^2/k_B T)^4 (k_B T/\epsilon)\Phi(\epsilon,T) \qquad 2.2.6$$

where s is the longitudinal velocity of sound and σ_1 is a constant cross section depending on the effective mass, velocity of sound, static dielectric constant and the acoustic deformation potential. The function Φ is given approximately by

$$\Phi \simeq k_B T/\epsilon; \quad \epsilon \gtrsim \tfrac{1}{2} m^* s^2, \qquad 2.2.7$$

so that σ varies approximately as T^{-2} and ϵ^{-2}. At high lattice temperatures the cross section σ is small and the distribution function f_o has the usual Maxwellian form. In that case the form (2.2.7) leads to a divergence in the total recombination rate. It is therefore necessary to introduce a cut off in Φ at low carrier energy. Lax has suggested the more accurate form

$$\Phi \simeq k_B T/(\epsilon + \delta\tfrac{1}{2} m^* s^2); \quad \epsilon \lesssim \tfrac{1}{2} m^* s^2. \qquad 2.2.8$$

where δ is a constant in the range $4 < \delta < 10$. However, the actual form of the cut-off is obscure and a detailed study of the capture of electrons close to the band edge has not yet been given. In our work we have employed both (2.2.8) and other empirical forms but find that the details of the cut off are unimportant for the predominantly high energy distribution of electrons

encountered in the study.   A particularly useful empirical form for the
recombination lifetime is

$$\frac{1}{\tau(\epsilon)} \propto T^{-x} \frac{\alpha}{\alpha+\epsilon^{3/2}} \qquad ; \quad x \text{ an integer;}$$

which has the advantage that by taking α as very large allows the investigation
of energy independent lifetimes with various temperature dependences.   For
$x = 2$, and appropriate choice of α this form is essentially identical to the
Lax model except at very low energies.

The distribution function f_o scales in the parameter W and is therefore
conveniently rewritten in terms of the reduced distribution function $\phi(K)$ defined
by,

$$\phi(K) = 4\pi\rho\gamma^{-3}W^{-1} f_o(\underline{k}) \qquad\qquad 2.2.9$$

where ρ is the density of like spin states in $\underline{k}$-space and

$$K^2 \equiv \gamma^2 k^2 \equiv \hbar^2 k^2/(2m^* k_B T). \qquad\qquad 2.2.10$$

Hence $K\phi(K)dK^2$ is the number of electrons per unit excitation rate in the
reduced energy range K^2 to $K^2 + dK^2$.   The rate equation (2.2.1) becomes

$$\bar{\omega}_e(K) - \phi(K)K/\tau(K) = KJ(\phi(K)) \qquad\qquad 2.2.11$$

with $\bar{\omega}_e(K)dK^2$ the excitation rate into dK^2 i.e.

$$\bar{\omega}_e(K) \equiv 4\pi\rho\gamma^{-3} K\omega_e(K) \qquad\qquad 2.2.12$$

and where the functional dependence of J on ϕ is indicated explicitly.   The
carrier concentration n is given by

$$n = W \int_o^\infty \phi(K)KdK^2 \qquad\qquad 2.2.13$$

The reduced distribution satisfies the normalisation condition (a consequence
of the sum rule 2.2.2),

$$\int_0^\infty K\phi(K) \ \tau^{-1}(K) \ dK^2 = 1 \qquad\qquad 2.2.14$$

and also

$$\int_0^\infty \bar{\omega}_e(K) dK^2 = 1 \qquad\qquad 2.2.15$$

The latter condition leads to

$$\bar{\omega}_e(K) = \frac{(T/T_r)^{\ell+3/2} K^{2\ell+1}}{\Gamma(\ell+3/2)} \ \exp(-K^2 T/T_r) \qquad\qquad 2.2.16$$

where Γ is the gamma function.

We observe that the high temperature Maxwellian limit for ϕ is

$$\phi \propto \exp(-K^2) \qquad\qquad 2.2.17$$

which must be normalised by equation (2.2.14). At low temperatures, scattering is negligible and recombination dominates leading to the limit

$$\phi = \tau(K)\bar{\omega}_e(K)/K. \qquad\qquad 2.2.18$$

The complete rate equation is written out explicitly in Appendix 2.1.

The structure of the rate equation is made more apparent by writing the scattering rate as

$$KJ(\phi(K)) = Z(K)\phi(K) - Y(\phi(K)), \qquad\qquad 2.2.19$$

we then have

$$\phi(K) = \frac{\bar{\omega}_e(K) + Y(\phi(K))}{Z(K) + K/\tau(K)} . \qquad\qquad 2.2.20$$

2.3 Numerical solution

The rate equation (2.2.11) or (2.2.20) is an integral equation for the distribution function ϕ and is solved numerically by iteration. It is assumed

that if ϕ_n is an approximate solution obtained after n iterations, then a better approximation ϕ_{n+1} is given by

$$\phi_{n+1}(K) = N_{n+1}\left\{\frac{\bar{\omega}_e(K) + Y(\phi_n)}{K/\tau(K) + Z(K)}\right\}.$$

The normalisation constant N_{n+1} is a measure of the convergence of the iterative process, and is chosen such that ϕ_{n+1} satisfies the normalisation condition (2.2.14). If the norm converges to unity for successive iterations, then the approximate solutions converge to the exact solution. In practice the iterative procedure is continued until either (a) the norm satisfies

$$|N-1| \leq \nu$$

where ν, the tolerance, is an arbitrary small positive number less than unity; or (b) until an arbitrary number, say P, iterations have been performed. Typically ν is chosen of the order 10^{-4}, and P = 10. In all cases investigated convergence was at worst to within a tolerance of 10^{-2}.

The inherent difficulty in the iterative procedure is the choice of a suitable starting function ϕ_1. The standard approach would involve using the normalised inhomogeneous part of the integral equation as a starting function. However, this is not in general a good approximation to the exact solution and leads to poor convergence. Instead we use a generalisation of the iterative technique due to Hearn (1966) in which a physically acceptable trial function is used for ϕ_1. A highly convergent procedure for solving the rate equation over a range of temperatures is to use the normalised Maxwellian limit as the starting function at the highest temperature, i.e.

$$\phi_1 = N_1 \exp(-K^2).$$

The resulting solution, when re-normalised, then acts as the starting function at the next lowest temperature and so on. For a set of very low temperatures it is more efficient to use ascending temperatures and the other asymptotic limit, i.e.

$$\phi_1 = N_1 \tau(K) \bar{\omega}_e(K)/K.$$

In order to check the iterative procedure the zero field distribution function was obtained for a few particular cases by a Monte Carlo method which effectively bypasses the Boltzmann equation. This technique is described in detail in Chapter III. The distribution functions obtained by the two methods were essentially identical. The Monte Carlo method has very much slower convergence that the iterative technique, particularly at high temperatures. This prohibited its use except at temperatures below about $5^{\circ}K$. However, the Monte Carlo technique is not restricted to low applied fields, and for high fields is superior to the conventional method of applying perturbation theory to the Boltzmann equation.

In numerical computation the continuous variable K is replaced by a discrete variable which spans a uniform discrete mesh in K-space, from zero up to a maximum of $K = 400\Delta$. Here Δ, the mesh gauge, is chosen as

$$\Delta = \frac{1}{8} \left(\frac{2m_D s^2}{k_B T} \right)^{\frac{1}{2}}$$

which represents a small fraction of the typical energy transferred in an electron phonon collision. The various functions appearing in the rate equation are tabulated at the mesh points and the integrations carried out by conventional techniques. The rate of convergence is not significantly improved by increasing the upper energy limit or by using a finer mesh.

Calculations were carried out on the Chilton ATLAS and Warwick Elliott 4130 computers.

2.4 Distribution functions

We have obtained distribution functions for a wide range of parameters in the temperature range 1°K to 40°K. The general form of the reduced distribution function, as a function of energy and lattice temperature, is illustrated in Figure 2.2. These curves were computed for n-germanium assuming a slope parameter $\ell = 1$, and a radiation temperature $T_r = 300^{\circ}$K. The other parameters employed are given in Table 2.1. The main features are as follows:

(i) at high temperatures, $T \geq 30^{\circ}$K, corresponding to long carrier lifetimes, the carriers are closely thermalised to the lattice and satisfy a Maxwellian distribution.

(ii) at lower temperatures the carrier lifetimes are shorter and the distribution function is non-Maxwellian. It may be approximately represented by the sum of two Maxwellian distributions, one for low energy and the other for high energy. The lower energy Maxwellian is characterised by an effective temperature near to the lattice temperature. On the other hand, the high energy Maxwellian has an effective temperature closer to the radiation temperature. For energies above the optical phonon emission threshold, optical phonon scattering dominates and induces a cut off to the distribution function (this is not shown in the figure).

(iii) at very low temperatures, $T \leq 3^{\circ}$K, the cascade capture cross section becomes large, and the distribution of carriers is essentially determined by competition between the excitation and recombination rates and reflects their detailed forms. Convergence of the iterated solutions in this region is slow, reflecting the rapid change of the low energy distribution with temperature. The curve for $T = 1^{\circ}$K in Figure 2.2 shows the occurrence of a peak to the distribution function. This is partly a consequence of the depletion of carriers with very low energies due to the fast recombination rate for low energy carriers on the Lax model.

REDUCED DISTRIBUTION FUNCTION

CARRIER ENERGY (ev)

$T = 24^{\circ}$ K

$T = 17^{\circ}$ K

$T = 10^{\circ}$ K

$T = 2^{\circ}$ K

$T = 1.5^{\circ}$ K

$T = 1^{\circ}$ K

$T = 3^{\circ}$ K

10^{-7}

10^{-8}

10^{-9}

10^{-10}

10^{-11}

10^{-12}

10^{-3} 5×10^{-3} 1×10^{-2} 1.5×10^{-2}
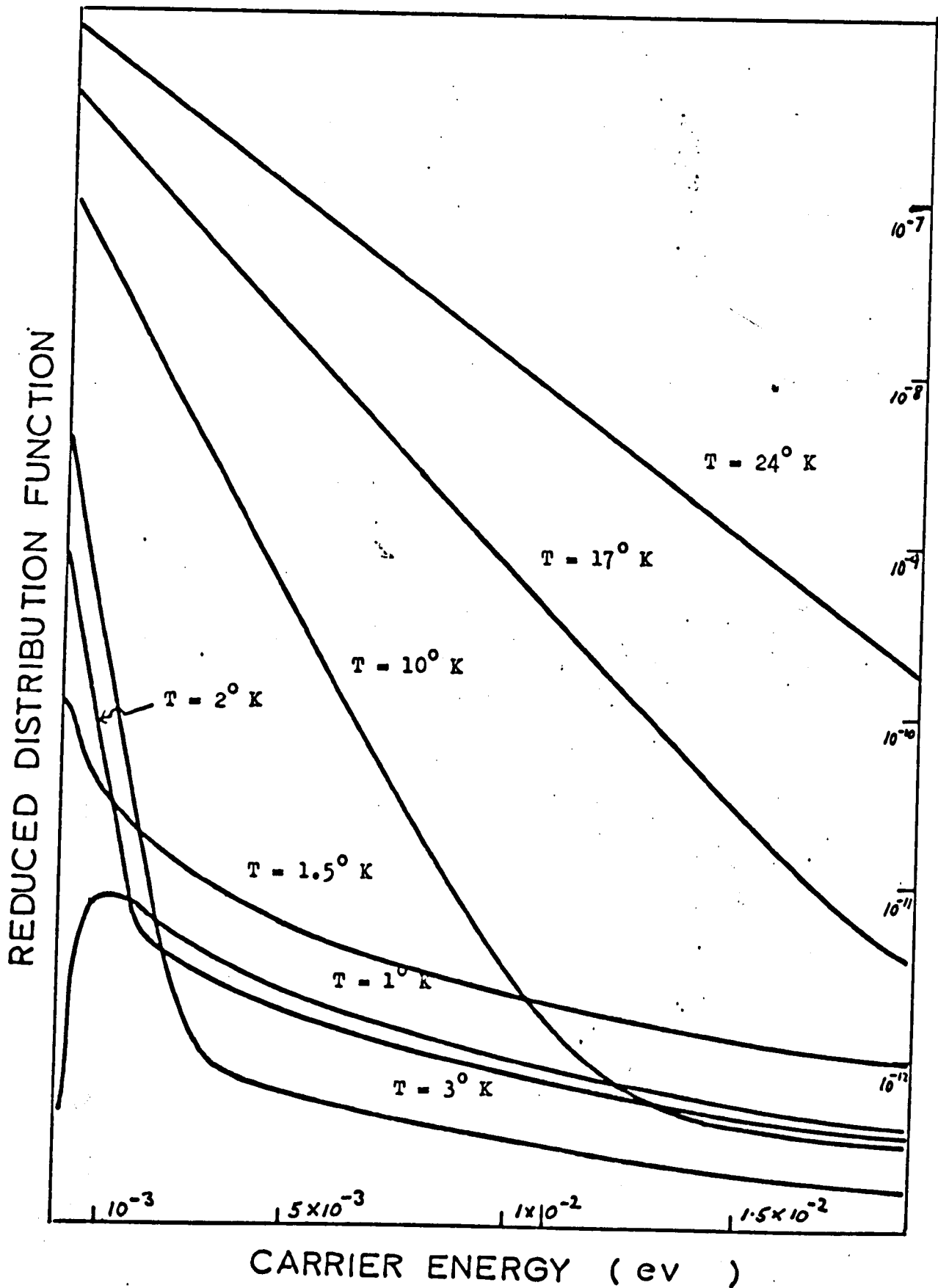
FIG 2.2   DISTRIBUTION FUNCTIONS FOR N-GERMANIUM

TABLE 2.1	DATA FOR CALCULATIONS ON N- GERMANIUM
RADIATION TEMPERATURE	300° K
SHAPE PARAMETER	1
DENSITY OF STATES EFFECTIVE MASS RATIO	0.218
VELOCITY OF SOUND	5.49×10^{5} cm sec^{-1}
DEFORMATION POTENTIAL (ACOUSTIC PHONONS)	11.8 eV
DEFORMATION POTENTIAL (LO PHONONS)	30 eV
DENSITY	5.32 gm cm^{-3}
TRAP DENSITY	10^{16} cm^{-3}

Similar forms are obtained for ϕ by using a constant recombination lifetime of the same magnitude as the average lifetime on the cascade model. However, this is a qualitative similarity only and the same temperature dependence is not obtained.

2.5 Low field transport

The low field trapping and transport parameters are obtained from the isotropic zero field distribution function $\phi(K)$ by the application of perturbation theory in a similar fashion to conventional low field transport theory (c.f. Ziman 1960). This approach is justified if the response to the external fields used experimentally is Ohmic (that is linear). In general these fields do not exceed about 1 V cm^{-1} and there is no experimental evidence of significant non-Ohmic effects. In fact one would not expect nonlinear effects at these fields because of the dispersed nature of the distribution of electrons over momentum space (this is to be contrasted with the situation in the oscillatory photoconductivity effect discussed in Chapters IV and V). Fortunately we were able to check the assumption of linear response to external fields in the Monte Carlo calculations discussed in section 2.3. These calculations were also performed with the inclusion of a field of order 1 V cm^{-1} which gave the various transport parameters directly. It was found that the Monte Carlo calculations were in very good agreement with those performed on the basis of the perturbation theory approach which we now outline.

The basic rate equation for the zero field distribution function $f_o(\underline{k})$ was shown in section 2 to have the form,

$$W\omega_e(\underline{k}) - f_o(\underline{k})/\tau(\epsilon) - J(\underline{k}) = 0 \qquad\qquad 2.5.1$$

In the presence of externally applied electric and magnetic fields (denoted

by $\underline{F}$ and $\underline{B}$) the new steady state distribution function $f(\underline{k})$ is no longer isotropic. The corresponding rate equation is then similar to (2.5.1) but now contains contributions from the elastic scattering processes and the accelerating effects of the applied fields. The latter term describes the rate of change of $f(\underline{k})$ due to the fields and takes the form (see for example Paige 1964),

$$\left.\frac{\partial f(\underline{k})}{\partial t}\right|_{fields} = -\frac{e}{\hbar}\left\{\underline{F} + \left(\frac{1}{\hbar}\frac{\partial\varepsilon}{\partial\underline{k}} \wedge \underline{B}\right)\right\}\cdot\frac{\partial f(\underline{k})}{\partial\underline{k}} \qquad . \qquad 2.5.2$$

To first order in the electric field the isotropic part of the finite field distribution function is given by $f_0(\underline{k})$. On the other hand the anisotropic part $f_1(\underline{k})$ is determined by the momentum relaxation processes involving electron-phonon and electron impurity interactions. These processes are characterised by a total momentum relaxation time $\tau_s(\underline{k})$ (see for example Paige 1964). Using the zero field equation (2.5.1) and the decomposition $f = f_0 + f_1$, we find to first order in electric field the basic finite field rate equation

$$-\frac{e}{\hbar}\underline{F}\cdot\frac{\partial f_0(\underline{k})}{\partial\underline{k}} - \frac{e}{\hbar^2}\left(\frac{\partial\varepsilon}{\partial\underline{k}} \wedge \underline{B}\right)\cdot\frac{\partial f_1(\underline{k})}{\partial\underline{k}} - f_1(k)\left[\frac{1}{\tau_s(\underline{k})} + \frac{1}{\tau(\underline{k})}\right] = 0.$$

$$2.5.3$$

This equation is identical to the conventional Boltzmann transport equation (c.f. Ziman 1960) except that the thermal equilibrium distribution function is replaced by $f_0(\underline{k})$ and the total momentum relaxation includes a contribution from the recombination process. In practice this latter term has negligible effect since $\tau \gg \tau_s$.

Conventional transport theory (e.g. Smith 1960) applied to equation (2.5.3) gives the low field transport parameters as averages over the zero field distribution function f_0. For a simple band structure characterised

by an energy-wave-vector dispersion relation

$$\epsilon = \frac{\hbar^2 k^2}{2m^*}$$

we find the drift mobility μ, Hall mobility μ_H, Hall number r and magneto-resistance number X as

$$\left.\begin{array}{l} \mu = \dfrac{e}{m^*} << \tau_s >> \; ; \\[2em] \mu_H = r\mu \qquad\qquad ; \\[2em] r = << \tau_s^2 >>/<< \tau_s >>^2 \; ; \\[2em] X = << \tau_s^3 >><< \tau_s >>/<< \tau_s^2 >>^2 \; . \end{array}\right\} \qquad 2.5.4$$

The averages are defined in terms of the reduced distribution function $\phi(K)$ rather than $f_o(\underline{k})$ as

$$<< \tau_s^P >> = -\frac{1}{3} \frac{\displaystyle\int_o^\infty K^3 . \partial\phi/\partial K . \tau_s^P (K) dK}{\displaystyle\int_o^\infty K^2 \phi(K) dK} \qquad . \qquad 2.5.5$$

We briefly recall the origin of the above transport parameters. The drift mobility is simply the average drift velocity acquired by the carriers in a unit electric field. The Hall coefficient R, which can be directly measured by experiment, is defined by

$$\underline{E}_H = R \underline{j} \wedge \underline{B}$$

where the Hall field $\underline{E}_H$ is the electric field which is induced at right angles to a constrained current flow $\underline{j}$ in the presence of magnetic field $\underline{B}$. A well known result from conventional transport theory (Paige 1964) then identifies the experimentally Hall coefficient in terms of the Hall number r and carrier density n as

$$R = \frac{r}{ne} \qquad .$$

Another important experimental observable is the magnetoresistance ξ defined as the fractional increase in resistivity due to the presence of a magnetic field. The low field magnetoresistance is related to the magnetoresistance X, which like the Hall number is generally not available experimentally,

$$\xi = (X - 1)r^2 \mu^2 B^2.$$

In applications to electrons in germanium and silicon the transport formulae (2.5.4) are amended to take into account the realistic energy bands and effective mass anisotropies (see for example, Paige 1964). This can be done in a systematic way by using suitably averaged values for the effective mass in the basic zero field rate equation and also in the expressions for low field transport properties (see for example Herring 1955). For example, the effective mass occurring in the scattering rate term arises from the density of states into which an electron may be scattered. The appropriate effective mass is m_D, the density of states effective mass which for electrons in germanium is given by

$$m_D = (m_1 \, m_2^2)^{1/3} \, .$$

Here m_1, m_2 are the longitudinal and transverse effective masses describing the structure of the conduction band minima in the <111> directions in K-space (these are the minima which are occupied by photoelectrons under the conditions of our model). Similarly the effective mass appearing in the expression for drift mobility is the conductivity effective mass m_c which again for germanium is defined by

$$1/m_c = (1/m_1 + 2/m_2)/3.$$

The Hall mobility, Hall coefficient and magnetoresistance number are also modified. Table 2.2 gives the modifications appropriate to electrons in germanium. Similar forms arise for silicon (Smith 1960).

TABLE 2.2	MODIFICATIONS TO THE LOW FIELD TRANSPORT PARAMETERS IN N*GERMANIUM
EFFECTIVE MASS ANISOTROPY	$K_m = m_1/m_2$
CONDUCTIVITY	$\sigma = ne^2 \langle \tau \rangle / m_c$
CONDUCTIVITY MOBILITY	$\mu = e \langle \tau \rangle / m_c$
HALL MOBILITY	$\mu_H = \dfrac{3 K_m (2 + K_m) \tau \mu}{(2 K_m + 1)^2}$
HALL COEFFICIENT	$R = \dfrac{\tau}{ne} \cdot \dfrac{3 K_m (K_m + 2)}{(2 K_m + 1)^2}$
MAGNETORESISTANCE NUMBER	$X_{100}^{001} = \dfrac{(2 K_m + 1)^2}{3 K_m (K_m + 2)} X$

m_1 : longitudinal effective mass; m_2 : transverse effective mass

Some caution has to be exercised with regard to the momentum relaxation processes considered. In hot carrier problems it is not always known which of the scattering mechanisms are likely to dominate and the situation may differ radically from that of thermalised carriers. Consequently it is difficult to establish a satisfactory model without including all possible mechanisms. Previously this has led to difficulties in the interpretation of some experiments. In application to germanium and silicon the momentum relaxation time is compounded from acoustic deformation, ionized and neutral impurity scattering. The forms of these relaxation times are given in Appendix 3.2, and have been described in detail by Conwell (1967). Optical phonon scattering is not significant as regards momentum loss in view of the low energy character of the distribution function $\phi(K)$. For ionized impurity scattering we adopt the Brooks-Herring model (Brooks 1955), choosing the effective temperature appearing in the screening length as the electron temperature T_e defined by

$$\frac{3}{2} k_B T_e = <\varepsilon>$$

2.5.6

where $<\varepsilon>$ is the average carrier energy. This involves the direct average $< >$ defined by

$$<\varepsilon> = \frac{\int_0^\infty \varepsilon \, \phi(K) \, K \, dK^2}{\int_0^\infty \phi(K) \, K \, dK^2}$$

2.5.7

This procedure is apparently valid for normal high field Maxwellian heating (Alba and Das 1968) but is an approximation in our work. Neutral impurity scattering is handled by Erginsoy's model (1950). Acoustic phonon scattering is considered on the deformation potential model due to Shockley and Bardeen (1950).

2.6 Lifetimes and cross sections

The steady state equation (2.2.1) may be integrated to give

$$W = n \ <1/\tau(K)> \ = n \ <V(K)\sigma(K)> \ N_A \qquad\qquad 2.6.1$$

where n is the carrier concentration. This equation expresses the steady state balance between the total excitation and recombination rates. As before we deal with photoexcited electrons; a similar analysis applies to holes. Here < > is the direct average defined in section 2.5. The average recombination lifetime and cross section are then defined by

$$\tau \equiv <1/\tau(K)>^{-1} , \qquad\qquad 2.6.2$$

$$\sigma \equiv <V(K)\sigma(K)>/V_t \qquad\qquad 2.6.3$$

where V_t is the mean thermal velocity. We have used here the customary definition for σ which is quoted in most experimental work. Clearly this is not a very meaningful definition from a physical point of view when the electrons are heated. For a thermal distribution of carriers it is easy to show that the temperature dependence of σ and τ on the Lax model for capture are approximately T^{-4} and $T^{3.5}$ respectively. This follows from equation (2.2.6).

There are two basic methods of investigating capture cross sections and trapping lifetimes which have been used for shallow impurities at low temperatures. One approach (e.g. Konig 1958) uses a transient technique involving observation of the time decay of the current following application of a voltage pulse to the sample. A more accurate method which has been used recently, and is of particular relevance to the present work, is typified in the steady state technique employed by Levitt and Honig (1960, 1961) and Loewenstein and Honig (1966). This method involves measurement of the lifetimes of electrons which are photoexcited from shallow impurities.

at low temperatures by extrinsic radiation peaked in the 2 to 20 micron range (or 0.6 eV to 0.01 eV). Impurity concentrations, that is N_A, N_D are determined by a combined optical and paramagnetic resonance technique at low temperature together with a room temperature measurement of resistivity. The carrier densities are kept low so that the neutral impurity concentration can be taken as $N_D^0 = N_D - N_A$. Impurity concentrations are generally kept between 10^{13} to 10^{16} cm^{-3} in these experiments. The rate W is determined by an electron spin resonance technique and the trapping parameters τ and σ deduced from measurements of W and   n   the steady state carrier concentration:

$$\tau = n/W \; ; \quad \sigma = W/(N_A V_t n) \qquad\qquad 2.6.4$$

Similar techniques were employed by Rollin and Rowell (1960) and Betjemann (1965).

Experimentally, the carrier concentration is deduced from the Hall coefficient R as $r/(Re)$ where the Hall number is inaccessible to experiment. Usually r is taken to be a constant of order unity. In the case of a thermal distribution or Maxwellian heating this approximation is valid (e.g. for momentum relaxation determined by ionized impurity scattering only $r = 1.93$, and for lattice scattering only $r = 1.18$). But this assumption fails for non Maxwellian heating. The carrier heating considered in our work is non Maxwellian (see section 2.4), and moreover the shape of the heated distribution varies rapidly with the lattice temperature. Consequently r becomes strongly dependent on lattice temperature through the energy dependence of the total momentum relaxation time τ_s (for ionized impurity dominated relaxation we have found values for r in excess of 30; although in practice other momentum relaxation processes act to reduce these large values). It is therefore vital to interpret the experimental work as actually providing curves of

$$\tau_E = \tau/r, \quad n_E = n/r$$

and $\sigma_E = r\sigma$ (Barker and Hearn 1968).

Figures 2.3 and 2.4 show the temperature variation of σ_E, n_E as reported by Levitt and Honig (1961) and Rollin and Rowell (1960). The sample data are given in Tables 2.3 and 2.4. These results pertain to n-silicon and p-germanium respectively. Both experiments involved radiation fields of the type basic to our model. Levitt and Honig used radiation peaked in the extrinsic radiation range from 0.045 eV (the approximate shallow trap depth) to 0.6 eV. This radiation was considered to excite electrons from the neutral donors (Phosphorus donors and compensating Boron acceptors) into the 6-fold degenerate lowest conduction band minima for silicon (see Figure 2.5, which sketches the conduction band and essential transitions involved). Rollin and Rowell used room temperature black body radiation to excite holes from neutral copper acceptors into the valence band. Copper acts as a triple acceptor in germanium with two deep levels and one shallow level ($E_i \simeq 0.04$ eV, Tyler 1959). The shallow states are compensated and recombination occurs at these shallow ionized acceptor levels. The energy band scheme is sketched in Figure 2.6. It is clear from these results that for decreasing lattice temperature the temperature variation of σ_E deviates from that predicted by the straightforward Lax model (T^{-4} dependence). Indeed an apparent cut-off in the temperature dependence occurs at very low temperatures. This takes the form of a $T^{-\frac{1}{2}}$ variation of σ_E below 3°K in silicon. In the case of holes in germanium the cut-off occurs at a higher temperature, exhibiting a change of slope of n_E (which is proportional to τ_E) to T^4 near 19°K, followed by a possible peaked region around 15°K. A similar effect was reported by Betjemann (1965). There have been previous attempts to explain the observed cut-off (Brown and Rogriguez 1967; Brown 1966) in terms of overlap of the excited states, screening and impurity conduction as well as improved calculations of the capture process. But although these processes undoubtedly play some part they do not explain the wide range of experimental results.
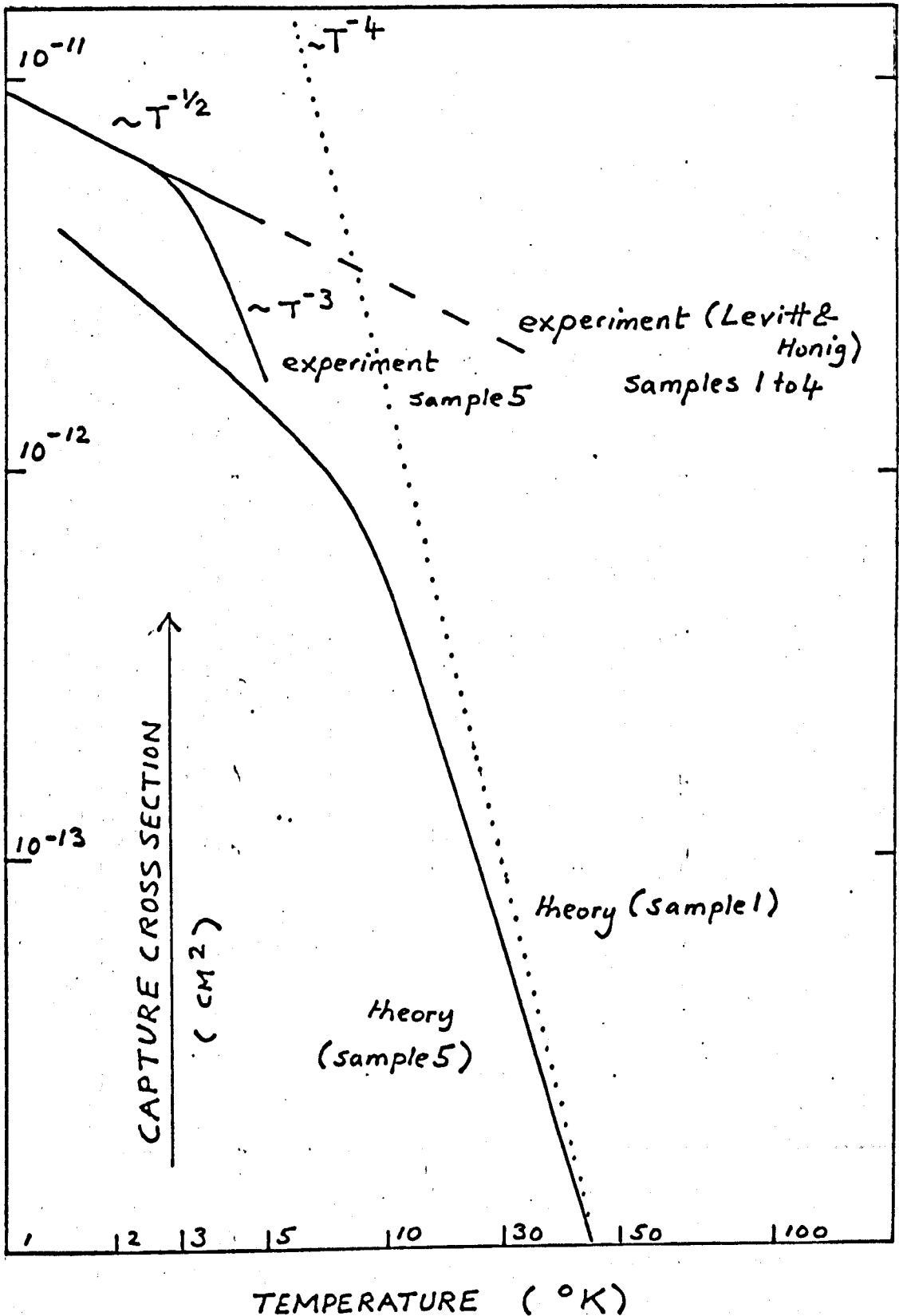
FIG 2.3   COMPARISON OF THEORETICAL AND EXPERIMENTAL CAPTURE
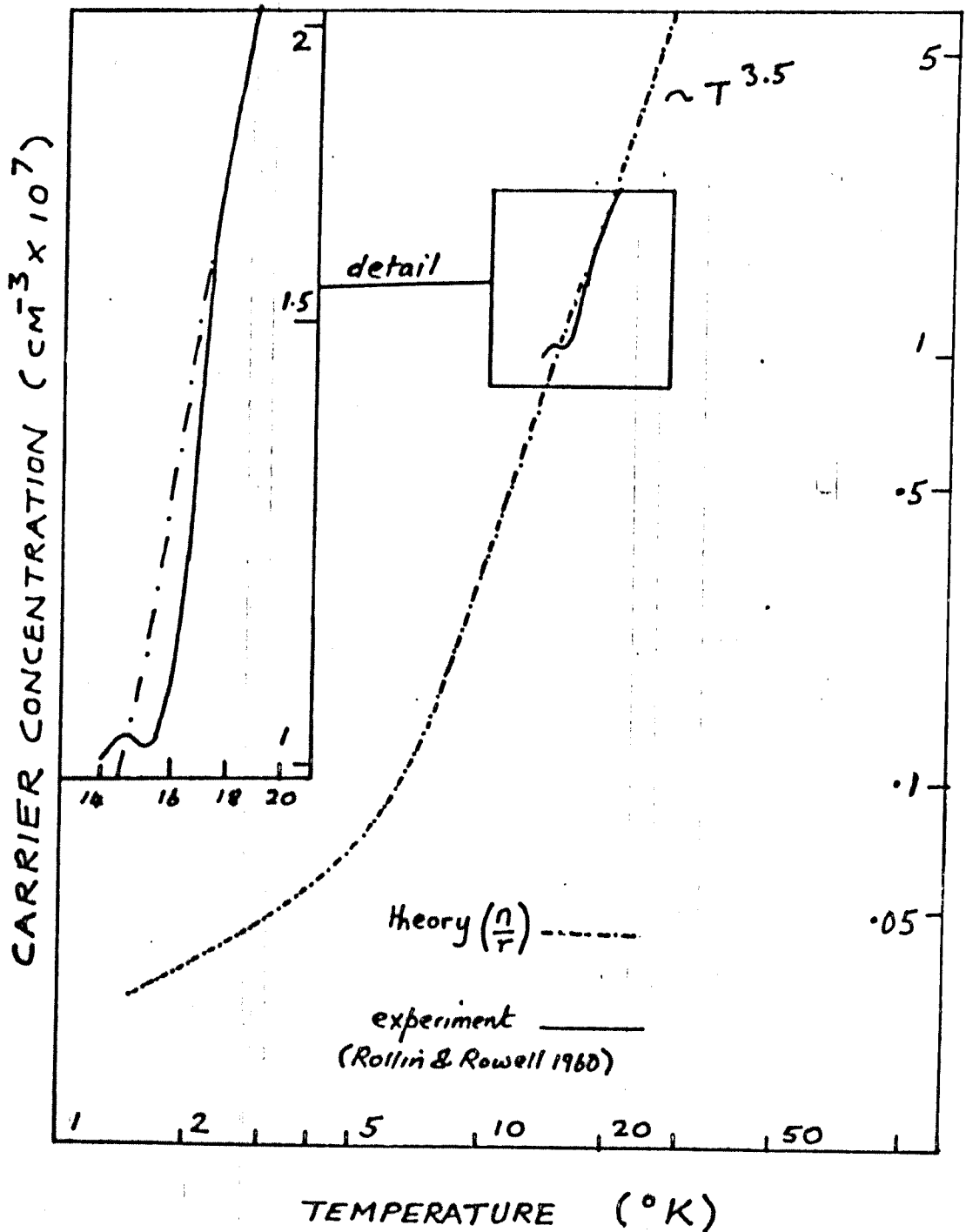CROSS SECTIONS FOR ELECTRONS IN SILICON

FIG 2.4 COMPARISON OF THEORETICAL AND EXPERIMENTAL VARIATION OF THE CONCENTRATION OF PHOTOEXCITED HOLES IN GERMANIUM

TABLE 2.3   SAMPLE DATA FOR N- SILICON

(AFTER LEVITT AND HONIG 1961)

Sample	N_A cm^{-3}	N_D cm^{-3}	$N_D^o = N_D - N_A$ cm^{-3}	N_A/N_D^o	N_D^o/N_A
1	0.5×10^{14}	1.5×10^{14}	1.0×10^{14}	0.5	2
2	0.2×10^{14}	1.9×10^{14}	1.7×10^{14}	0.12	8.3
3	1.7×10^{14}	6.5×10^{14}	4.8×10^{14}	0.35	2.8
4	6.0×10^{15}	2.0×10^{15}	4.0×10^{15}	0.66	1.5
5	4.5×10^{16}	0.15×10^{16}	4.4×10^{16}	0.03	33.3

TABLE 2.4   SAMPLE DATA FOR P- GERMANIUM

(AFTER ROLLIN AND ROWELL 1960)

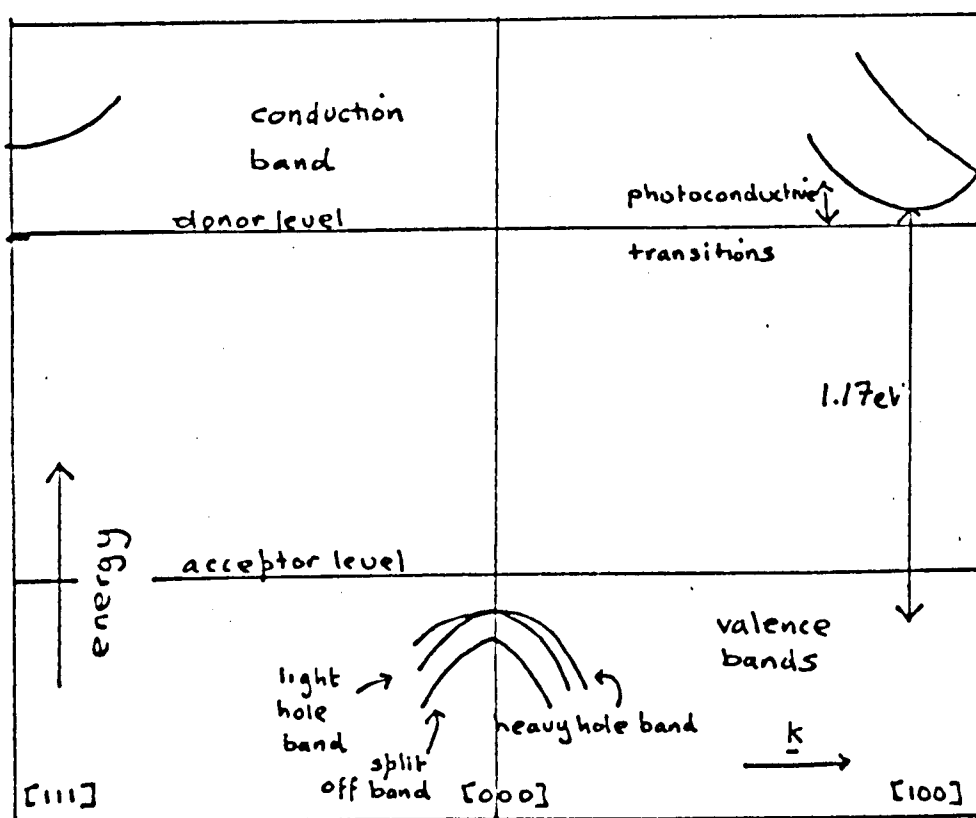|	N_A cm^{-3}	N_D cm^{-3}	$N_A^o = N_A - N_D$ cm^{-3}	
	1.3×10^{16}	1.0×10^{15}	1.2×10^{16}	

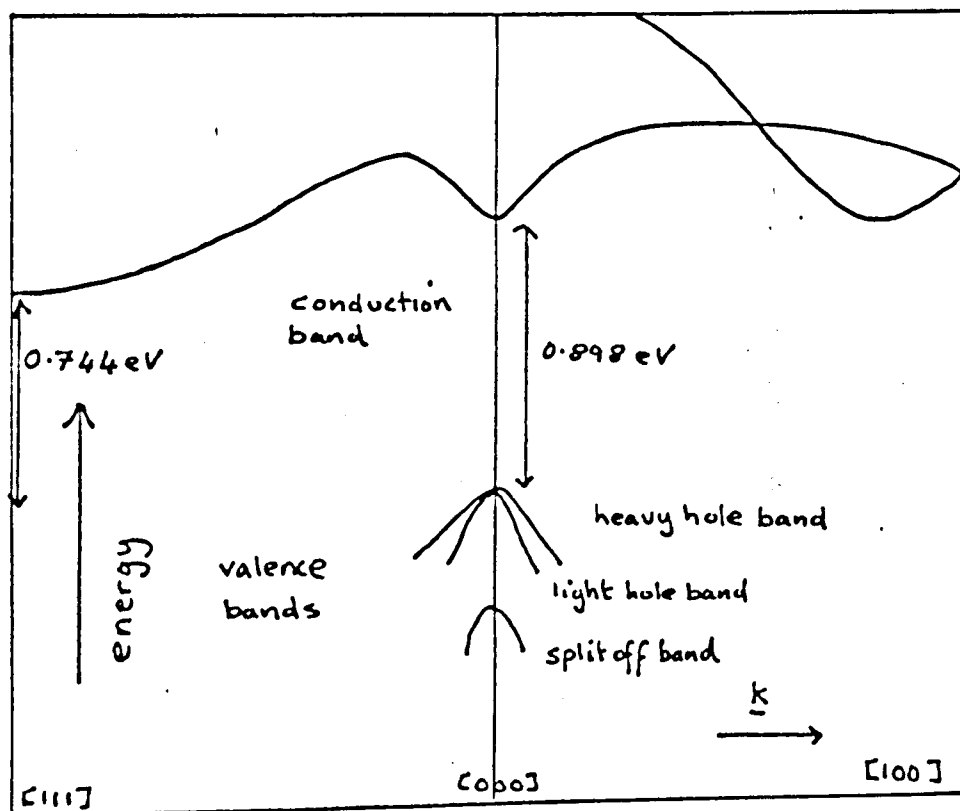FIG 2.5 SKETCH OF ENERGY BANDS IN SILICON

FIG 2.6 SKETCH OF ENERGY BANDS IN GERMANIUM

Shown alongside the experimental results are our computed curves for $r\sigma$, n/r based on a similar set of parameters. (The data used is given in Tables 2.5, 2.6; the curve for $r\sigma$ corresponds to the data for sample 5 of Table 2.3.) Despite the simplicity of the model we obtain reasonable agreement with the experiment of Rollin and Rowell and for sample 5 in Levitt and Honig's work. No agreement was found for samples 1 to 4. Only with sample 4 is there any noticeable carrier heating and this has little effect on the temperature dependence of $r\sigma$. In fact samples 1 to 4 give the temperature variation of σ_E as approximately T^{-4}, as expected for closely thermalised carriers. We note that the trap densities for these samples is much less than for sample 5 so the overall recombination lifetimes are larger. The temperature dependence of $r\sigma$ for sample 1 is shown as the dotted line in Figure 2.3. Discussion of the significance of these anomalous experimental results, which are at variance with the Lax theory, is deferred until section 8. To some extent the deviation from the simple Lax model for sample 5 is due to averaging over a hot carrier distribution which becomes increasingly independent of lattice temperature as the lattice is cooled. In fact Mattis (1961) has previously suggested that the cut-off is due to carrier heating arising from the capture process becoming faster than that of thermalisation at low temperatures. An objection to this interpretation was given by Loewenstein and Honig (1966): namely that a temperature independent distribution of carriers cannot give rise to a $T^{-\frac{1}{2}}$ variation of σ_E, since there must remain a residual temperature dependence from the terms in T in equation (2.2.6) which involve the "sticking probability" in the excited states of the traps. However, the major source of the cut-off may be attributed to the temperature dependence of the Hall number. If the Hall number is assumed constant in the calculations we do not find any close agreement with experiment. The temperature dependence arises from the non Maxwellian character of the distribution functions (which are similar to those in Figure 2.2) and the energy dependence of the momentum relaxation time. The detailed form of the temperature dependence of r is determined by the

TABLES 2.5 & 2.6	DATA FOR CALCULATIONS ON SILICON & GERMANIUM	
SEMICONDUCTOR	P- Ge	N- Si
TEMPERATURE RANGE (LATTICE)	$1.5 - 28^{\circ}$K	$1.5 - 28^{\circ}$K
RADIATION TEMPERATURE	300°K	300°K
DENSITY	5.32 gm cm^{-3}	2.33 gm cm^{-3}
VELOCITY OF SOUND	5.4×10^{5} cm s^{-1}	5.0×10^{5} cm s^{-1}
DENSITY OF STATES EFFECTIVE MASS RATIO	0.347	0.3
CONDUCTIVITY EFFECTIVE MASS RATIO	0.293	0.26
EFFECTIVE DEFORMATION POTENTIAL (ACOUSTIC PHONONS)	5.7 eV	6 eV
EFFECTIVE DEFORMATION POTENTIAL (LO PHONONS)	34 eV	30 eV
LO PHONON ENERGY - EQUIVALENT TEMPERATURE	315°K	190°K
DONOR DENSITY	10^{15} cm^{-3}	4.5×10^{16} cm^{-3}
ACCEPTOR DENSITY	1.3×10^{16} cm^{-3}	0.15×10^{16} cm^{-3}

MOBILITY LIMITED BY ACOUSTIC PHONONS, IONIZED AND NEUTRAL IMPURITIES.

degree of carrier heating and the relative strengths of the various momentum relaxation processes. The effect is most pronounced in the case of dominant ionized impurity scattering because of the strong energy dependence of the associated momentum relaxation time. An extreme case occurs for dominant neutral impurity scattering which has a constant relaxation time; in this case the Hall number is a constant at unity.

The general temperature dependence of the Hall number is illustrated in Figure 2.7 for various admixtures of momentum relaxation processes. The parameters used in the calculation are given in Table 2.7. Curve (a) is for ionized impurity scattering only: the extreme case; curve (b) shows the effect of including lattice scattering; and curve (c) displays the effect of including neutral impurity scattering. The degree of carrier heating for this situation is shown in Figure 2.8, by plotting mean carrier energy against lattice temperature. We note that in the presence of strong non-Maxwellian carrier heating it is difficult to provide an accurate estimate of the effect of the Hall number on the trapping parameters because of the critical dependence of r on the correct admixture of scattering processes. Analytical forms for the temperature dependence of r, similar to those in Figure 2.7, can be obtained on the basis of a double-Maxwellian approximation suggested by the results given in section 4.

2.7 Transport properties

The effect of carrier heating is most pronounced in the temperature dependence of the low field transport parameters. If only ionized impurity scattering is present the momentum relaxation time τ_s is a function of carrier energy only. This leads to p'th order averages $<< \tau_s^p >>$ which are independent of lattice temperature and hence show very strongly any departures from thermalisation. In view of the detailed form of the distribution functions
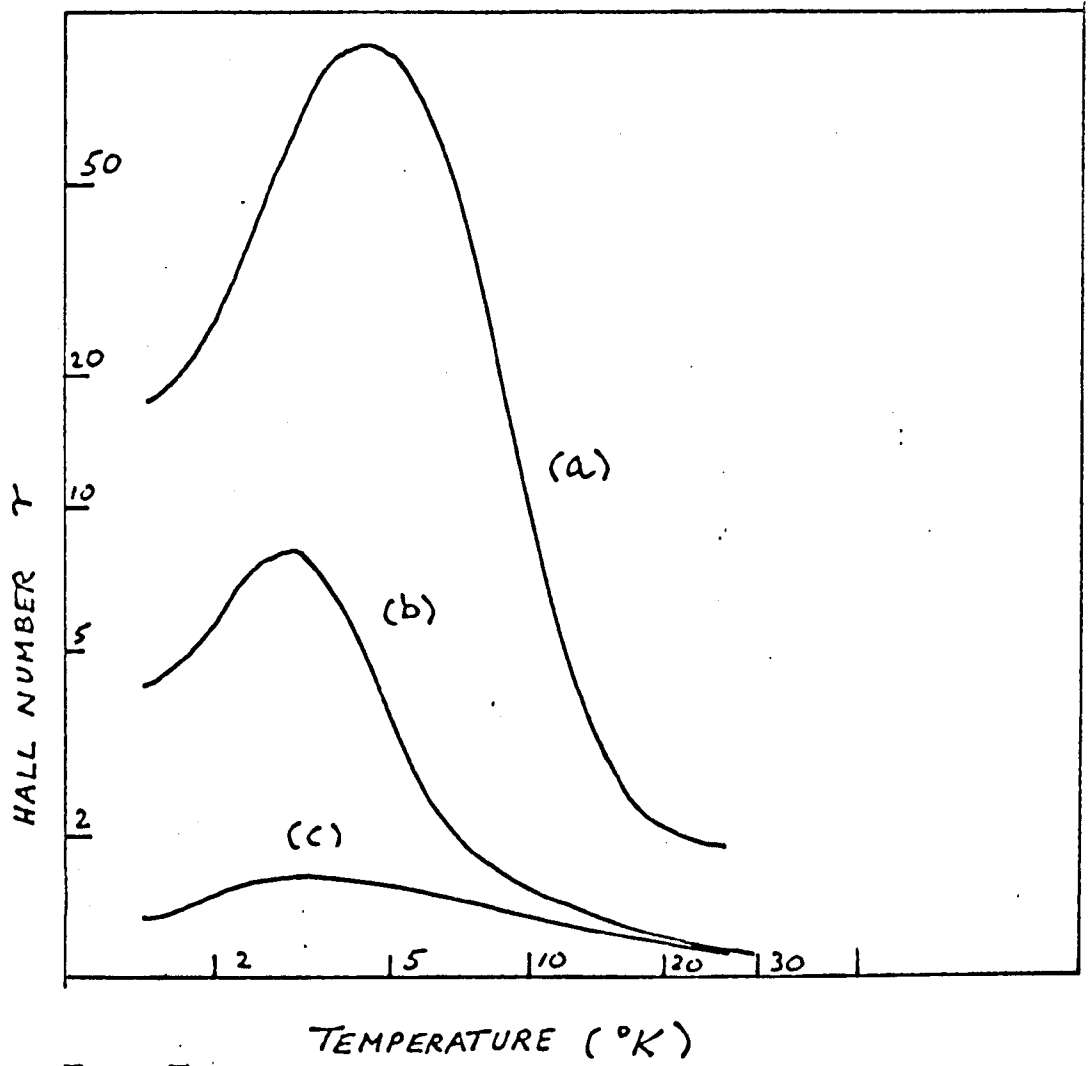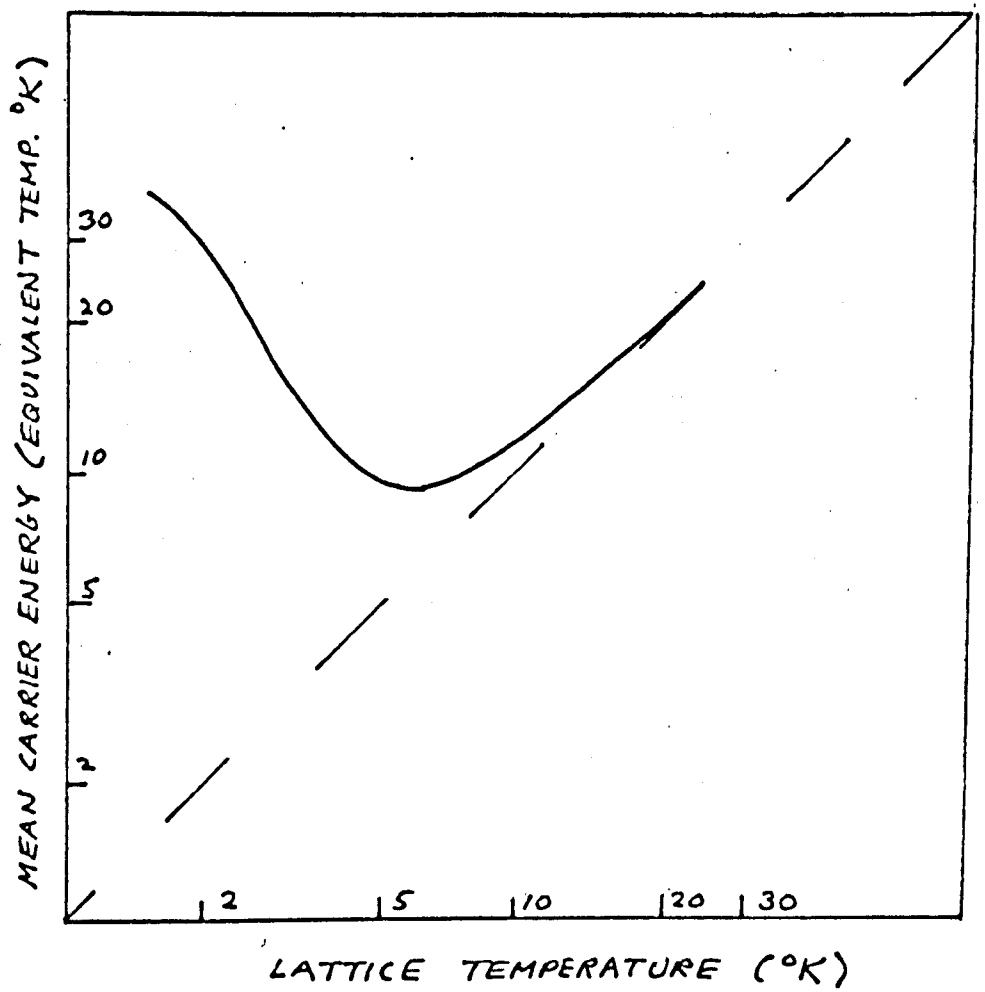
FIG 2.7

FIG 2.8

TABLE 2.7

DATA FOR FIGURES 2.7 AND 2.8 : BASED ON N-GERMANIUM

BASIC DATA FOR THE CALCULATIONS IS GIVEN IN TABLE 2.1 .

AUXILIARY DATA FOR CALCULATION OF TRANSPORT PROPERTIES IS

AS FOLLOWS:

IN FIGURE 2.7 CURVE (a) REPRESENTS DOMINANT IONIZED IMPURITY
SCATTERING WHERE THE DENSITY OF IONIZED CENTRES IS CHOSEN TO
GIVE A HALL MOBILITY OF 3×10^4 CM^2 V^{-1} SEC^{-1} AT 20° K.

             CURVE (b) SHOWS THE EFFECT OF INCLUDING LATTICE
SCATTERING,

             CURVE (c) SHOWS THE EFFECT OF INCLUDING NEUTRAL
IMPURITY SCATTERING FOR 10^{16} NEUTRAL IMPURITIES PER CUBIC
CENTIMETRE.

(c.f. section 4) the higher order moments $<< \tau_s^p >>$ sample the high energy hot tail of the distribution, exhibiting deviations from the thermalised behaviour at higher temperatures than the lower order moments. For example, the magneto-resistance number X defined for a simple band structure by equation (2.5.4) is strongly peaked and shows the effect of carrier heating at higher lattice temperatures than the Hall mobility μ_H, or the Hall number r. As an example we display r and X as functions of temperature in Figure 2.9, for the case of dominant ionized impurity scattering and the very hot distributions shown in Figure 2.2. The large values of r and X are a consequence of the single momentum relaxation process and the large degree of carrier heating. Similar remarks apply for lattice scattering but τ_s then contains a residual dependence on lattice temperature and a weaker energy dependence. With ionized impurity scattering, the carrier heating is exhibited by an increase in Hall mobility with decreasing temperature as compared with the $T^{3/2}$ behaviour for thermalised carriers. The effect is more complicated for lattice scattering and depends on the competition between the residual temperature dependence and the increase in mean carrier energy with decreasing temperature.

When several scattering processes are present, for example lattice, neutral and ionized impurity scattering, the heating effects are extremely complicated and depend critically on the relative contributions to τ_s.

Experimental measurements of the transport parameters for optically excited hot carriers are unfortunately scarce, and we have only been able to apply the theory to the work of Rollin and Rowell (1960) and Betjemann (1965). Calculations for the Hall mobility of holes in germanium based on the parameters given in Table 2.6, are compared with experiment in Figure 2.10. The heating observed by Rollin and Rowell is confirmed and reasonable agreement is obtained for the temperature dependence. Figure 2.11 shows the effective electron temperature
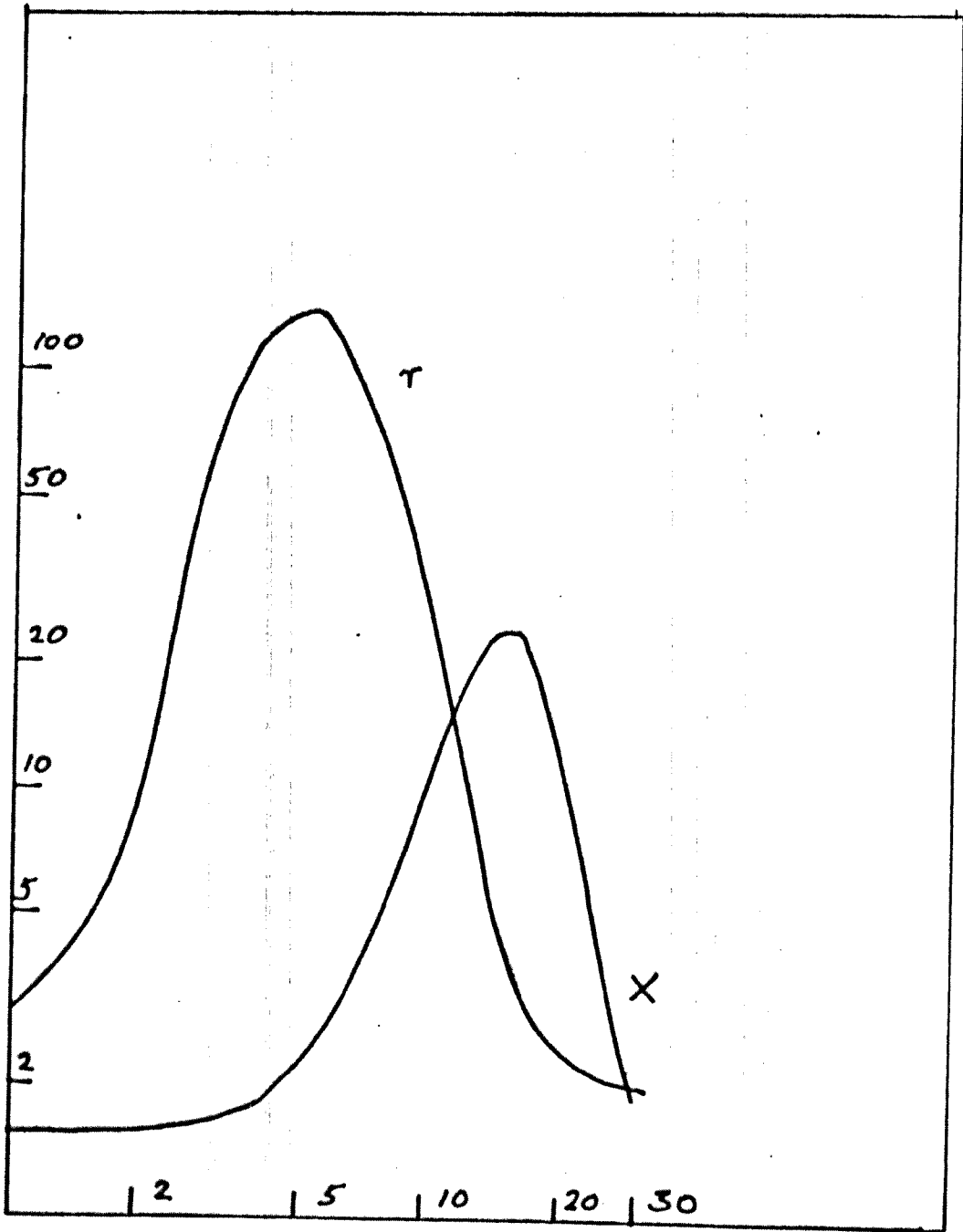
FIG 2.9 HALL NUMBER r AND MAGNETORESISTANCE NUMBER X
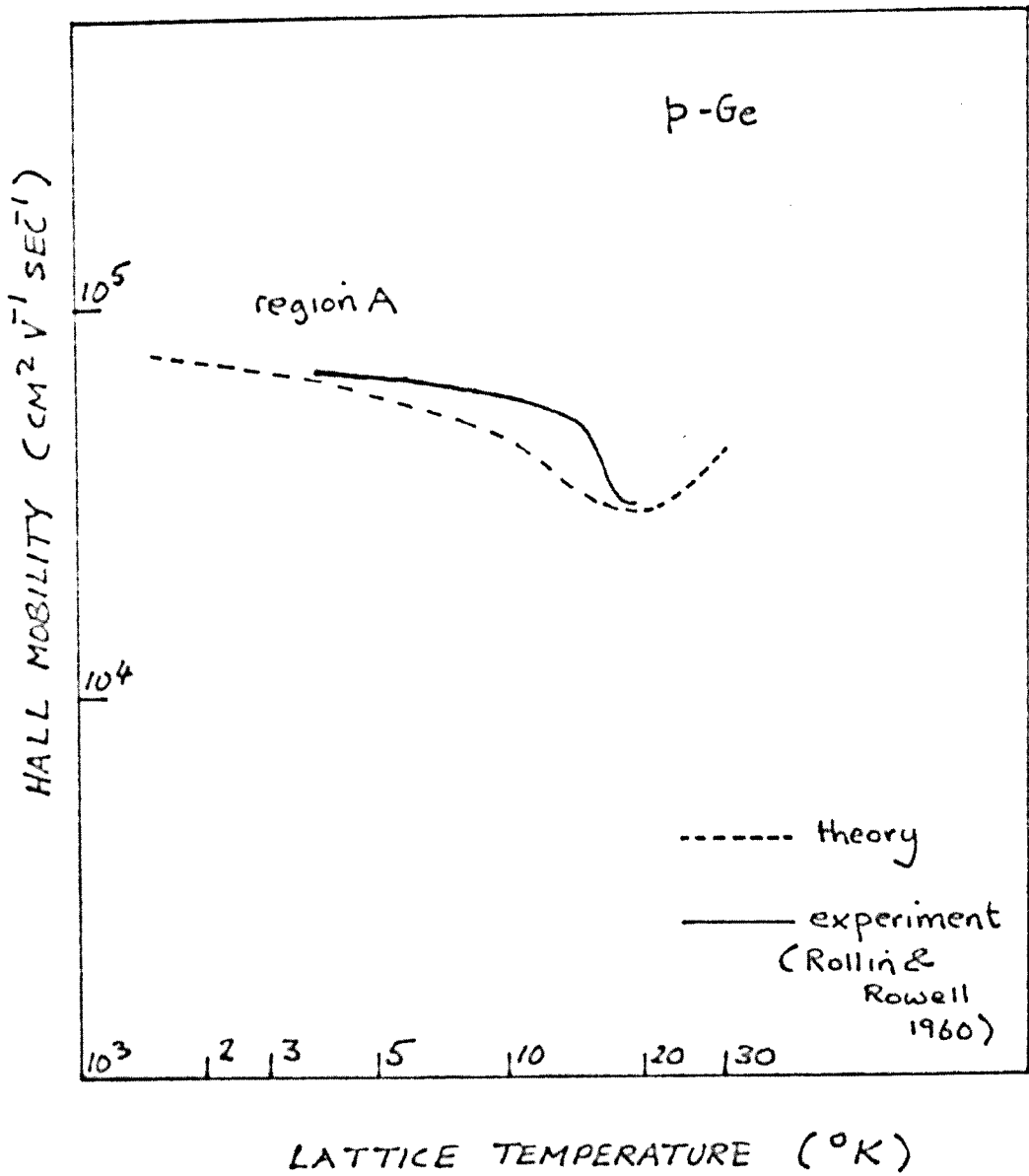AS FUNCTIONS OF TEMPERATURE FOR DOMINANT IONIZED
IMPURITY SCATTERING

FIG 2.10   COMPARISON OF THEORETICAL AND
EXPERIMENTAL HALL MOBILITY OF
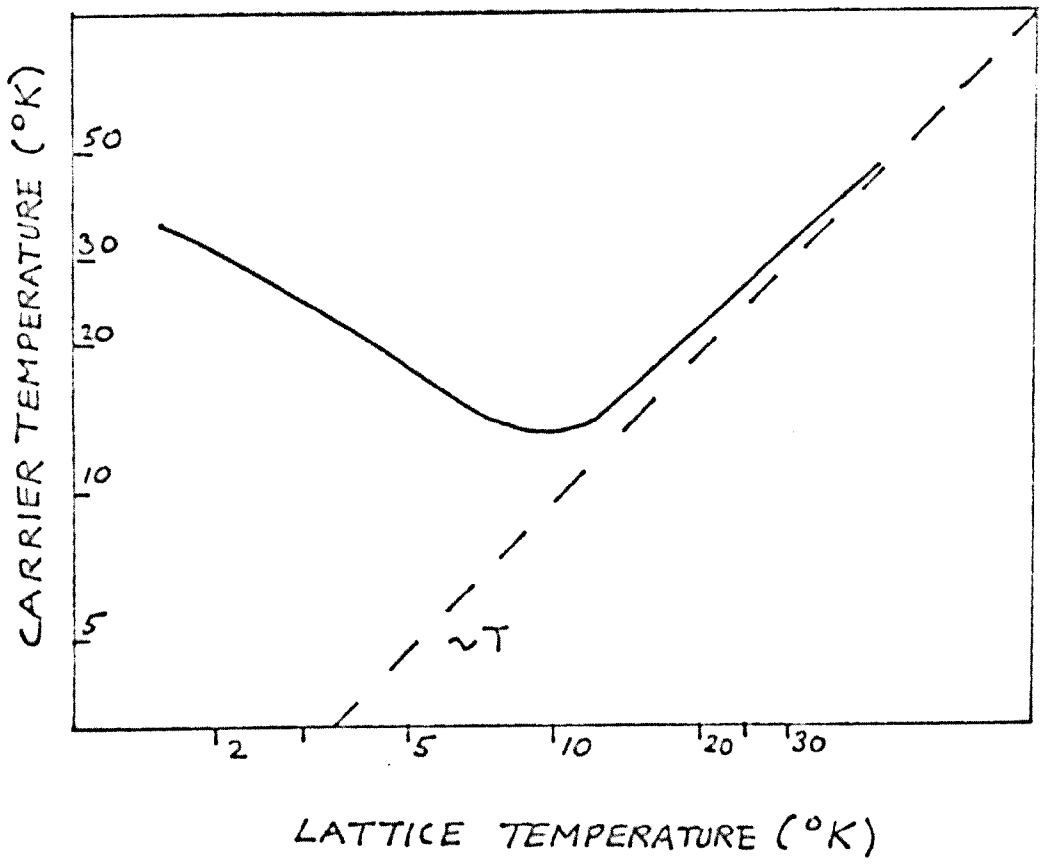HOT HOLES IN GERMANIUM

FIG 2.11

T_e, where $T_e = 2<\varepsilon>/(3k_B)$, as a function of lattice temperature for this problem. Experimentally, the Hall mobility was found to be proportional to $T^{3/2}$ for the thermalised background carriers in the absence of extrinsic radiation. This indicates the dominance of ionized impurity scattering at low temperatures. Similar behaviour occurs under extrinsic radiation but for temperatures above 24°K, where carriers reach quasi-equilibrium with the lattice. However, the theoretical calculations indicate that neutral impurity and lattice scattering play an important role at lower temperatures where carrier heating sets in. Neglect of these processes leads to a considerable increase in the theoretical Hall mobility at low temperatures. The major part of the 'temperature independent' portion of the Hall mobility curve (region A in Figure 2.10) is in fact attributable to the influence of neutral impurity scattering and not to a temperature independent distribution of carriers as suggested by Rollin and Rowell.

Conduction in p-germanium presents special difficulties (Lawaetz 1968) and must await more detailed knowledge of the scattering processes and refinement of our simple model before better theoretical agreement can be obtained. We note finally that for strong carrier heating at very low temperatures, the simple model breaks down as the detailed form of the excitation spectrum becomes more important and this is not known with any precision.

Calculations were also performed for the Hall mobility in n-silicon corresponding to the experiments of Betjemann (1965) but we can find no evidence for any significant carrier heating. This is a consequence of the low density of traps ($N_A \simeq 3 \times 10^{12}$ cm^{-3}) giving rise to relatively long carrier lifetimes. We have not been able to find any alternative explanation for the cut-off (which is manifest as a change from a $T^{-3/2}$ dependent mobility to a temperature independent mobility below 10°K) in the experimental Hall mobility. The radiation used by Betjemann was room temperature radiation peaked at about 10 micron or

0.12 eV, and as such no carriers could have been excited into the higher

minima in the (111) direction which lies some 0.5 eV above the usual (100)

minima.

2.8 Summary and discussion

The simple model for carriers which are photoexcited by black body type

radiation (or broad spectrum radiation) predicts the possibility of observing

hot carrier effects in semiconductors at low temperatures. The origin of the

heating lies in the rapid decrease of carrier lifetime with decreasing lattice

temperature such that thermalisation to the lattice is prohibited. The energy

dependence of the carrier lifetimes as given by the Lax model is irrelevant to

the occurrence of heating, but is vital in its contribution to the temperature

dependence of the total capture cross section and average lifetime. The

general form of the hot carrier distribution function approximates to the sum

of two Maxwellian distributions; at least below the threshold energy for

optical phonon emission. The low energy dependence of the distributions is

governed by an effective temperature close to that of the lattice, whilst the

high energy dependence reflects the excitation spectrum. At sufficiently

high temperatures the theory shows that carriers come into quasi-equilibrium

with the lattice, verifying the earlier qualitative work of Mattis (1960).

Despite the simplicity of the model, reasonable agreement is found with

the experimentally observed transport properties. Application of Monte Carlo

methods for the low field transport properties has confirmed our assumption

that Ohm's law holds under the experimental conditions considered and that

carrier heating by the applied fields does not occur.

The non-Maxwellian nature of the heating requires a careful understanding of the parameters actually measured in experiment, particularly with regard to the Hall coefficient and capture cross section. Carrier heating could offer an explanation in certain cases of the apparent cut off observed in the capture cross section for cascade capture without a modification of the simple Lax theory. However, as mentioned in sections 1 and 6 the full problem of this cut off cannot be solved solely in terms of the present hot carrier model. We conclude this chapter with a few speculations on the nature of the observed cut-off to the capture cross section for n-silicon as observed by Levitt and Honig (1961).

Apart from sample 5, the majority of specimens used by Levitt and Honig show the same temperature dependent cross section corresponding to a temperature independent mean lifetime. This result is completely at variance with the predictions of the cascade model, even when carrier heating is considered. There have been several theoretical attempts to explain these results (Ascarelli and Rodriguez 1961; Hamann and McWhorter 1963; Brown 1964, 1966; Brown and Rodriguez 1967), all based on thermalised carriers but giving calculations for the effects of overlap of excited states, screening and impurity conduction and also improved calculations for the basic capture process. Only the hot carrier model of the present work has given any agreement with experiment, and that only for a single sample, sample 5. It is interesting to note from Table 2.3 that sample 5 is unique in having a very large ratio of neutral to ionized donors and also the highest ionized donor density. The latter is responsible for the carrier heating.

Levitt and Honig produce some evidence which suggests that the electrons in their experiment were not excited predominantly to the lowest (100) minima (see Figure 2.5) but to the higher (111) minima. This represents a further aspect of the hot carrier problem which is not considered in our basic model. However, it appears doubtful that this alternative situation could have a

serious effect since we would expect the relatively fast non-equivalent inter-valley optical phonon scattering processes to bring carriers back into the (100) minima in a time less than the recombination lifetime. This situation is also complicated by the possibility of impurity assisted intervalley scattering which at least for equivalent valleys in n-germanium can dominate at very low temperatures (Weinreich, Sanders Jr., White 1959).

If we neglect intervalley optical phonon scattering and accept Levitt and Honig's idea that carriers are excited into the higher (111) minima then we can speculate on the influence of impurity assisted intervalley transitions on the observed capture cross sections. The following remarks are highly qualitative. Weinreich et al (1959) have shown that impurity assisted interequivalent valley transitions can occur in n-germanium. Capture of an electron into a bound donor state is followed later by re-emission into a new valley. The scattering is elastic. As one electron is captured another one nearby is re-emitted, so that from the point of view of the conduction band this is an instantaneous process. Neutral donors also participate where the scattering is essentially exchange scattering. The main features are that the neutral impurity contribution dominates at low temperatures and has an effective relaxation time comparable to the Lax cascade recombination lifetimes. We might expect that a similar process could occur between non-equivalent valleys in silicon. Presumably this process also includes the possibility of capture into a metastable state associated with the (111) valley and arising from the donor level assoicated with the (100) valleys, followed by a transition into the (100) valley (see Figure 2.12). This would be similar to the resonant scattering of free electrons from hydrogen like atoms. If these processes occur and are largely temperature independent we can give a crude explanation of the cross section data of Levitt and Honig. Consider the situation sketched in Figure 2.13. Let the applied radiation excite carriers
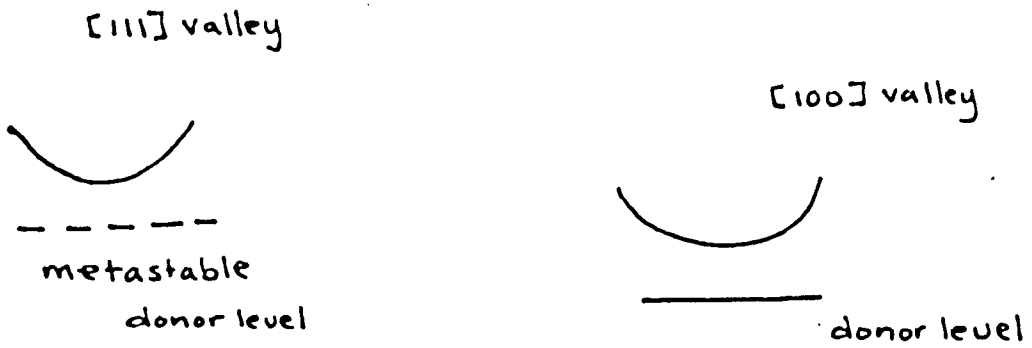
[111] valley

[100] valley

metastable
donor level

donor level

FIG 2.12   THE TWO VALLEY NATURE OF
THE CONDUCTION BAND OF SILICON

[111]
valley

n_1

τ_{12}

[100]
valley

n_2

intervalley
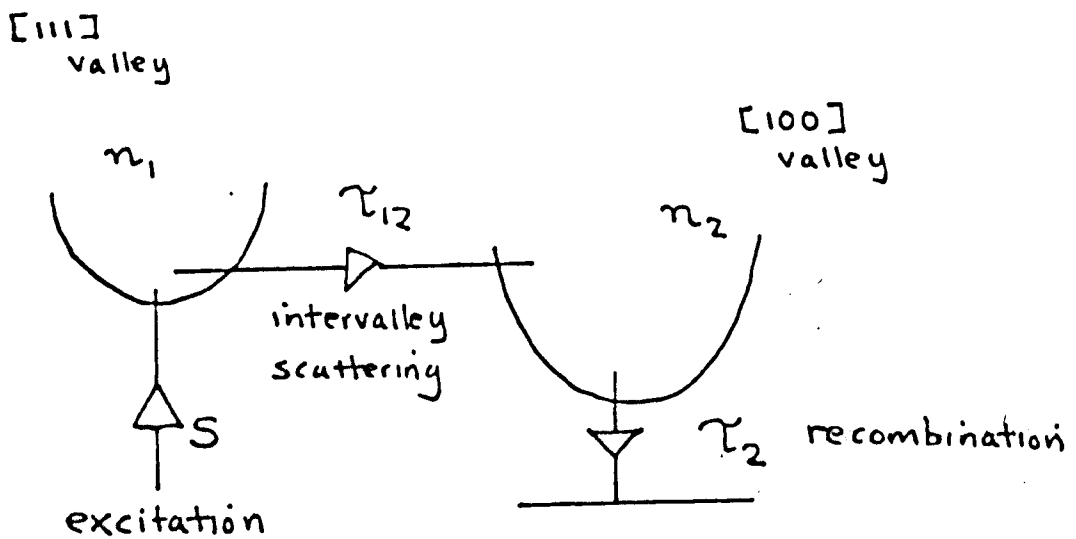scattering

S

τ_2 recombination

excitation

FIG 2.13   THE TWO VALLEY MODEL FOR

HOT ELECTRONS IN SILICON

into the (111) minima at a rate S, with no carriers excited into the (100) minima. The steady state rate equations for the (111) and (100) valleys then take the simple form:

$$S = \frac{n_1}{\tau_{12}} \qquad (111) \text{ valley} \qquad 2.8.1$$

$$0 = \frac{n_2}{\tau_2} - \frac{n_1}{\tau_{12}} \qquad (100) \text{ valley} \qquad 2.8.2$$

where n_1, n_2 are the populations of the (111) and (100) valleys respectively, τ_{12} is the impurity assisted intervalley scattering time and τ_2 is the recombination lifetime due to the Lax cascade mechanism. Here we suppose that recombination only occurs from the (100) valley. From equations (2.8.1) and (2.8.2) we find

$$\frac{n_1}{n_2} = \frac{\tau_{12}}{\tau_2} \quad ; \quad S = \frac{n_2}{\tau_2} . \qquad 2.8.3$$

The essential factor in this problem is the ratio of neutral to ionized donors. The latter are responsible for the cascade capture, the former for the inter-valley transfer. If this ratio is small then intervalley transfer will be slower than the recombination process, i.e. $\tau_{12} > \tau_2$, and hence $n > n_2$: most of the carriers will be in the (111) valley. In which case a Hall coefficient measurement will essentially measure n_1 and hence from (2.8.1) will derive τ_{12} the temperature independent recombination lifetime rather than τ_2. If the ratio of neutral donors to ionized donors is large then similarly we find $n_2 > n_1$, and a Hall measurement will give τ_2. At lower temperatures, however, the cascade recombination lifetime can decrease below τ_{12} and we return to a measurement of τ_{12}. Inspection of Table 2.3 shows that sample 5 would satisfy the latter criterion and our hot carrier model would apply, whereas for samples 1 to 4 the carriers are probably in the (111) valley and the experiments have measured τ_{12}. Clearly this idea is very speculative and more theoretical and experimental work is required in this area.

CHAPTER III

THE MONTE CARLO APPROACH TO TRANSPORT THEORY

3.1 Introduction

During the last three years Monte Carlo methods have been applied

successfully to highly non equilibrium electron transport problems in

solids.   Such situations arise for example, in considering the effects

of high fields where the usual method of solving the Boltzmann equation

using a truncated series of spherical harmonics fails (Pinson and Bray

1964).   This failure will occur in general whenever the distribution

function of carriers in k-space is strongly asymmetric.   Rather than solve

the Boltzmann equation for an ensemble of carriers it is possible to obtain

the steady state distribution function and transport parameters by following

the motion of one carrier for a sufficiently long period of time.   The

ensemble average is then essentially replaced by a time average.   Kurosawa

(1966) first demonstrated the power of the Monte Carlo method in a simple

simulation study of high field hot carrier effects in p-type germanium.

The technique was later employed by Boardman, Fawcett and Rees (1968) in

a more sophisticated form to high field effects in GaAs.   These ideas have

been refined and adapted to the present studies of photoexcited carriers

at low temperatures in semiconductors, where the carriers have effectively

a finite lifetime, (Barker and Hearn 1969a,b,c).   Application to hot

electron effects in silicon and germanium has already been discussed in

Chapter II, and in Chapter IV we make full use of the technique to study

oscillatory photoconductivity in the III-V compounds.   In view of the

potential importance of the Monte Carlo method in electron transport theory

we devote the whole of this chapter to an outline of the basic theory and

the innovations we have introduced.

In our applications the method involves the computer simulation of the motion of a single electron (or hole) in k-space from injection into the band until subsequent recapture. A large number of carrier histories are recorded from which the distribution function and macroscopic transport properties follow as suitable averages. The basic ideas involved are described in sections 2 and 3.

In semiconductors the scattering mechanisms are of an extremely complex nature and one of the consequences of this is that the total scattering cross section is an intractable implicit function of the time of free flight. This difficulty has been overcome by the introduction of a self-scattering channel (Boardman, Fawcett and Rees 1968) which makes the total scattering cross section constant in time, and if entered merely feeds the carrier back into free flight. This work is reviewed in section 4 and the first proof of the method offered. It has proved necessary to generalise the simple ideas of the self scattering device in two ways. The first innovation is the introduction of energy dependent primary self scattering which provides a time dependent total scattering cross section which can be handled analytically as regards the time of flight sampling. This leads to higher convergence and efficiency. A further advance described in section 5 involves the retention of some of the self scattering within the individual scattering channels. This secondary self scattering device greatly facilitates the handling of the differential scattering cross sections and removes the problem of storage capacity in the machine.

3.2 Carrier histories

To be specific let us consider a steady state ensemble of photoexcited carriers within a single band of a non degenerate semiconductor. We suppose

that the lattice temperature is sufficiently low that thermal excitation into the band is negligible. Each carrier is taken to be completely described by its wavevector $\underline{k}$ within the band. Four competing processes determine the properties of the ensemble. They are: (1) the photo-excitation process: the probability that an injected carrier enters the band in a given state, either from another band or an impurity level, depends on the photoexcitation spectrum. For example, with uniform monochromatic photoexcitation, carriers are injected into states which are distributed at random on a constant energy surface in $\underline{k}$ space. (2) The accelerating effects of external applied fields: we consider only a constant uniform electric field which induces a uniform drift of carriers in $\underline{k}$ space at a rate given by

$$\dot{\underline{k}} = e\underline{F}/\hbar \qquad\qquad 3.2.1$$

where $\underline{F}$ is the applied field, and e the charge on a carrier. (3) Scattering processes: collisions with phonons and impurities scatter the carriers between states within the band. We suppose the collision process to be instantaneous; in between collisions the carriers drift freely.
(4) Recombination: the carriers have finite lifetimes within the band and may recombine at impurities or within another band. We shall find it convenient to regard recombination as a special form of scattering in which the carrier is removed from the band. All four processes take place during the history of a particular carrier. Figure 1 shows a simplified history in k-space for two monoenergetically excited carriers in a simple band.

The essence of the Monte Carlo method is to simulate the four physical processes mentioned above, and involves tracking carriers from injection into the band until subsequent recombination. It is presupposed that all relevant probabilities for the elementary events in the life history of a carrier are known. A sufficiently large number of carrier histories,
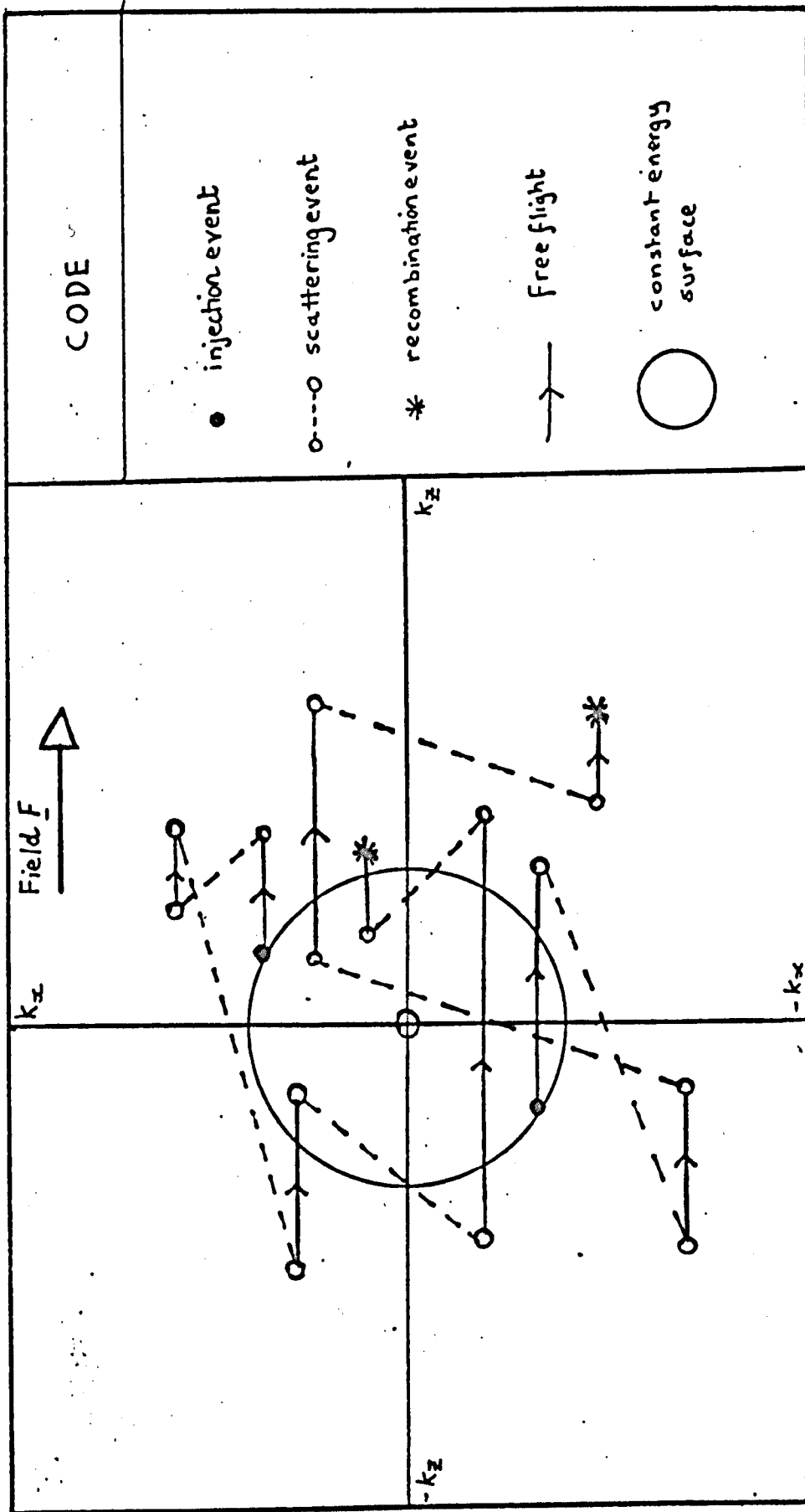
CODE

● injection event

o---o scattering event

✳ recombination event

→ Free flight

◯ constant energy surface

Field $\underline{F}$

k_z

k_x

$-k_x$

$-k_z$

FIG 3.1 SIMPLIFIED CARRIER HISTORIES FOR TWO MONO-ENERGETICALLY EXCITED

CARRIERS IN A TWO DIMENSIONAL $\underline{k}$-SPACE.

typically a few thousand, are recorded from the computer simulation to form a reasonable statistical sample of the much larger ensemble of carriers actually present in the semiconductor. The simple macroscopic properties of the total ensemble are then obtained by suitable averages over the history of the test ensemble.

The mean carrier lifetime τ is calculated as the arithmetic mean

$$\tau = \sum_{j=1}^{N_o} \tau_j / N_o \qquad\qquad 3.2.2$$

where τ_j is the lifetime of the jth test particle and N_o is the population of the test ensemble. Assuming a constant average photoexcitation rate W, the steady state carrier population is deduced as

$$N = W\tau \qquad\qquad 3.2.3$$

(c.f. Chapter II, section 2.2). However, calculation of other average properties of the ensemble is less straightforward.

Consider the experimental measurement of some macroscopic property of the steady state ensemble, for example the momentum per carrier $\hbar\underline{k}$. In practice the measurement will involve a time average of the total carrier momentum over a macroscopic time interval T, where T is greater than any of the characteristic microscopic times associated with the ensemble. Clearly we are ignoring fluctuation phenomena. The average momentum per particle is then measured as

$$\langle \hbar\underline{k}\rangle_E = \frac{\hbar \int_o^T \sum \underline{k}(t)\,dt}{N \int_o^T dt} \qquad\qquad 3.2.4$$

where N is the average number of carriers, $\hbar\underline{k}(t)$ is the momentum of a particular carrier at time t, and the summation is over all carriers present at time t. If we ignore the fluctuations in carrier population and

consider the number of carriers to be a constant N, we can obtain a more precise mathematical expression for the experimental average. To do this we label a particular carrier with index j and suppose that if the carrier recombines it is instantaneously photoexcited back into the band to maintain the constant population. Recombination then, is treated as a special form of inelastic scattering. What we have done is to replace a fluctuating number of carriers of finite lifetimes with a constant population of quasi-carriers with infinite lifetimes. The experimental average is then

$$\langle \hbar \underline{k} \rangle_E = \frac{\hbar \sum_1^N \int_0^{T_j} \underline{k}_j \, dt}{N \int_0^{T_j} dt} = (\hbar/N) \sum_1^N \bar{\underline{k}}_j \qquad 3.2.5$$

where we define $T_j = T$ for all j. Since we are dealing with a statistical system we make the assumption that the individual quasi-carrier average $\bar{\underline{k}}_j$ is the same for all carriers provided the averaging time T is sufficiently large. Consequently the experimental average is essentially an average over a single quasi-carrier:

$$\langle \hbar \underline{k} \rangle_E = \frac{\hbar \int_0^T k(t) \, dt}{\int_0^T dt} \qquad 3.2.6$$

where we now drop the index j. The Monte Carlo simulation of the problem involves tracking a single quasi-carrier over a large number of real carrier lifetimes, say N_o (where $N_o \ll N$). The average momentum per particle is then obtained as

$$\langle \hbar \underline{k} \rangle_M = \frac{\hbar \int_0^{T_o} \underline{k}(t) \, dt}{\int_0^{T_o} dt} \qquad 3.2.7$$

$$T_o = \sum_1^{N_o} \tau_j$$

where τ_j is the lifetime of the jth real carrier making up the quasi-carrier. The basic premise in Monte Carlo is the identification of $\langle \hbar \underline{k} \rangle_M$ with the experimental average $\langle \hbar \underline{k} \rangle_E$.

Similar averages are readily found for other properties of interest. We note that the drift mobility μ and conductivity σ are immediately obtained if the average carrier momentum and carrier density n are known:

$$\sigma = ne\mu$$

$$\mu = \hbar <k>_M / (m^*F) \ .$$

3.2.8

Here m^* is some appropriate effective mass.

Distribution functions are readily obtained by imposing a suitable discrete mesh in $\underline{k}$-space (Kurosawa 1966). The fractional time spent by a quasi-carrier in a particular element of $\underline{k}$-space is proportional to the steady state distribution function $f(\underline{k})$ in that element. If the mesh element is small, the calculated distribution function will exhibit pronounced fluctuations unless the quasi-carrier history is simulated over a long period of time. The fluctuations are most severe for the high energy tail of the distribution function which generally represents a low population of carriers. Average properties such as the mean carrier drift velocity are essentially averages over the entire distribution function and the effect of fluctuations is largely cancelled out. Consequently the Monte Carlo calculation of distribution functions generally requires a longer machine time than calculation of simple ensemble averages.

The actual simulation is commenced by selecting a first test carrier making up the quasi-carrier with an injection wavevector $\underline{k}$ and energy ϵ which are sampled from the probability distribution appropriate to the photoexcitation process. The time of free flight in $\underline{k}$-space is then sampled from a probability distribution determined by the scattering processes (including recombination as a special case). The carrier has then evolved to the new state $\underline{k}' = \underline{k} + e\underline{F}/\hbar$, where t is the time of free flight. If distribution functions are required the visiting time of the

carrier in each cell of k-space traversed during free flight is recorded. The collision channel, corresponding to the mode of scattering, is then selected by a sampling technique from a knowledge of the various collision channel probabilities associated with state $\underline{k}'$. The scattered state $\underline{k}''$ is determined in a similar fashion from the differential scattering cross section of the chosen channel. This new state acts as the initial state for the next free flight. The procedure is repeated until the recombination channel is entered at which time the entire carrier history is complete. The quasi-carrier history is continued by generating further test carriers and the procedure repeated until a sufficiently large sample has been obtained. Averages are readily calculated as the simulation proceeds; for example, by storing the cumulative time integral of the quasi-carrier momentum.

No hard and fast rule can be given for how many carrier histories must be recorded to obtain a reasonable statistical sample. Each problem has to be treated on its own merits. For example, the calculation of drift velocity for very low applied fields requires extremely long simulation times as the fluctuations are of the same order of magnitude as the derived average. For high fields the fluctuations are less important and reasonable convergence is obtained with a much smaller simulation time. In practice the simulation is continued until the averages of interest converge to within a given tolerance, typically 1%. For the problems discussed in this thesis, the sample size has varied from 1000 to 10000 test carriers and involves a total number of collisions of the order 10^5 for each ensemble average.

Figure 2 shows a simplified flow diagram for the simulation routine. The details of the simulation are given in the following sections.

FIG 3.2
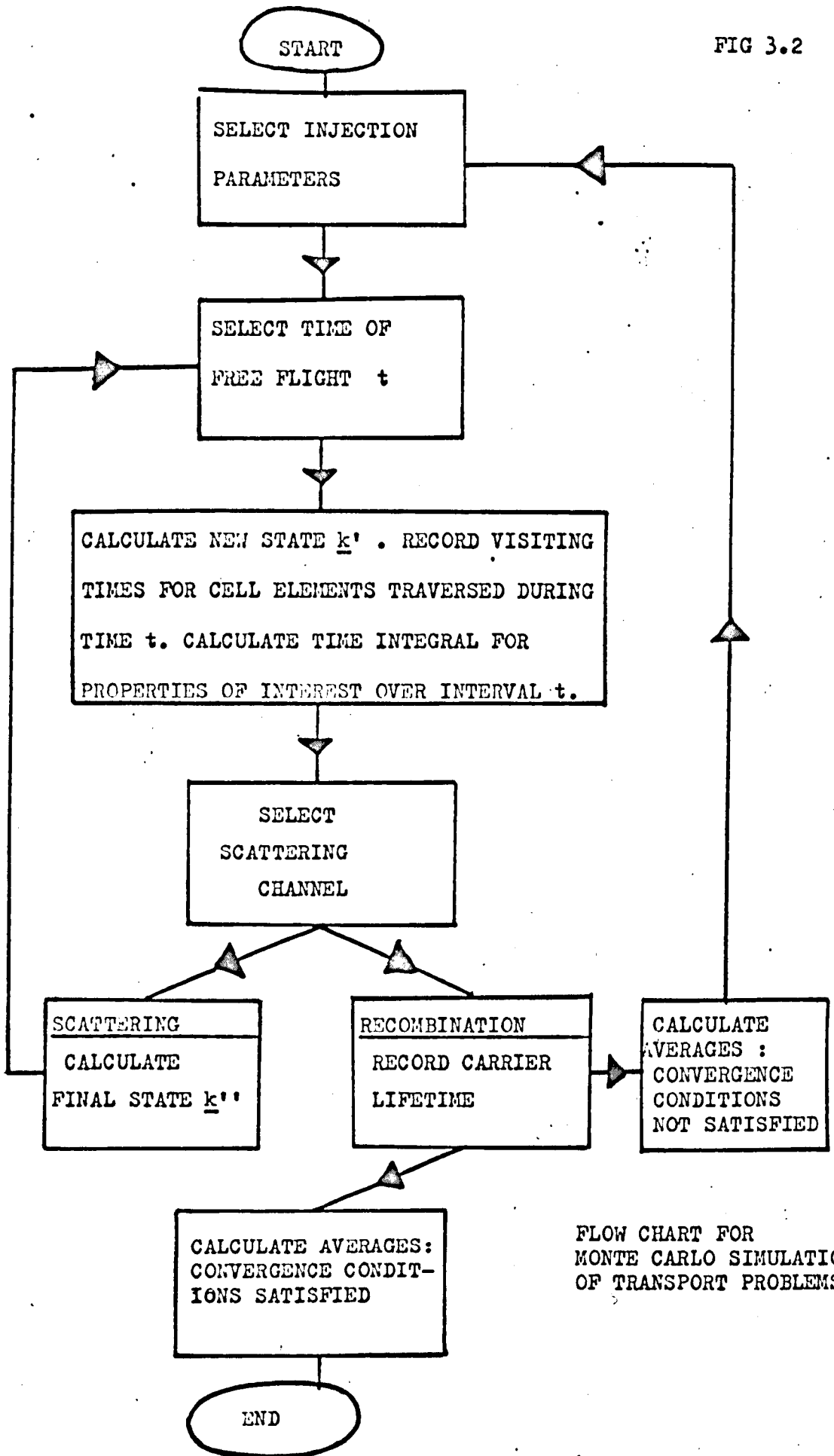
FLOW CHART FOR
MONTE CARLO SIMULATION
OF TRANSPORT PROBLEMS

3.3 Basic Monte Carlo

The basic simulation is performed as follows. Consider a carrier at $\underline{k}(0)$ at time zero. Provided it does not scatter the carrier evolves according to the dynamical relation

$$\underline{k}(t) = \underline{k}(0) + e\underline{F}t/\hbar \qquad\qquad 3.3.1$$

where $\underline{F}$ is the applied uniform constant electric field. The probability density for a first scattering at time t is then

$$p(t) = \lambda(\underline{k}(t))\exp(-\int_0^t \lambda(\underline{k}(t'))dt') \qquad\qquad 3.3.2$$

where $\lambda(\underline{k})$ is the total scattering rate out of state $\underline{k}$ due to all the scattering mechanisms (capture is regarded as a special form of scattering). This form arises since p(t) is just the joint probability of the carrier surviving for a time t and $\lambda(\underline{k}(t))$ the probability per unit time for scattering at that time. The survival probability is determined by considering the rate at which a number of carriers n(t), belonging to a test group all with the same wave vector $\underline{k}$, are attentuated by collisions. This rate is given by

$$\frac{dn}{dt} = -n\lambda$$

from which we find

$$n(t) = n(0) \exp(-\int_0^t \lambda dt')$$

where n(0) is the population at time zero. Equation (3.3.2) follows when we identify the survival probability with n(t)/n(0). The time of scattering is deduced from the equation

$$P(t) = \int_0^t p(t')dt' = r \qquad\qquad 3.3.3$$

where r is a computer generated random number, uniformly distributed on (0,1). The procedure is justified since the probability P(t) that the carrier will have been scattered by time t is uniformly distributed between 0 and 1.

Having determined the scattering time, the scattering channel is selected by generating a second random number r' and using the inequality

$$\sum_{j<j'} \frac{\lambda_j(\underline{k}(t))}{\lambda(\underline{k}(t))} < r' < 1 - \sum_{j>j'} \frac{\lambda_j(\underline{k}(t))}{\lambda(\underline{k}(t))} \qquad 3.3.4$$

to decide whether channel j' is entered.   Integers j label the possible scattering mechanisms and

$$\lambda(\underline{k}(t)) = \sum_j \lambda_j(\underline{k}(t)) \quad , \qquad 3.3.5$$

The channel probabilities p(j) are given by

$$p(j) = \lambda_j/\lambda \equiv \int d\underline{k}' K_j(\underline{k},\underline{k}')/\lambda(\underline{k}) \quad . \qquad 3.3.6$$

The kernels $K_j(\underline{k},\underline{k}')$ are the usual probabilities per unit time for transition out of state $\underline{k}$ into state $\underline{k}'$.   Those which are of concern to us are tabulated in Appendix 3.2.   It is not always convenient to calculate a particular $\lambda(\underline{k})$ and this can be avoided by a mathematical device discussed in section 5.

The scattered state $\underline{k}'$ is determined in a similar fashion by generating further random numbers satisfying probability distributions appropriate to the differential scattering rates $K_j(\underline{k},k')$ of the channels involved.   The new state $\underline{k}'$ becomes the initial state for the next free flight.   For completeness, an outline of the Monte Carlo procedure involved is given in Appendix 3.1.

The channel for ionized impurity scattering is a source of some computational difficulty in that there is a predominance of small angle elastic scattering, particularly at high energies.   From a computational point of view, the recording of small angle collisions is wasteful as we are mainly interested in large angle scattering in transport theory.   A way round this problem is to introduce a cut off to the differential cross section for ionized impurity scattering so as to ignore collisions for which the scattering

angle is less than some small value. This procedure is sketched in Appendix 3.2.

To complete the description of the basic simulation process we review the procedure for carrier injection. In our applications we are concerned with isotropic excitation into isotropic spherical energy bands. Two cases are of interest, the monoenergetic excitation associated with oscillatory photoconductivity (Chapter IV) and the black body excitation discussed in Chapter II.

Suppose that the injection energy ε_o has been selected (this is trivial is the case of oscillatory photoconductivity), then we calculate the direction of the corresponding wave vector $\underline{k}_o$ as follows. The vector $\underline{k}_o$ is randomly oriented in $\underline{k}$ space and the probability distributions for the cosine of its polar angle θ and azimuthal angle ϕ in the simulation frame are simply

$$P(\cos\theta) = \cos\theta/2; \quad P(\phi) = \phi/2 \ . \tag{3.3.7}$$

Generation of two random numbers r, r' in the range 0 to 1 then gives the angular components of $\underline{k}_o$ according to

$$\cos\theta = 2r - 1; \quad \phi = 2\pi r' \ . \tag{3.3.8}$$

In applications to transport theory we exploit the cylindrical symmetry about the applied field direction and require only k_ρ and k_z the radial and polar components of $\underline{k}_o=$, which involves only one random number:

$$k_z = k_o\cos\theta = k_o(2r - 1); \quad k_\rho = (k_o^2 - k_z^2)^{\frac{1}{2}} \ . \tag{3.3.9}$$

Here k_o is given by

$$k_o = (2m^*\varepsilon_o/\hbar^2)^{\frac{1}{2}}$$

where m^* is the appropriate effective mass.

In general it is difficult to sample a given probability distribution
of injection energies $P(\varepsilon)$ by inverting the relation $P(\varepsilon) = r$; and in
some cases only the probability density distribution $p(\varepsilon)$ is available. Von
Neumann (1951) has developed a routine, the rejection method, which is useful
in such cases. The technique requires the generation of a sequence of
pairs of random numbers (ξ_1, ξ_2) which are uniformly distributed on a
rectangle of area A enclosing the curve $p(\varepsilon)$ as sketched in Figure 3. The
first random number ξ_1, is a test energy defined on the energy range of
interest, say 0 to ε_1 (if this range is infinite it is necessary to introduce
a cut off to the excitation spectrum at some appropriate point). The second
random number ξ_2, is uniformly distributed between zero and the maximum
value of $p(\varepsilon)$. Both numbers are trivially obtained from numbers generated
on the range $(0,1)$. The test energy is selected or rejected as the correct
injection energy according to whether ξ_2 is less than or in excess of $p(\xi_1)$.
In the rejection case, the procedure is repeated until the selection condition
is satisfied.

We show that the rejection method correctly selects injection energies
satisfying the probability distribution $p(\varepsilon)$ by considering a large number of
random points to be thrown into the rectangle. Of the points which fall
below the curve $p(\varepsilon)$, the proportion that fall in the strip ε to $\varepsilon + d\varepsilon$ tends,
in the limit of large numbers, to the ratio of the area of the strip to the
total area under the curve. This last ratio is just $p(\varepsilon)d\varepsilon$, and the
procedure is confirmed.

The fraction of wasted points in the rejection method is clearly $1 - 1/A$,
where A is the area of the rectangle. For many applications A may be large
with a consequent large loss in efficiency. In these instances it is better
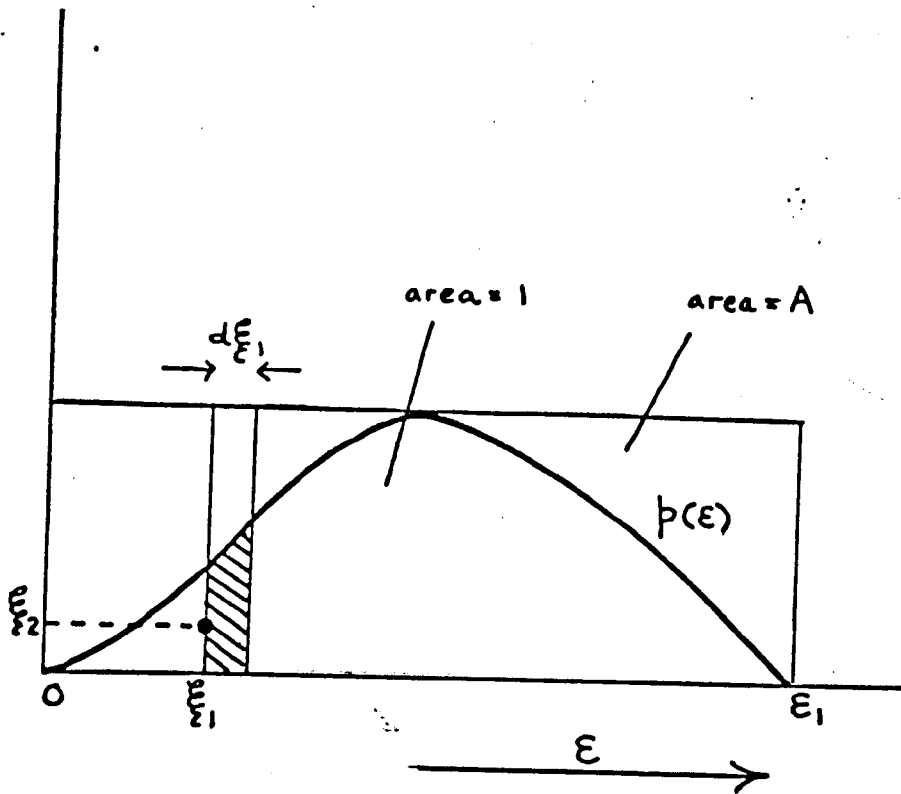to use the envelope method, developed in section 3.5, which essentially
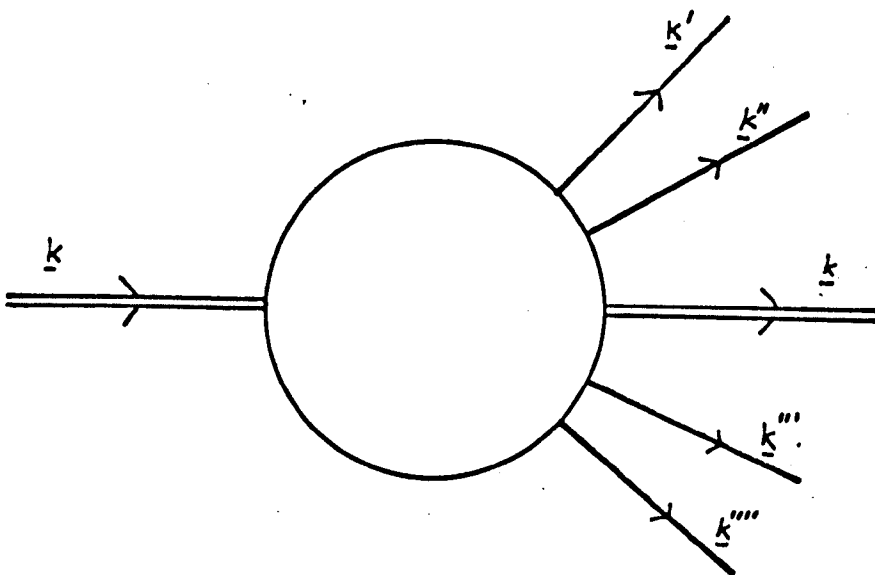
FIG 3.3 · THE REJECTION METHOD

FIG 3.4 PRIMARY SELF-SCATTERING

minimizes A. The rejection method was employed to sample the excitation

spectrum in the Monte Carlo calculations discussed in Chapter II.

3.4 The self scattering device I - primary self scattering

For certain scattering processes, for example polar optical phonon

scattering, equations (3.3.2) and (3.3.3) cannot be solved analytically

and the determination of free times is difficult. Boardman, Fawcett and

Rees (1968) avoid this problem by introducing a non physical 'self scattering'

device whereby a carrier may scatter from a state $\underline{k}$ into itself. The

scattering rate for this process is $\Gamma - \lambda(\underline{k})$ where Γ is a positive constant

(chosen greater than $\lambda(\underline{k})$ for all energies of interest to avoid negative

probabilities). Inclusion of self scattering is equivalent to replacing

$\lambda(\underline{k})$ in equation (3.3.2) by Γ and solution of euqation (3.3.3) for the free

time t is then straightforward. In detail we replace $\lambda(\underline{k})$ by

$$\Gamma = \int d\underline{k}' \left\{ \sum_j K_j(\underline{k},\underline{k}') + (\Gamma - \lambda(\underline{k}))\delta(\underline{k} - \underline{k}') \right\} . \qquad 3.4.1$$

The probability for a first collision at time t is then given by

$$P(t) = 1 - \exp(-\Gamma t) \qquad 3.4.2$$

and the free time t is generated from

$$t = -\Gamma^{-1} \log_e r. \qquad 3.4.3$$

The disadvantage of this simplification is that there is now a finite

probability of self scattering which does not contribute to the determination

of the transport properties or distribution function. This must be accounted

for at the collision channel stage.

At a collision either real or self scattering may occur, with respective

probabilities p_R, p_S given by

$$p_R = \frac{\lambda(\underline{k})}{\Gamma} \; ; \quad p_S = 1 - \frac{\lambda(\underline{k})}{\Gamma} \; . \qquad\qquad 3.4.4$$

The collision channel is selected by the routine described in section 2; and if the self scattering channel is chosen the carrier state is unchanged, and a new random time selected. The entire procedure is shown schematically in Figure 4.

As far as the author is aware, no proof has previously been given that the distribution of free times between real collisions as generated by the self scattering device is equivalent to the actual distribution of free times. We give a proof of this important equivalence in Appendix 3.3.

In practical applications the number of self collisions must be minimized. This may be achieved, in certain circumstances, by removing the restriction that Γ be a constant. For example, in the simulation of oscillatory photoconductivity, to be described in Chapter IV, it is found that more rapid convergence is achieved by choosing Γ as a step function of carrier energy. We complete this outline of primary self scattering by sketching the generalization of Γ.

Suppose that the total scattering rate is of the form

$$\lambda(\underline{k}) = \lambda_o(\underline{k}) + \theta(\varepsilon - \varepsilon_1)\lambda_1(\underline{k}) \qquad\qquad 3.4.5$$

where

$$\left. \begin{aligned} \theta(\varepsilon - \varepsilon_1) &= 0 \quad \text{for } \varepsilon < \varepsilon_1 \\ &= 1 \quad \text{for } \varepsilon \geq \varepsilon_1 \end{aligned} \right\} \qquad\qquad 3.4.6$$

Here $\varepsilon = \hbar^2 k^2/2m^*$, the carrier energy and $\varepsilon_1 = \hbar^2 k_1^2 * 2m^*$. The constant energy ε_1, could be for instance, the threshold energy for optical phonon emission. In situations where $\lambda_1 \gg \lambda_o$ (as in oscillatory photoconductivity) we can usefully exploit the form (3.4.5) by introducing the step function

behaviour into the self scattering parameter Γ:

$$\Gamma = \Gamma_0 + \Gamma_1 \theta(\epsilon - \epsilon_1) \qquad\qquad 3.4.7$$

where Γ_0, Γ_1 are constants. In the presence of a uniform field, Γ then becomes a function of time. Consider a carrier with energy ϵ at (k_ρ, k_z) in k-space at time zero. Suppose that the applied electric field $\underline{F}$ is directed along the negative k_z axis in $\underline{k}$-space. There are three situations to contend with as illustrated in Figure 5.

The simplest case occurs for $\epsilon > \epsilon_1$, subject to the constraint $|k\rho| \geq k_1$ if $k_z < 0$ (see Figure 5(a)). Here the dynamical relation (3.3.1) ensures that the carrier energy always exceeds threshold provided no scattering occurs. The time of free flight is then obtained by setting $\Gamma = \Gamma_0 + \Gamma_1$ in equation (3.3.3).

The second case (shown in Figure 5(b)) involves $\epsilon < \epsilon_1$. The self scattering term Γ may then be written

$$\Gamma = \Gamma_0 + \Gamma_1 \theta(t - \lambda) \qquad\qquad 3.4.8$$

where λ, the time required for the carrier to accelerate freely to the threshold energy, is given by the dynamical relation as
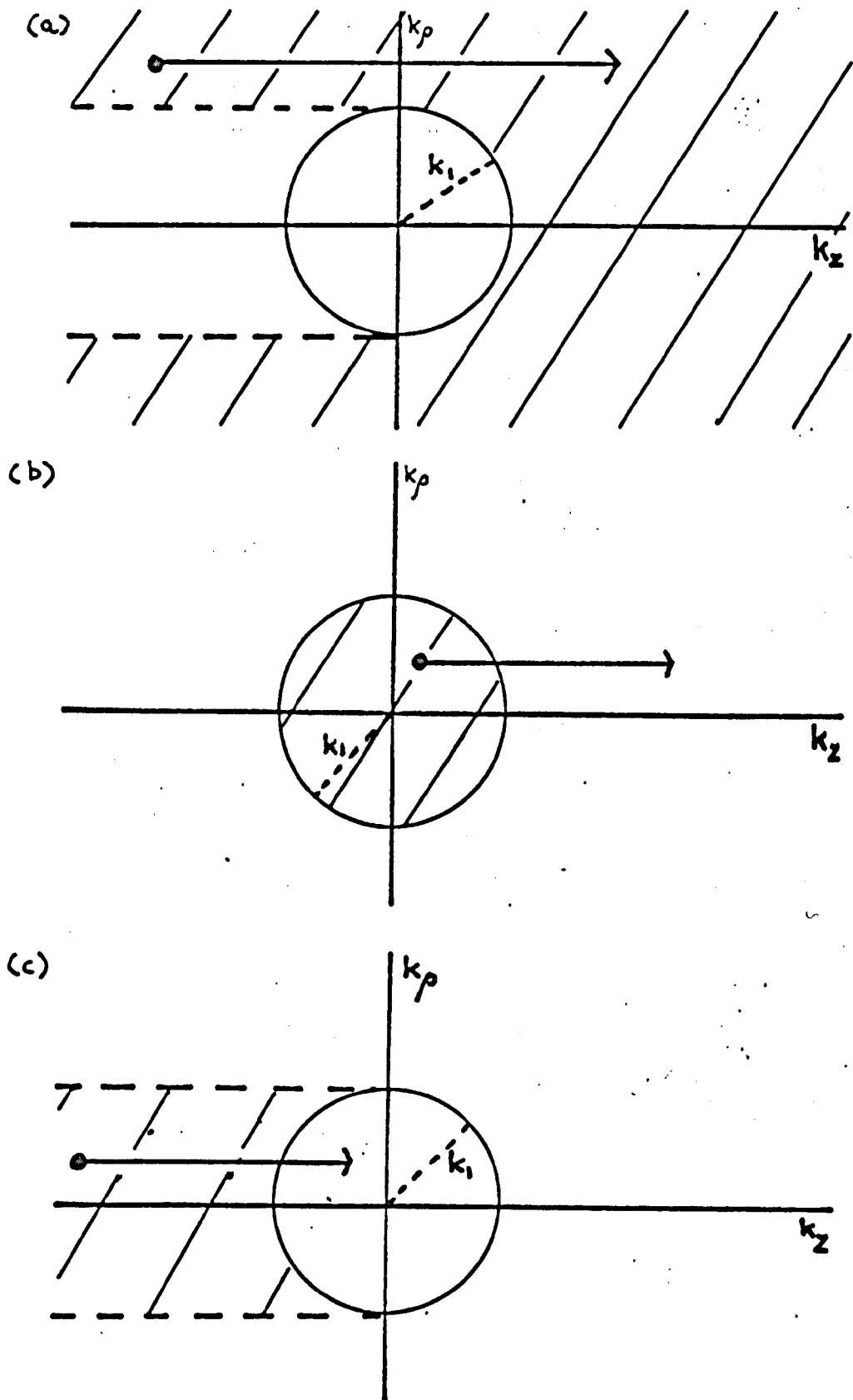
$$\lambda = \left\{ -k_z + (k_1^2 - k_\rho^2)^{\frac{1}{2}} \right\} / G \qquad\qquad 3.4.9$$

where $G = eF/\hbar$.

Substituting the expression (3.4.9) for $\lambda(\underline{k})$ in equations (3.3.2) and (3.3.3), and carrying out the integrations gives the time of free flight according to

$$\left.\begin{array}{l} t = -\Gamma_0^{-1} \log_e (1 - r) \qquad \text{if } r < r_\lambda \\[2mm] t = (\Gamma_0 + \Gamma_1)^{-1}(\Gamma_1 \lambda - \log_e (1 - r)) \text{ if } r > r_\lambda \end{array}\right\} \qquad 3.4.10$$

FIG 3.5

ENERGY DEPENDENT PRIMARY SELF-SCATTERING

where r_λ is defined by

$$r_\lambda = 1 - \exp(-\Gamma_o \lambda) \qquad\qquad 3.4.11$$

and r, as before, is a random number on (0,1).

The remaining case (sketched in Figure 5(c)) involves the initial carrier energy in excess of the threshold energy, but subject to the constraints $|k_\rho| < k_1$; $k_z < 0$. The appropriate self scattering term is

$$\Gamma = \Gamma_o + \Gamma_1(\theta(\lambda_1 - t) + \theta(t - \lambda_2)) \qquad\qquad 3.4.12$$

where λ_1, λ_2 are the times at which the free carrier crosses the energy shell $\epsilon_1 = \hbar^2 k^2/2m^*$. As before λ_1, λ_2 are calculated from the dynamical relation as

$$\begin{aligned}
\lambda_1 &= (-k_z(k_1{}^2 - k_\rho{}^2)^{\frac{1}{2}})/G) \\
\lambda_2 &= (-k_z + (k_1{}^2 - k_\rho{}^2)^{\frac{1}{2}})/G \\
&= \lambda_1 + 2\left\{k_1{}^2 - k_\rho{}^2\right\}^{\frac{1}{2}}/G \quad .
\end{aligned} \qquad\qquad 3.4.13$$

For this case the time of free flight is given by

$$\begin{aligned}
t &= -(\Gamma_o + \Gamma_1)^{-1} \log_e (1 - r) && \text{if } r < r_{\lambda_1} \\
t &= -\Gamma_o{}^{-1}(\log_e (1 - r) + \Gamma_1\lambda_1) && \text{if } r_{\lambda_1} < r < r_{\lambda_2} \\
t &= -(\Gamma_o + \Gamma_1)^{-1}\left\{\log_e (1 - r) - \Gamma_1(\lambda_2 - \lambda_1)\right\} \\
& && \text{if } r > r_{\lambda_2}
\end{aligned} \qquad\qquad 3.4.14$$

where r_{λ_1}, r_{λ_2} are defined by

$$\begin{aligned}
r_{\lambda_1} &= 1 - \exp\left\{-\lambda_1(\Gamma_o + \Gamma_1)\right\} \\
r_{\lambda_2} &= 1 - \exp\left\{-\Gamma_1\lambda_1 - \Gamma_o\lambda_2\right\} \quad .
\end{aligned} \qquad\qquad 3.4.15$$

We note that if $\lambda_1 = 0$, these results reduce to the second case considered.

The technique may be extended to an arbitrary number of energy thresholds and is not restricted to isotropic spherical energy bands. The validity of time dependent self scattering is shown in Appendix 3.3.

3.5 The self scattering device II – secondary self scattering

In some circumstances, for example with inelastic acoustic phonon scattering, a particular channel scattering rate $\lambda_j(\underline{k})$ cannot be evaluated analytically and determination of the scattered state is therefore difficult. One approach (c.f. Boardman, Fawcett and Rees 1968) is to tabulate numerically calculated values for $\lambda_j(\underline{k})$ separately at selected points in $\underline{k}$-space and to use interpolation to find intermediate values where required. This procedure is not always convenient and instead we circumvent the problem by retaining a finite probability of self scattering within the appropriate scattering channel. Suppose that channel j is a 'difficult' channel. Then we essentially replace the actual scattering rate $\lambda_j(\underline{k})$ by a constant $\Gamma_j(>\lambda_j)$, so that the probability of scattering into channel j is, if scattering occurs, $p(j) = \Gamma_j/\Gamma$. The decision as to which channel is selected is then trivial but now involves the probability that the final state is the same as the initial state, i.e. secondary self scattering may occur. This second decision is reached by a generalisation of the rejection method which auto-matically yields the final state parameters. The self scattering devices are summarized in symbolic form in Figure 6 (for three real scattering channels).

For high efficiency, the secondary self scattering may be minimized by replacing Γ_j by an envelope function $E_j(\underline{k})$ which is defined in terms of the differential scattering rate $K_j(\underline{k},\underline{k}')$ by
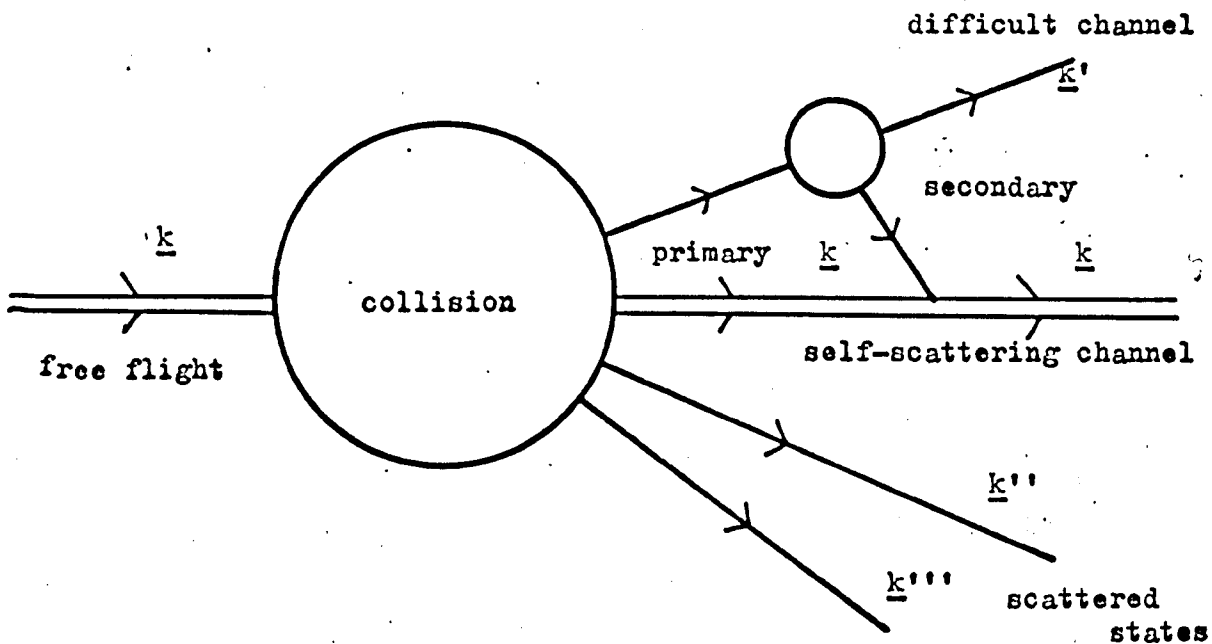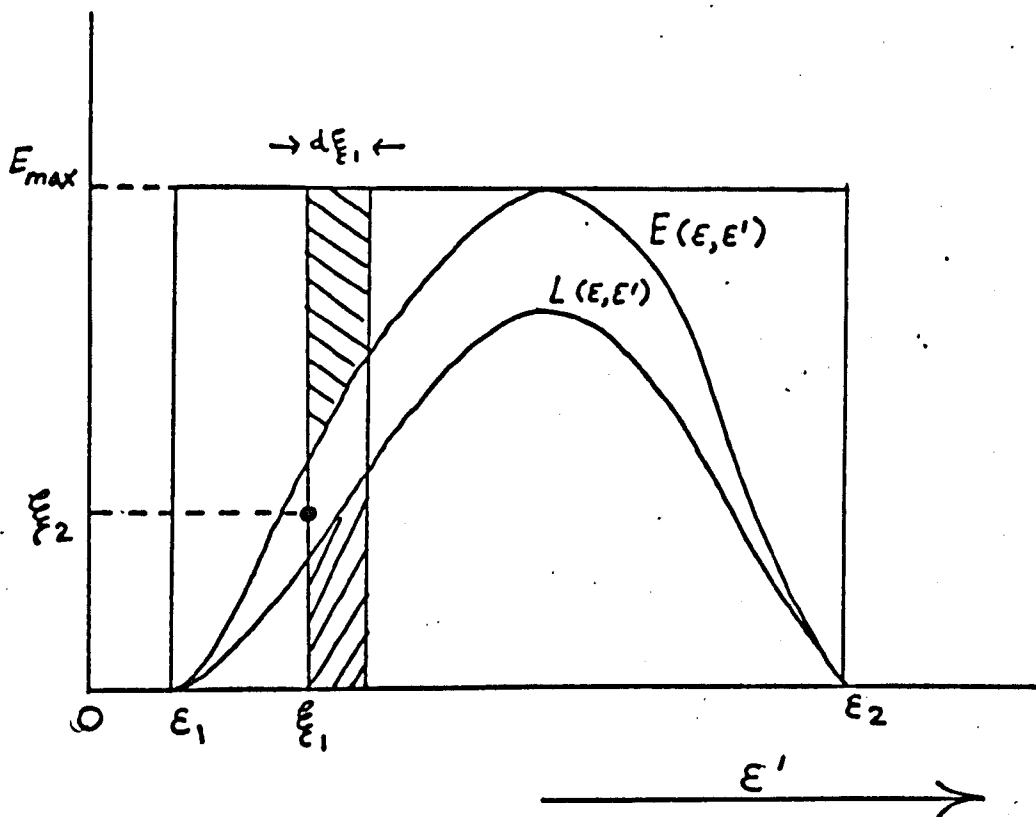
FIG 3.6   THE SELF-SCATTERING DEVICES

FIG 3.7   THE ENVELOPE METHOD

$$E_j(\underline{k}) \equiv \int_D E_j(\underline{k},\underline{k}')d\underline{k}' \text{ where}$$

$$\lambda_j(\underline{k}) \equiv \int_D K_j(\underline{k},\underline{k}')d\underline{k}' \text{ and } E_j(\underline{k},\underline{k}') \geq K_j(\underline{k},\underline{k}') \text{ for all } \underline{k},\underline{k}'.$$ Here $E_j(\underline{k},\underline{k}')$

is defined on the same domain of integration D as $K_j(\underline{k},\underline{k}')$ and can be

handled analytically.

To illustrate the procedure we consider the simple case where channel j is

difficult and the scattering term reduces to the form:

$$\lambda_j(\underline{k}) = \int_{\varepsilon_1}^{\varepsilon_2} L(\varepsilon,\varepsilon')d\varepsilon' \qquad . \tag{3.5.1}$$

Here ε' is a final state parameter such as energy, or a simple function of

energy. The limits ε_1, ε_2 are in general functions of the initial state

parameter ε. An envelope function $E(\varepsilon,\varepsilon')$ is chosen such that

$$\int_{\varepsilon_1}^{\varepsilon_2} E(\varepsilon,\varepsilon')d\varepsilon' = E_o(\varepsilon) \tag{3.5.2}$$

where $E_o(\varepsilon)$ can be calculated exactly. The secondary self scattering rate

is then

$$\int_{\varepsilon_1}^{\varepsilon_2} d\varepsilon'' \left\{E_o - \int_{\varepsilon_1}^{\varepsilon_2} L(\varepsilon,\varepsilon')d\varepsilon'\right\}\delta(\varepsilon-\varepsilon''). \tag{3.5.3}$$

The probability of secondary self scattering P^{SS} is then

$$P^{SS} = 1 - \int_{\varepsilon_1}^{\varepsilon_2} L(\varepsilon,\varepsilon')d\varepsilon'/E_o \tag{3.5.4}$$

whereas the probability density of real scattering $P^R(\varepsilon,\varepsilon')$ is given by

$$P^R(\varepsilon,\varepsilon')d\varepsilon' = L(\varepsilon,\varepsilon')d\varepsilon'/E_o \qquad . \tag{3.5.5}$$

If we choose $E(\varepsilon,\varepsilon') \approx L(\varepsilon,\varepsilon')$ then P^{SS} becomes very small as required.

The Monte Carlo routine here is the generation of a pair of random numbers ξ_1,

ξ_2 where ξ_1 is uniformly distributed on $(\varepsilon_1,\varepsilon_2)$ and ξ_2 is uniformly distributed on

the interval 0 to the maximum of E for the range $(\varepsilon_1,\varepsilon_2)$. If the random point

(ξ_1,ξ_2) lies between the curves L and E then we exit through the self-scattering

channel, if between O and L through channel j with final state parameter ξ_1, otherwise (ξ_1, ξ_2) is regenerated. The routine may be justified by a similar argument to that for the rejection method given in section 3. In certain cases it may be possible to sample the envelope function directly in which case only a single random point (ξ_1, ξ_2) is required For this situation ξ_1 is the solution of

$$r = \int_{\varepsilon_1}^{\xi_1} E(\varepsilon, \varepsilon') d\varepsilon' / E_o \qquad , \qquad r \varepsilon (0,1)$$

whilst ξ_2 is uniformly distributed on O to $E(\varepsilon, \xi_1)$. If (ξ_1, ξ_2) lies between the curves E and L we have self-scattering, otherwise real scattering with final state parameter ξ_1.

This method may be extended to general situations in which the carrier state is specified by a large number of parameters, although the choice of an envelope function may be made more exacting.

The major use we have made of the envelope technique concerns inelastic acoustic deformation scattering in simulation of the hot carrier problem in germanium and silicon. The technique was also used in simulation of oscillatory conductivity. Suitable envelope functions for acoustic deformation scattering are given in Appendix 3.2.

3.6 Conclusions

We have reviewed the basic ideas of the Monte Carlo method as applied to electron transport theory and indicated the modifications required to allow for photoexcitation and recombination processes. The complex nature of electron collisions with phonons and impurities requires special handling of the time of flight sampling and collision channel selection. Generalisations of the self scattering device to overcome these problems has been presented and the validity

of the methods proved.   With the techniques developed any physical scattering process can be handled without recourse to approximation.   The method is therefore a powerful one for testing physical models and more approximate methods of solution.   Unlike the Boltzmann equation approach, Monte Carlo methods are particularly suited to high field studies or situations involving highly field dependent distribution functions.   Generalisation to include magnetic fields poses no problem in principle and extension to multivalley processes is straightforward.

In the following chapter we exploit the techniques of Monte Carlo to support theoretical studies of the oscillatory photoconductivity effect.

CHAPTER IV

OSCILLATORY PHOTOCONDUCTIVITY

4.1 Introduction

In this chapter we focus attention on a second situation in which photoexcited hot carriers may arise, where the applied radiation is responsible for a narrow band excitation spectrum. The phenomenon has come to be known as the oscillatory photoconductivity effect. It turns out that this is a complicated 'mixed' hot carrier problem in which the steady state distribution functions are highly non-equilibrium due to optical heating and are severely distorted by applied electric fields.

At low temperatures the photoconductivity of many III-V semiconductors is an oscillatory function of the energy of the monochromatic incident light, with a period equal to the longitudinal optical (LO) phonon energy. This effect is due to the strong polar interaction between the photoexcited carriers and optical phonons. It was first observed by Blunt (1958) and has since received considerable experimental attention. The basic theory of the effect has been presented by Stocker and Kaplan (1966) using certain approximations regarding the form of the non-equilibrium carrier distribution function. A brief review of the earlier work is given in section 2. The present study was initiated to investigate the reported strong dependence of the oscillatory structure on electric field (Habeggar and Fan 1964).

The major causes of oscillatory photoconductivity are the short carrier recombination lifetimes and the preferential momentum losses in the direction of the electric field induced by the strong optical polar phonon-electron interaction. As we shall see the carrier distribution function $f(\underline{k})$ is very

far from equilibrium and shows a highly non linear dependence on electric field. Consequently the precise calculation of $f(\underline{k})$ and the transport parameters from the Boltzmann equation is a formidable problem unless severe approximations are made with respect to the form of the distribution function and the scattering processes. To avoid these difficulties we have performed detailed Monte Carlo calculations for the photoconductivity as a function of photon energy and electric field strength. These are described in section 3. Provided that the carriers are not injected into the band with an energy very close to a multiple number of optical phonon energies, these calculations show good agreement with experiment (Barker and Hearn 1969a).

An interesting situation occurs for carriers which are photoexcited mono-energetically into the band with an energy just less than an integral number of LO phonon energies. Our calculations, and also those of Stocker (1967) suggest that the conductivity and differential conductivity can theoretically become negative, for a certain range of electric fields (typically from a few mV/cm to a few V/cm). However, this aspect of oscillatory photoconductivity has not yet been observed experimentally. These effects arise from the field dependence of the mean drift velocity of the photoexcited carriers. Our Monte Carlo calculations, and also an exact analysis based on a simple one dimensional model (section 4), support the form predicted by Stocker for the variation of conductivity with the strength of the uniform electric field. This suggests that the occurrence of a negative drift velocity for certain electric field strengths is a real effect (Barker and Hearn 1969b).

The possibility of observing bulk time independent negative conductance, in which part of the incident optical energy is transferred to the electric field, is considered in detail in Chapter V.

4.2 Oscillatory photoconductivity - a brief review

The earliest reported observations of oscillatory photoconductivity involved measurements of the low temperature (less than $12^{\circ}K$) extrinsic photo-conductive spectral response of samples of p-type indium antimonide doped with either copper, silver or gold (Blunt 1958, Engeler, Levinstein and Stannard, Jr., 1961a, b). Each of these dopants gives rise to two deep acceptor levels in InSb. Optically induced transitions between the lower level and the valence band (heavy hole) are responsible for the photoconductivity. These are indicated in Figure 4.1, where we sketch the form of the band structure of InSb and summarize some of its properties. The essential experimental technique involves exposing the sample to monochromatic radiation (in the 4 to 28 micron range), chopped at about 200 c.p.s. Photocurrents are measured by applying a d.c. voltage across the sample in series with a load resistance. By amplifying the a.c. voltage across the load resistance only the photocurrent is measured and the d.c. dark current due to thermally excited carriers is suppressed. Typically the doping densities are in the range $10^{13} - 10^{15}$ cm^{-3}, and the maximum steady state excess carrier densities are of the order $10^{11} cm^{-3}$, so that intercarrier collision effects are expected to be negligible.

Monochromatic radiation induces transitions between the impurity levels and the valence band such that the photoexcited holes enter the band with a well defined energy. There is always a slight spread due to the width of the impurity level and any residual energy spread of the incident light.

The early experiments established that oscillations occur in the spectral response, with minima at photon energies given by

$$\hbar\omega = E_i + n\hbar\omega_o$$

$$\text{4.2.1}$$

where $\hbar\omega_o$ is the long wavelength longitudinal optical (LO) phonon energy.

conduction band

electron energy

0.235 eV

acceptor levels

photoconductive transitions

heavy hole band

valence bands

light hole band

split off band

k space

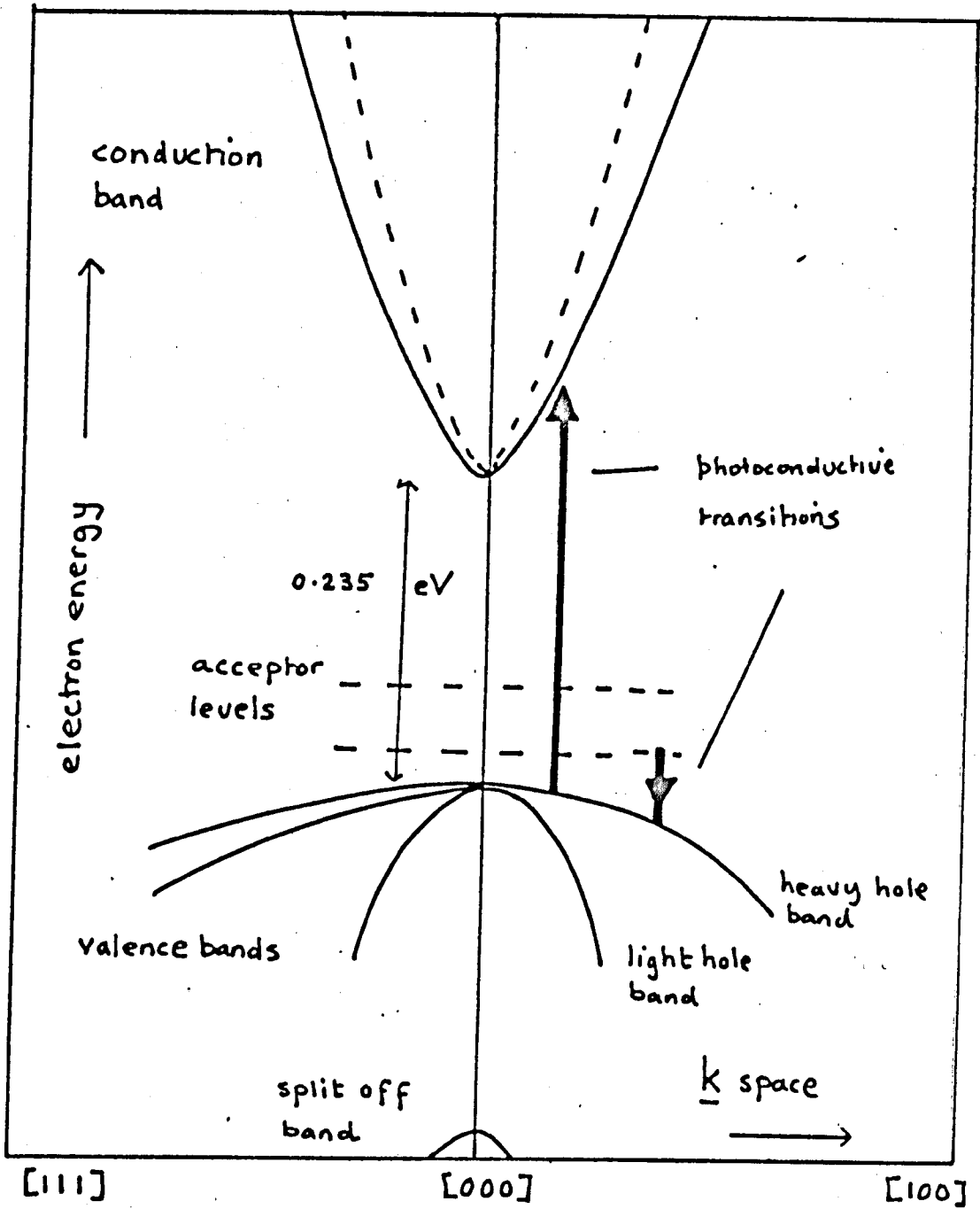[111]   [000]   [100]

FIG 4.1   SKETCH OF BAND STRUCTURE

OF INDIUM ANTIMONIDE

The oscillations were originally attributed to an oscillatory structure in the absorption spectrum. On this model the spectral curves (an example is shown in Figure 4.2) were interpreted as the superposition of a series of spectral curves with thresholds separated by a single LO phonon energy. The first threshold would correspond to a direct impurity to valence band transition. Whereas the second and higher thresholds would arise from indirect transitions involving the emission of one or more LO phonons. Later work (Stocker, Levinstein, Stannard, Jr., 1966) has shown that no such oscillatory structure exists in the absorption spectrum.

The first observations of intrinsic oscillatory photoconductivity, involving valence to conduction band transitions (see Figure 4.1), were made by Habeggar and Fan (1964) and Stocker et al (1964), again with p-type InSb and for the temperature range 4°K to 50°K. Similar observations were reported in n-type InSb by Nasledov et al (1965). The photoconductivity is largely due to the photoelectrons since the measured light and heavy hole mobilities are some two orders of magnitude lower than the electron mobility. Extrinsic transitions are negligible since these involve absorption coefficients of the order 10^{-2}cm^{-1} as compared with 10^{3}cm^{-1} for intrinsic transitions. The spectral response again shows minima occurring at photon energies

$$\hbar\omega = (1 + m_e/m_h)n\hbar\omega_o + E_g, \qquad\qquad 4.2.2$$

where the conduction and valence bands are assumed parabolic with effective masses m_e, m_h respectively. The energy gap is denoted by E_g. The factor $(1 + m_e/m_h)$ arises from the three body nature of the transition.

No oscillatory structure was observed in the absorption spectrum. Consequently, Stocker et al (1964) reinterpreted the oscillations in terms of oscillatory variations in the energy dependence of the lifetime of the photo-

electrons. Their model assumed that electrons are captured at impurities by both direct and cascade processes; the trapping being more efficient for lower energy electrons. Electrons injected with energies close to a multiple LO phonon energy would cascade rapidly to the bottom of the band by emitting optical phonons, followed by rapid capture. For injection energies intermediate to two successive multiple LO phonon energies, the cascade process would still occur but would leave the electron with a higher residual energy. Hence there would be a lower probability for capture.

An alternative explanation was advanced by Habeggar and Fan (1964), again of a qualitative form. They suppose that the electron recombination lifetime is intermediate between the relaxation time for optical phonon emission and the energy relaxation time due to acoustic phonons. The electrons then recombine before losing appreciable energy. If the injection energy exceeds $\hbar\omega_o$, the electron loses one or more quanta of $\hbar\omega_o$ very rapidly, and with increasing energy, the steady state energy oscillates in the range 0 to $\hbar\omega_o$, going through a minimum every time $\hbar\omega$ is a multiple of $\hbar\omega_o$. At low temperatures the mobility is determined by scattering from ionized impurity centres and varies with energy, thus giving rise to the oscillations. As in previous explanations no discussion of the role of the applied field was given.

A comprehensive experimental analysis of oscillatory photoconductivity was made by Stocker et al (1966) and included measurements of the temperature and applied field dependence of the intrinsic and extrinsic oscillations in p-type InSb. This work showed that the oscillatory structure gradually disappeared for applied fields in excess of about 20 Volts/cm whilst as a function of increasing temperature the oscillation minima shifted to lower photon energies. The latter shift was interpreted as due to the temperature variation of the energy gap in InSb. The separation of the minima remained unchanged however.
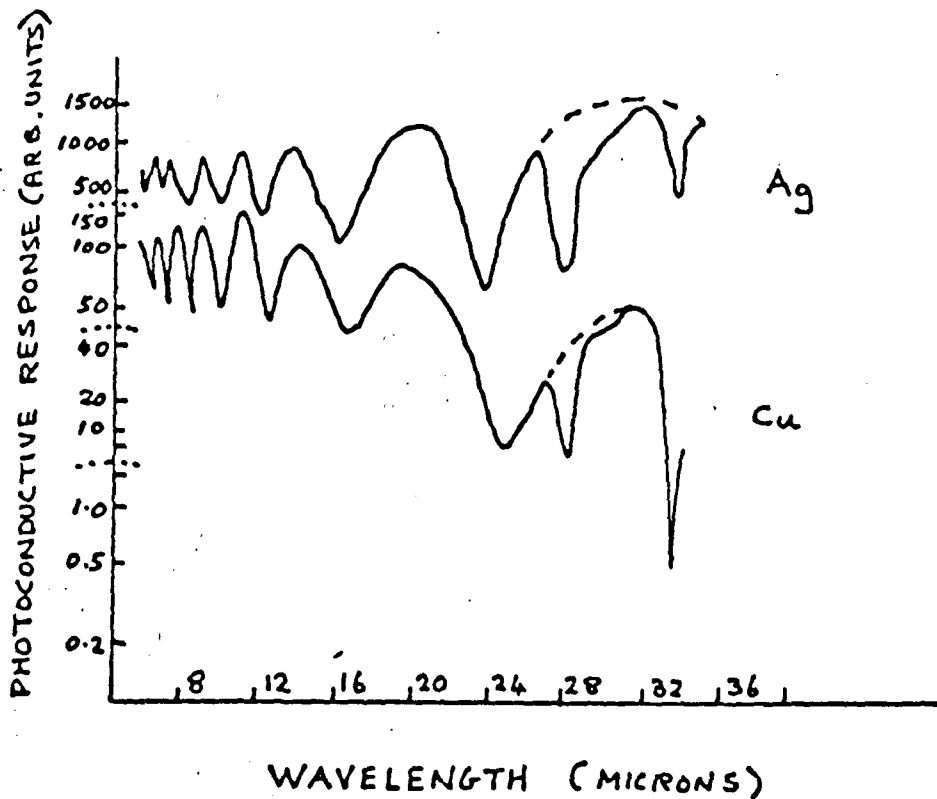
FIG 4.2   OSCILLATORY PHOTOCONDUCTIVE RESPONSE

ASSOCIATED WITH THE LOWER LEVEL OF

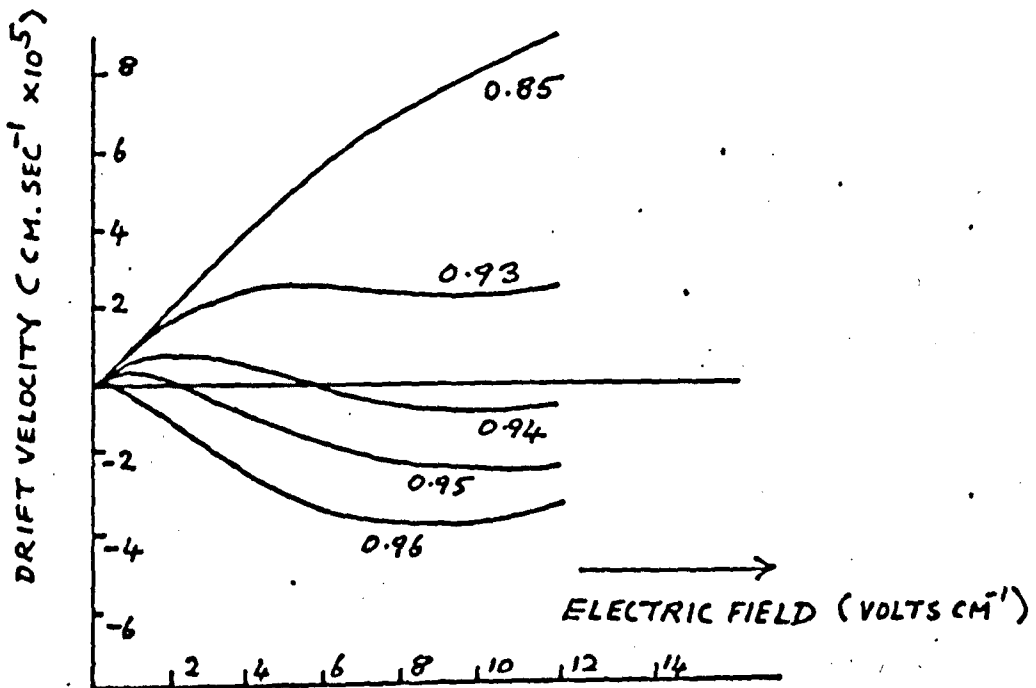Ag AND Cu in InSb (AFTER ENGELER ET.AL.1961a)

FIG 4.3. A DRIFT VELOCITY-FIELD CHARACTERISTIC FOR INSb

FROM THE CALCULATIONS OF STOCKER (1967)

(NUMBERS DENOTE INJECTION ENERGY IN UNITS OF $\hbar\omega_0$)

Above about 30°K the oscillations decreased rapidly in magnitude and disappeared entirely above 60°K. On the basis of these observations Stocker et al concluded that the minima in the spectral response were due to preferential momentum losses of carriers due to optical phonon emission in the opposite direction to the applied field and that the electron distribution function was very far from equilibrium. Their argument is very similar to that of Habegger and Fan and supposes that because of the strong optical polar phonon interaction the electrons have mean energies in the range 0 to $\hbar\omega_o$. However, the minima in the oscillations are not attributed to the variation of mobility with electron energy. Instead for injection energies close to the optical phonon emission threshold, the applied field accelerates a large number of electrons moving antiparallel to the field to sufficient energies for optical phonon emission and these are scattered rapidly to the bottom of the band. The consequent loss of momentum to the lattice antiparallel to the field leads to a large reduction in the average electron momentum and the photocurrent is diminished. For injection energies intermediate to 0 and $\hbar\omega_o$ few carriers gain sufficient energy from the field for optical phonon emission and the average momentum is determined by the momentum relaxation processes due to the ionized impurities.

These ideas were supported by calculations based on a Boltzmann equation approach made by Stocker and Kaplan (1966) and Stocker (1967). Their calculations involved an expansion of the distribution function in a truncated series of Legendre polynomials about the field direction, only the first two polynomials P_o and P_1 being included. No quantitative comparison was possible with experiment because of the severe approximations made for the scattering processes. The calculations did, however, give the qualitative form of the oscillations and the disappearance of the oscillations at high field strengths was also displayed. A surprising feature of this work is the prediction of negative photocurrents for injection energies very close to a multiple number of optical phonon energies although this effect has not been observed experimentally.

The occurrence of negative differential conductance and total negative conductance was investigated theoretically by Stocker (1967). The results of Stocker's calculation for the variation of electron drift velocity with applied field are shown in Figure 4.3, and show regions of negative resistance. Stocker also examined the small signal stability of a uniform field distribution biased into the negative resistance regions. Unfortunately this analysis is inconsistent and leads to a false dispersion relation for the frequency and wavevector of small signal space-charge waves and also predicts that recombination has a stabilising effect. The analysis took no account of diffusion processes although as we shall see later diffusion plays a critical role in oscillatory photoconductivity. A similar theoretical treatment of oscillatory photoconductivity was given independently by Elesin and Manykin (1966).

4.3 Simulation of oscillatory photoconductivity

Basic model

The Monte Carlo techniques developed in Chapter $\underline{\text{III}}$ were used to simulate oscillatory photoconductivity in indium antimonide taking precise account of the scattering and recapture processes. Two aspects of this problem have been investigated. The first concerns the overall spectral response, that is the variation of photocurrent with photon energy for a fixed electric field strength. The second concerns the variation of conductivity or mean drift velocity with electric field strength when photoexcitation occurs at a given energy.

We have adopted the following basic model for steady state oscillatory photoconductivity. Electrons are considered to be uniformly photoexcited into a parabolic conduction band, centred on $\underline{k} = 0$, by applied monochromatic radiation from a source external to the band (either a single well defined impurity level or from the valence band). The excitation spectrum is taken

to be exactly monoenergetic, a condition very closely realised in experiment, which implies that electrons enter the conduction band with a random distribution on a constant energy surface in $\underline{k}$-space. We ignore the non-parabolic nature of the actual conduction band in InSb (see Figure 4.1, where the dotted line represents the shape the conduction band would have if it were parabolic with a constant effective mass equivalent to the $\underline{k} = 0$ value). The experiments of Stocker et al (1966) and also the calculations of Kane (1957) suggest that non parabolic effects are unimportant for electron excitation energies less than 0.5eV relative to the band edge. This involves the first seventeen or so oscillations in photocurrent whilst we shall be only concerned with the first few.

In between collisions with phonons and impurities the electrons are considered to drift uniformly in $\underline{k}$-space under the influence of a constant uniform applied field $\underline{F}$, according to the dynamical relation (3.2.1).

As the experiments considered deal with electron densities less than $10^{11} cm^{-3}$, we have the non degenerate low density limit as in Chapter II. Therefore we neglect interelectronic collisions and the effects of non-equilibrium phonon distributions. The most important scattering mechanisms in InSb in order of increasing strength are acoustic deformation scattering, ionized and neutral impurity scattering and longitudinal polar mode optical phonon scattering (Conwell 1967). The detailed forms for these processes have already been discussed and are given in Appendix 3.2. The major part of the electron-optical phonon scattering involves longitudinal optical phonons with small wave-vectors, since the electron wavevectors in the neighbourhood of the (000) minima are very small compared to the maximum wavevector of the Brillouin zone (typically 10^{-2} of the maximum wavevector). We therefore neglect the dispersion of the optical phonons since for InSb (and most semiconductors) the longitudinal optical branch is nearly flat near $\underline{k} = 0$.

Several different forms for the recombination lifetime were considered, ranging
from a constant recombination lifetime (i.e. energy independent) to a Lax type
cascade model. In each instance the mean lifetime was chosen to be of the order
10^{-10} seconds, the typical experimentally observed value for InSb at low temperatures
The results discussed here are mainly based on the cascade type model since capture
into shallow states is expected to be faster than radiative processes at the low
temperatures considered.

The four basic processes considered above were simulated exactly by the Monte
Carlo technique. The steady state photocurrent is proportional to

$$nV$$

where n is the steady state carrier density and V the mean drift velocity. In
practice we calculate τV where τ is the mean carrier lifetime since $n \propto \tau$
in the steady state. The contribution of photoexcited holes (in the intrinsic case)
in the heavy and light hole bands is negligible as the experimentally measured
mobilities are some two orders of magnitude lower for electrons and their contribu-
tion to conductivity is therefore neglected. Effects of thermalised carriers
are also neglected as these are largely cancelled out of the actual experimental
measurements, and in any case for the low temperatures considered their concentra-
tion is much less than the photoexcited carrier density.

The step function primary self-scattering device (c.f. Chapter III, section 4
was employed to enhance numerical convergence for carrier energies in the vicinity
of the threshold for optical phonon emission. The secondary self scattering
device was also employed for the inelastic acoustic deformation scattering channel.
Distribution functions were obtained by using a 50 x 30 mesh in the (k_z, k_ρ) plane,
where the electric field $\underline{F}$ was taken in the negative Z direction. Larger meshes
would have been desirable but the available computer storage space was too small.
The distributions obtained are therefore fairly crude histrograms and do not show

the detail one would like. Fortunately the calculations for the transport

parameters are carried out independently of the distribution functions, and

have no such restrictions.

Spectral response

Figure 4.4a shows a comparison between the theoretical calculations (full

lines) based on the simulation study and the experimental work of Stocker and

Kaplan (1966) (dotted lines) for a similar set of parameters. The results apply

to intrinsic photoconductivity in p-type InSb at 8°K. Curve (a) is for an

electric field of 1.2 V/cm and curve (b) for 2.5 V/cm. A complete list of

parameters is given in Table 4.1. The agreement between the theoretical model

and experiment is good as regards both the spectral dependence and field

dependence except for injection energies close to a multiple optical phonon

energy. Here the conductivity is highly non linear and may become negative.

This effect was also predicted by Stocker and Kaplan (1966). We shall examine

this interesting result in detail later on. The calculations were extended

to a few higher oscillations and these are shown in Figure 4.4b (no experimental

data was available for this region). Each point on the theoretical curves

required some 2×10^5 simulated collisions of which 75% were self-collisions.

The convergence was well within 1%.

Distribution functions

To examine the physics of oscillatory conductivity in more detail it is

useful to calculate the carrier distribution function $f(\underline{k})$ as well as the spectral

response. In order to reduce the long computational time we artificially reduce

the number of collisions per electron by choosing a constant recombination life-

time of 10^{-11} seconds. Figure 4.5 shows the calculated photocurrent in the

region of the first oscillation for InSb at 10°K, for a constant electric field

of 3 V/cm, corresponding to the data given in Table 4.2. One thousand test
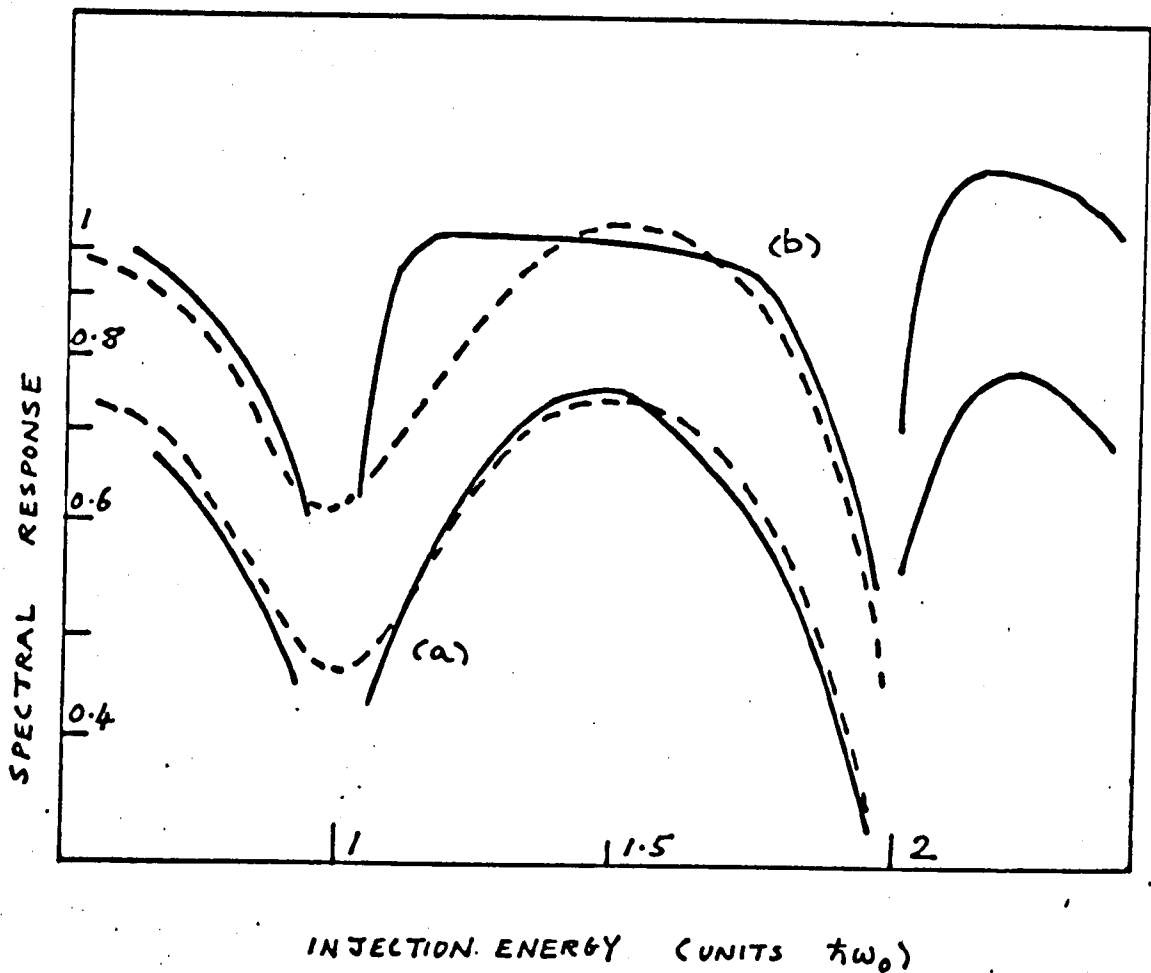
FIG 4.4a   A COMPARISON OF THE MONTE CARLO CALCULATIONS

(FULL CURVES) WITH THE MEASURED (STOCKER ET AL. 1966)

SPECTRAL VARIATION OF THE PHOTOCONDUCTIVITY OF A SAMPLE

OF InSb AT 8° K . CURVE (a) IS FOR AN ELECTRIC FIELD OF

1.2 V/CM AND CURVE (b) FOR 2.5 V/CM.

SPECTRAL RESPONSE (ARB. UNITS)

INJECTION ENERGY (UNITS OF $\hbar\omega_0$)

(b) F=2.5 V/CM

(a) F=1.2 V/CM
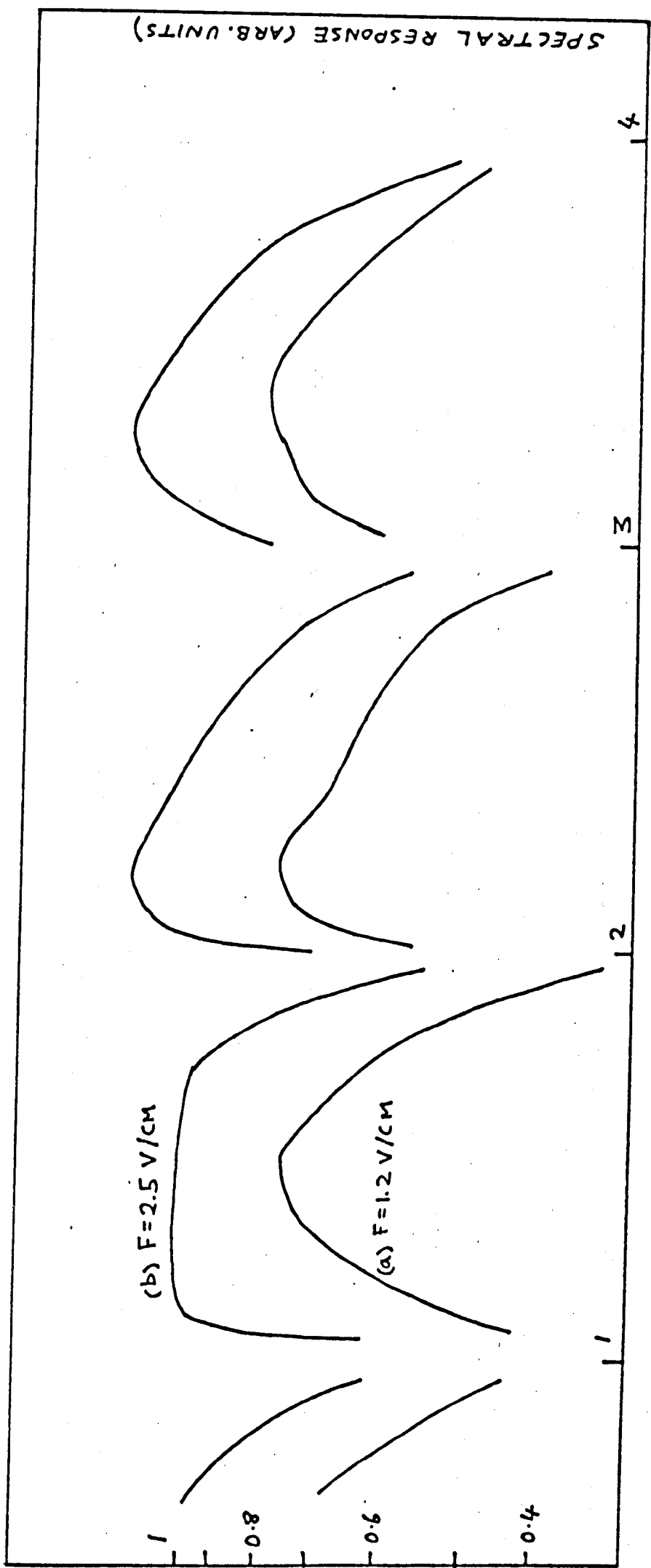
FIG 4.4 (b)   MONTE CARLO CALCULATIONS FOR THE SPECTRAL RESPONSE OF $In_{}Sb$ AT $8°K$.

TABLE 4.1	PARAMETERS USED IN MONTE CARLO CALCULATIONS OF OSCILLATORY PHOTOCONDUCTIVITY

SEMICONDUCTOR	P — InSb
TEMPERATURE	8° K
DENSITY	5.78 gm cm^{-3}
VELOCITY OF SOUND	5X10^{5} cm sec^{-1}
DENSITY OF STATES EFFECTIVE MASS RATIO	0.012
DEFORMATION POTENTIAL (ACOUSTIC PHONONS)	7 eV
DIELECTRIC CONSTANTS ε_{∞}	16.8
ε_{o}	18.7
LO PHONON ENERGY	0.0244 eV
DONOR DENSITY	10^{14} cm^{-3}
ACCEPTOR DENSITY	1.0X10^{15} cm^{-3}
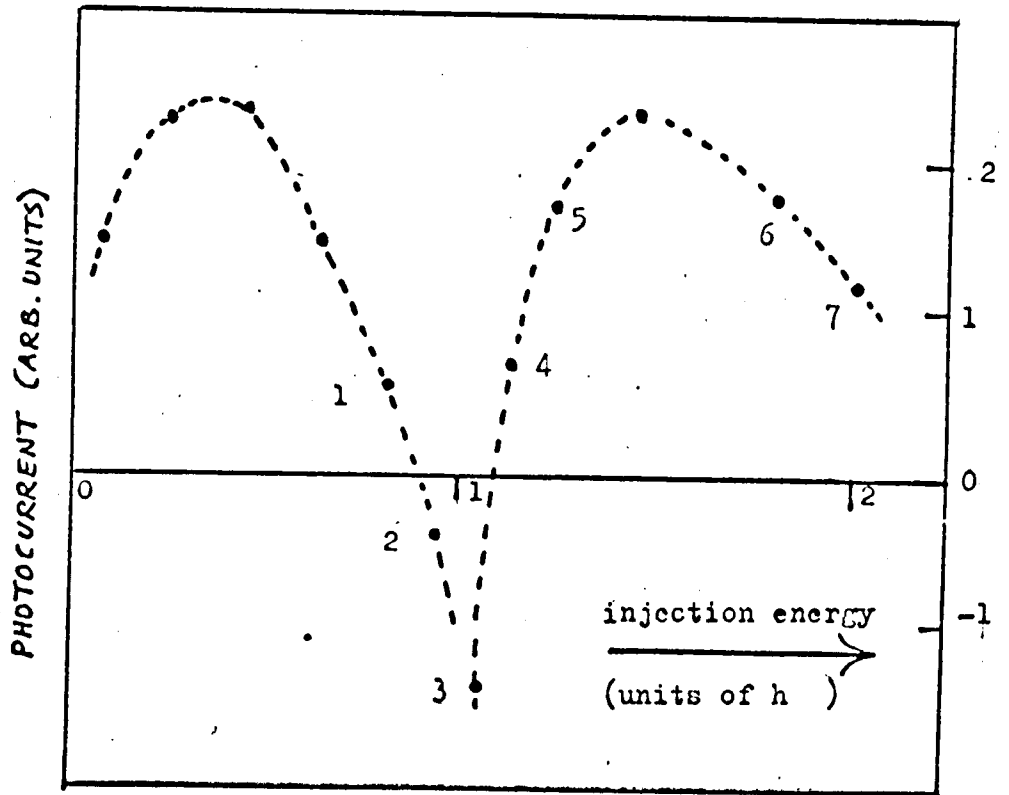
FIG 4.5   SPECTRAL RESPONSE AT 10°K, F = 3 V/cm
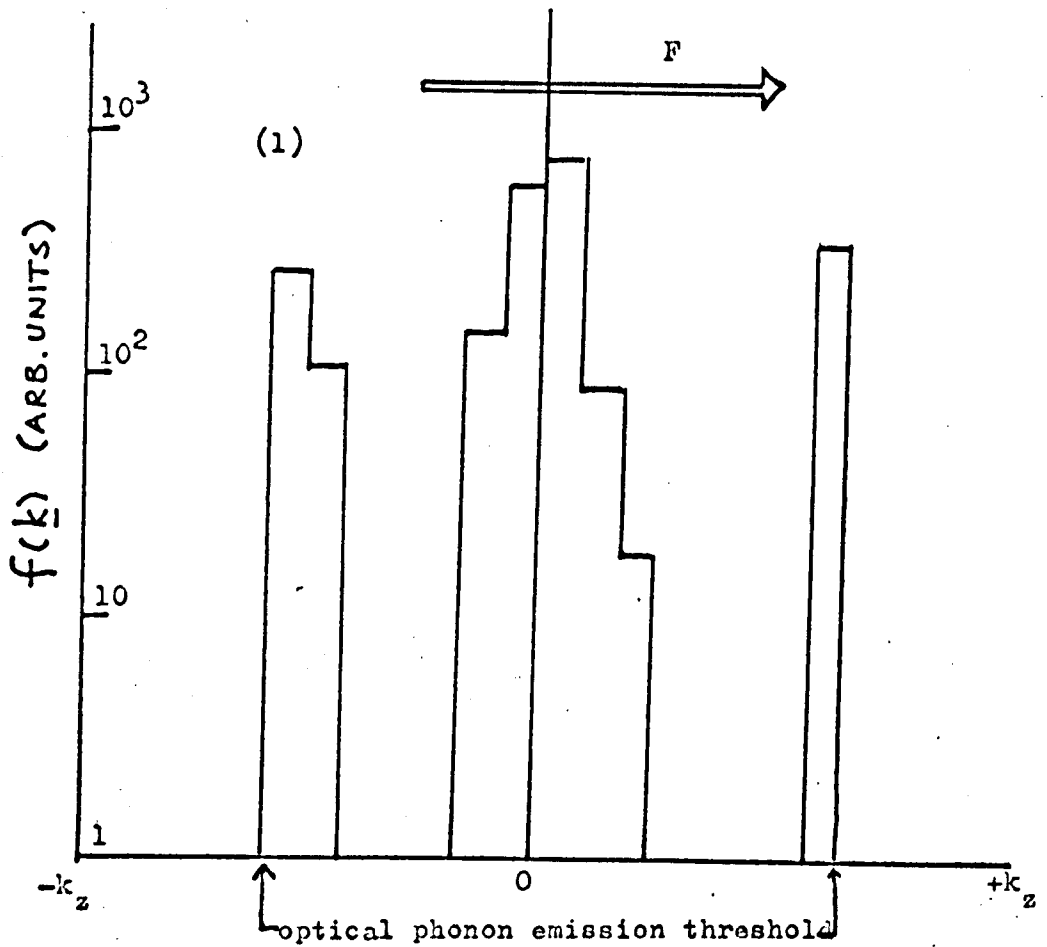
FIG 4.6 : DISTRIBUTION FUNCTION (HISTOGRAM FORM)
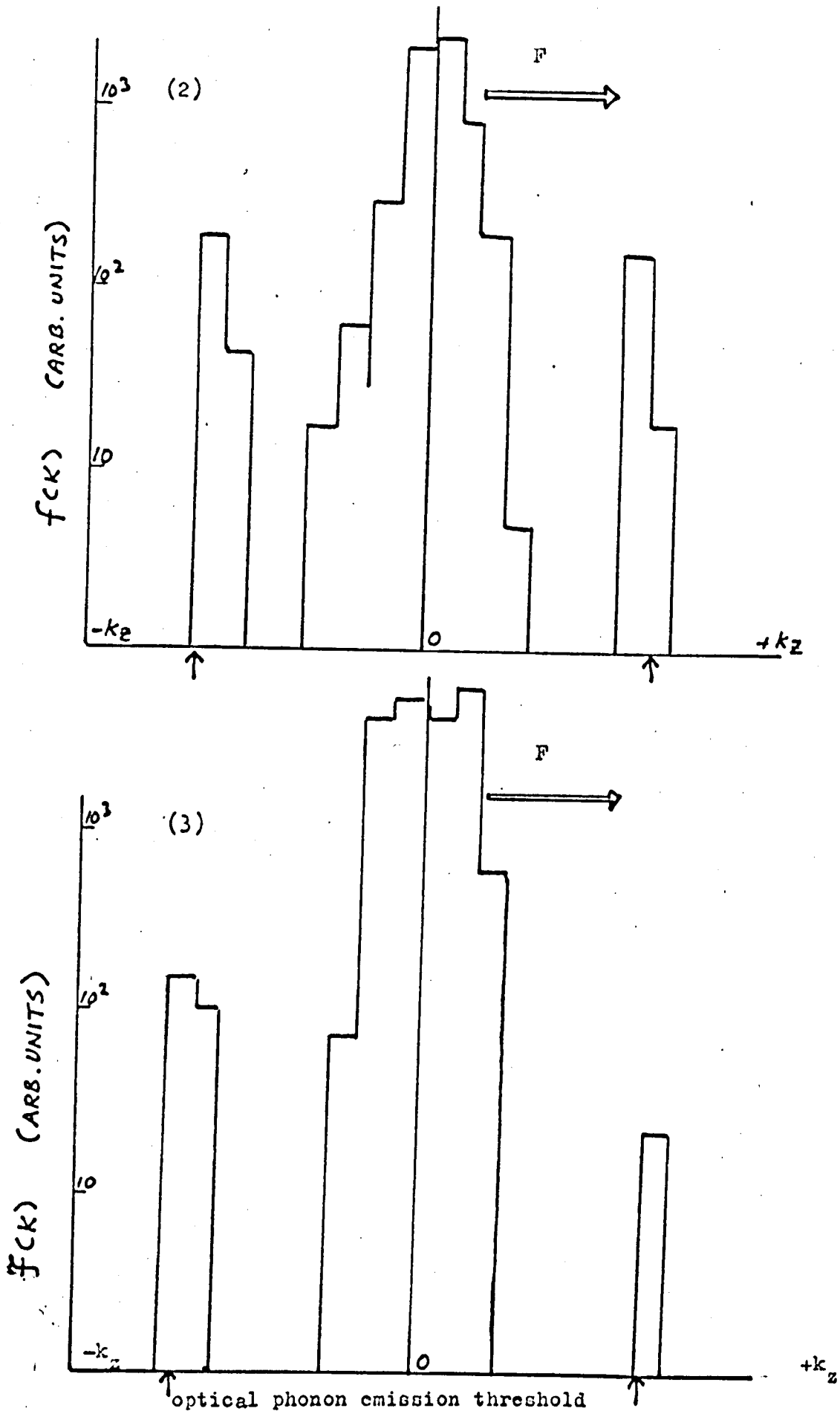
FIG 4.6 Continued.

TABLE 4.2	PARAMETERS USED IN MONTE CARLO CALCULATIONS OF OSCILLATORY PHOTOCONDUCTIVITY
SEMICONDUCTOR	InSb
TEMPERATURE	10° K
INJECTION ENERGY	0.978 X OPTICAL PHONON ENERGY
DENSITY	5.78 GM CM^{-3}
VELOCITY OF SOUND	5×10^{5} CM SEC^{-1}
DENSITY OF STATES EFFECTIVE MASS RATIO	0.012
DEFORMATION POTENTIAL (ACOUSTIC PHONONS)	7 EV
DIELECTRIC CONSTANTS ε_{∞}	16.8
ε_{o}	18.7
LO PHONON ENERGY	0.0244 EV
NEUTRAL IMPURITY DENSITY	10^{14} CM^{-3}
IONIZED IMPURITY DENSITY	10^{16} CM^{-3}

electrons are used in the simulation. Figures 4.6, 4.7, 4.8 show the corresponding distribution functions f($\underline{k}$) for the direction $\underline{k} \equiv (0, 0, k_z)$ in momentum space. This corresponds to the section $k_x = k_y = 0$ and is parallel to the applied field. The distributions are numbered from 1 to 7 and refer to the points on the spectral response curve of Figure 4.5. We consider now the physical processes involved as the injection energy ε is increased from zero to nearly $2\hbar\omega_o$, where $\hbar\omega_o$ is the energy of the longitudinal optical phonon.

(i) Injection near $\underline{k} = 0$, $\varepsilon \simeq 0$

Here the electrons are excited on to a spherical constant energy surface in $\underline{k}$-space, centred on $\underline{k} = 0$. The general scheme is illustrated in Figure 4.9, where the injection shell appears as a circle on a two dimensional section in $\underline{k}$-space. The inelastic collision processes are relatively slow compared with the recombination lifetime and this prevents thermalisation and dispersal of the initial distribution. The faster elastic scattering moves electrons around the energy shell and maintains the sharp distribution. This initial distribution is displaced in momentum space by the applied field, the displacement being determined by the recombination and momentum relaxation processes. Electrons moving antiparallel to the field gain energy, from the field, whilst those moving parallel to the field lose energy. At the lower injection energies few carriers survive to cross the energy threshold for optical phonon emission and we are led to a net positive momentum antiparallel to the field and hence a positive photocurrent.

(ii) Injection just below threshold, $\varepsilon \leq \hbar\omega_o$

As the injection energy approaches threshold the electric field produces severe distortion of the injected electron distribution. (Points 1, 2 of Figures 4.5, 4.6.) Many of the electrons gain sufficient energy from the field
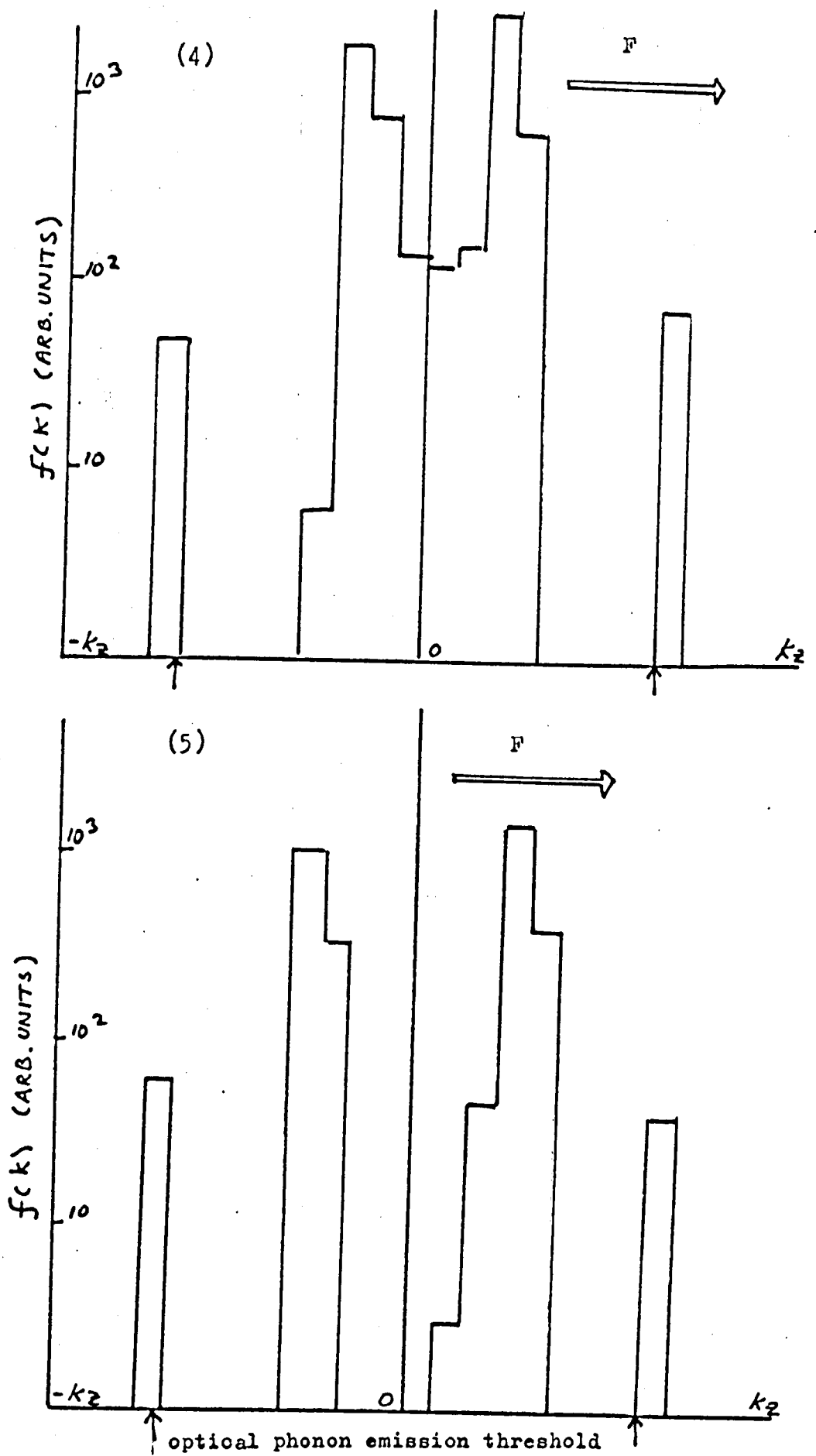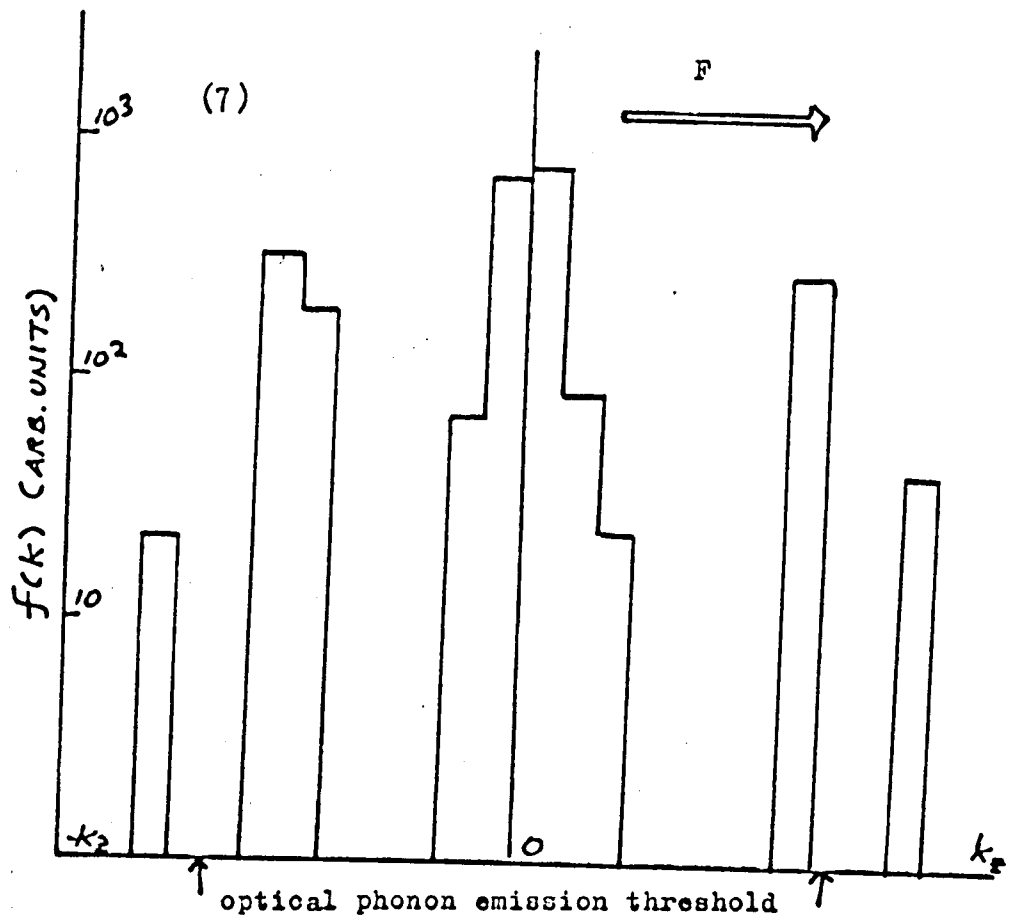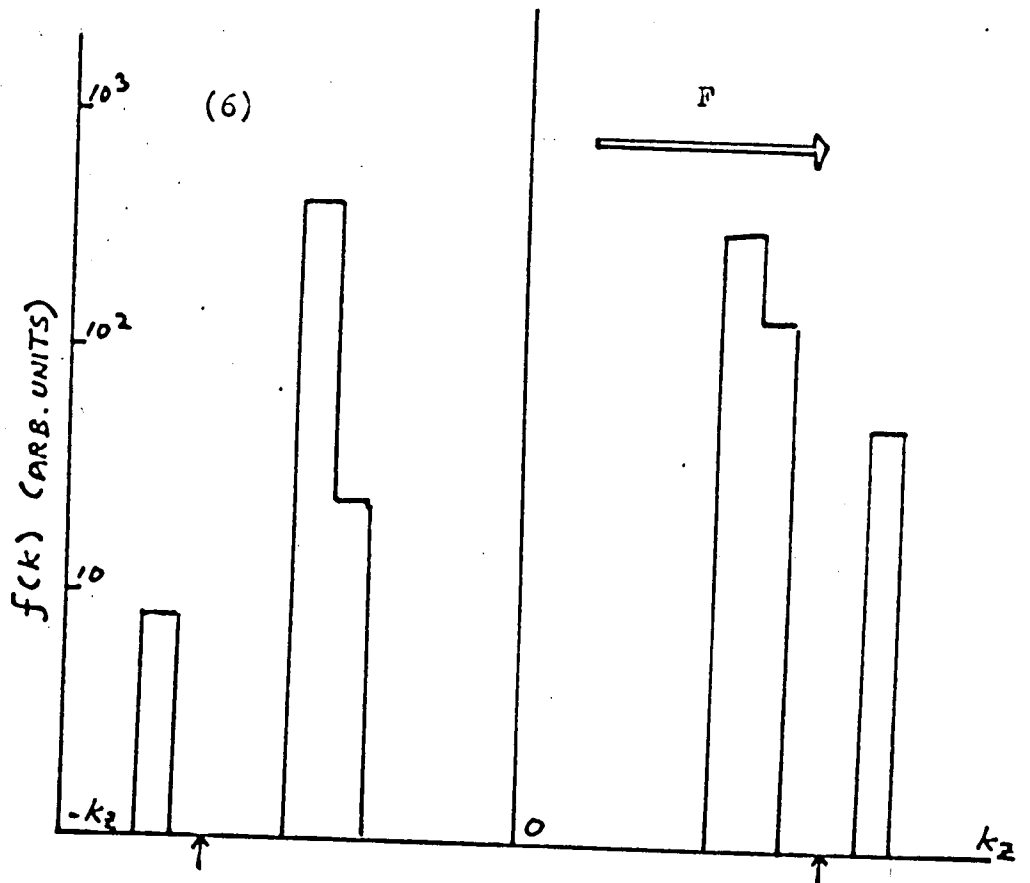
FIG 4.7 :   DISTRIBUTION FUNCTION (HISTOGRAM FORM)

(6)

F

(7)

F

optical phonon emission threshold

FIG 4.8 : DISTRIBUTION FUNCTION (HISTOGRAM FORM)

section in **k**-space

(i)

$\varepsilon \approx 0$

→ Field

optical phonon emission
threshold

(ii)

→ field

$\varepsilon \lesssim \hbar\omega$

(iii)

→ Field

$\varepsilon \gtrsim \hbar\omega$
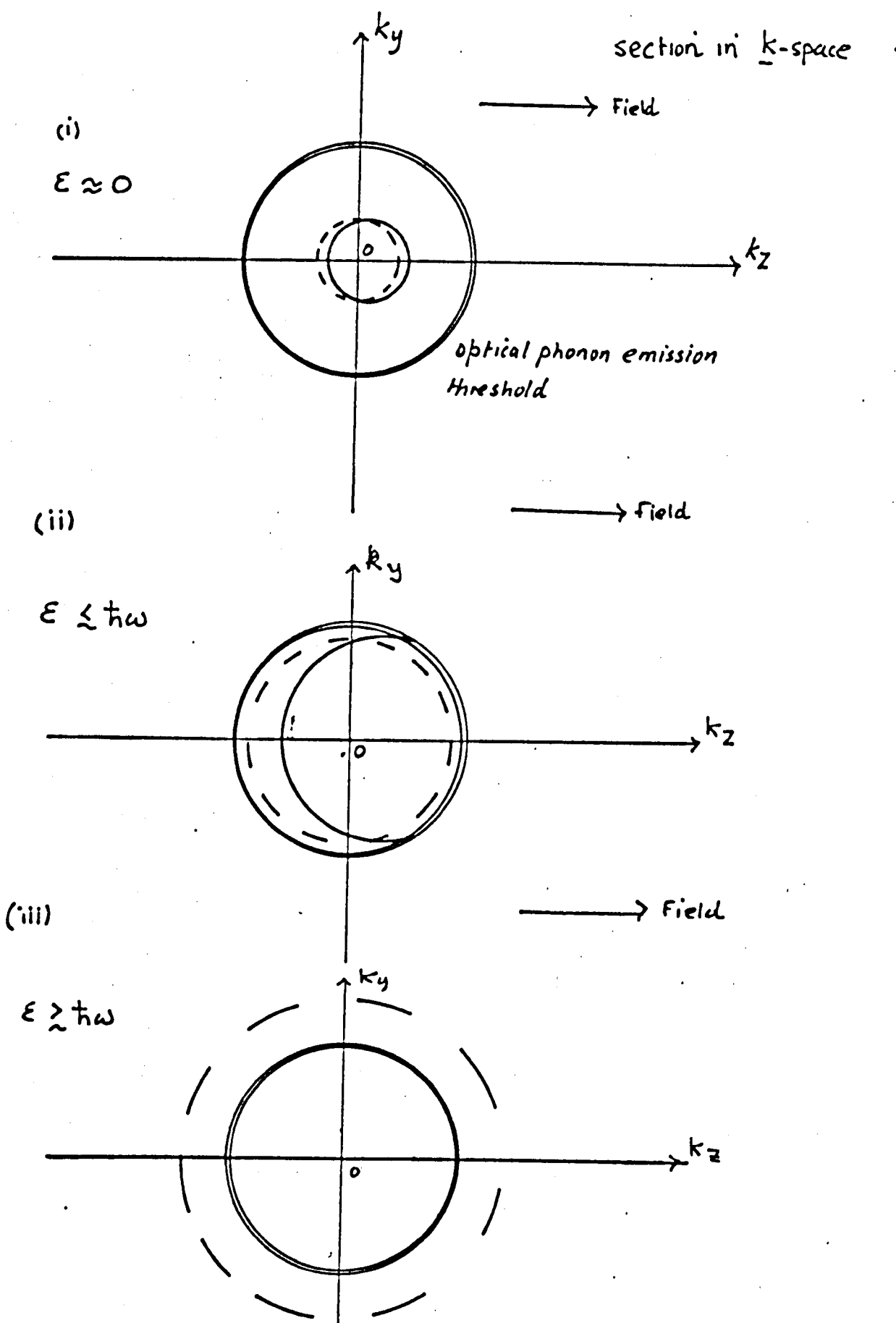
FIG 49 : INJECTION SCHEME FOR $\varepsilon \approx 0$, $\varepsilon \lesssim \hbar\omega$, $\varepsilon \gtrsim \hbar\omega$.

– – – –   INJECTION SPHERE

———   DISPLACEMENT OF INJECTION SPHERE IN
           ELECTRIC FIELD

to reach energies in excess of one optical phonon energy. These electrons, which have momentum antiparallel to the field, rapidly emit a longitudinal optical phonon and are scattered to the bottom of the band. There is then a net preferential momentum loss, antiparallel to the field, from the electron assembly to the lattice. This leads to a reduction in photocurrent. In case 2 of Figures 4.5 and 4.6 the momentum loss is such that the residual net momentum is in the direction of the applied field and a negative photocurrent occurs.

(iii) Injection above threshold, $\hbar\omega_o < \varepsilon < 2\hbar\omega_o$

In this case all the electrons are able to emit optical phonons. At injection energies just above threshold (Point 3 of Figures 4.5 and 4.6) some of the electrons moving parallel to the field are sufficiently decelerated before interacting with the optical phonons to reach energies less than $\hbar\omega_o$. For this situation the net momentum loss due to optical phonon emission is antiparallel to the field. The photocurrent is therefore reduced and may become negative. For higher injection energies (cases 4, 5, 6 in Figures 4.5, 4.6, 4.7) very few of the injected electrons survive to decelerate to below threshold and the optical phonon emission is essentially isotropic in momentum space. The net momentum loss due to optical phonon emission is then close to zero and much less than the net gain in momentum from the field. Almost all the electrons lose energy by optical phonon emission (absorption of optical phonons is negligible at 10^oK) and the situation is very similar to case (i). The majority of electrons have energies less than $\hbar\omega_o$ and populate an approximately spherical shell in momentum space with the centre of the distribution slightly displaced antiparallel to the field. There is also a low population outer shell, the remnants of the injected shell, with electron energies greater than $\hbar\omega_o$. The spectral response is almost exactly a repetition of the response for case (i) with a net positive photocurrent.

(iv) Injection just below the second threshold, $\varepsilon \lesssim 2\hbar\omega_o$

This situation is an almost exact repetition of case (ii) but the electrons injected with momenta antiparallel to the field emit two optical phonons in succession to cascade down to energies less than $\hbar\omega_o$. Figure 4.8, corresponding to point 7 of Figure 4.5 illustrates this case and we note that the distribution function is composed of concentric spherical shells in momentum space with energies at approximately ε, $\varepsilon - \hbar\omega_o$, $\varepsilon - 2\hbar\omega_o$. Comparison with Figures 4.5, 4.6 (point 1) shows that the distribution functions and spectral response are almost identical.

The higher order oscillations occur in a similar fashion with the spectral response showing a repetition of the response for the range $0 < \varepsilon < \hbar\omega_o$.

Velocity field characteristics

The details of the field dependence of oscillatory photoconductivity are most clearly revealed by calculating the variation of the mean carrier drift velocity with applied field for a fixed injection energy. We find that independently of the energy dependence of the capture cross section, the drift velocity-field characteristics have the same general form provided that (a) the magnitude of the capture cross section is sufficiently large; and (b) the lattice temperature is sufficiently low (typically less than 30^oK). The main result is that the velocity-field characteristics are highly non-linear and, for carriers injected just below a multiple optical phonon energy, show a region of negative velocity. Severe difficulties with numerical convergence arise when the drift velocity is vanishingly small. These arise from the increased importance of the statistical fluctuations compared with the small mean drift velocity. In order to verify the occurrence of vanishing and negative drift velocities it has proved necessary to establish convergence within 0.5%. This was achieved by using between 10^4 and 10^5 test carriers in the simulation and involved a considerable increase in computing time.

Figure 4.10 shows the best computed velocity-field curve for photoexcited electrons in p-type InSb at 10^OK, corresponding to an injection energy of 0.978 times an optical phonon energy. A full list of parameters is given in Table 4.2. The recombination process was assumed to be of the cascade model type giving a mean lifetime, under zero field conditions, of 10^{-10} seconds. The slope of the drift velocity curve is always positive at very low fields until a threshold field (F_t) is reached where the slope becomes negative. The velocity changes from positive to negative at a critical field (F_c), reaches a minimum value at the valley field (F_v), and then a restoring field (F_r) is reached where v becomes positive again. The labelling is illustrated in Figure 4.11.

Figures 4.12, 4.13 show the form of the distribution function along the direction (0,0,F) in momentum space corresponding to the fields F = 0.3, 0.9, 5.7 and 15.5 V/cm of Figure 4.10. These calculations were made separately using 3000 test electrons. At zero field the distribution function is spherically symmetric about $\underline{k}$ = 0. At very low fields, the electrons respond linearly to the applied field, very few electrons gain sufficient energy to emit an optical phonon, and Ohm's law is obeyed. For F = 0.3 V/cm (Figure 4.12), a significant number of electrons are accelerated beyond the threshold for optical phonon emission. There follows a significant loss of momentum to the lattice antiparallel to the field. The net momentum acquired by the electrons is thereby reduced, although still positive. Beyond the threshold field F_t, further increase in field leads to a large loss in momentum to the lattice and the net momentum is gradually reduced to zero. At F = 0.9 V/cm, the distortion to the zero field distribution induced by the field is further increased and the net loss of momentum to the lattice antiparallel to the field exceeds the net gain from the field: a negative mean drift velocity is set up. Figure 4.13, shows the situation at F = 5.7 V/cm where the drift velocity is negative and the electron distribution is smeared out by the field. Here the

FIG. 4.10

Electric Field (volts cm⁻¹)
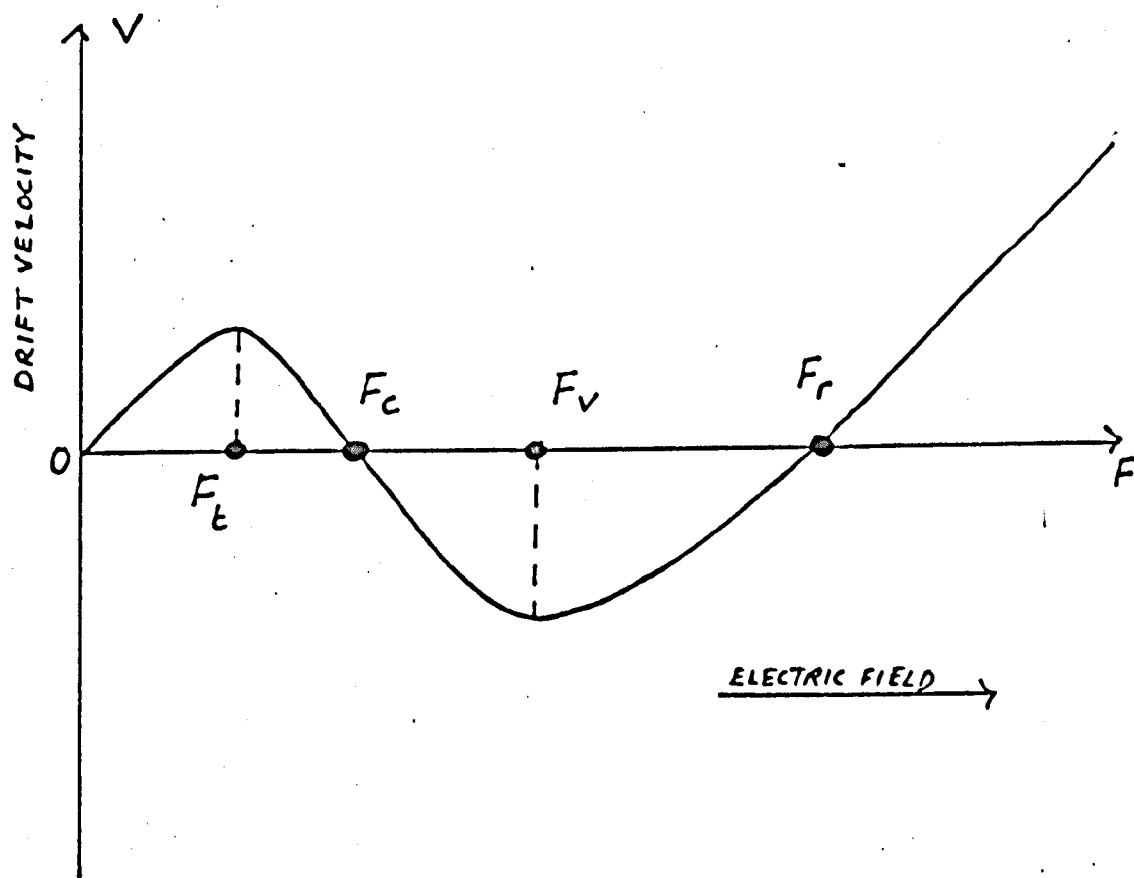
Drift Velocity (cm sec⁻¹) ×10⁶
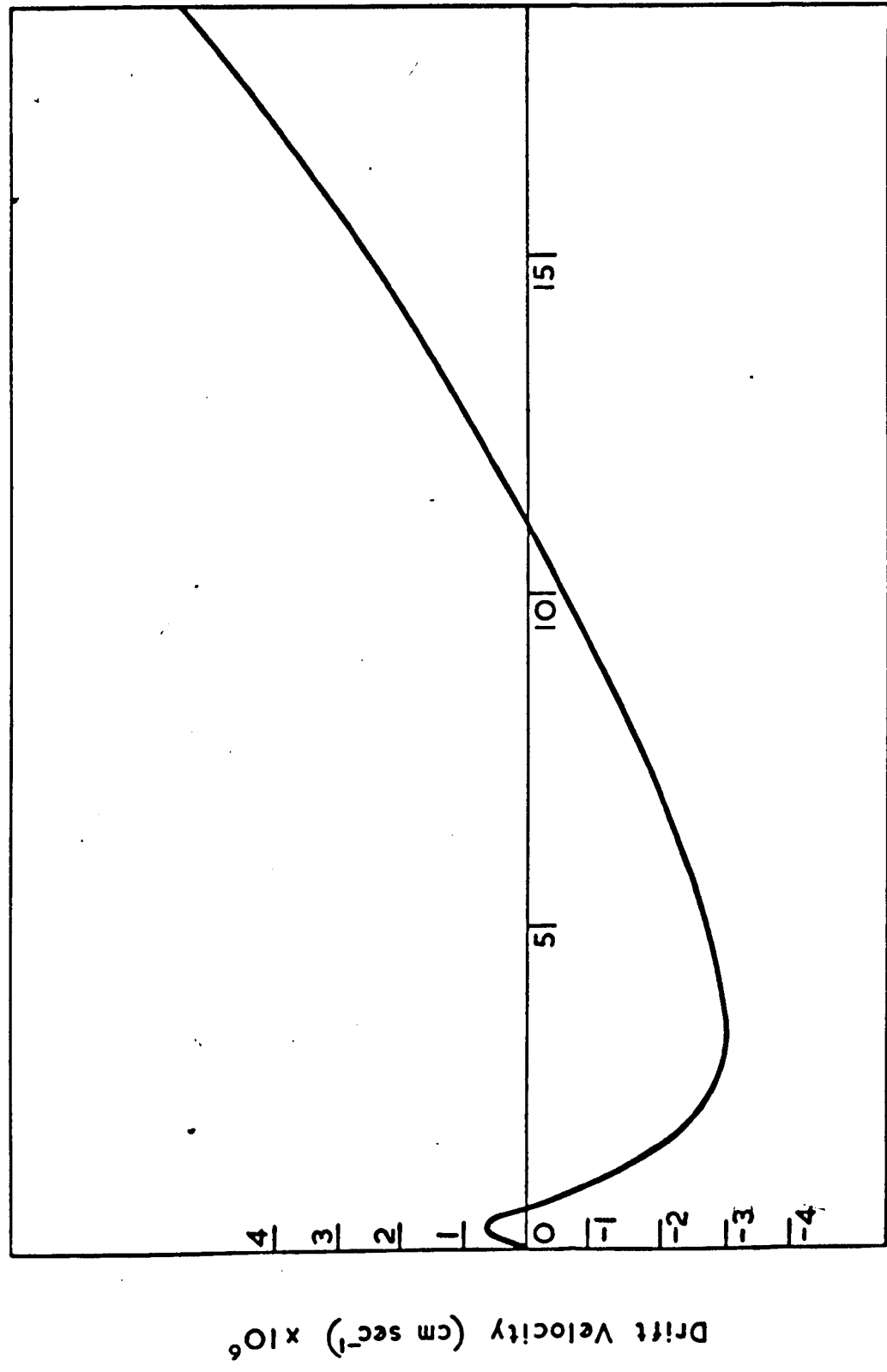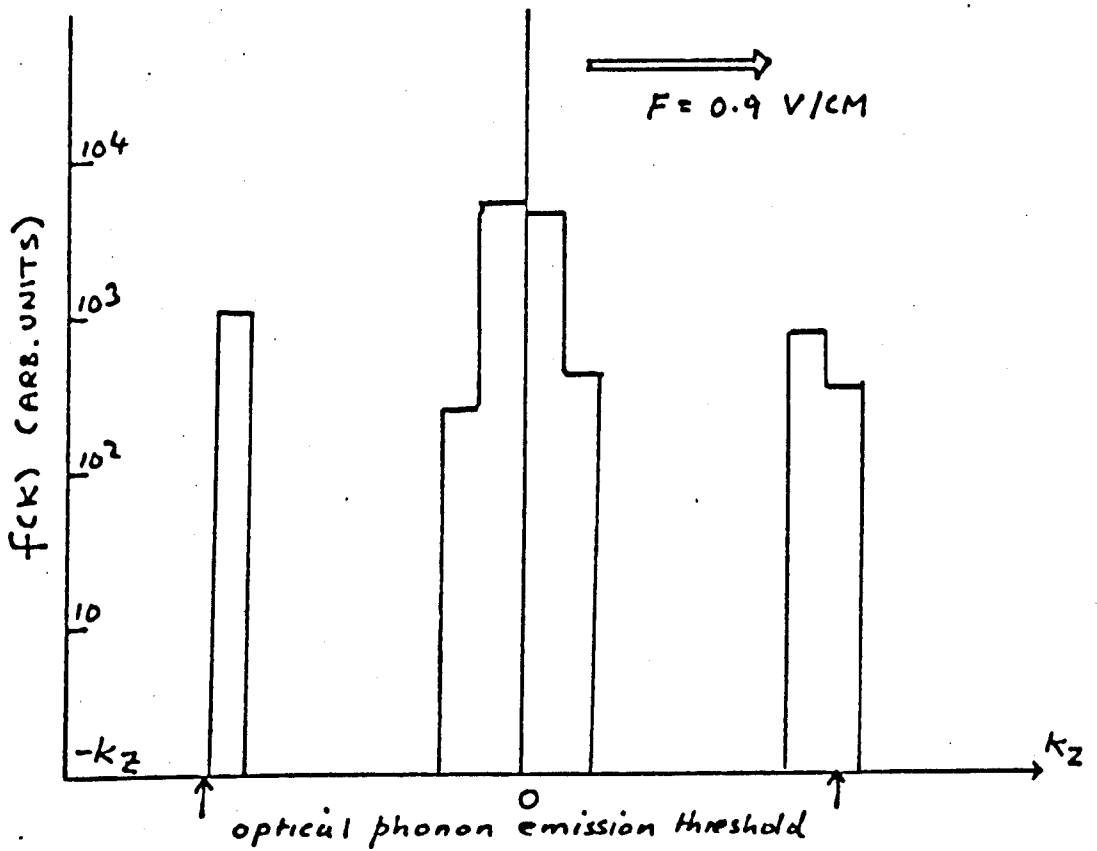
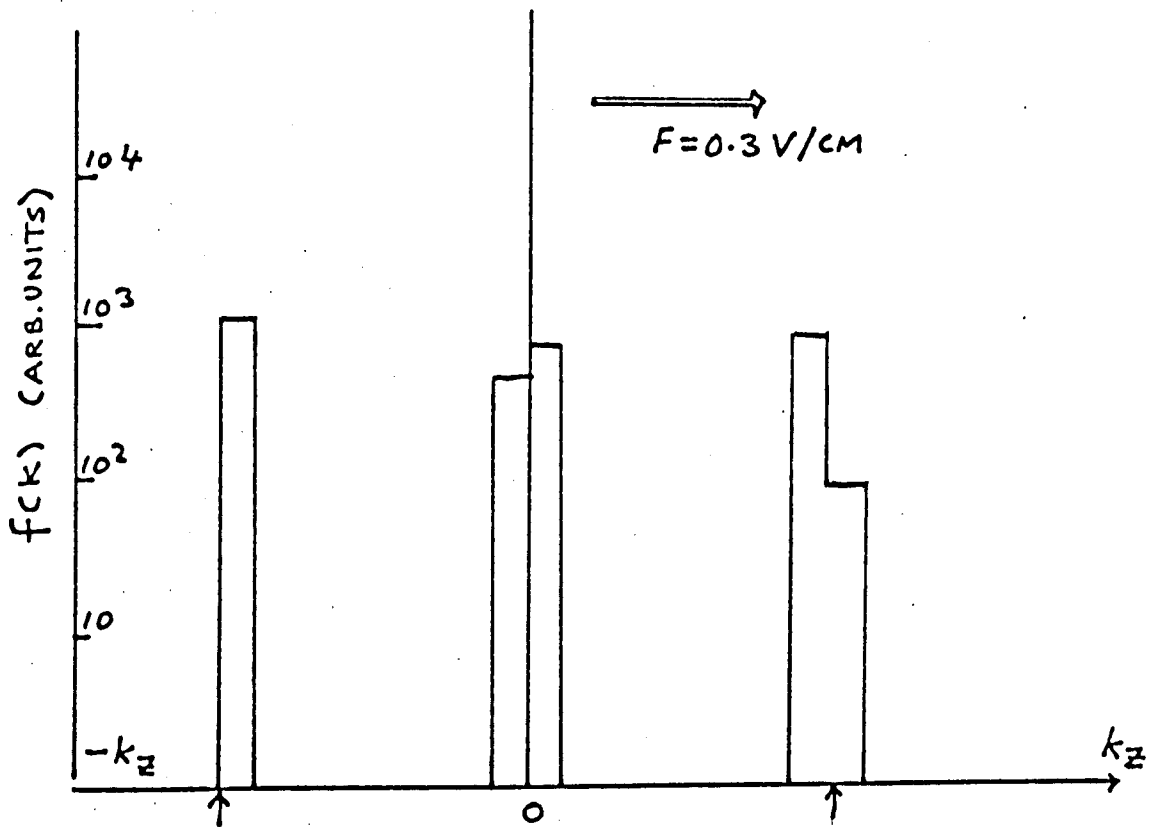FIG 4.11 : NOTATION FOR VELOCITY-FIELD CHARACTERISTIC
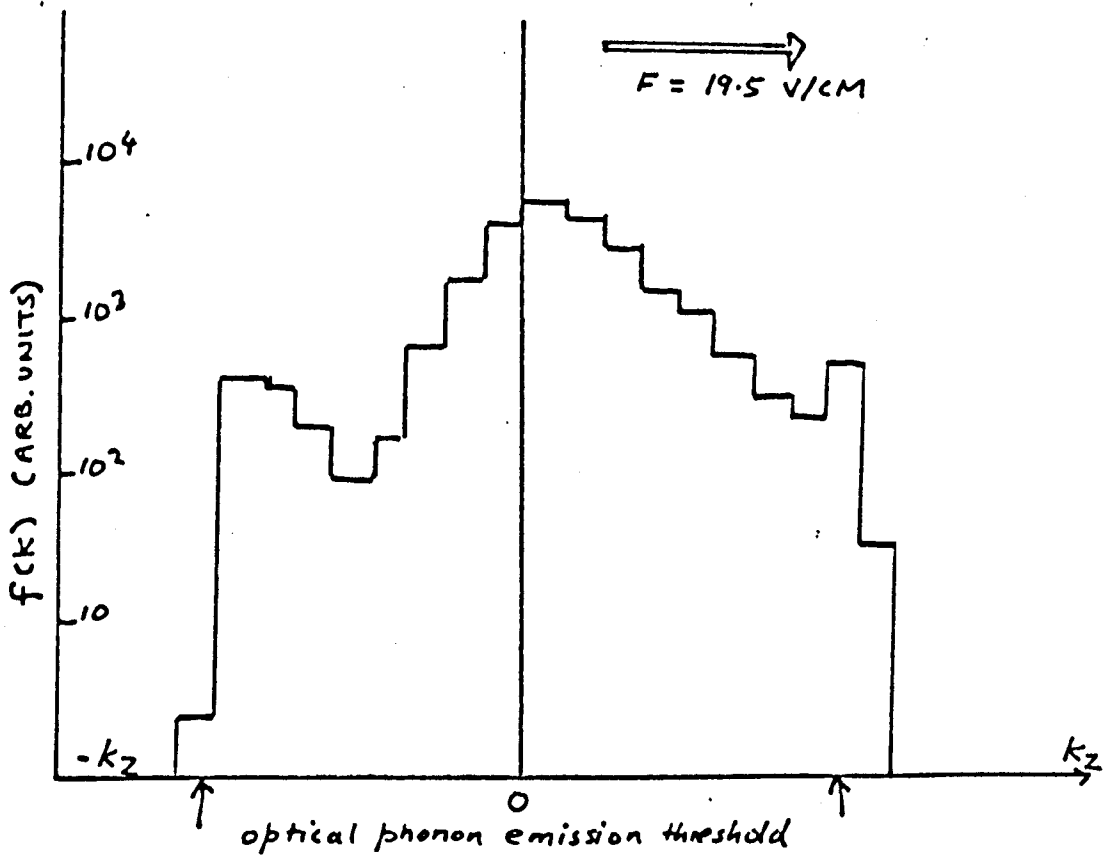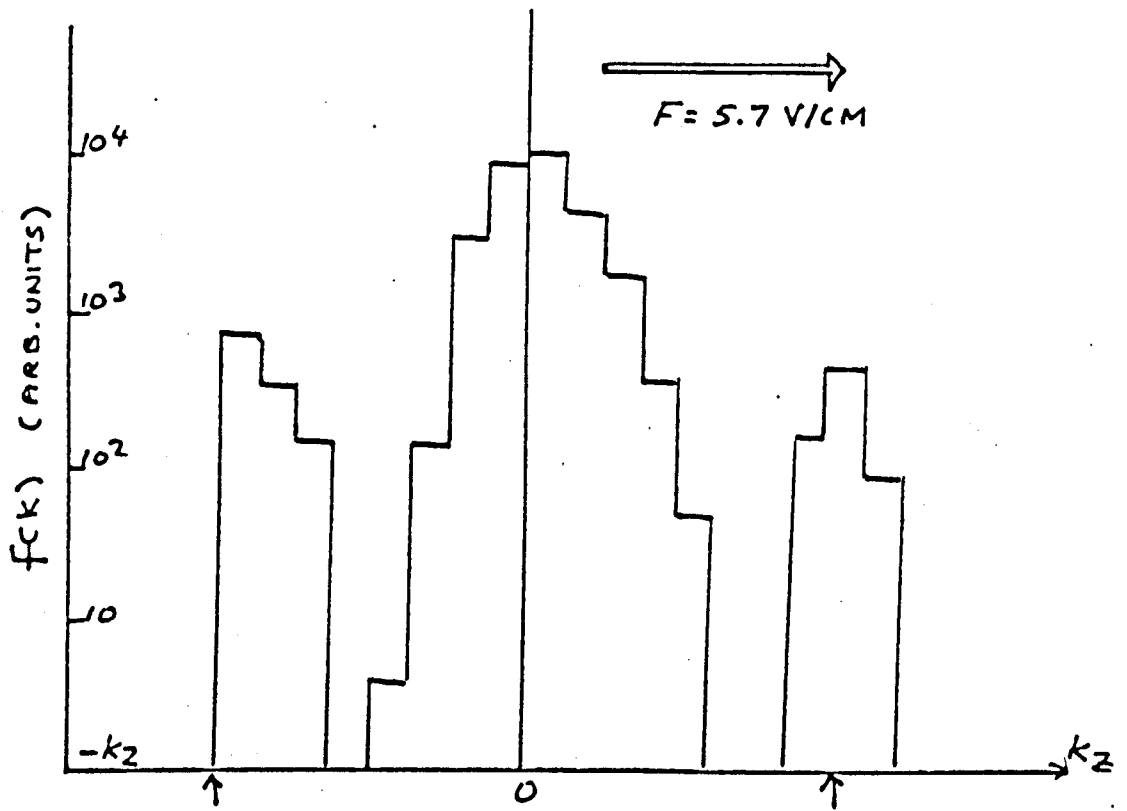
FIG 4.12 : DISTRIBUTION FUNCTIONS (HISTOGRAM FORM)

FIG 4.13 : DISTRIBUTION FUNCTIONS (HISTOGRAM FORM)

electrons which have scattered to the bottom of the band acquire an increasing amount of momentum from the field which tends to oppose the preferential momentum losses to the lattice. This process culminates at the restoring field F_r when the net gain in momentum from the field again balances the net loss to the lattice. At larger fields, for example, F = 19.5 V/cm, Figure 4.13, the positive drift velocity is restored as the net gain of momentum from the field exceeds the loss to the lattice. The distribution function at these higher fields is considerably smeared out.

In the next section we describe a simple one dimensional model which can be solved exactly and leads to forms for the distribution function and drift velocity which are surprisingly close to those of the Monte Carlo calculations.

4.4 A one-dimensional model for the velocity-field characteristic

Basic model

The qualitative form of the characteristics for injection near a multiple phonon energy can be reproduced surprisingly well by a simple one dimensional model which can be handled analytically. This model involves uniform mono-energetic excitation of carriers into a simple parabolic band characterized by an effective mass m^*, centred on k = 0 in a one dimensional k-space. We assume here and throughout the next two chapters that the carriers have a positive charge e, even though electrons are normally discussed. This is of no consequence and avoids confusing negative signs. Carriers drift under a uniform electric field F directed along the +k direction, and are scattered elastically (i.e. from k to -k) with a constant relaxation time λ, or inelastically by optical phonon emission if the carrier energy ε exceeds the emission threshold $\varepsilon = \hbar^2 L^2/(2m^*)$. To simplify the analysis we choose the probability of optical phonon emission to be effectively unity if the carrier energy exceeds threshold.

The points $\pm$ L in k-space then act as perfectly absorbing barriers which scatter all carriers reaching threshold to the bottom of the band, $k = 0$. There is then an effective source of carriers at $k = 0$, with a strength depending on the rate at which carriers cross the thresholds $k = \pm$ L. The carrier recombination lifetime is taken to have a constant value τ. Carriers are injected into the band at a rate G with an energy

$$\varepsilon = \frac{\hbar^2 k_o^2}{2m^*}$$

where $k_o < $ L.

Translating the model into mathematical terms we can write the steady state Boltzmann equation for the distribution function $f(k)$ in the form

$$\left.\frac{\partial f(k)}{\partial t}\right|_{field} + \left.\frac{\partial f(k)}{\partial t}\right|_{excitation} + \left.\frac{\partial f(k)}{\partial t}\right|_{recombination}$$

$$+ \left.\frac{\partial f(k)}{\partial t}\right|_{\substack{elastic \\ scattering}} + \left.\frac{\partial f(k)}{\partial t}\right|_{\substack{inelastic \\ scattering}} = 0 \qquad 4.4.1$$

The first four terms are straightforward and give

$$- \hbar \frac{df(k)}{dk} + \frac{G}{2}\left\{\delta(k-k_o) + \delta(k+k_o)\right\} - f(k)/\tau$$

$$+ \left\{f(-k) - f(k)\right\}/\lambda + \left.\frac{\partial f(k)}{\partial t}\right|_{\substack{inelastic \\ scattering}} = 0 \qquad 4.4.2$$

The latter term accounts for the optical phonon scattering and is derived as follows.

In our approximation optical phonon scattering couples the states $k = \pm$ L to the state $k = 0$. Clearly the distribution function $f(k)$ must vanish

identially for all $|k| > L$, since the scattering rate is infinite for these states and where the only solution to the rate equation is the trivial solution. We then represent the inelastic scattering rate term as the sum of two sources (at $k = 0$) and two sinks (at $k = \pm L$) for carriers. That is

$$\frac{\partial f(k)}{\partial t}\Bigg|_{\substack{\text{inelastic}\\\text{scattering}}} = P\left\{\delta(k) - \delta(k-L)\right\} + P'\left\{\delta(k) - \delta(k+L)\right\} \qquad 4.4.3$$

where P, P' are positive constants. We determine P by the condition that the barrier at $k = L$ be infinitely absorbing; namely the number of carriers drifting into state L per unit time, due to the field, be equal to the number of carriers leaving state L per unit time due to optical phonon transitions (the elastic scattering and recombination terms are negligible in comparison with the optical phonon term). Choosing η as a small positive infinitesimal quantity, we write this condition as

$$\int_{L-\eta}^{L+\eta} \dot{k}\,\frac{df}{dk}\,dk = -\int_{L-\eta}^{L+\eta} \delta(k-L)P\,dk \quad .$$

Integrating, we find

$$P = -E\left\{f(L+\eta) - f(L-\eta)\right\}$$

where we have used the dynamical relation $\dot{k} = eF/\hbar \equiv E$. But $f(L+\eta) \equiv 0$, therefore

$$P = Ef(L-\eta) \qquad\qquad 4.4.4$$

A similar analysis applies for P'. We have

$$\int_{-L-\eta}^{-L+\eta} \dot{k}\,\frac{df}{dk}\,dk = -\int_{-L-\eta}^{-L+\eta} \delta(k+L)P'\,dk$$

giving

$$P' = -Ef(-L+\eta) \qquad\qquad 4.4.5$$

since

$$f(-L-\eta) \equiv 0.$$

An important boundary condition on $f(k)$ follows from the asymmetry induced by the field. The quantities $P, P', f(k)$ and E are all positive so that relation 4.4.5 only holds if

$$P' \equiv f(-L+\eta) \equiv 0 \ . \tag{4.4.6}$$

Alternatively, if E had been chosen negative we would have had

$$P' = f(-L+\eta) \neq 0; \quad P = f(L-\eta) = 0. \tag{4.4.7}$$

Inserting the expressions for optical phonon scattering, the complete Boltzmann equation reads

$$- E \frac{d}{dk} f(k) + \frac{G}{2}\{\delta(k-k_o) + \delta(k+k_o)\} + \frac{f(-k)}{\lambda} - f(k) \left\{\frac{1}{\lambda}+\frac{1}{\tau}\right\}$$

$$+ Ef(L)\{\delta(k) - \delta(k-L)\} = 0 \tag{4.4.8}$$

where $f(L) \equiv \lim\limits_{\eta\to 0^+} f(L-\eta)$.

Integrating equation (4.4.8) over all k-space, and using the condition that $f(\pm\infty) \equiv 0$, we obtain an expression of the conservation of carriers

$$\int f(k)dk = G\tau = n \tag{4.4.9}$$

where we adopt the normalisation that n is the carrier density.

We proceed now to evaluate the drift velocity v acquired in the applied field F. The drift velocity is defined by

$$v = \left(\frac{\hbar}{m^*}\right) \int \frac{f(k)kdk}{n} \ . \tag{4.4.10}$$

To evaluate the integral over momentum $\hbar k$ we decompose the distribution function as

$$f(k) = f_o(k) + f_1(k) \tag{4.4.11}$$

where $f_o(k)$ is the distribution function obtained in the absence of an applied field. Symmetry prescribes that this distribution will not support a current. Inspection of equation (4.4.8) with $E = 0$ leads immediately to an expression for f_o:

$$f_o(k) = (n/2)\{\delta(k-k_o) + \delta(k+k_o)\} \tag{4.4.12}$$

If we substitute expressions (4.4.11), (4.4.12) into equation (4.4.8) for non zero E, multiply by k and integrate over all k-space we obtain

$$\int_{-\infty}^{\infty} k\left\{E\,\frac{df_1(k)}{dk} + f(k)\left[\frac{1}{\tau}+\frac{2}{\lambda}\right]\right\}dk =$$

$$\int_{-\infty}^{\infty} kE\left\{f(L)(\delta(k) - \delta(k-L)) - \frac{n}{2}\frac{d}{dk}(\delta(k-k_o) + \delta(k+k_o))\right\}dk \tag{4.4.13}$$

Performing the integrals we find

$$\int_{-\infty}^{\infty} kf(k)\,dk \equiv \int_{-\infty}^{\infty} kf_1(k)\,dk = \frac{nE}{\left(\frac{1}{\tau} + \frac{2}{\lambda}\right)}\left\{1 - \frac{f(L)L}{G\tau}\right\}$$

giving the drift velocity as the exact expression

$$v = \frac{eF\,\tau'}{m^*}\left\{1 - \frac{f(L)L}{G\,\tau}\right\} = \frac{eF\,\tau'}{m^*}\left\{1 - \frac{f(L)L}{n}\right\} \tag{4.4.14}$$

As in Chapter II, we find that the recombination process contributes to the effective momentum relaxation to give a composite relaxation time

$$\tau' \equiv (1/\tau + 2/\lambda)^{-1} \tag{4.4.15}$$

In equation (4.4.14), there is an apparent dependence of drift velocity on the generation rate G. This is not so, since the distribution function f(k) and hence f(L) scales in G, as may be seen from inspection of the basic rate equation (4.4.8). We note also the expression for drift velocity is unchanged for negative fields, except that f(L) is replaced by f(-L). However, the most important point is that there is the possibility of obtaining a negative drift velocity for a positive applied field. For this to occur the applied field must be sufficiently strong to accelerate a significant number of carriers up to the optical phonon emission threshold. We anticipate that recombination and scattering processes would oppose this tendency although this is not immediately apparent from equation (4.4.14). To proceed further it is necessary to solve the Boltzmann equation, (4.4.8) for f(k).

Exact solution

The simplest approach is to solve equation (4.4.8) in the four separate regions of k-space, I to IV, denoting the distribution function in each region as follows:

$$
\begin{array}{llll}
X' \equiv f(k) & \text{for} \quad k_o < k < L & \text{Region} \quad \text{I} \\
X \equiv f(k) & \text{for} \quad 0 < k < k_o & \text{Region} \quad \text{II} \\
Y' \equiv f(k) & \text{for} \quad -L < k < -k_o & \text{Region} \quad \text{III} \\
Y \equiv f(k) & \text{for} \quad -k_o < k < 0 & \text{Region} \quad \text{IV}
\end{array}
\qquad 4.1.16
$$

The regions are shown in Figure 4.14. Since we exclude the singular points $k = 0, \pm k_o, \pm L$, the functions X, X', Y, Y' must be matched at these points.

The matching conditions are as follows.

$$\left. \begin{array}{rlll} \left(X' - X\right)_{k=k_o} & = G/(2E) & ; & MC\ 1 \\[2ex] \left(Y - Y'\right)_{k=k_o} & = G/(2E) & ; & MC\ 2 \\[2ex] \left(X - Y\right)_{k=0} & = X'(L) & ; & MC\ 3 \\[2ex] Y'(L) = 0 & & ; & MC\ 4 \end{array} \right\} \qquad 4.4.17$$

where from now on we adopt the convention that k means modulus of k, and

$$\left. \begin{array}{ll} X'(L) & \lim_{\eta \to 0^+} \quad X'(L-\eta) \\[2ex] Y'(L) & \lim_{\eta \to 0^+} \quad Y'(L-\eta) \end{array} \right\} \qquad 4.4.18$$

The first matching condition MC 1, is obtained by integrating the rate equation (4.4.8) from $k_o - \eta$ to $k_o + \eta$ and taking the limit $\eta \to 0^+$. We have

$$- \int_{k_o - \eta}^{k_o + \eta} E \frac{df}{dk}\, dk + \frac{G}{2} - \int_{k_o - \eta}^{k_o + \eta} \left\{ f(k)/\tau + (f(k) - f(-k))/\lambda \right\} dk = 0 \quad .$$

The right hand term is of order η and vanishes in the limit. Carrying out the integration in the first term and using the definitions of X, X' we readily obtain the condition MC 1. The conditions MC 2, MC 3 are found in a similar fashion whilst MC 4 has already been derived (equation (4.4.6)).

Using the basic rate equation the equations for X(k) and Y(k) in regions II and IV take the form:

$$DX = -\alpha X + \beta Y \qquad\qquad 4.4.19$$

$$DY = \alpha Y - \beta X \qquad\qquad 4.4.20$$

where $\quad D \equiv \dfrac{d}{dk} \; ; \quad \alpha \equiv \dfrac{1}{E}\left(\dfrac{1}{\tau} + \dfrac{1}{\lambda}\right) ; \quad \beta \equiv \dfrac{1}{E\lambda} \quad .$

These equations are decoupled by differentiation with respect to k to give

$$D^2 X = q^2 X \; ; \quad q^2 \equiv \alpha^2 - \beta^2. \qquad\qquad 4.4.21$$
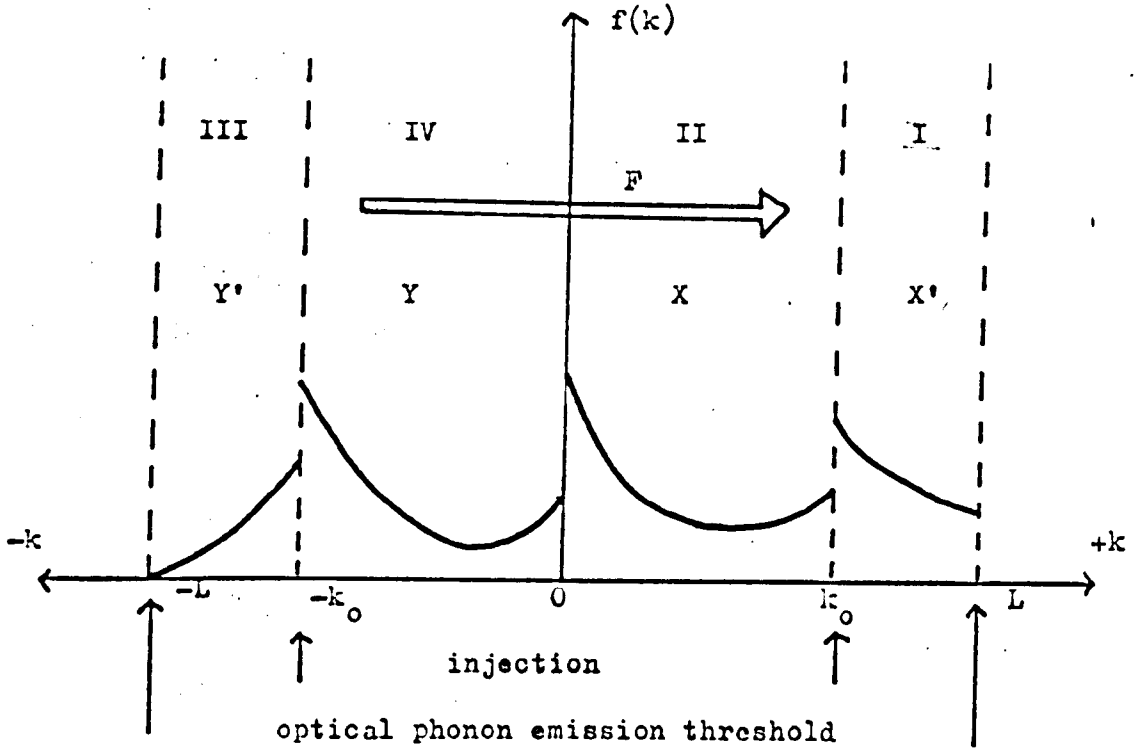
FIG 4.14 SCHEMATIC FORM OF THE DISTRIBUTION FUNCTION FOR THE ONE*DIMENSIONAL MODEL
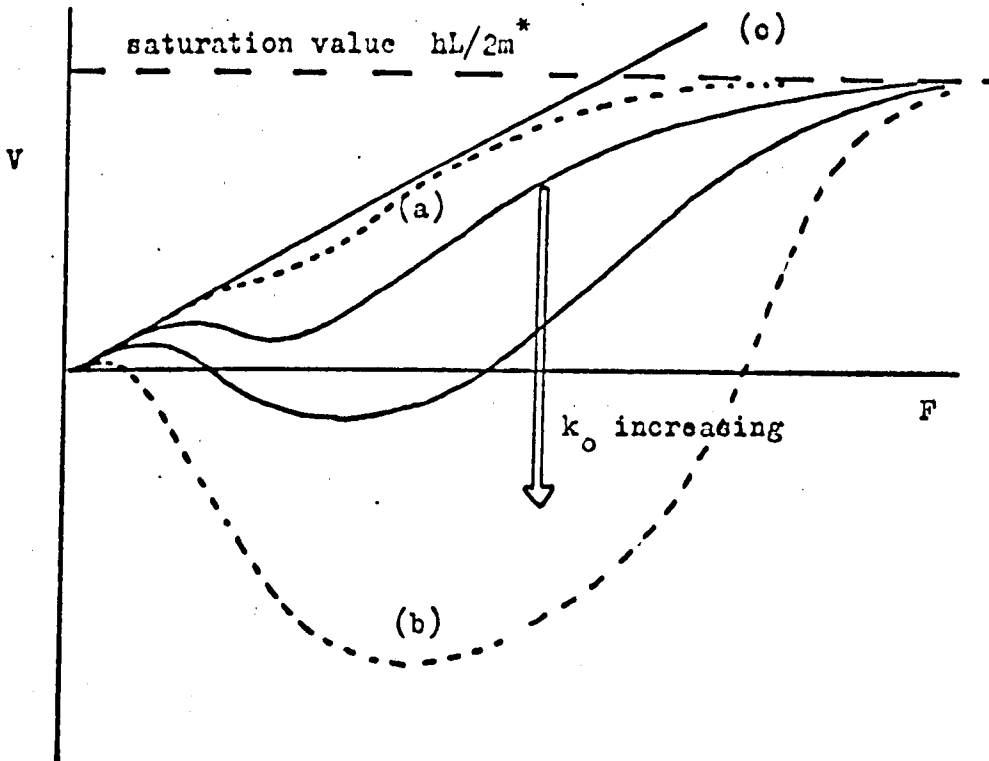

FIG 4.15 GENERAL FORM OF THE VELOCITY-FIELD CHARACTERISTIC

The general solution to (4.4.21) is

$$X = Ae^{qk} + Be^{-qk} \qquad\qquad 4.4.22$$

where A and B are constants.   Substituting for X(k) in (4.4.19) then yields

$$Y = (A/\Gamma)e^{qk} + B\Gamma e^{-qk} \qquad\qquad 4.4.23$$

where we define

$$\Gamma \equiv (\alpha - q)/\beta \quad , \qquad\qquad 4.4.24$$

Similarly we find for X'(k), Y'(k) in regions I and III

$$\left.\begin{array}{l} X' = ae^{-q(k-k_o)} + be^{q(k-k_o)} \\[2mm] Y' = a\Gamma e^{-q(k-k_o)} + (b/\Gamma)e^{q(k-k_o)} \end{array}\right\} \qquad\qquad 4.4.25$$

where a and b are constants.

The constants A, B, a and b are determined from the four matching conditions
MC 1 to MC 4.   After some algebra we get

$$\left.\begin{array}{l} a = \dfrac{(G/2E)(e^{\Delta} + e^{-\Delta})/(1-\Gamma)}{\left\{e^{\Delta} + \Gamma e^{-2\delta}e^{-\Delta} - (1+\Gamma)e^{-\delta}\right\}} \\[4mm] b = -\Gamma^2 e^{-2\delta} a \quad ; \\[3mm] A = -\Gamma e^{-\Delta}\left\{a\Gamma e^{-2\delta} - G/\big(2E(1-\Gamma)\big)\right\} \\[3mm] B = e^{\Delta}\left\{a - G/\big(2E(1-\Gamma)\big)\right\} \end{array}\right\} \qquad\qquad 4.4.26$$

where we define

$$\Delta \equiv qk_o \quad ; \quad \delta \equiv q(L - k_o). \qquad\qquad 4.4.27$$

A useful check at this stage is to calculate the total recombination rate
$R = \int f(k)dk/\tau$.   It is found that the particular values for the integration
constants lead to the condition R = G as required by equation (4.4.9).   A further
check is to compute the drift velocity v as

$$v = \left(\frac{\hbar}{m^*n}\right)\left\{\int_0^{k_o} k(X-Y)dk + \int_{k_o}^{L} k(X'-Y')dk\right\} \quad .$$

This form reproduces equation (4.4.14) precisely except for the change in notation X'(L) ≡ f(L).

An explicit exact expression for the drift velocity is obtained by substituting for X'(L) using relations (4.4.14), (4.4.22), (4.4.26),

$$v = \frac{eF\tau'}{m^*} \left\{ 1 - \left(\frac{\hbar L}{eF\tau}\right) \frac{(1+\Gamma)e^{-\delta}\cosh\Delta}{(e^\Delta - (1+\Gamma)e^{-\delta} + \Gamma e^{-2\delta}e^{-\Delta})} \right\} \qquad 4.4.28$$

A similar procedure leads to an exact expression for the mean carrier energy ε:

$$\varepsilon = eFv\tau + \varepsilon_o - \varepsilon_L \, eFX'(L)/(G\tau\hbar) \qquad 4.4.29$$

where $\varepsilon_L \equiv \hbar^2 L^2/(2m^*)$. $\varepsilon_o \equiv \hbar^2 k_o^2/(2m^*)$. The first term on the R.H.S. of (4.4.29) is the net energy gained from or given to the applied field (depending on whether v is positive or negative), the second term is the injection energy whilst the third term represents the energy dissipated to the lattice.

Properties of the velocity-field characteristic

Equation (4.4.28) contains a large amount of information on the drift velocity-field characteristic for a wide range of physical situations. Some of the more important properties are summarized in Table 4.3. It is interesting to note that for the cases given in the Table, the drift velocity and hence photocurrent is independent of injection energy although the distribution functions are in general strong functions of injection energy. The general form of the velocity-field characteristic is sketched in Figure 4.15. The dotted lines (a) and (b) represent the envelopes for the family of curves obtained by varying k_o from 0 to L. The straight line (c) is the curve $v = eF\tau'/m^*$. The velocity is generally linear in the applied field for very low and very high fields, but at intermediate values passes through a non-linear region. If the injection energy is close to the

TABLE 4.3

PROPERTIES OF THE VELOCITY FIELD CHARACTERISTIC

$$v = \frac{eF\tau'}{m^*} \left\{ 1 - \left(\frac{\hbar L}{eF\tau}\right) \frac{(1 + \Gamma)e^{-\delta} \cosh \Delta}{(e^{\Delta} - (1 + \Gamma)e^{-\delta} + \Gamma e^{-2\delta} e^{-\Delta})} \right\}$$

LIMIT	DRIFT VELOCITY
(1) $L \rightarrow \infty$	$v = eF\tau'/m^*$
(2) $\lambda \rightarrow 0$	$v = eF\tau'/m^*$
(3) $\tau \rightarrow 0$	$v = eF\tau'/m^*$
(4) $G \rightarrow 0$, $\tau \rightarrow \infty$ with $G\tau \rightarrow n$ (finite)	$v = \frac{\hbar L}{2m^*} \Big/ \left(1 + \frac{\hbar L}{eF\lambda}\right)$
(5) $F \rightarrow \infty$	$v = \frac{\hbar L}{2m^*}$

optical phonon energy the non-linear region may involve negative velocities. For the highest electric fields the velocity saturates, as might be expected, to the value $\hbar L/(2m^*)$. In this situation the electron distribution function is uniformly smeared out between 0 and L. Crude velocity-field characteristics can be deduced from the measurements of Stocker et al (1966) and these have the form of curve (b) but insufficient experimental data exists for conclusive evidence.

Our main concern is with carriers injected close to the optical phonon emission threshold, such that $k_o \lesssim L$. We now make the approximation that the momentum gained from the field is much less than the momentum at threshold, i.e.

$$\Delta \equiv \frac{\hbar k_o}{eF\tau'} \gg 1 \; ; \quad k_o \simeq L \; ; \qquad \qquad 4.4.30$$

This is a good approximation for low fields. For example with electrons in InSb, choosing the parameters $m^* = 0.012\ m_e$, $h\omega = 0.024$ eV, $\tau = 10^{-10}$ seconds, $\lambda = 2 \times 10^{-12}$ seconds we find that conditions (4.4.30) hold for fields less than 30 V/cm. Considerable simplification follows if we then make the approximation $\lambda \ll \tau$, a condition fulfilled in most practical cases. The velocity-field relation is then approximated by

$$v = v_d \left\{ 1 - \sqrt{1 + \frac{\lambda}{2\tau}} \; \left(\frac{\hbar L}{eF\tau}\right) \exp\left[-\frac{\hbar(L-k_o)}{eF\tau} \sqrt{1 + \frac{2\tau}{\lambda}} \right] \right\} ,$$

$$v_d = eF\tau'/m^*.$$

$$4.4.31$$

Figure 4.16 shows the family of curves plotted from (4.4.31) for the parametric values $m^* = 0.012\ m_e$, $\hbar\omega = 0.024$ eV, $\lambda = 10^{-12}$ seconds, $\tau = 10^{-10}$ seconds, corresponding to electrons in InSb. The numbers on the curves indicate the electron injection energies measured in units of one optical phonon energy. These forms are analagous to our detailed Monte Carlo calculations and the results of an approximate Boltzmann equation approach employed by Stocker (1967). Three corresponding distribution functions, calculated for an injection ratio of 0.96 are shown in Figure 4.17. Curve (a) is for a field less than the threshold

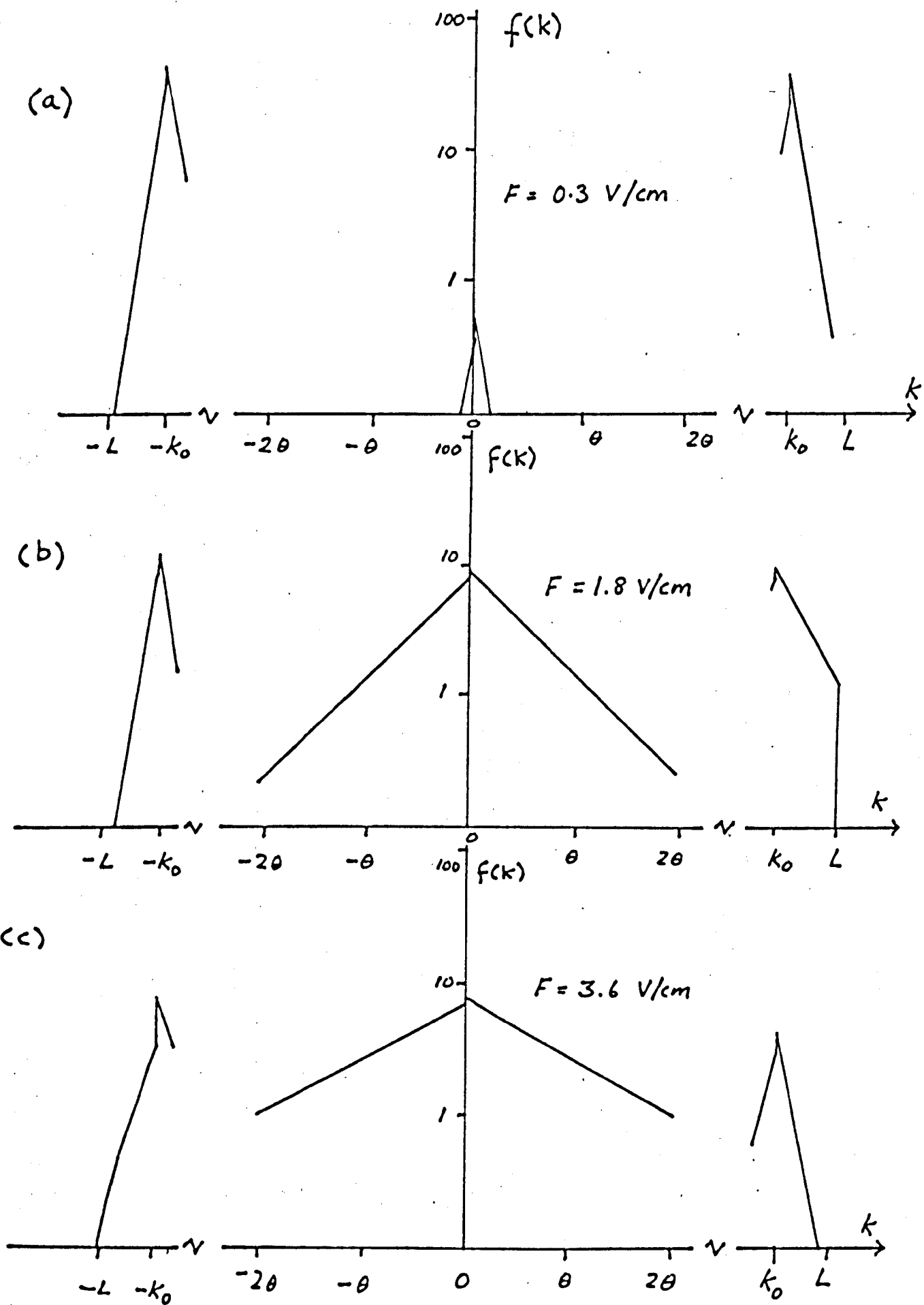FIG. 4.16

Electric Field (volts cm⁻¹)

Drift Velocity (cm sec⁻¹) x 10⁴

(a)

100 — f(k)

F = 0.3 V/cm

10 —

1 —

−L −k₀   −2θ   −θ   0   θ   2θ   k₀   L   k

100 — f(k)

(b)

10 —

F = 1.8 V/cm

1 —

−L −k₀   −2θ   −θ   0   θ   2θ   k₀   L   k

100 — f(k)

(c)

10 —

F = 3.6 V/cm

1 —

−L −k₀   −2θ   −θ   0   θ   2θ   k₀   L   k
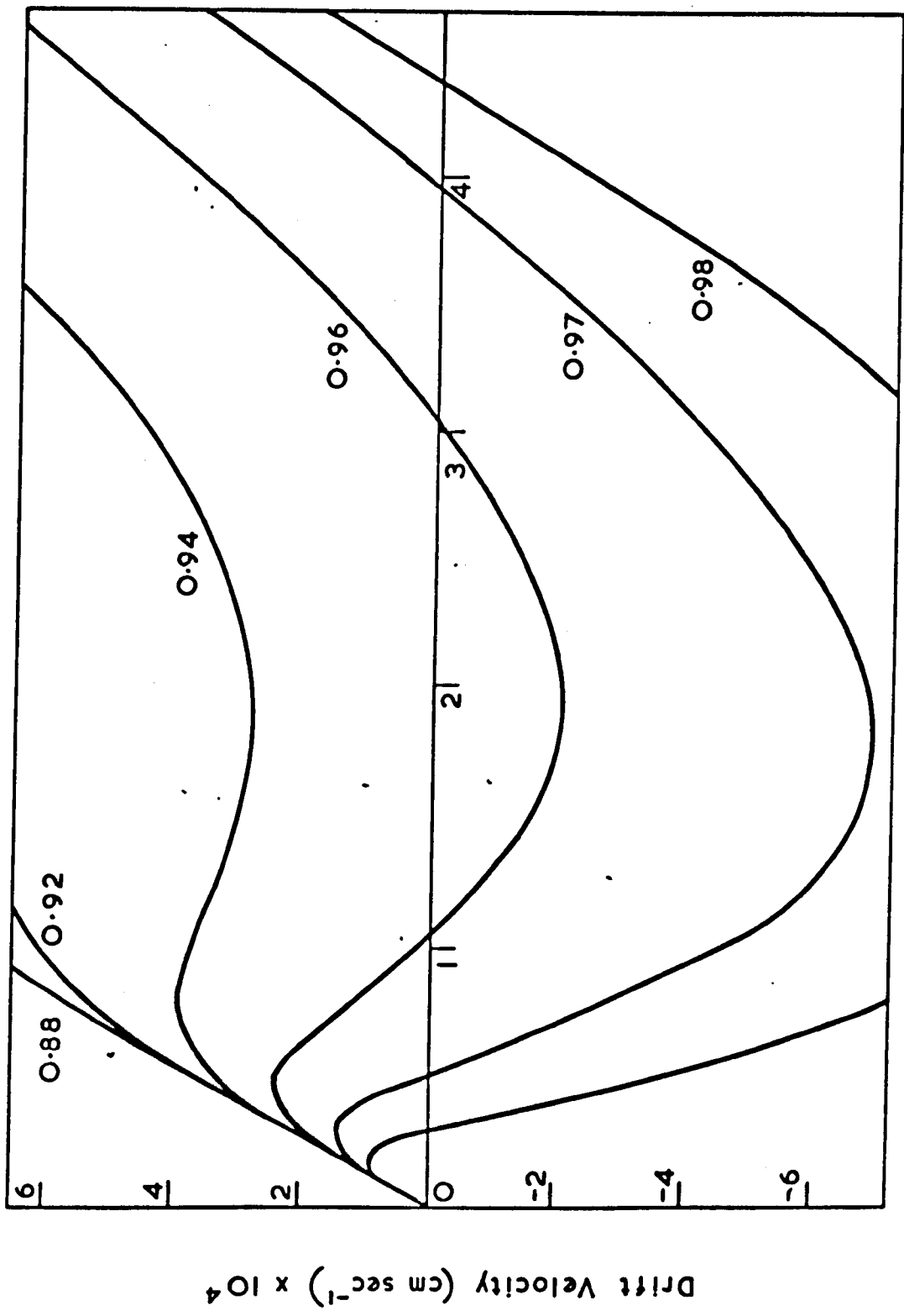
FIG 4.17   DISTRIBUTION FUNCTIONS BASED ON ONE-DIMENSIONAL MODEL. $\theta \equiv 2(L - k_0)$

Code

- optical excitation
- recombination
- impurity level
- acceleration due to field
- intraband optical phonon transition
- optical phonon emission
- distribution of carriers
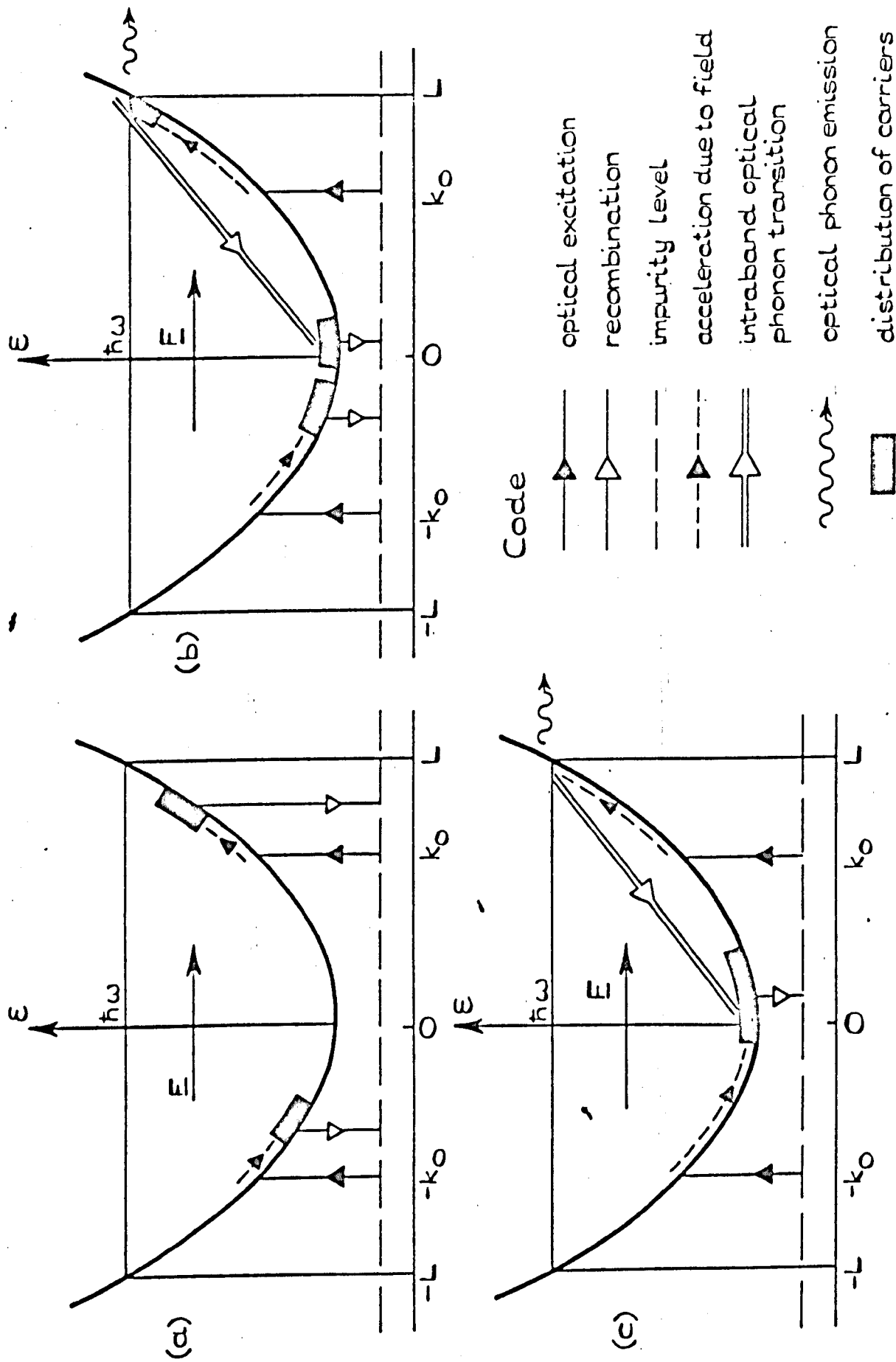
FIG 4.18 :   Schematic representation of the processes leading to negative photoconductivity.

(a) $F < F_{\ell}$, positive conductivity , (b) $F_c < F < F_r$, negative conductivity, (c) $F > F_r$, positive conductivity regained.

field: positive conductivity; curve (b) is for a field intermediate to the

initial field and restoring field: negative conductivity; whilst curve (c)

shows the restoration of positive conductivity for a field greater than the

restoring field. The overall conclusions on the processes leading to negative

drift velocities, discussed on the basis of the Monte Carlo calculations are also

valid here and we summarize the scheme in Figure 4.18. For clarity we have left

out the effects of elastic scattering.

4.5 Conclusions

The detailed Monte Carlo calculations strongly support the physical model

proposed for oscillatory photoconductivity by Stocker and Kaplan (1966), but

detailed agreement is found with experiment which was not possible with the earlier

approximate theory. Of particular interest is the predicted occurrence of bulk

negative conductivity for carrier injection sufficiently near the optical phonon

emission thresholds. The negative conductivity results from the field distortion

of the non-equilibrium carrier distribution function and from the threshold

character of the optical phonon-electron interaction. The main contribution to

the electronic current comes from carriers having energies in the range 0 to

$\hbar\omega_o$. If the energy relaxation due to optical phonon emission is much faster

than that due to acoustic phonon scattering, the carriers can contribute to a

reduced or negative current before the energy distribution is smeared out. This

leads to the condition

$$\tau_A \gg \tau_o \text{ ,}$$

the requirement for oscillatory conductivity, where τ_A is a time characteristic

of the energy relaxation due to acoustic phonons, and similarly τ_o for optical

phonons. This is a less restrictive condition that that proposed by Habeggar and

Fan (1964) which was

$$\tau_o < \tau < \tau_A$$

where τ is the mean carrier lifetime. This conclusion was also reached by Elesin and Manykin (1966) using a similar approximate method to Stocker and Kaplan (1966).

The detailed Monte Carlo calculations, Stocker's model (1966) and the exact one dimensional model suggest that the negative conductivity effect is a real one and does not depend on the details of the physical models. The essential elements of each approach are the sharp distribution of injected carriers and the short recombination lifetime. The major differences between the velocity field characteristics obtained by Monte Carlo, Stocker's method and the one dimensional model are the predicted values of the critical, valley and restoring fields. This occurs because of the respective approximations made for the transition probability per unit time for optical phonon scattering. The one dimensional model, for which this is infinite above threshold, is the extreme case and yields the lowest values of critical field.

CHAPTER V

FIELD EFFECTS IN OSCILLATORY PHOTOCONDUCTIVITY

5.1 Introduction

Both the analytical model and the detailed Monte Carlo calculations discussed in Chapter IV show that the velocity-field characteristic for the oscillatory photoconductivity problem is highly non-linear, and for injection energies close to a multiple optical phonon energy shows a region of negative conductivity. In this chapter we are concerned with the consequences of the N-shaped velocity-field curve illustrated by Figure 4.10. The possibility of observing bulk time independent negative conductivity, in which part of the incident optical energy is transferred to the electric field is considered in section 3. This would involve a static field distribution in the sample, and phase plane analysis is applied to a phenomenological model in order to classify the type of field distributions which could occur.

In section 4 we deal with the stability of the system with respect to space charge formation, in a long sample. Small signal perturbation theory is utilized to derive a double branched dispersion relation which describes the linear response to small fluctuations. We show that for long wave-length fluctuations recombination does not have a stabilizing effect (Barker and Hearn 1969b), contrary to the predictions of an analysis of this problem due to Stocker (1967).

A complete description of the steady state field distributions can only be provided by a full time dependent analysis taking into account contacts and the external circuit. Such an approach, based on numerical solution of the non-linear phenomenological equations, is described in sections 5, 6, 9. Both the

evolution of the steady state, where it exists, and the form of the instabilities are considered. The numerical results show that a stable negative resistance steady-state does not exist if ordinary contacts are used. Instead a series of instabilities can occur, in particular a stable high field domain instability which gives rise to current oscillations in the external circuit.

The instabilities discovered in this problem bear a strong resemblance to those occurring in the Gunn effect, and this analogy is discussed in section 7. The origin of the high field domain instabilities is discussed in section 8 with the aid of phase plane analysis.

5.2 The velocity-field characteristic

Our main concern is with the case of carriers photoexcited monoenergetically into the band with an energy just less than an integral number of optical phonon energies. The drift velocity-field characteristic is highly non linear under these conditions, and shows a region of negative velocity. The main features of the N-shaped velocity-field characteristic are sketched in Figure 5.1, where we have extended the characteristic to negative fields by taking it to be an odd function of F. The slope of the characteristic is positive at very low positive fields until a threshold field (F_t) is reached where the slope becomes negative; we shall generally denote the velocity at F_t as u. The velocity changes from positive to negative at a critical field (F_c), reaches a minimum value of -w at the valley field (F_v), and then a restoring field (F_r) is reached where v becomes positive again. The slope of the characteristic is always positive at the origin and this is of prime importance in determining the form of the static field distributions.

FIG. 5.1
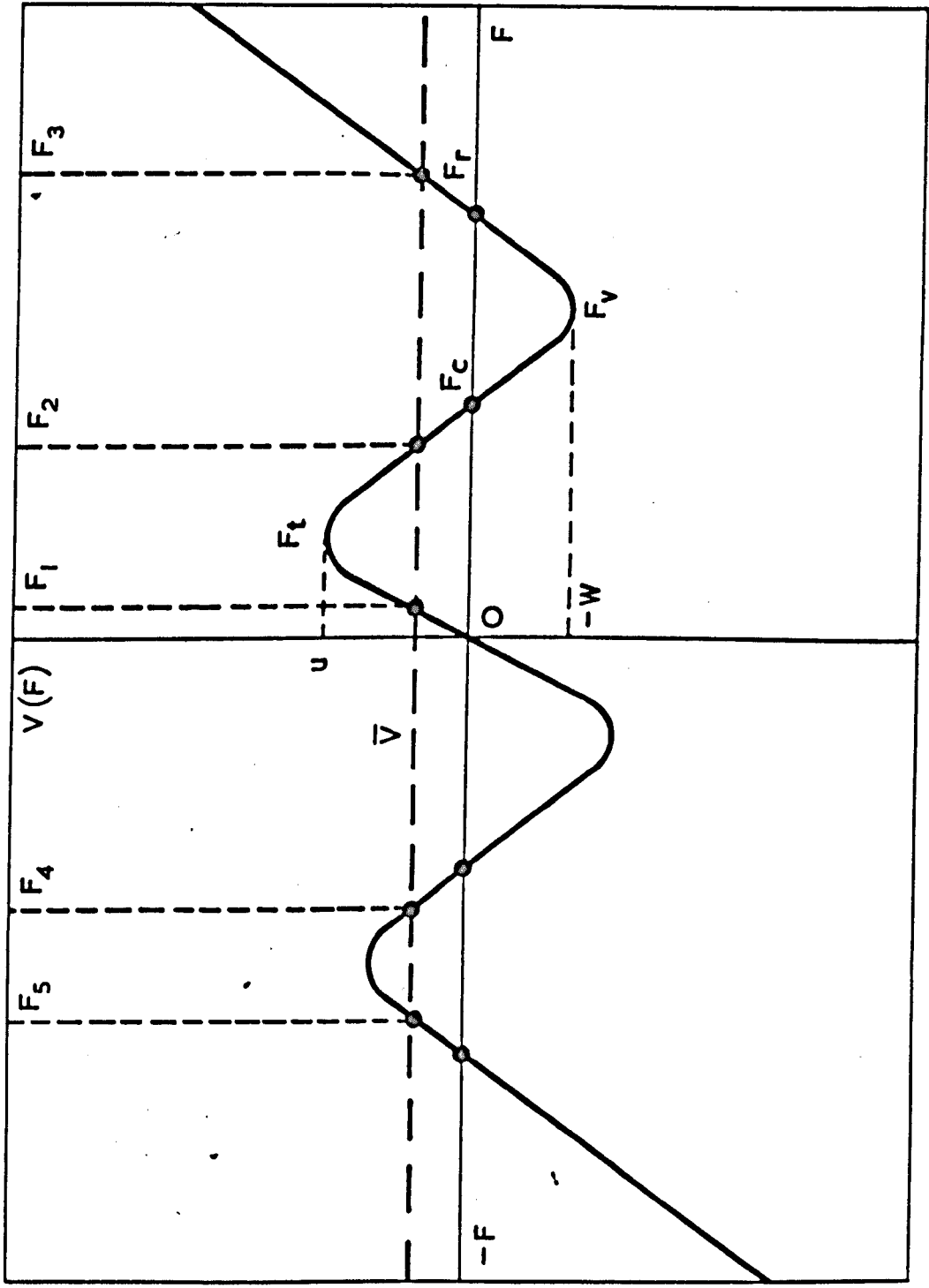
SCHEMATIC VELOCITY - FIELD CHARACTERISTIC

5.3 Static field distributions

In a sample of finite length the electric field must be non-uniform because of the effects of boundary conditions imposed by contacts.   For the normal linear velocity-field characteristic only a minor departure from uniformity occurs, and this near the cathode.   The current-voltage relation is then a suitably scaled version of the velocity-field characteristic.   Shockley (1954) has pointed out that if the characteristic has a region of negative slope the field will depart severely from uniformity and the current will never decrease with increasing applied voltage.   This observation has been emphasized more recently by Kroemer (1964,1966) and McCumber and Chynoweth (1966) in connection with high-field effects in gallium arsenide.   In the present case the distortion of the field uniformity is extremely severe.   Normally the effect of electronic diffusion on the field distribution is negligible except in very small regions immediately adjacent to the cathode and anode.   In the present case diffusion is of vital importance, and leads us to a second order non-linear differential equation for the field and the possibility of negative resistance solutions.

We consider a one dimensional problem with a cathode at $x = 0$ and a positive current density J.   The carriers are assumed to have a drift velocity which is just a function of field $F(x)$ in spite of spatial variations in the field and carrier concentrations.   We thus ignore retardation effects.   Let $n(x)$ be the carrier concentration and let us first consider a constant fixed background negative space charge density of $-en_o$.   Then if we define

$$J = en_o \bar{v} \qquad\qquad 5.3.1$$

we would expect a uniform saturation field $\bar{F}$ to occur for which $\bar{v} = v(\bar{F})$.   Now if $\bar{v}$ is less than u and w there are five values of $\bar{F}$, which we may denote by F_i (where $i = 1$ to 5), which occur in the order shown in Figure 5.1.   Bulk negative conductance would occur if saturation to F_4 or F_5 occurred.   For a

highly doped contact, the boundary condition at the cathode x = 0 is F = 0 and so the field must fall away from the cathode. Until F falls below $-F_c$ the carrier drift current cannot be positive so n must decrease rapidly with x to provide a substantial positive diffusion current. However, extreme difficulties arise when diffusion enters the problem of contacts because it is no longer possible to specify a unique set of boundary conditions at x = 0. Intuitively, we might expect the solution to the problem to involve saturation of the field to F = F_1 as it would do in an Ohmic material; this is clearly a possible solution. Its existence does not, however, preclude a solution which saturates at F_4 or F_5 which might be selected by the original time development of the distribution. If w < u then F_4 and F_5 cease to exist when $\bar{v}$ exceeds w. If, however, w > u then F_1 and F_2 disappear when $\bar{v}$ exceeds u. In this case saturation must involve the field passing through a region of negative drift velocity either for $-F_c$ < F < 0 or F_c < F < F_r. When $\bar{v}$ becomes greater than w and u only F_3 remains and the field must pass through the region between F_c and F_r. Thus if we ignore diffusion there is only a solution for the field distribution if $\bar{v}$ is less than u.

Difficulty arises when the diffusion current is considered because of our lack of knowledge of the form of diffusion coefficient appropriate to the extremely non-equilibrium carrier distributions occurring in this problem. Future work might usefully calculate the diffusion coefficient as a function of field by the Monte Carlo method. However, we have resorted to the simplest possible form for the current J,

$$J = nev(F) - eD \, dn/dx \qquad\qquad 5.3.2$$

where D, the effective diffusion coefficient, is a positive constant. We now relax the restriction on the background space charge density. Because of the generation and recombination processes the background space charge density p is in

general a function of n. To be specific we consider that we have electrons excited from an immobile donor level of uniform density N_D, and that the recombination also occurs into this level. In the steady-state the generation rate G and recombination rate R are equal. We may further assume the presence of compensating acceptors of uniform density $N_A (< N_D)$. Thus

$$G = S(N_D - N_A - p) \qquad\qquad 5.5.3$$

where S is a constant proportional to the optical flux density, and

$$R = \sigma(F)n \, (p + N_A) \qquad\qquad 5.3.4$$

where σ is a capture coefficient whose field dependence arises from the field dependence of the carrier distribution in k-space. Thus

$$p = \frac{N_D - N_A - (\sigma n/S)N_A}{1 + \sigma n/S} \, .$$

We now assume that $S \gg n\sigma$, which implies that the optical flux density is sufficiently high to keep the donors fully ionized. Thus p becomes a constant which in our previous notation is n_o,

$$n_o = N_D - N_A$$

and hence Poisson's equation has the simple form

$$\frac{dF}{dx} = \frac{4\pi e}{\varepsilon} \, (n - n_o) \qquad\qquad 5.3.5$$

where ε is the dielectric constant.

We can combine equations (5.3.1), (5.3.2), (5.3.5) as

$$\left.\begin{array}{l} \dfrac{dF}{dx} = \psi \; , \\[2mm] D\dfrac{d\psi}{dx} = (\psi + g) \, v(F) - g\bar{v} \end{array}\right\} \qquad\qquad 5.3.6$$

where $g = 4\pi e n_o/\varepsilon$. This set of equations is autonomous for $x > 0$ and can be analysed in the phase plane (F, ψ). The relevant properties of autonomous

systems are summarized in Appendix 5.1, where we give the general classification
of singular points for a second order non linear system. Only the half plane
$\psi \geq - g$, which corresponds to $n \geq 0$, is physically meaningful. This must be
imposed as a boundary condition at this stage and is a necessary consequence of
our assumption of time-independence. The singular points in the phase plane are
$F = F_i$ ($i = 1$ to 5), $\psi = 0$; and can be classified (see Appendix 5.1) as saddle,
focus, saddle, focus and saddle respectively. With respect to increasing x the
foci (for $i = 2, 4$) are both unstable (trajectories leave the singular point).
The foci degenerate into unstable nodes when

$$0 < 4D/\left(\bar{v}^2 |\tau_d(F_i)|\right) < 1$$

where $\tau_d \equiv |\ g\ dv/dF|^{-1}$ is the dielectric relaxation time at F. However, this
has no significant effect on the topology of the phase plane. The topology is
shown in Figure 5.2 for the case in which all five singular points exist (i.e.
$\bar{v} < u, w$), and the trajectories leaving the focus at F_4 are entirely contained
within the negative field region of the phase plane. This latter condition
appears to be fulfilled for parameters corresponding to any practical situation.
The arrows indicate increasing x, whilst the positive and negative signs refer
to the sign of $d\psi/dF$ in particular regions. The broken lines forming the
boundaries between these regions are the zero isoclines $d\psi/dF = 0$, and correspond
to the trajectories for the zero diffusion limit.

If we could specify F and ψ at $x = 0$ the phase-plane would furnish the com-
plete field variation up to the anode. In practice we have a two-point boundary-
value problem involving the asymptotic behaviour of the field within the cathode
and anode, and the form of the external circuit is important. An exact solution
would therefore necessarily involve numerical calculations. In fact severe
computational difficulties arise from the non linear nature of the equations.
Solutions involving saturation to saddle points are highly unstable with respect
to numerical errors in the field, as may be seen by inspection of the trajectories

FIG. 5.2
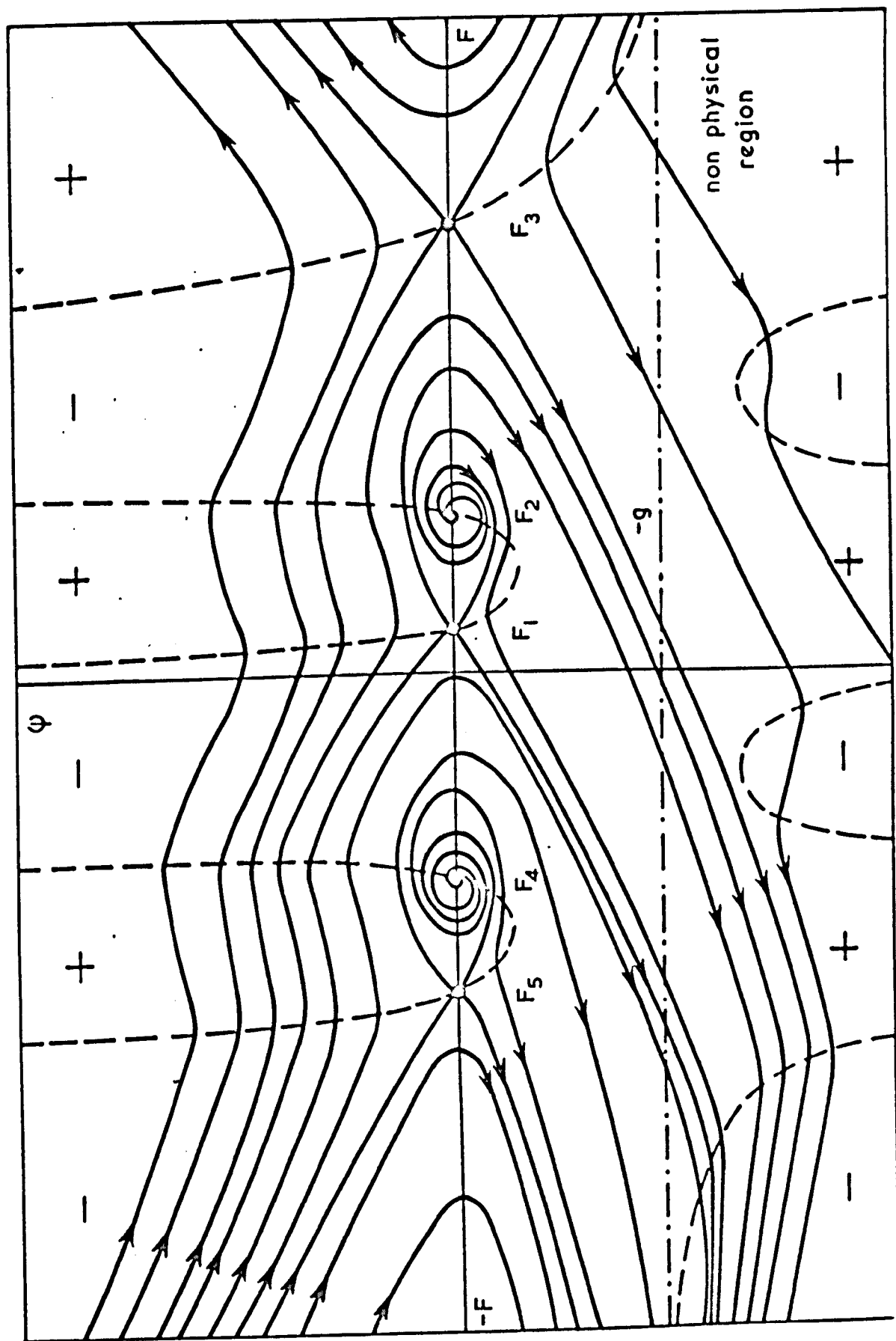
PHASE PLANE TRAJECTORIES

around the saddles in Figure 5.2. The virtue of phase plane analysis is that it allows us to classify the types of solution which could arise. In doing this it is sufficient to state that at x = 0 we would expect that for an 'ordinary' cathode F would be very small on the characteristic topological scale of the phase plane. As we shall see the magnitude of ψ at x = 0 is actually topologically unimportant. The condition on F has been justified by numerical calculations involving the detailed nature of the illumination and doping profiles for simple contacts. This approach was based on a time dependent analysis which is numerically stable and will be described in detail in a later section.

If we consider the case of a linear velocity-field characteristic the solution is known to involve saturation to the saddle at F_1. An important feature of this type of singularity is that it involves a unique line of approach. The boundary conditions at x = 0 must therefore adjust so that the system enters the phase plane at x = 0 on the unique trajectory leading to the saddle. In the case of zero diffusion this is the broken line which passes through the point $F = F_1$, $\psi = 0$ and becomes asymptotic to the ψ axis, so that for a highly doped cathode we have $F \simeq 0$, $\psi \to \infty$ at x = 0. For finite diffusion a highly doped cathode would give $F \simeq 0$ but finite ψ.

Let us consider the present N-shaped velocity-field characteristic. We see that saturation to the foci at F_2 and F_4 is not possible. But saturation to the foci at F_1 or F_3 is possible. We note that the form of the zero isoclines shows that saturation to F_3 would not be possible from $F \simeq 0$ at x = 0 in the absence of diffusion. Diffusion is crucial, in that it allows trajectories to cross the regions of negative velocity. Or, more physically, a positive net current can only be maintained under conditions of negative drift current if there is a substantial positive electronic diffusion. Saturation to F_5 would

involve entering the phase plane on one of two unique trajectories. The first of these has $F \leq F_5$ and $\psi > 0$, whilst the second runs from the focus at F_4 to F_5. For the first trajectory we would require $F > F_5$ at $x = 0$, and we would therefore exclude this possibility. For the second trajectory the initial value of F must be negative and comparable with F_4 for the case shown in Figure 5.2 . If, however, the trajectories from the focus enter the region of positive field it would be possible to saturate at F_5 from an initially small field. According to the point of entry on this trajectory the field may saturate monotonically to F_5 or oscillate about F_4 and then saturate (these cases are sketched in Figure 5.3). Consideration of the dependence of the trajectories on the diffusion constant and the background space charge density shows that the most likely conditions for negative resistance solutions are low background doping and large diffusion. For the case shown in Figure 5.2, negative conductivity could still occur without saturation in the field, but it is observed that, apart from the unique trajectories leading to the saddle at F_5, all the trajectories eventually enter the positive field region or the non physical half plane.

For larger $\bar{v}$ either the pair of singularities at F_4 and F_5 or a pair at F_1 and F_2 disappear and when $\bar{v} > u$, w both pairs disappear. The phase planes for these cases are suitably modified forms of Figure 5.2, and we conclude that for high doping and small diffusion saturation occurs to the saddle at F_1 if this is present, and if not, to the saddle at F_3. The field variation would then be of the form shown in Figure 5.3. The slope of the curve (b) of Figure 5.3 between F_c and F_r is determined by the magnitude of the diffusion coefficient; for small diffusion the slope would be extremely large.

Neglecting considerations of stability, the analysis of the steady state equations does not provide an unambiguous answer as to which steady state solution would be realised in practice. Only when a single singularity is present in the

FIG.5.3
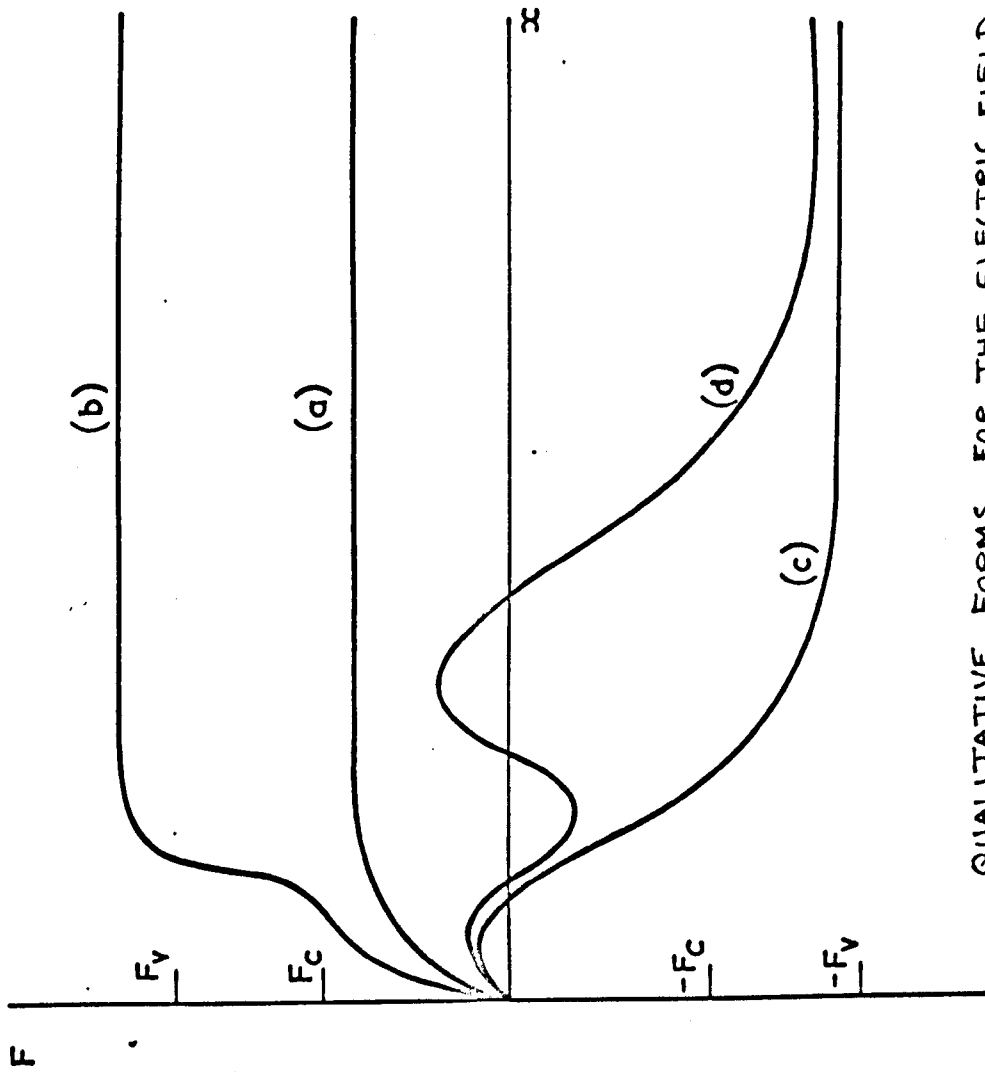
QUALITATIVE FORMS FOR THE ELECTRIC FIELD DISTRIBUTION
IN A LONG SAMPLE :

(a) $\bar{v} < u$, POSITIVE RESISTANCE

(b) $\bar{v} > u$, POSITIVE RESISTANCE

(c),(d) $\bar{v} < u$, POSSIBLE NEGATIVE RESISTANCE

phase plane would this be possible. A complete description of the steady state, if it exists, can only be provided by a full time dependent treatment taking into account contacts and the external circuit.

5.4 Small signal analysis

We have so far considered the possible forms of steady-state field distribution in a sample with contacts present. We now consider the problem of a long sample in which the field is initially uniform and constant in time at some value F_o. To study the stability of the steady state we examine the time and space evolution of small perturbations introduced into the density of electrons and ionized donors. The restriction to small pertubations allows a linear analysis to be made. For a fixed background space-charge density any space charge introduced by fluctuations in the electron density propagates with a velocity $v(F_o)$ and has a time dependence $\exp\left(- t/\tau_d(F_o)\right)$ controlled by the differential dielectric relaxation time $\tau_d(F_o)$ defined in section 5.3. If $\tau_d(F_o)$ is positive as in an Ohmic conductor the space charge is damped and the uniform field is stable; whilst if $\tau_d(F_o)$ is negative the space-charge grows and the uniform field is un-stable, as for example in the Gunn effect (Butcher, 1967). If $|\tau_d|$ in the latter case is small compared to the propagation time through the sample , small signal space-charge waves can be observed. On the other hand if $|\tau_d|$ is large the non-linear regime is reached and the final form of the disturbance will be controlled by the boundary conditions. Our problem is complicated by the variable ionization of the donors and this additional degree of freedom leads to a second normal mode for the system. A simple analysis of the present problem has been given by Stocker (1967) but unfortunately, this oversimplified treatment contains some inconsistencies which lead to a false stability criterion.

The equations describing the system are, in the notation of section 5.3,

$$\frac{\partial F}{\partial x} = \frac{4\pi e}{\epsilon} (n - p) \qquad \text{(a)}$$

$$\frac{\partial n}{\partial t} = G - R - \frac{\partial}{\partial x}\left\{nv(F) - D\frac{\partial n}{\partial x}\right\} \qquad \text{(b)}$$

$$\frac{\partial p}{\partial t} = G - R \qquad \text{(c)}$$

5.4.1

where G and R are functions of n and p. The first equation is Poisson's equation, whilst the last two are the continuity equations for electrons and ionized donors respectively. The initial uniform steady-state solution is $F = F_o$ (arbitrary) and $n = p = n_o$ where n_o is the solution of $G = R$ with $n = p$:

$$n_o = \frac{S}{2\sigma}\left\{-1 - N_A\sigma/S + \left((1 - N_A\sigma/S)^2 + 4N_D\sigma/S\right)^{\frac{1}{2}}\right\}.$$

We consider small perturbations from this solution so that $F = F_o + \delta F(x,t)$, $p = n_o + \delta p(x,t)$, $n = n_o + \delta n(x,t)$. For convenience we neglect the field dependence of the quantity σ which enters into R. Since any initial arbitary disturbance can be Fourier analysed with respect to its space and time dependence we look for the normal modes of the linearized form of equation (5.4.1) in which the space and time dependence of δF, δp and δn is described by $\exp\left(i(kx - \omega t)\right)$. This leads to the dispersion relation $\omega(k)$ for $k \neq 0$,

$$\omega^2 + \omega\left(i(\omega_d + \omega_e + \omega_h) - kv_o + iD k^2\right)$$
$$- \omega_d(\omega_e + \omega_h) - i(kv_o - iDk^2)\omega_h = 0 \qquad 5.4.2$$

where $v_o = v(F_o)$, $\omega_d = \left(\tau_d(F_o)\right)^{-1}$, $\omega_e = \tau_e^{-1} = \sigma(N_A + n_o)$, $\omega_h = \tau_h^{-1} = S + \sigma n_o$. The quantity τ_e is the electron lifetime i.e. for $\delta p = 0$, $\delta R = \delta n/\tau_e$, whilst τ_h is the lifetime of a 'hole' in the donor level so that, for $\delta n = 0$, $\partial p/\partial t = - \delta p/\tau_h$. A derivation of the dispersion relation is sketched in Appendix 5.2. The ratio of δn to δp for a particular ω is given by (5.4.1) as

$$\frac{\delta p}{\delta n} = \frac{\omega_e}{i\omega - \omega_h} \qquad 5.4.3\text{(a)}$$

or alternatively,

$$\frac{\delta p}{\delta n} = \omega_e \left((\omega_h + \text{Im } \omega)^2 + (\text{Re}\omega)^2\right)^{-\frac{1}{2}} e^{i\theta} \qquad\qquad 5.4.3(b)$$

where θ is a phase factor describing the phase relationship between δp and δn given by

$$\exp(i\theta) \equiv - \frac{(i\omega^* + \omega_h)}{\sqrt{(\omega_h + \text{Im}\omega)^2 + (R_e\omega)^2}} .$$

Here $*$ denotes complex conjugate, and we write

$$\omega = R_e \omega + i \text{ Im } \omega.$$

We denote the two branches of the dispersion relation, corresponding to the two modes, as ω_1 and ω_2:

$$\omega_j = - i \left(\omega_d + \omega_e + \omega_h - iZ(k)\right)/2$$

$$+ \Theta_j \left(- (\omega_e + \omega_h - \omega_d)^2 + z^2 + 2iZ(\omega_d + \omega_e - \omega_h)\right)^{\frac{1}{2}},$$

$$j = 1 \text{ or } 2; \quad \Theta_1 = \tfrac{1}{2}, \ \Theta_2 = - \tfrac{1}{2}; \quad Z \equiv - kv_o + iDk^2.$$

The usual case in which G and R are zero corresponds to ω_e and ω_h vanishing and this involves $\omega_2 = 0$ and

$$\omega_1 = - i\omega_d + kv_o - iDk^2$$

which describes a wave propagating with velocity v_o with a time dependent amplitude $\exp(-t/\tau_d)$ suitably modified by diffusion for short wavelengths. This space-charge wave clearly involves $\delta p = 0$. In general we note the sum rule,

$$\omega_1 + \omega_2 = - i(\omega_d + \omega_e + \omega_h) + kv_o - iDk^2. \qquad\qquad 5.4.4$$

For disturbances which vary slowly in space we can consider $k \to 0$ and to zero order in k equation (5.4.2) gives

$$\omega_1 = - i\omega_d, \quad \omega_2 = - i(\omega_e + \omega_h) .$$

94

For the second mode equation (5.4.3) shows that δp = δn which describes a disturbance involving no space charge in which electrons are simply moved from donors to the conduction band. This mode decays with time as $\exp\{-t(1/\tau_e + 1/\tau_h)\}$. The first mode carries space-charge and has a time dependence of $\exp\{-t/\tau_d\}$ as in the case when generation and recombination are absent. We see therefore that these processes do not affect the growth factor of the space-charge mode. This is physically reasonable in so far as electronic transitions do not change the magnitude of the space-charge and only affect the relative proportions of the space-charge which are carried by electrons and 'holes'. For an arbitrary small disturbance of n and p at time t = 0+, both modes will be excited. The cases of physical interest correspond to lifetimes which are very short compared to $|\tau_d|$ and indeed this is a necessary condition for assuming v to be a unique function of F. The second mode will therefore be rapidly damped out leaving only the space-charge mode which will decay or grow according to the sign of τ_d, so that the steady-state will be unstable for $F_t < F_o < F_v$. This result is different from that of Stocker (1967) who predicted that the recombination process would stabilize the space-charge mode.

For mode 1, writing the space-charge as δρ, equation (5.4.3) gives

$$\frac{\delta n}{\delta \rho} = \frac{\gamma - \delta}{\gamma - \delta(1 + \gamma)} \qquad 5.4.5$$

where $\delta = \omega_e/\omega_d$ and $\gamma = \omega_e/\omega_h$. The usual case of no recombination or generation corresponds to δ= 0 so δρ = δn. For undamped space-charge waves with fast recombination, $\delta \to -\infty$, so $\delta n/\delta \rho \to (1 + \gamma)^{-1}$. The fact that γ is positive shows that only a part of the space-charge is carried by electrons, the remainder being carried by holes. We note that for damped waves a special case occurs when $\delta = \gamma/(1 + \gamma)$ i.e. $\omega_d = \omega_e + \omega_h$, so both modes are damped at the same rate. This leads to δn = δp for both modes. We discuss the nature of this resonance condition in more detail later on. The value of γ is dependent on n_o, N_D and N_A and from equations (5.3.3) and (5.3.4) we find

$$\gamma = \left(1 - \frac{N_A + n_o}{N_D}\right) \left(1 + \frac{N_A}{n_o}\right) . \qquad 5.4.6$$

Hence for an uncompensated sample γ is the fractional neutrality of the donors

and so $(1 + \gamma)^{-1}$ changes from $\frac{1}{2}$ to 1 as the photo-ionization increases. For a

compensated sample, $(1 + \gamma)^{-1}$ increases from 0 to 1 as the photo-ionization is

increased. The limit $(1 + \gamma)^{-1} \to 1$ involves $\delta p \to 0$ which corresponds to the

'complete ionization' limit of section 5.3 and involves $\omega_h \to \infty$. An interesting

point is that the quantity $n_o(1 + \gamma)$ is the 'effective concentration' appearing in

the Debye length for screening in a compensated semiconductor (Paige, 1964) and

this results from an effective equilibrium being established between the conduction

band and donors in the limit $\delta \to -\infty$.

Provided that

$$\left| \frac{Z^2 + 2iZ(\omega_d + \omega_e - \omega_h)}{(\omega_e + \omega_h - \omega_d)^2} \right| < 1$$

we can expand $\omega(k)$ as a Taylor series in ascending powers of k. The expansion is

valid for sufficiently small k, except for the critical condition $\omega_d = \omega_e + \omega_h$.

The first order terms in k give the propagation velocities of the two modes.

Thus writing $\omega_1 = - i\omega_d + kv_1$ and $\omega_2 = -i(\omega_e + \omega_h) + kv_2$, we find from equation

(5.4.4) the sum rule

$$v_1 + v_2 = v_o$$

and equation (5.4.2) gives

$$\frac{v_1}{v_o} = \frac{\delta n}{\delta \rho} = \frac{\gamma - \delta}{\gamma - \delta(1 + \gamma)} .$$

The propagation velocity of the space-charge waves is reduced, for negative τ_d,

from v_o by the fraction of the space-charge carried by the electrons, and the

other mode propagates at the difference between these two velocities. For the

special case of equal electron and hole lifetimes, i.e. $\gamma \to 1$, corresponding to

$$n_o = N_A \left(\sqrt{N_D/N_A} - 1 \right),$$

the propagation velocities take the form,

$$\left. \begin{array}{l} v_1/v_o = 1 + \delta/(1 - 2\delta) \\[2mm] v_2/v_o = \delta/(2\delta - 1) \ . \end{array} \right\} \qquad\qquad 5.4.7$$

These forms are sketched in Figure (5.4), and are seen to be rectangular hyperbolae centred on $(\frac{1}{2},\frac{1}{2})$ in the plane $(v/v_o,\delta)$. The regions of physical interest correspond to our approximation that the electron and hole lifetimes are much shorter than the dielectric relaxation time, that is the regions for which $|\delta| \gtrsim 1$. The reduction in propagation velocity for both damped and undamped space-charge waves is apparent.

The second order terms in k of the dispersion relation give the effective diffusion coefficients for the two modes, describing the spread in the disturbances. Expanding the two modes as

$$\omega_1 = - i\omega_d + kv_1 - iD_1 k^2 \quad \text{and}$$

$$\omega_2 = - i(\omega_e + \omega_h) + kv_2 - iD_2 k^2 \text{ we find from equation (5.4.4) the sum}$$

rule,

$$D_1 + D_2 = D$$

and for the space-charge mode,

$$D_1 = D \left\{ \frac{v_1}{v_o} - \Delta \left[\left(\frac{v_1 - v_2}{v_o} \right)^3 \gamma^3 - \frac{v_2}{\delta v_o} \right] \right\} \ . \qquad\qquad 5.4.8$$

The quantity Δ is a dimensionless diffusion coefficient defined by

$$\Delta \equiv v_o^2 \tau_d/(4D) \quad .$$

The diffusion term stabilizes waves in the space charge mode for which
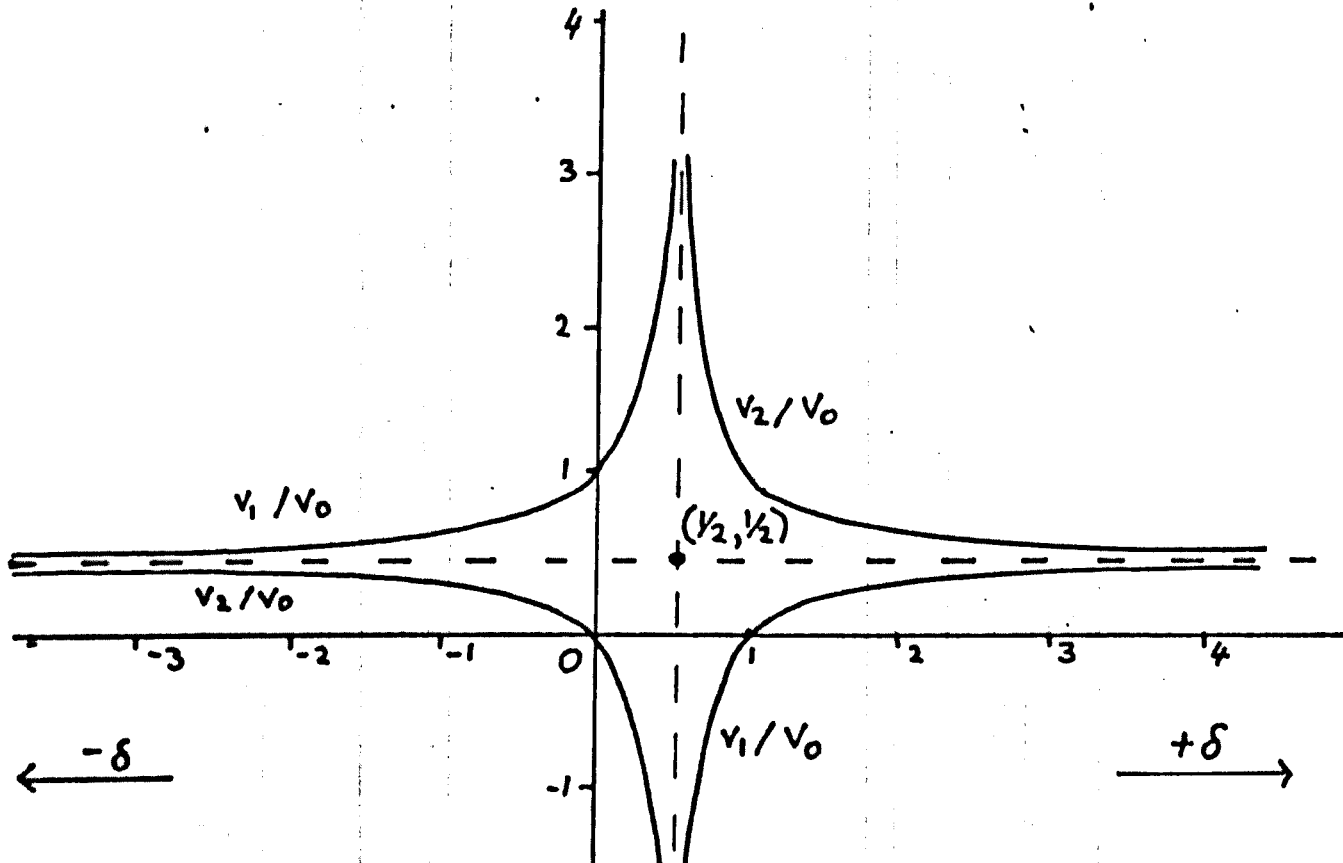
FIG 5.4
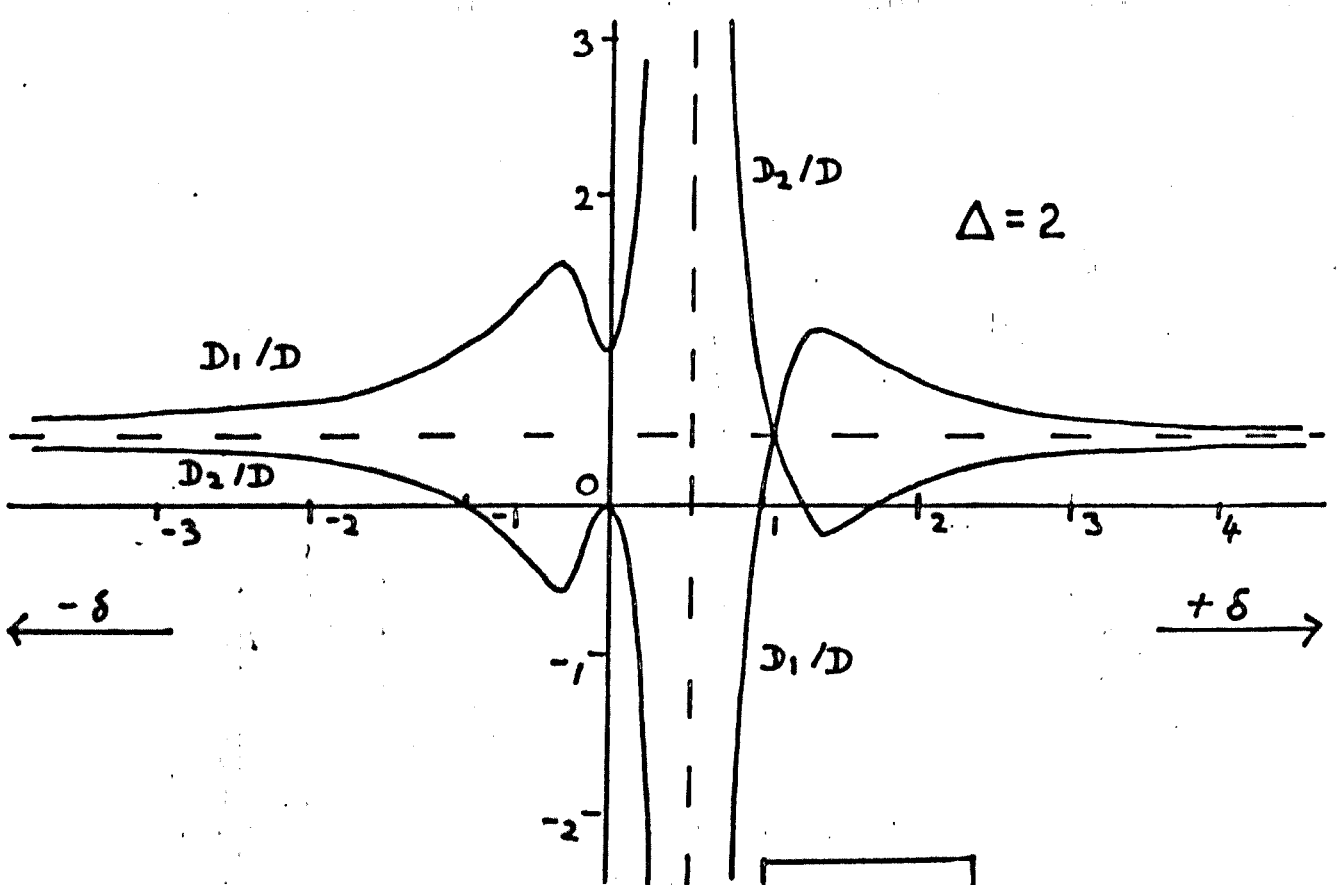
FIG 5.5

$$k > \left\{ D_1 / |\omega_d| \right\}^{-\frac{1}{2}} \; ; \quad D_1 > 0.$$

For very small values of Δ, i.e. $D \gg v_o^2 \tau_d / 4$, the effective dimensionless diffusion coefficients D_j/D (where $j = 1,2$) are identical to the dimensionless propagation velocities v_j/v_o. In particular the effective diffusion coefficient for undamped space-charge waves is reduced from D, by the fraction of the space-charge carried by the electrons. As a consequence the stabilizing influence of diffusion is reduced. In the special case of equal electron and hole lifetimes (for a compensated sample), the diffusion coefficients for the two modes are:

$$D_1/D = 1 + \delta/(1 - 2\delta) - \Delta \left\{ \frac{1}{1 - 2\delta} - \frac{1}{(1 - 2\delta)^3} \right\}$$

$$D_2/D = 1 - D_1/D.$$

These forms are sketched in Figure 5.5, for the case $\Delta = 2$. The maximum in the diffusion coefficient for the undamped space charge mode occurs at

$$\delta = \tau_d/\tau_e = \frac{1}{2} \left[1 - \sqrt{\frac{6|\Delta|}{1 + 2|\Delta|}} \right] .$$

In the limit of a very long dielectric relaxation time $|\Delta| \gg 1$, and the maximum is displaced asymptotically to $\delta = -0.361$. It is interesting to recall that the condition $|\Delta| > 1$ is the condition for the unstable foci to transform into unstable nodes in the phase plane analysis of section 5.3. The complicated form for the diffusion coefficient for the space-charge mode, equation (5.4.8), can be roughly interpreted as the superposition of two competing diffusion coefficients, a static part D_s and a dynamic part D_d,

$$D_1 = D_s + D_d \; ;$$

$$D_s = \frac{v_1}{v_o} D \; ; \quad D_d = - \frac{v_o^2 \tau_d}{4} \left[\left(\frac{v_1 - v_2}{v_o} \right)^3 \gamma^3 - \frac{v_2}{v_o \delta} \right] .$$

The static part D_s, dominates at low drift velocities v_o, and for undamped waves is always less than D, reaching the asymptotic value $D/2$ as the electron lifetime

approaches zero in the case $\gamma = 1$. The spreading out of a slowly moving pulse of space charge is thus inhibited by the recombination process. On the other hand, for very large drift velocities v_o, the dynamic part D_d dominates and acts to enhance the diffusion of an undamped space charge pulse. This may be roughly understood as due to the pinning effect of trapping which tends to smear out a fast moving pulse.

In summary, the results of the small signal analysis suggest that if the sample is initially biased into the region $F_t < F_o < F_v$ a steady state can be established but this is unstable since τ_d is negative in this region. This corresponds to the conclusion of section 5.3 that saturation to a steady state field in this region is not possible. The final form of the disturbance could be either a steady-state associated with the saddle points discussed in 5.3 or a propagating non-linear wave. The system is unstable against space-charge formation over the negative slope regions of the drift-velocity field characteristic (for positive and negative velocities) and the recombination does not directly stabilize the process. However, for very large values of τ_d the quantity Δ can dominate and the enhanced diffusion may act to stabilize relatively short wavelength space-charge waves.

5.5. Time development of the field distributions

So far we have classified the possible forms of steady-state field distributions for a sample with contacts and examined the small-signal stability of the homogeneous field distributions by linear analysis. In this section we turn to the full non-linear problem of the time evolution to a steady-state field distribution and the formation and growth of instabilities in the system. The highly non-linear nature of the problem prevents an analytical approach and we have to resort to numerical techniques. Numerical solutions to non-linear

partial integro-differential equations can often lead to spurious results because of numerical instabilities associated with the finite-difference schemes adopted. Fortunately, the system under investigation bears some resemblance to the systems responsible for the Gunn effect. We can therefore test the numerical procedures adopted by applying them to the Gunn effect, for which the form of solutions are now well known (Butcher 1967). In the complete ionization limit this procedure comes down to inserting the velocity-field characteristic associated with the Gunn effect into our equations, testing the numerical technique, and if successful re-inserting the velocity-field characteristic for oscillatory photoconductivity. We choose as the basis for our investigation the simplest situation of a finite length sample with simple contacts connected to a constant external voltage supply. A homogeneous field distribution of value F_o is introduced into the sample at time $t = 0$ and its time evolution then followed.

We first cast the full time-dependent equations for the system (equations 5.4.1) into a form more suitable for analysis. Combining equations (b) and (c) of the set (5.4.1) and eliminating $(n - p)$ via Poisson's equation (equation (a)) we obtain,

$$\frac{\epsilon}{4\pi} \frac{\partial^2 F}{\partial x \partial t} + e \frac{\partial}{\partial x} \left[nv(F) - D \frac{\partial n}{\partial x} \right] = 0 \ . \qquad 5.5.1$$

A partial integration with respect to x then gives

$$C(t) = \frac{\epsilon}{4\pi} \frac{\partial F}{\partial t} + env(F) - eD \frac{\partial n}{\partial x} \ . \qquad 5.5.2$$

The terms on the R.H.S. of equation (5.5.2) are recognised as the displacement, drift and diffusion current densities respectively. The integration constant $C(t)$ is then identified with $J(t)$, the total current density. Conservation of charge is then implicit in the relation $\partial J / \partial x = 0$. As in previous sections we consider D to be a constant. At this stage it is convenient to introduce an important boundary condition imposed by the form of the external circuit. The

circuit consists of a constant voltage source of strength V_o connected in series with the sample. The circuit condition is then

$$V_o = \int_o^\ell F \, dx \qquad\qquad 5.5.3$$

where ℓ is the length of the sample plus contacts (we neglect any potential drop down the connecting wires). Since V_o is constant we have

$$\frac{\partial V_o}{\partial t} = \int_o^\ell \frac{\partial F}{\partial t} \, dx = 0,$$

which combined with equation (5.5.2) and Possion's equation allows us to eliminate J and n from the equations. We find,

$$\frac{\partial F}{\partial t} = \chi\left(\frac{\partial F}{\partial x} , \, p, \, F\right) - \frac{1}{\ell} \int_o^\ell \chi \, dx \qquad\qquad 5.5.4$$

where

$$\chi \equiv \left(\frac{4\pi e}{\varepsilon} p + \frac{\partial F}{\partial x}\right) v(F) - D \left(\frac{\partial^2 F}{\partial x^2} + \frac{4\pi e}{\varepsilon} \frac{\partial p}{\partial x}\right) . \qquad\qquad 5.5.5$$

The time development of p follows from the continuity equation (5.4.1b) as

$$\frac{\partial p}{\partial t} = S(N_D - N_A - p) - \sigma \, (p + N_A)\left(p + \frac{\varepsilon}{4\pi e} \frac{\partial F}{\partial x}\right) \qquad\qquad 5.5.6$$

where we have again eliminated n via Poisson's equation. The carrier density n is easily recovered from Poisson's equation if $p(x,t)$ and $F(x,t)$ are specified,

$$n = \frac{\varepsilon}{4\pi e} \frac{\partial F}{\partial x} + p .$$

Equations (5.5.4) and (5.5.6) are the basic equations for studying the time evolution of the system. In the complete ionization limit we have $S/\sigma \gg n$ which prescribes the electron and 'hole' lifetimes and dielectric relaxation time by the inequality

$0 \lesssim \tau_h \ll \tau_e \ll |\tau_d|$. For this approximation $\frac{\partial p}{\partial t} \to 0$

and we are left with the single equation (5.5.4) where p is replaced by

$n_o = N_D - N_A$.

To fully specify the system we must impose suitable boundary conditions at the contacts. Two situations have been investigated. In the first we treat the problem of contacts in a somewhat cavalier fashion by assuming a sample of length ℓ subject to a constant external voltage $V_o (= F_o \ell)$ with the boundary condition $\partial F/\partial x = 0$ at either end of the sample ($x = 0$ and $x = \ell$). The second, and more realistic situation, involves an attempt to simulate the presence of contacts by increasing the doping density (and hence the carrier density in the steady-state) via N_A and N_D at the ends of the sample. In the complete ionization limit this involves choosing n_o to be 10 x larger in the contacts than in the sample (in the general case N_A is held fixed whilst N_D is increased in the contacts). The contacts are considered to be illuminated so that the same velocity-field characteristic applies to both the contacts and the sample. The boundary conditions are $\partial F/\partial x = \partial p/\partial x = 0$ at the outer ends of the contacts; these are based on the assumption that the field is uniform and that there is no space-charge well within the contact regions. Choice of boundary conditions at the contact-sample boundaries is then avoided as these are determined automatically by the time development of the system. The stability of the sample is tested by the introduction of a permanent doping discontinuity in a small notch in the sample which simulates the microscope doping fluctuations always present in real materials. The discontinuity introduces a built in space-charge perturbation to the system. Typically the doping in the notch is reduced by 0.1% from the otherwise uniform doping density in the sample. The doping density profiles used are illustrated in Figure 5.6.

We adopt an idealised three line form for the OPC velocity-field characteristic given by

$$
\begin{aligned}
v &= \mu F & (0 < F < F_t) \\
&= u - \mu'(F - F_t) & (F_t < F < F_v) \\
&= -w + \mu(F - F_v) & (F > F_v); \\
v(-F) &= -v(F) ;
\end{aligned}
$$

<div align="right">5.5.7</div>

(a)

cathode

anode

bulk sample

DISTANCE ALONG SAMPLE (MICRONS)

(b)

cathode

anode

bulk sample

DISTANCE ALONG SAMPLE (MICRONS)
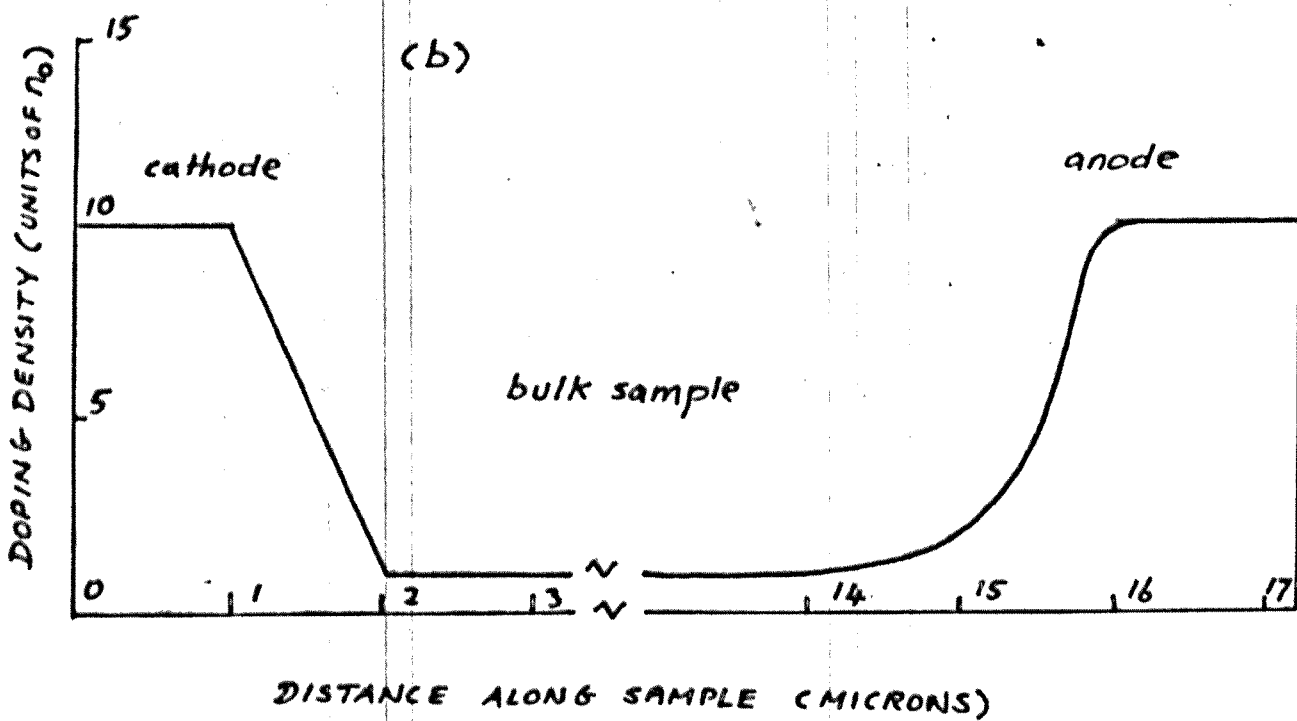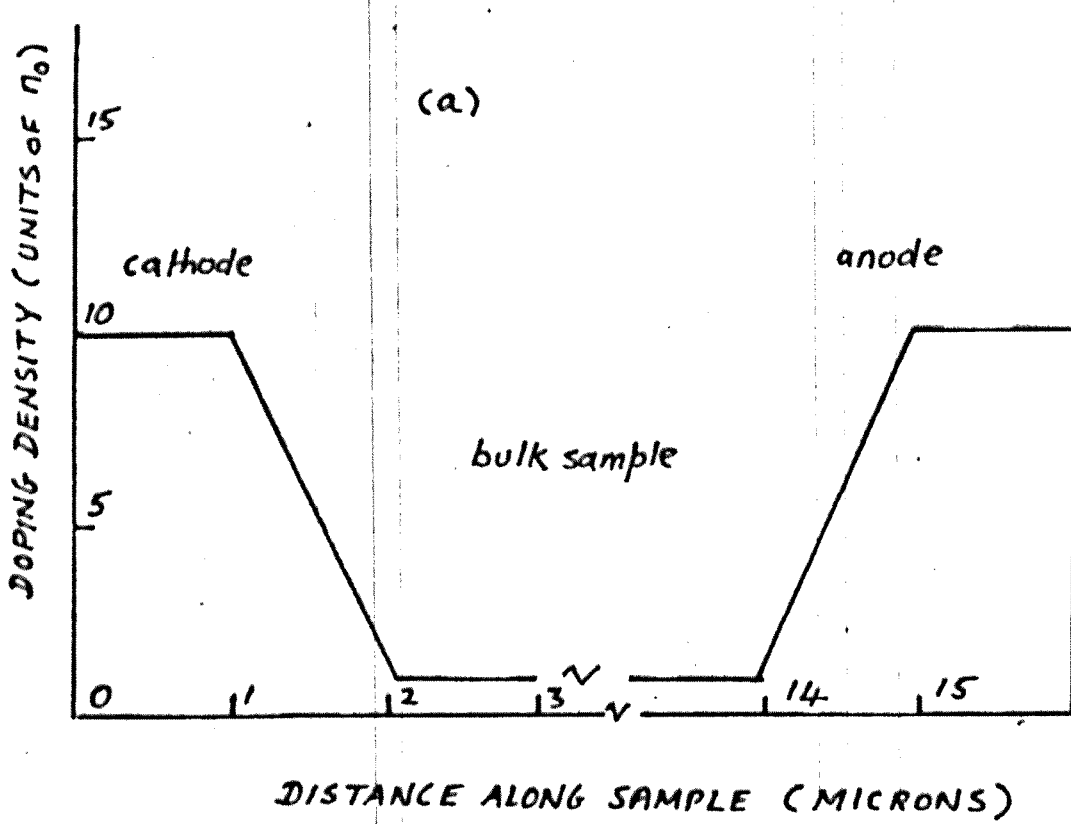
FIG 5.6   DOPING PROFILES USED IN COMPUTER EXPERIMENTS

where $\mu = 2.058 \times 10^6$ cm^2 stat volt^{-1} sec^{-1}, $\mu' = 8.928 \times 10^5$ cm^2 stat volt^{-1} sec^{-1}

$F_t = 10.83$ stat volt cm^{-1}, $\qquad$ $F_v = 50$ stat volt cm^{-1}

$u = 2.23 \times 10^7$ cm sec^{-1}, $\qquad$ $w = 1.267 \times 10^7$ cm sec^{-1}.

This form is shown in Figure 5.7 and is a modification of the analytical approximation for the Gunn effect velocity-field characteristic (Butcher and Fawcett 1966). This latter characteristic is discussed in section 5.7 and is defined by

$$\left.\begin{aligned}
v &= \mu F & (0 < F < F_t) \\
&= u - \mu'(F - F_t) & (F_t < F < F_I) \\
&= v_v + a(F_v - F)^3 & (F_I < F < F_v) \\
&= v_v & (F > F_v)
\end{aligned}\right\} \qquad 5.5.8$$

where $\mu = 2.058 \times 10^6$ cm^2 stat volt^{-1} sec^{-1}, $\mu' = 8.928 \times 10^5$ cm^2 stat volt^{-1} sec^{-1}

$F_t = 10.83$ stat volt cm^{-1}, $\qquad$ $F_v = 66.66$ stat volt cm^{-1}

$v_v = 8.6 \times 10^6$ cm sec^{-1}, $\qquad$ $a = 60.21$ stat volt^{-3} cm^{-2}

$F_I = 18.33$ stat volt cm^{-1}.

We point out that whilst the differential mobility dv/dF for the velocity-field characteristic (5.5.7) is of the correct order for the oscillatory photo-conductivity effect, the values of threshold, critical, valley and restoring field are three orders of magnitude too large. Similarly the velocities involved are 10^3 x too large. Consequently the time, space, electric field and carrier density scales involved in our numerical calculations must be suitably scaled in order to apply to the OPC problem. A consistent scheme is reached if we cast the basic equations into dimensionless form. For simplicity consider the complete ionization limit in which $p = n_o = N_D - N_A = $ constant. Defining new dimensionless quantities (primed) by the transformations

$x = Lx'$; $\quad t = Tt'$; $\quad F = fF'$;

$v = v(F)v'$; $\quad J = en_o v(f)J'$; $\quad D = L^2 T^{-1} D'$;

where $\quad T = \left[\dfrac{4\pi e}{\varepsilon} \dfrac{v(f)}{f} n_o\right]^{-1}$, $\quad L = v(f)T$
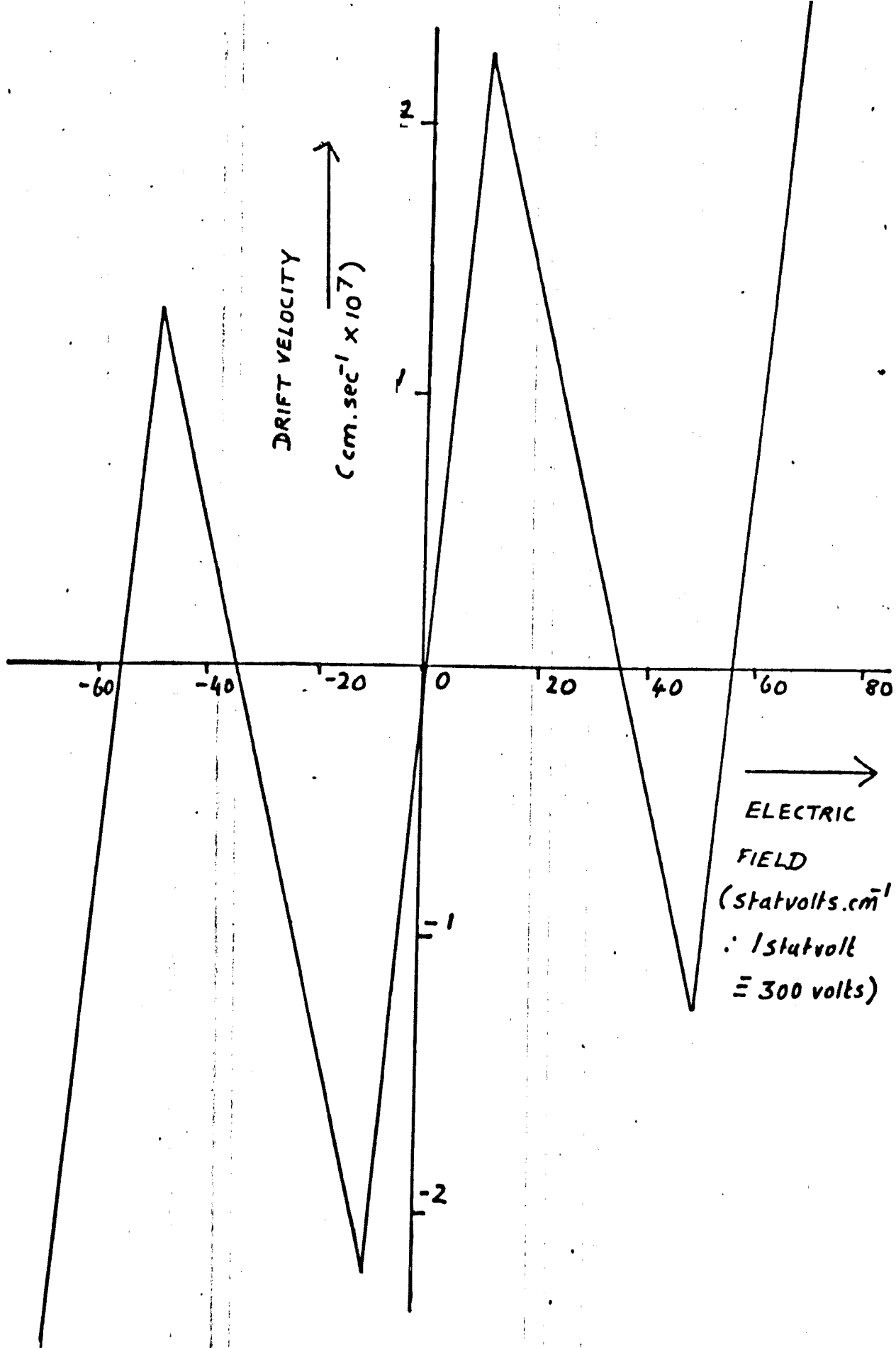
FIG 5.7   MODEL OPC VELOCITY - FIELD CHARACTERISTIC

and f is any characteristic field strength in v, the basic current equation

reduces to

$$- D' \frac{\partial^2 F'}{\partial x'^2} + v'(F') \frac{\partial F'}{\partial x'} + \frac{\partial F'}{\partial t} = J'(t') - v'(F').$$

This equation is characterized by the single dimensionless constant D' given by

$$D' = \left(\frac{4\pi e}{\varepsilon}\right) D \left(\frac{n_o}{fv(f)}\right) \quad ,$$

consequently any solution of the dimensional equations (5.5.4), for particular

physical systems with different parameters, will be related by the above

transformations provided the value of D' is the same for each system.

Fortuitously the system describing oscillatory photoconductivity in InSb has an

almost identical value for D' as does the system describing the Gunn effect in

1 ohm cm GaAs, provided we choose the same value for the diffusion coefficient D

in each system. As we have no information on D for the OPC problem we choose

$D = 178$ cm^2 s^{-1} which has been used by Butcher and Fawcett (1966) in their Gunn

effect studies. The characteristic field f is chosen as the threshold field for

the two systems. Typical values of D', n_o, v, f, ε for the two cases are shown

in Table 5.1. Our numerical studies are based on values of n_o, f etc. appropriate

to the Gunn effect and to obtain the corresponding OPC solutions the transformations

shown in Table 5.1 must be applied. The static dielectric constant is chosen

as $\varepsilon = 4\pi$.

The basic time dependent equations are solved by standard finite difference

numerical techniques where we adopt forward differences for first order derivatives

and central differences for second order derivatives. For example,

$$\frac{\partial F}{\partial x}(x,t) \rightarrow \frac{F(x + \Delta x, t) - F(x,t)}{\Delta x}$$

$$\frac{\partial^2 F}{\partial x^2}(x,t) \rightarrow \frac{F(x + \Delta x, t) - 2F(x,t) + F(x - \Delta x, t)}{(\Delta x)^2}$$

$$\frac{\partial F}{\partial t}(x,t) \rightarrow \frac{F(x, t + \Delta t) - F(x,t)}{\Delta t}$$

TABLE 5.1   COMPARISON OF PARAMETERS ENTERING THE GUNN EFFECT PROBLEM AND THE OPC PROBLEM

PARAMETER	OPC	GUNN
n_o	10^{10} cm^{-3}	10^{15} cm^{-3}
f	10^{-2} statvolt cm^{-1}	10 statvolt cm^{-1}
$v(f)$	2×10^5 cm sec^{-1}	2×10^7 cm sec^{-1}
ε	$\sim 4\pi$	$\sim 4\pi$
D	200 cm^2 sec^{-1}	200 cm^2 sec^{-1}
D'	~ 0.5	~ 0.5
T,	$\sim 10^{-8}$ sec	$\sim 10^{-12}$ sec
L	$\sim 10^{-3}$ cm	$\sim 10^{-5}$ cm

CONVERSION FACTORS

QUANTITY IN OPC PROBLEM	= FACTOR X	QUANTITY IN GUNN EFFECT PROBLEM
LENGTHS	$\sim 10^2$	
TIMES	$\sim 10^4$	
FIELDS	$\sim 10^{-3}$	
CARRIER DENSITIES	$\sim 10^{-5}$	

where Δx, Δt are the basic finite difference meshes in space and time. Numerical stability is only achieved if the velocity of the numerical disturbances $\Delta x/\Delta t$ exceeds the maximum velocity expected for the physical disturbances in the model. In practice we choose $\Delta x = 10^{-5}$ cms, $\Delta t = 5 \times 10^{-14}$ seconds giving $\Delta x/\Delta t = 2 \times 10^8$ cm/sec which is 10 x faster than the maximum drift velocities anticipated for physical instabilities. To speed up the computation, the calculations reported here were all carried out for short samples of length $\ell = 12$ microns, contacts of length 2 microns, and a perturbation notch of width 1.2 microns. The corresponding sample length in the real OPC problem is of the order 1200 microns, by the similarity transformations given in Table 5.1. The initial conditions at $t = 0$ are chosen such that a uniform bias field F_o exists in the sample under conditions of space charge neutrality $n = p = n_o$ (solution of $G = R$) everywhere, with the fields in the contacts and perturbation notch chosen to satisfy $en(x) \, v(F) = J$ where J is the drift current in the sample. The last condition implies continuity of the drift current.

5.6 Time development in the complete ionization limit

The simplest situation in oscillatory photoconductivity occurs when p the background density of positive charge is a constant in time. We denote this constant by $n_o (= N_D - N_A$ for a compensated semiconductor). In general we allow n_o to be a function of x to allow for the doping changes in the perturbation notch and the contacts.

We first consider the trivial case of an Ohmic sample in which the velocity-field characteristic is of the form $v = \mu F$, where μ the mobility is a constant. The analysis of section 5.4 showed that in this case a unique steady-state exists in which the field in the sample rises rapidly near the cathode and saturates to a constant field in the bulk of the sample. The saturation field is given

approximately by v_o/ℓ. The trajectory involved saturates to the single saddle point singularity present in the phase plane. Figure 5.8(a) shows a computed field distribution for such a case after an elapsed time of 10^{-11} seconds for the parameters $\mu = 2.058 \times 10^6$ cm^2 stat volt^{-1} sec^{-1}, $D = 178$ cm^2 sec^{-1}, $F_o = 9$ stat volts/cm. The initially imposed field distribution quickly adjusts to the stable steady state distribution shown in a time the order of the dielectric relaxation time for the contacts. The dip in the field near the cathode boundary and the peak near the anode are due to the effects of diffusion arising from the rapid change in carrier density across the electrode-sample boundaries. Figure 5.8(b) shows a sketch of the qualitative space-charge distribution estimated from Poisson's equation. The characteristic features are the presence of a pinned depletion layer of electrons just within the contacts and associated accumulation layers a short distance within the sample. The perturbation notch leads to a built in dipole of space-charge formed from adjacent accumulation and depletion layers. We note the important feature that the field is very small at the cathode boundary, whilst the field gradient $\partial F/\partial x$ is very large. This feature is maintained even for the complex velocity-field characteristics associated with oscillatory photoconductivity and the Gunn effect.

We turn now to the velocity-field characteristic for oscillatory photoconductivity. For a bias field F_o in the range $0 < F_o < F_t$, the field distributions evolve precisely as for the case of an Ohmic sample and are stable.

The first interesting case arises for an initial bias field F_o in the range $F_t < F_o < F_c$. As anticipated in sections 5.3 and 5.4, this situation does not admit a steady-state and is unstable. Figure 5.9 shows selected frames from the time development of the field distribution for $F_o = 15$ stat volts/cm. The relevant doping profile is shown in Figure 5.6(b). The initial behaviour is reminiscent of the Ohmic case, with a rapid adjustment of the field distribution

(a) FIELD DISTRIBUTION : OHMIC SEMICONDUCTOR

F (statvolts.cm^{-1} : 1 statvolt ≡ 300 volts)

distance into sample (microns)

cathode · · · anode

(b)

SPACECHARGE (not to scale)

depletion layers

accumulation layers

bulk sample

cathode · · · anode
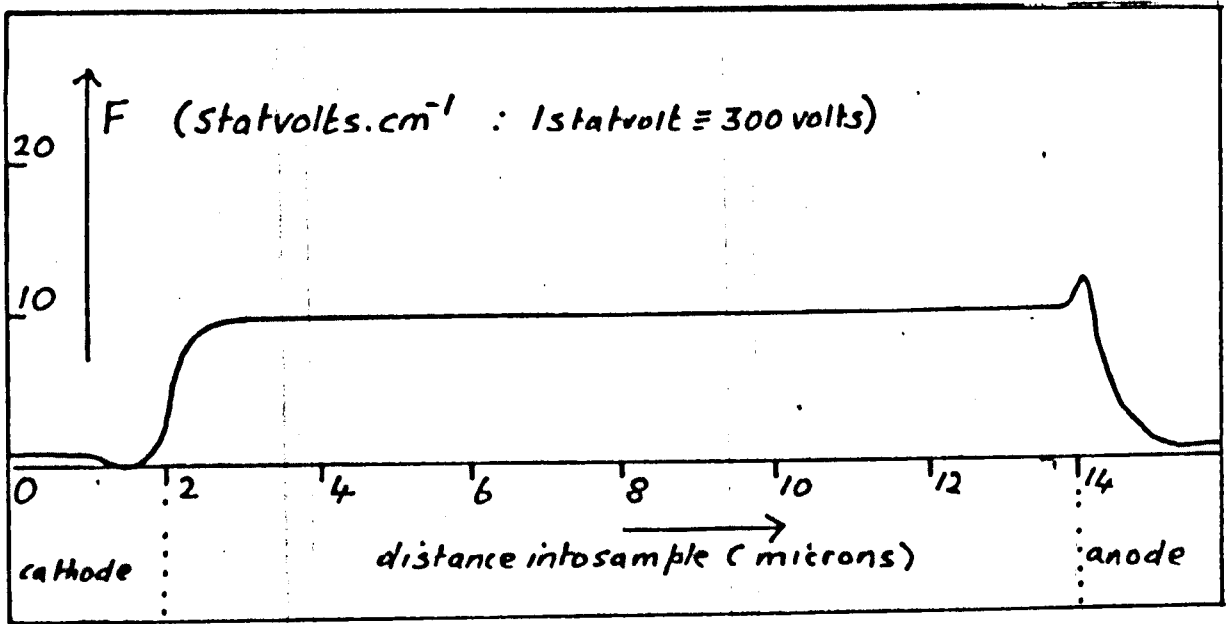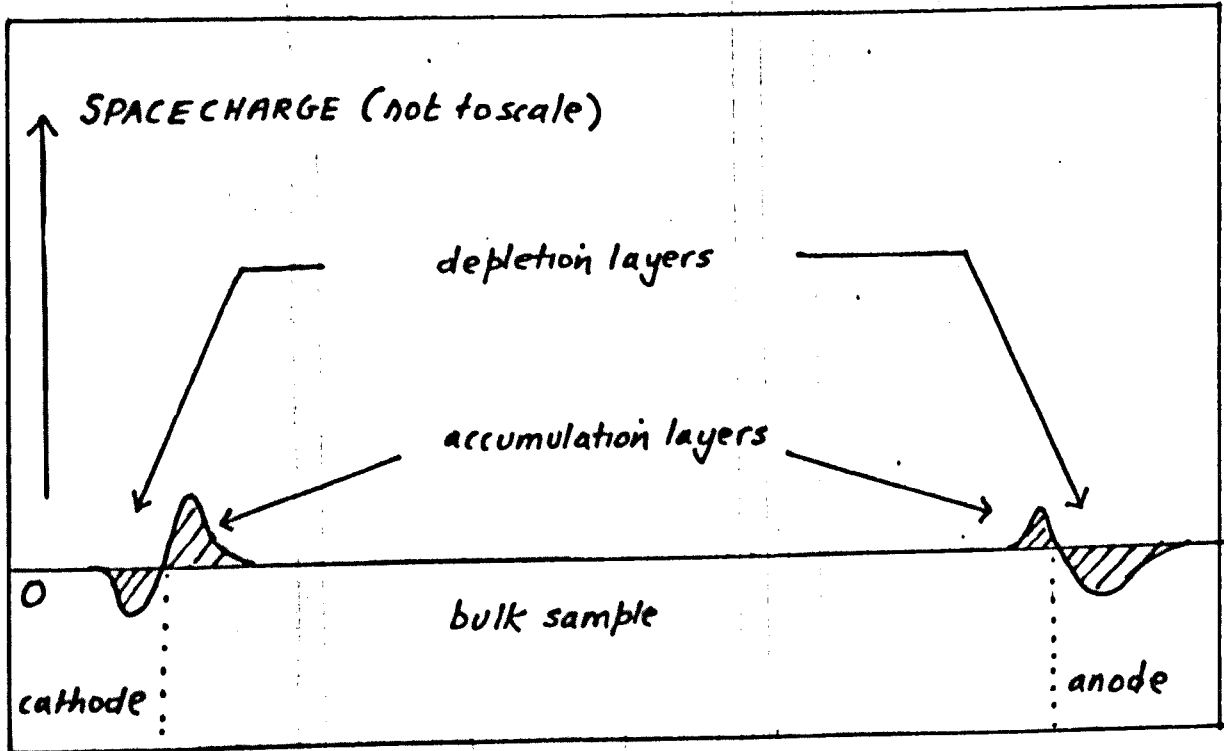
QUALITATIVE SPACECHARGE DISTRIBUTION : OHMIC SEMICONDUCTOR

FIG 5.8

FIG 5.9

FIELD DISTRIBUTION:
TIME DEVELOPMENT

horizontal scale :
distance along sample
0 to 14 microns.

vertical scale :
electric field
-8 to 78 statvolt cm⁻¹
(1 statvolt ≡ 300 volt).

numbers indicate
time elapsed in units
of 10⁻¹⁰ seconds.

dotted line indicates
initial bias field in bulk
of sample F_0 = 15 statvolt cm⁻¹.

doping notch at 4.2 microns
from cathode.
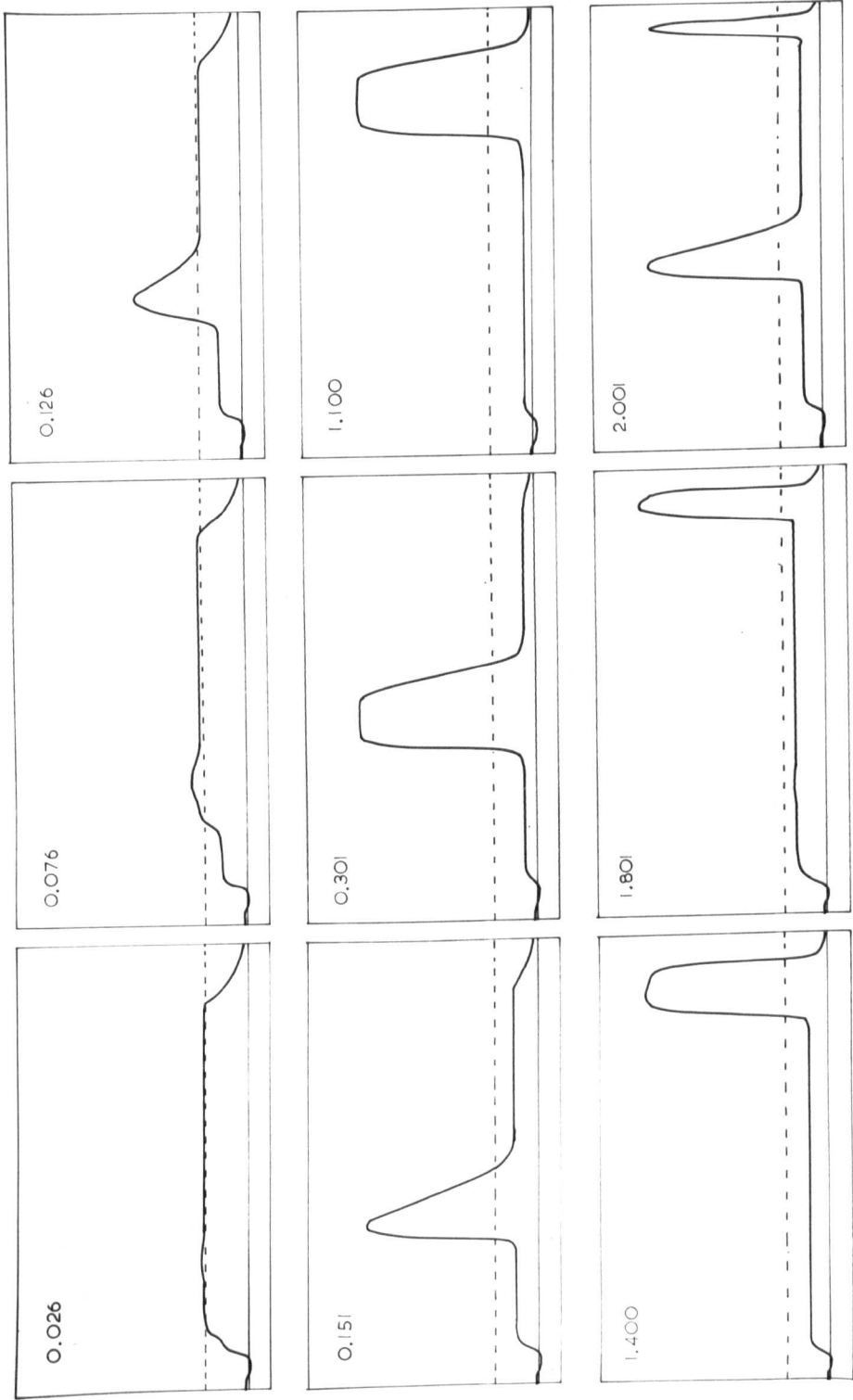
near the contacts such that the field rises rapidly from near zero at the cathode to an almost uniform field (above threshold) in the bulk of the sample. The usual effects of diffusion at the contacts are apparent. However, there are two significant differences from the Ohmic case. The first is that the initial rise in field near the cathode has a step in it, corresponding to an additional accumulation layer of electrons. In the absence of the perturbation notch the accumulation layer grows non-linearly and travels across the sample with a non-uniform velocity. The layer is then absorbed at the anode and the entire process repeats cyclically. This behaviour is entirely analogous to the accumulation layer instability discovered by Kroemer (1966) in theoretical studies of the Gunn effect. We shall come back to this analogy later. The second difference from the Ohmic case is that the initial field in the bulk of the sample is above threshold and by the linear analysis of section 5.4 is unstable with respect to space-charge perturbations. This can be seen in the first few frames of Figure 5.9 where the disturbance introduced by the perturbation notch grows with an initial growth rate of $1/|\tau_d|$ and travels towards the anode at the drift-velocity v_o. Both τ_d and v_o are associated with the field immediately adjacent to the disturbance which we denote by F_R. However, the accumulation layer instability, nucleated at the cathode, travels faster than the dipole perturbation and after a short time (of the order τ_d) combines with it to nucleate a high field domain. This behaviour is shown in the first few frames of Figure 5.9. The presence of the depletion layer at the perturbation notch appears to be crucial for the nucleation of a domain. The initial domain shape is roughly triangular but changes to the flat topped domain shown in the last few frames when the peak domain field exceeds F_r, the restoring field. The flat-topped form is stable and reached within a time the order of a few τ_d where τ_d is associated with the final outside field F_R. Once the domain is fully formed, it propagates uniformly along the sample at a velocity $v(F_R)$. We note that the leading and trailing edges of the domain have fields in the range F_c to F_r which implies that the electrons in these sections have negative drift
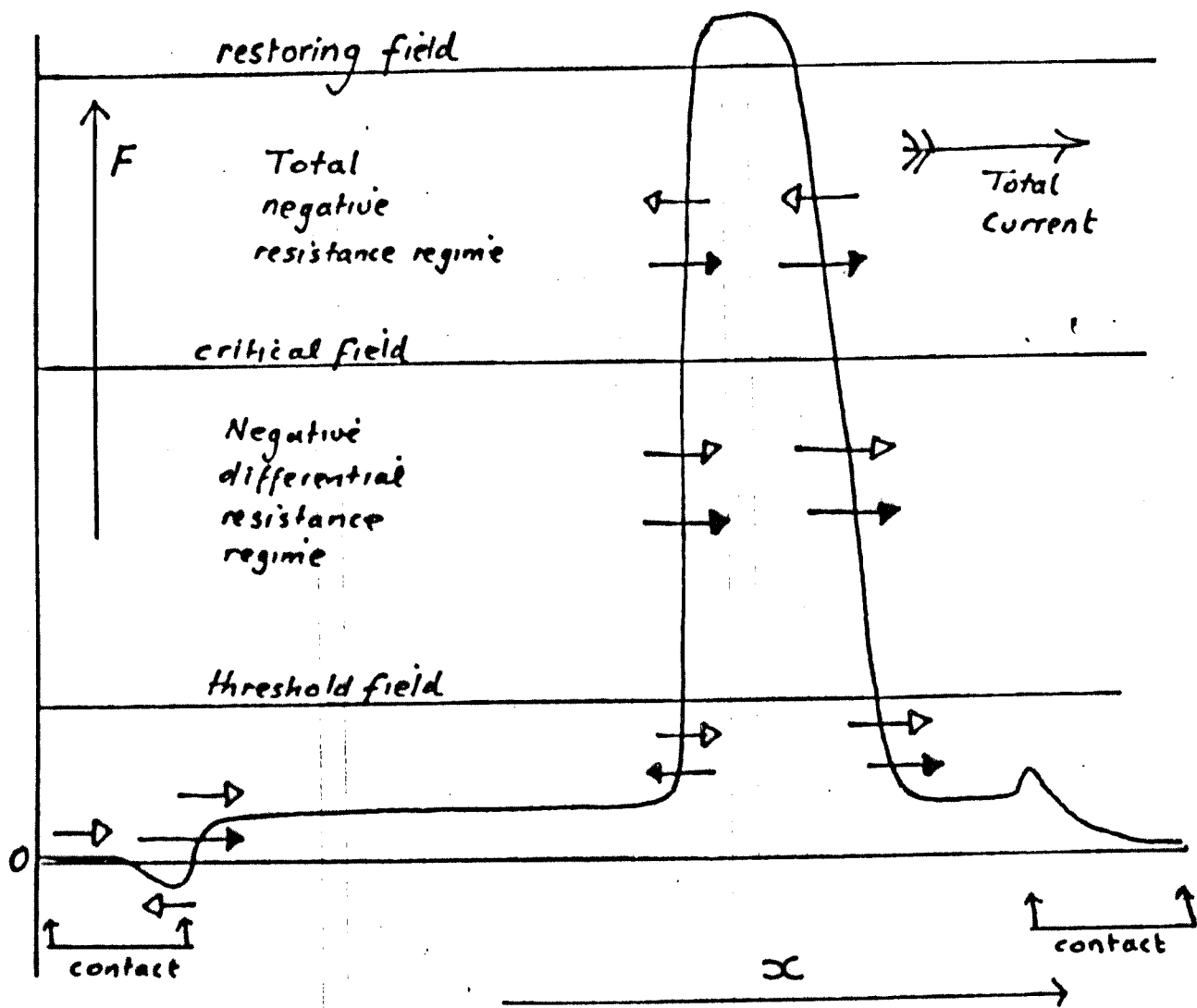
FIG 5.10   DIFFUSION AND DRIFT CURRENTS
▷ : drift current ; ➤ : diffusion current
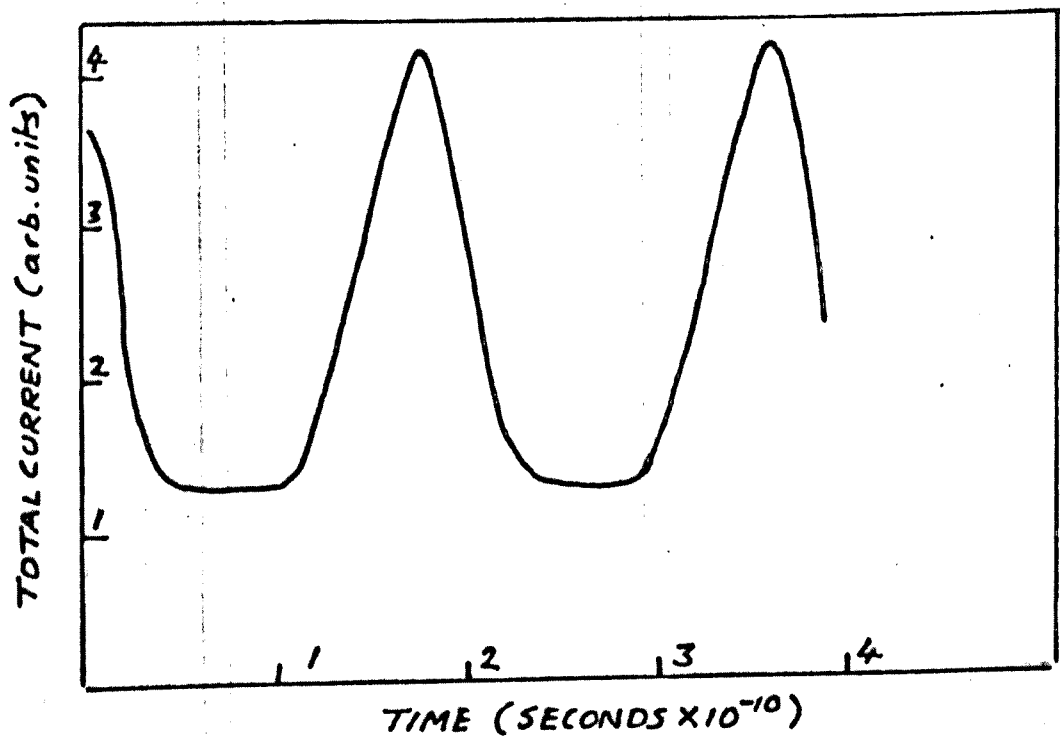
FIG 5.11   TOTAL CURRENT : $F_0 = 15$ statvolts/cm.

velocities. The total current is positive however, and this achieved by large diffusion currents present in these regions induced by the very steep domain walls. Figure 5.10 shows the directions of the diffusion and drift current in the flat-topped domain. As noted in section 5.3, diffusion is crucial to this problem in that it allows the field to cross regions of negative drift velocity. At the anode the domain is slowly absorbed and a new domain nucleates as before and the whole process repeats. The total current behaviour is shown in Figure 5.11. The total current falls initially as the domain nucleates and is constant whilst the fully formed domain propagates along the sample, finally rising again as the domain is absorbed at the anode. The overall current thus shows an oscillatory structure in time with a period close to the domain transit time.

The crucial role of the contacts is well illustrated if we consider a similar case but for no contacts present, Figure 5.12. Here, the initial field is uniform everywhere, and the space-charge perturbation at the notch grows into an unstable flat topped domain which is followed by a large depletion layer of electrons. The system finally reaches a non-uniform steady-state when the domain collapses near the anode wall. This final state has a stationary shock-wave structure; the corresponding phase plane trajectory connects the two saddle points F_1 and F_3 where $F_1 < F_t$ and $F_3 < F_r$. The time development of the total current is shown in Figure 5.13, the two peaks being associated with the domain nucleation and final collapse.

For an initial bias field in the range $F_c < F_o < F_v$, the system supports an initially negative current. As before the field quickly adjusts to $F \approx 0$ near the contacts. Figure 5.14 shows the time development for this case, where $F_o = 42$ stat volts/cm. Whilst the total current is negative the cathode ($x = 0$) exchanges roles with the anode and electrons are brought into the sample from the anode ($x \approx \ell$). In the extended velocity-field characteristic scheme

FIG 5.12
FIELD DISTRIBUTION :
TIME DEVELOPMENT.

horizontal scale :
distance along sample
0 to 12 microns.

vertical scale :
electric field
0 to 70 statvolts cm⁻¹
(1 statvolt = 300 volts).

numbers indicate time
elapsed in units
of 10^{-10} seconds.

dotted line indicates initial
bias field in sample
F_0 = 30 statvolt cm⁻¹
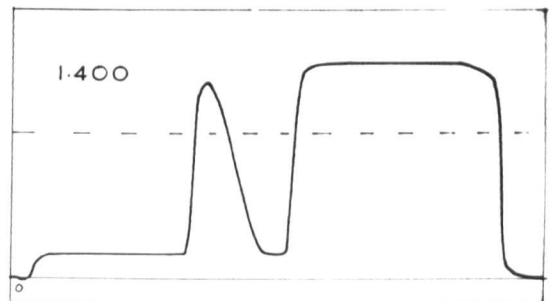
doping notch at 2.5 microns.
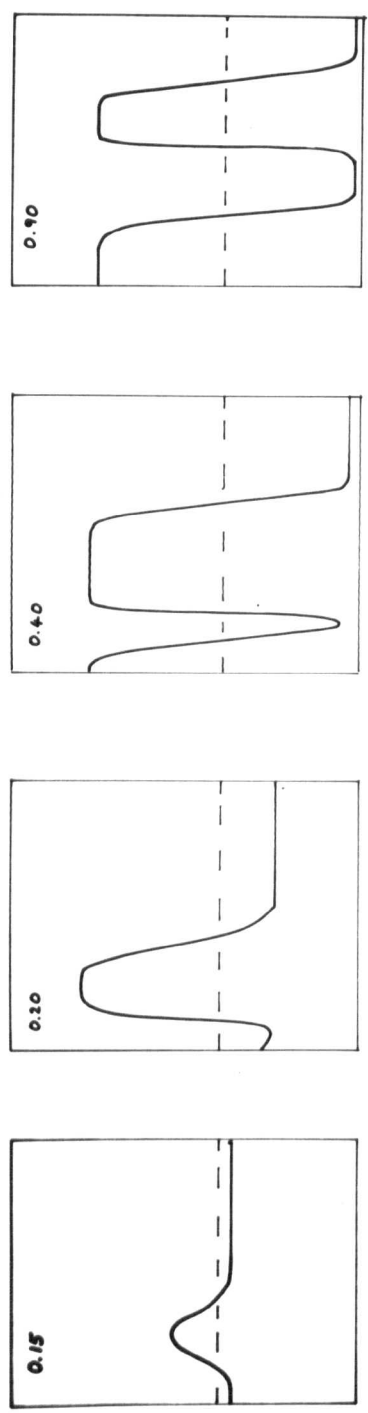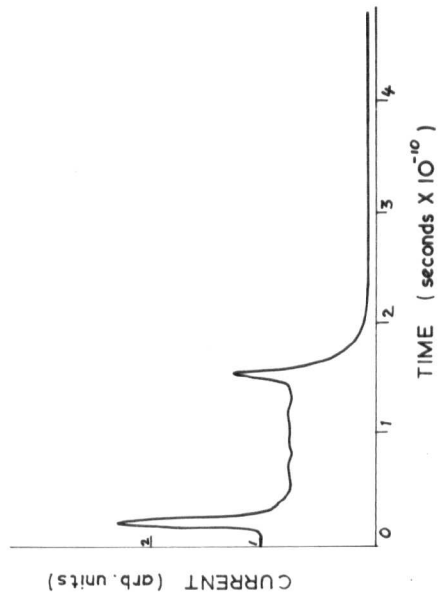
FIG 5.13
TIME DEVELOPMENT
OF TOTAL CURRENT
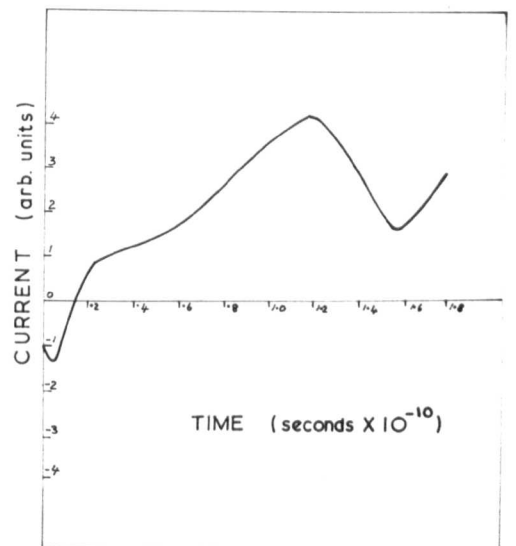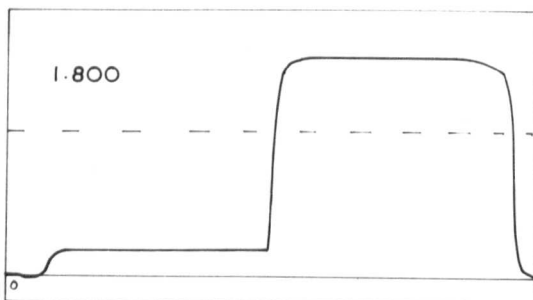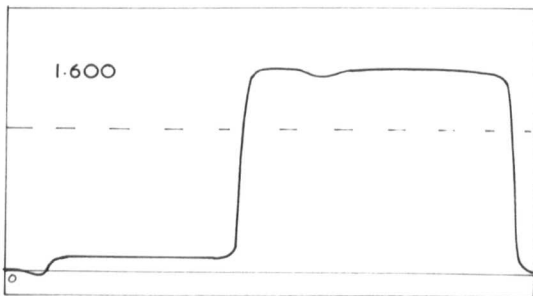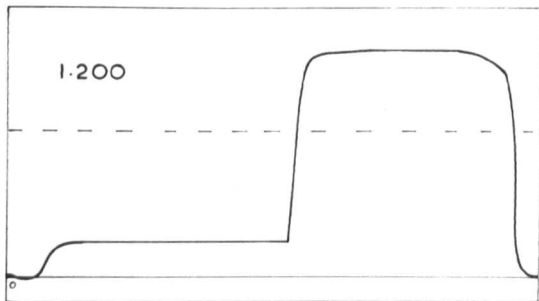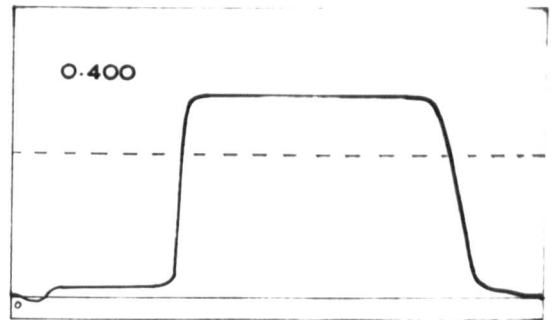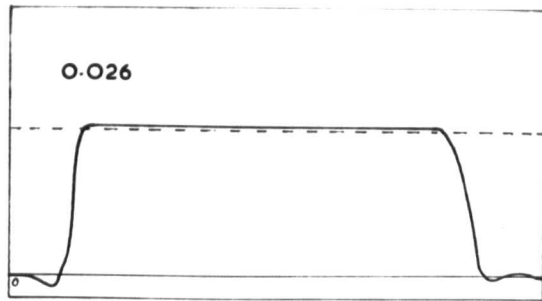
FIG 5.12

FIG 5.13

FIG 14

FIG 15

FIG 5.14 : TIME DEVELOPMENT OF FIELD DISTRIBUTION FOR $F_0 = 42$ statvolt cm^{-1}

horizontal scale : distance along sample, 0 to 14 microns ; vertical scale : electric field : -8 to 78 statvolt cm^{-1} (1 statvolt $\equiv$ 300 volt) ; numbers indicate time elapsed in units of 10^{-10} seconds ; dotted line indicates initial bias field in bulk of sample; doping notch at 4.2 microns.

FIG 5.15 : TIME DEVELOPMENT OF TOTAL CURRENT

(c.f. section 5.3) in which we only consider positive total currents, the corresponding field distributions are obtained by rotating Figure 5.14 by 180° (see Figure 5.16). This follows from the invariance of the basic equations under the transformation $J \rightarrow -J$, $F \rightarrow -F$, $x \rightarrow -x$. The most important feature here is the accumulation layer formed near the new anode (x=0). This layer is essentially the trailing edge of a large flat topped high field domain. The trailing edge of the domain moves away from the new anode against the total current flow. To maintain the total potential across the sample the peak field in the domain rises. Eventually the peak domain field exceeds F_r, the restoring field, and a positive drift current is regained. At the same time the field outside the domain and within the contacts builds up such that the total current J increases from negative values into the positive region and bulk positive resistance is restored. The behaviour of the total current is shown in Figure 5.15. The perturbation introduced by the notch is initially amplified as predicted by the linear theory, but is rapidly absorbed into the accumulation layer. It appears at first sight that with the restoration of positive resistance the field distribution reaches a steady-state in which there are two plateaux of low and high field within the sample. This would be analagous to the shock-wave solution in the no contacts case discussed earlier. However, the low field plateau has a value within the range F_t to F_c and is unstable. Consequently the built in perturbation at the notch is amplified and a narrow domain forms which propagates into the high field plateau. The two plateau regions appear to be a persistent feature of the ultimate field distribution. The final situation involves the cyclic nucleation, propagation (within the low field plateau) and absorption (into the high field plateau) of a narrow high field domain. The total current thus oscillates somewhere in the range $en_o v(F_t)$ to $en_o v(F_c)$, whilst the high field plateau oscillates in value at fields in excess of F_r. The total negative resistance state is never regained. There is a possibility that for a sample of suitable length, the low field plateau might be below threshold

F

← total current

anode   cathode

0

O   ℓ

→ x

(a) negative total current

-F

F

total current →

cathode   anode

0

O   ℓ

→ x
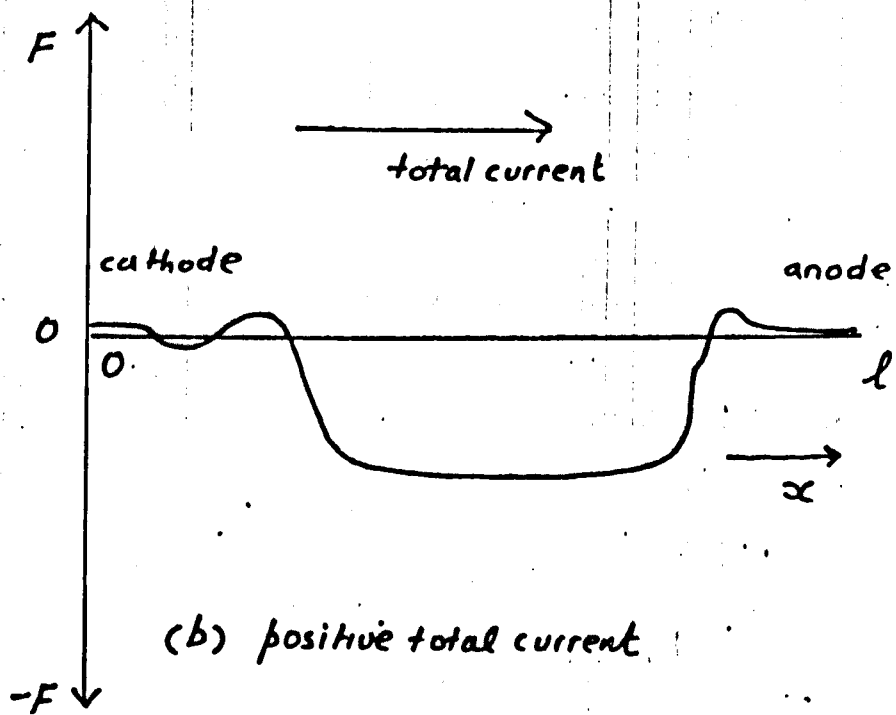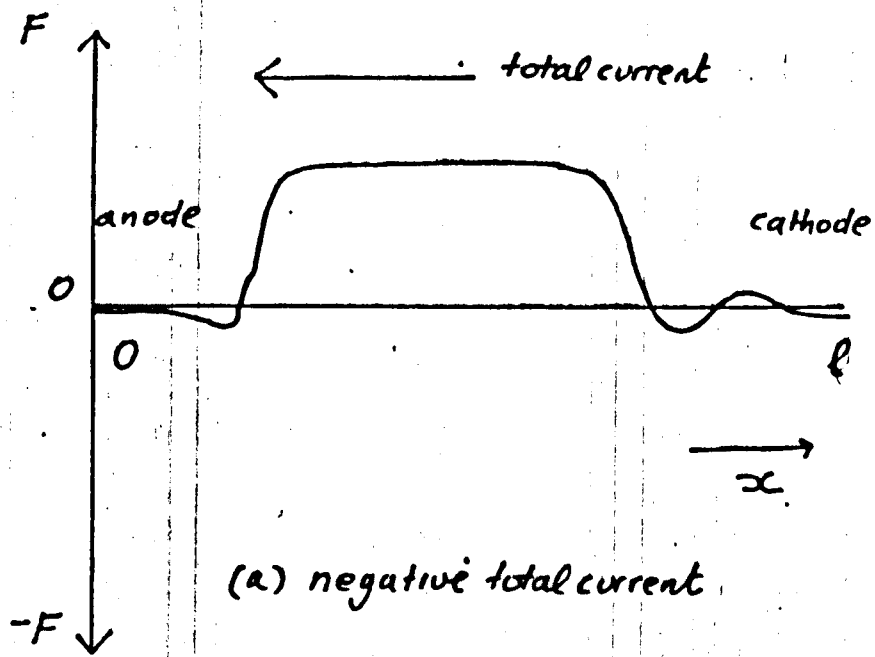
(b) positive total current

-F

FIG 5.16   FIELD DISTRIBUTION IN THE NEGATIVE RESISTANCE STATE
           FOR (a) THE RESTRICTED, AND (b) THE EXTENDED VELOCITY
           FIELD CHARACTERISTIC SCHEME (THE LATTER CONSIDERS ONLY
           POSITIVE CURRENT)

and we would obtain a steady-state, but this has not been observed in the limited numerical experiments carried out.

Again a different behaviour is found if the contacts are removed. In this case an inverted domain is nucleated at the perturbation notch with a minimum field greater than zero as shown in Figure 5.17. The domain is stable but is absorbed into the anode and the final state is a non-uniform steady state in the form of a stationary shock wave. Again the negative resistance state is rejected (the behaviour of the total current is shown in Figure 5.18).

The phase plane analysis and small signal analysis suggest that if the sample is biased into the region $F_v < F_o < F_r$ then a negative resistance steady state could be possible. However, the numerical calculations for such an initial bias field lead to the development of a non-uniform steady state of the shock-wave form, as shown in Figure 5.19 for an initial bias field of $F_o = 53$ stat volts/cm. The negative resistance state is rejected in a similar fashion to the case $F_c < F_o < F_r$, but the perturbation induced by the notch is damped out. The total current evolution is shown in Figure 5.20. The final state consists of a two-plateau distribution, one at a high field in excess of F_r, the other at a low field which lies below the threshold field F_t. The fields are approximately related by the condition $v(F_a) = v(F_b)$ where a and b refer to the low and high field plateaux respectively. The corresponding trajectory in the phase-plane is shown in Figure 5.21, and involves a near saturation to the saddle point $F_1(\approx F_a)$ and final saturation to the saddle $F_3(\approx F_b)$. This significant result shows that saturation to the negative field solution F_5 (in the terminology of section 5.3) is not possible and appears to be a consequence of the boundary condition $F \approx 0$, $\partial F/\partial x$ large and positive at the cathode. As anticipated in section 5.3 all our numerical calculations show that this boundary condition is upheld when ordinary contacts are used. In the case where contacts

FIG 5.17

FIELD DISTRIBUTION:
TIME DEVELOPMENT.

horizontal scale: distance along sample:
0 to 12 microns.

vertical scale: electric field:
0 to 70 statvolt cm^{-1}
(1 statvolt ≡ 300 volts).

numbers indicate time
elapsed in units of 10^{-10} seconds.

dotted line indicates initial
bias field in sample,
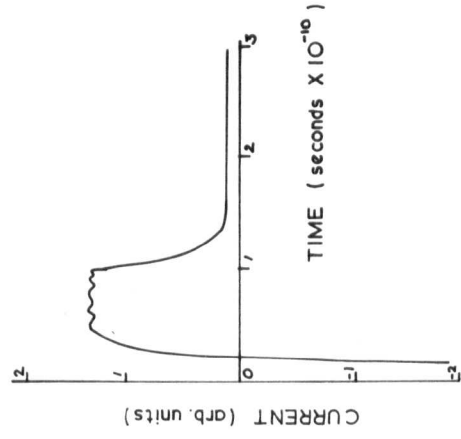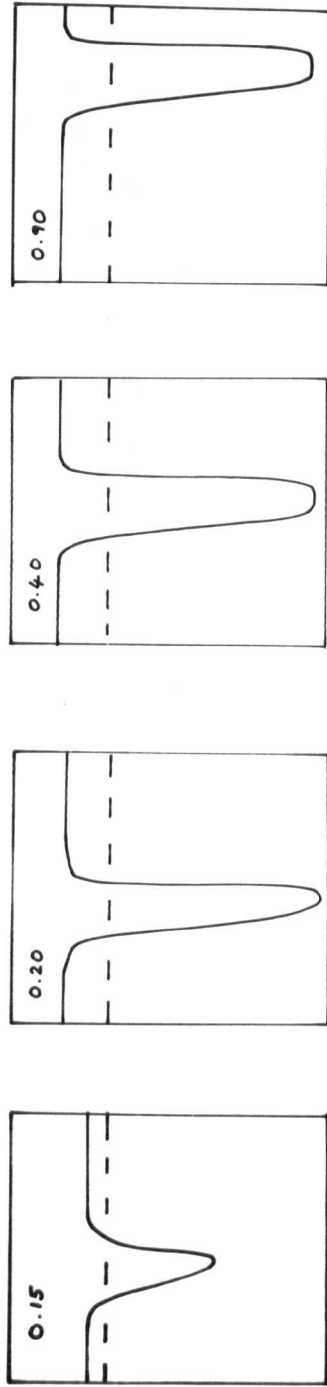F_0 = 48 statvolt cm^{-1}.

doping notch at 6 microns.

FIG 5.18
TIME DEVELOPMENT OF
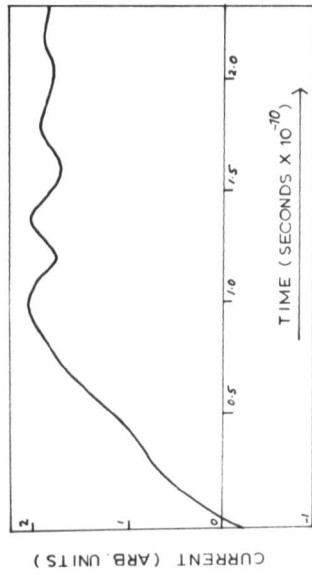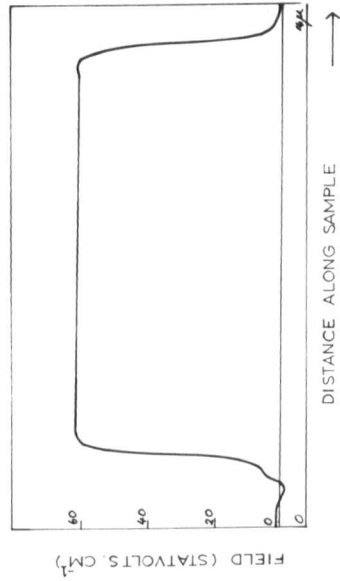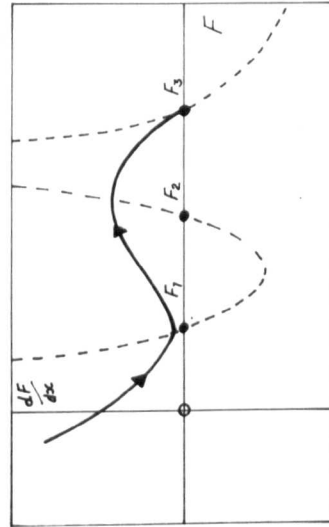TOTAL CURRENT.

FIG 17

FIG 18

FIG 5.20

FIG 5.22
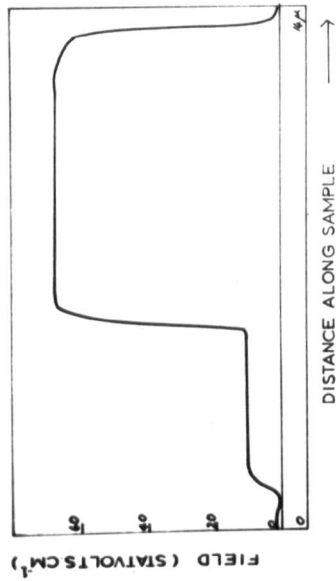
FIG 5.19

FIG 5.21

are absent a uniform stable negative resistance steady state occurs.

The final cases involve $F_o > F_r$. These all lead to stable steady-states of the type predicted by the phase-plane analysis and involve saturation to the saddle point at F_3. The final state for F_o = 60 stat volt/cm is shown in Figure 5.22. A stable uniform steady state occurs in the absence of contacts.

5.7 Analogies with the Gunn effect

In the complete ionization limit several features of the instabilities discussed in section 5.6 bear a marked resemblance to those found in materials exhibiting the Gunn effect. Indeed some of the theory applicable to the Gunn effect can be carried over to the present problem. The Gunn effect involves the occurrence of microwave current oscillations in n-type multivalley polar semi-conductors, notably in gallium arsenide, at room temperatures and in the presence of high electric fields. The effect was first observed by Gunn (1963) and partly because of its important applications has received considerable experimental and theoretical attention (a review has been given by Butcher 1967, and a recent bibliography is given by Gaylord et al 1968). The basic physical process involves the electron transfer mechanism first proposed by Ridley and Watkins (1961) and Hilsum (1962). At high electric field strengths hot electrons within the central high mobility valley in the conduction band structure are transferred to satellite low mobility valleys as the electric field increases. This gives rise to a negative differential mobility in the sample characterized by an N-shaped drift velocity-field characteristic and the electron system is unstable. The current oscillations are produced by the cyclic nucleation, uniform propagation and absorption of narrow high field domains, and occur for bias fields in excess of a threshold field.
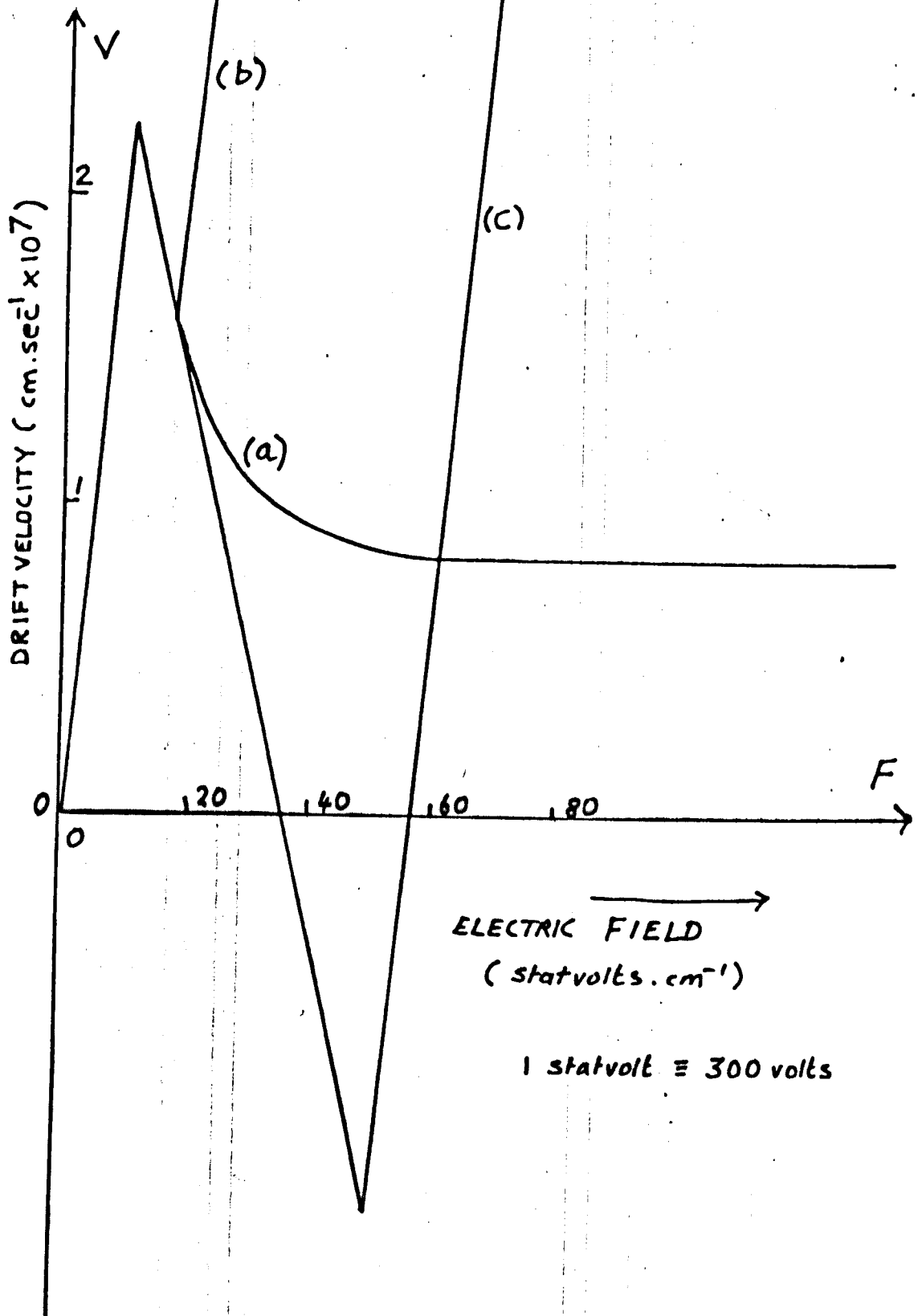
FIG 5.23 COMPARISON OF THE OPC AND GUNN VELOCITY*FIELD
CHARACTERISTICS

(a) Gunn — saturating characteristic

(b) Gunn — non-saturating characteristic

(c) OPC characteristic

Theoretical treatments of the Gunn effect have proposed two slightly different forms for the drift velocity-field characteristic, an N-shaped form (Conwell and Vassal 1966, McCumber and Chynoweth 1966), and a saturating characteristic (Butcher and Fawcett 1966). The latter gives better agreement with experiment. These forms are shown in Figure 5.23 where they are compared with the approximate oscillatory photoconductivity (OPC) characteristic (curve (c)) used in our numerical experiments. Curve (a) is the analytical approximation due to Butcher and Fawcett (1966), whilst curve (b) is qualitatively similar to the form suggested by McCumber and Chynoweth (1966). We adopt the same nomenclature as in section 5.3 to describe the threshold, critical, valley and restoring fields where these exist.

The phase-plane for the general case of an N-shaped Gunn characteristic is shown in Figure 5.24 for a steady state total current $J = en_o v_o$, where $v_o < v_o$ and n_o is the background density of positive charge. Three singular points occur and are classified as saddle (F_1) unstable focus (F_2) and saddle (F_3) and are analogous to the OPC case. For the saturating Gunn characteristic F_3 is at infinity. The phenomenological space-charge and field equations are the same as for the OPC problem in the complete ionization limit, but $v(F)$ now refers to the Gunn characteristic.

Small signal perturbation theory shows that a uniform field distribution of value F_o in an infinite sample is stable if $F_o < F_t$, unstable if $F_t < F_o < F_v$ and stable if $F_o > F_v$. The unstable situation for a finite sample with contacts is illustrated in Figure 5.25 for an initial bias field $F_o = 11$ stat volts/cm ($>F_t$) for the saturating Gunn characteristic. Our numerical calculation shows the nucleation of a narrow 'triangular' high field domain which propagates uniformly along the sample. The process repeats cyclically with a well defined frequency. The total current evolution shown is Figure 5.26. If the perturbation notch is removed the instability takes the form of an accumulation layer instability which
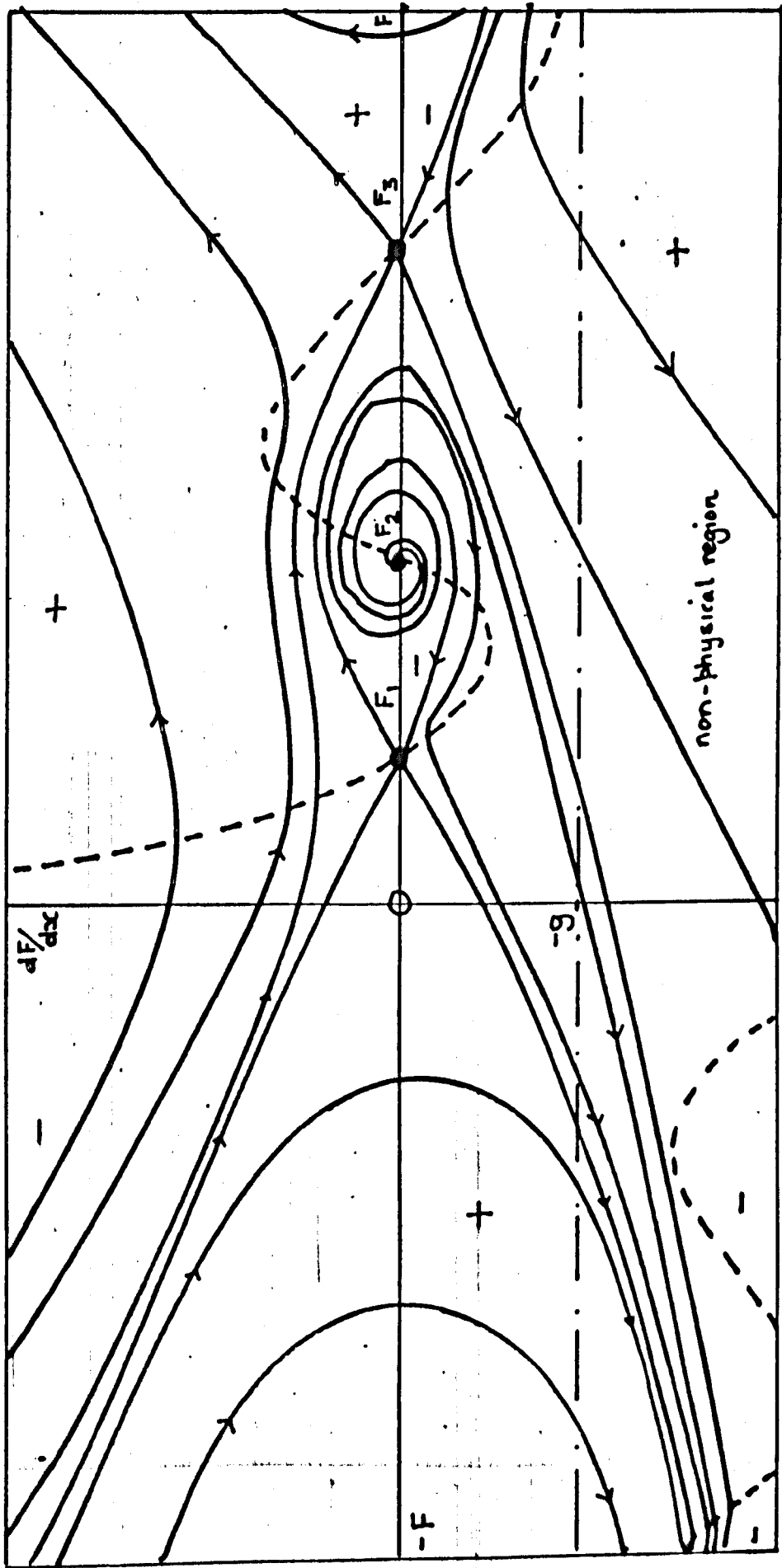
FIG 5.24   PHASE PLANE TRAJECTORIES

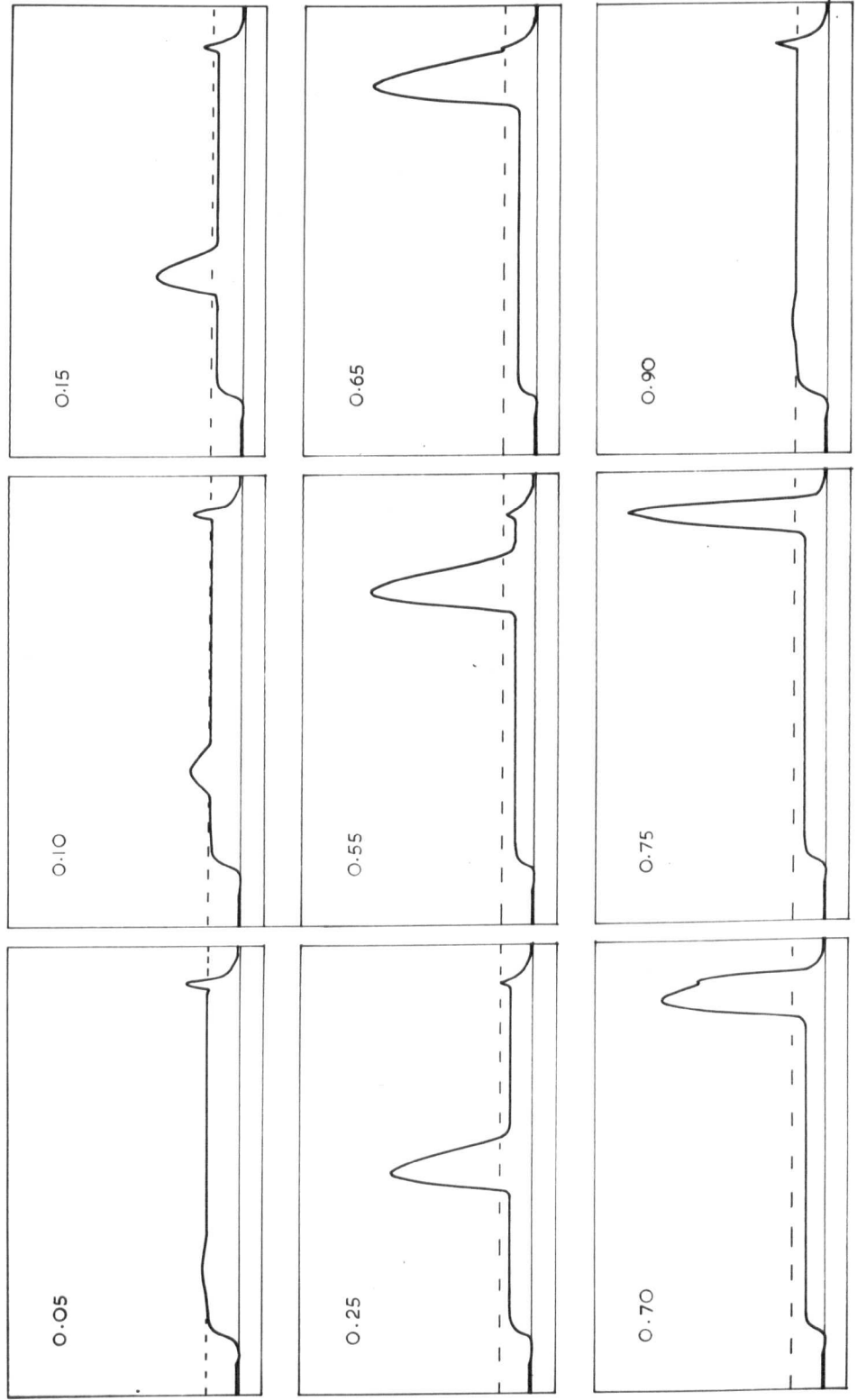FIG 5.25

FIELD DISTRIBUTION:
TIME DEVELOPMENT.

horizontal scale : distance
along sample : 0 to 14 microns.

vertical scale : electric field :
-8 to 78 statvolt cm⁻¹
(1 statvolt = 300 volts).

numbers indicate time
elapsed in units of 10⁻¹⁰ seconds

dotted line indicates
initial bias field in sample,
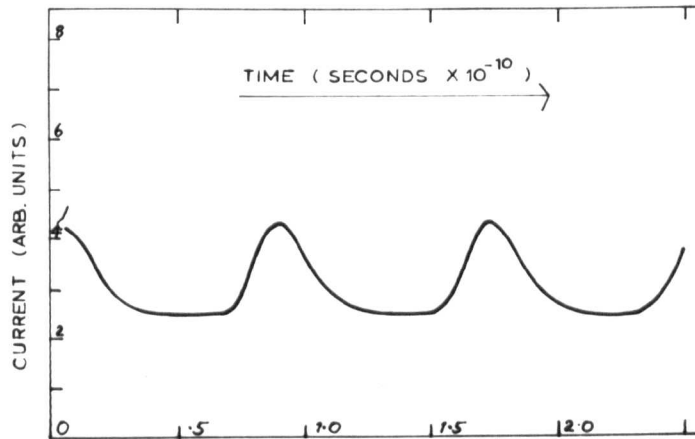F₀ = 11 statvolt cm⁻¹.
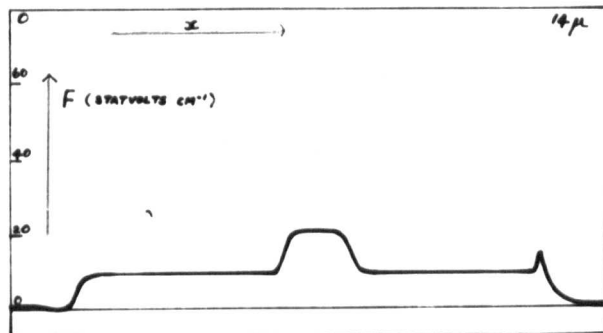
doping notch at 4.2 microns.
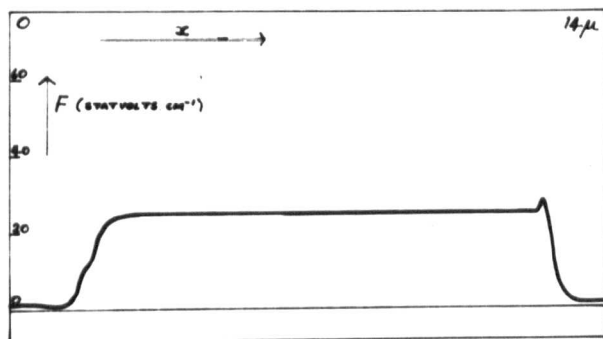
FIG 5·26

FIG 5·27

FIG 5·28

propagates non uniformly, and corresponds to the instability predicted by Kroemer (1964). The domain nucleation is exactly the same as in the OPC problem for bias fields in the range F_t to F_c. The total current shows a spikey waveform as shown in Figure 5.26, the spikes occurring during the nucleation-absorption stage. Our numerical calculations also show the occurrence of stable domains for the non-saturating Gunn characteristic. One such example, for a sample with contacts is shown in Figure 5.27 for an initial bias field $F_o = 11$ stat volts/cm. The flat topped form is a consequence of the non-saturating characteristic and its origin is discussed in the next section. For the same sample but with a bias field of 15 stat volts/cm there occurs an initial accumulation layer instability followed by the cyclic nucleation and propagation of an unstable domain which travels non uniformly along the sample. For bias fields above the valley field, a non-uniform steady state is achieved rather similar to the OPC steady states. An example, for $F_o = 20$ stat volts/cm is shown in Figure 5.28.

An analysis of uniformly propagating stable domains due to Butcher and Fawcett (1966) shows that if the diffusion coefficient is constant the fully-formed domain travels at a velocity v_D equal to the drift velocity v_R of the electrons in the essentially uniform field F_R outside the domain. The numerical experiments confirm this result. The same argument holds for domains in the OPC problem. For a constant diffusion coefficient D, the peak domain field F_D varies with F_R the outside field according to an equal areas rule (Butcher and Fawcett 1966). This rule is illustrated in Figure 5.29. For a constant diffusion coefficient D, the exact analysis of Butcher and Fawcett gives the stable domain shape as

$$y = \frac{\epsilon}{4\pi e} \int_{F_D}^{F} \frac{dF'}{n - n_o} \qquad \qquad 5.7.1$$

where $y = x - v_D t$, and n is given as a function of F by

$$\frac{n}{n_o} - \log_e \frac{n}{n_o} - 1 = \frac{\epsilon}{4\pi e n_o} \int_{F_R}^{F} \left(v(F') - v_R\right)\frac{dF'}{D} \qquad \qquad 5.7.2$$
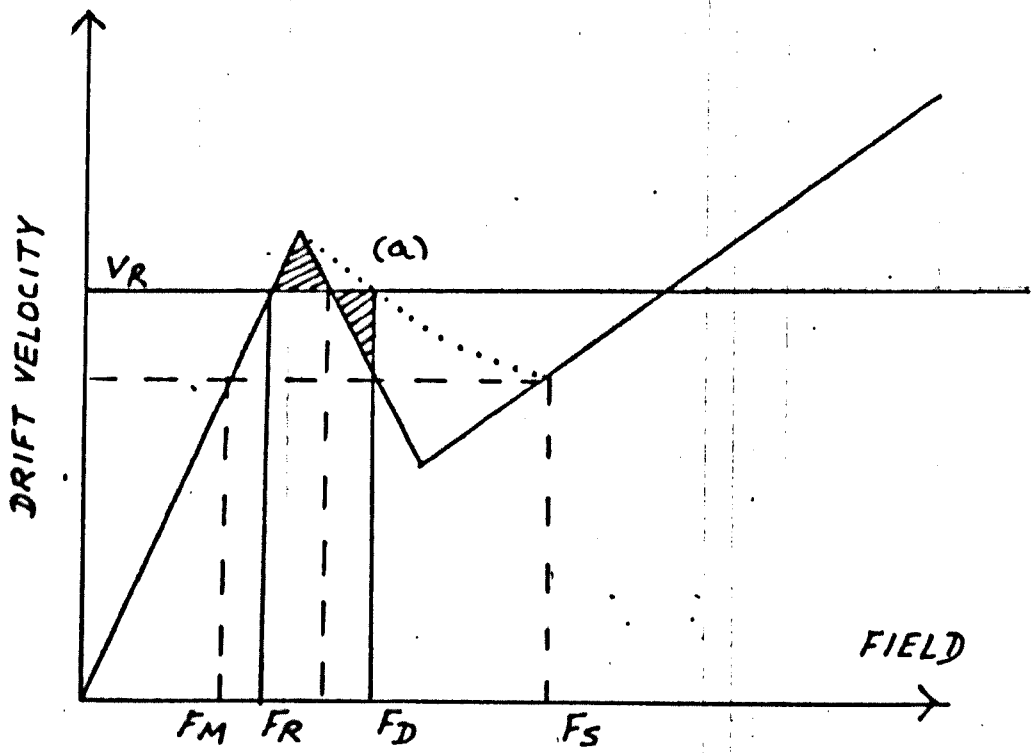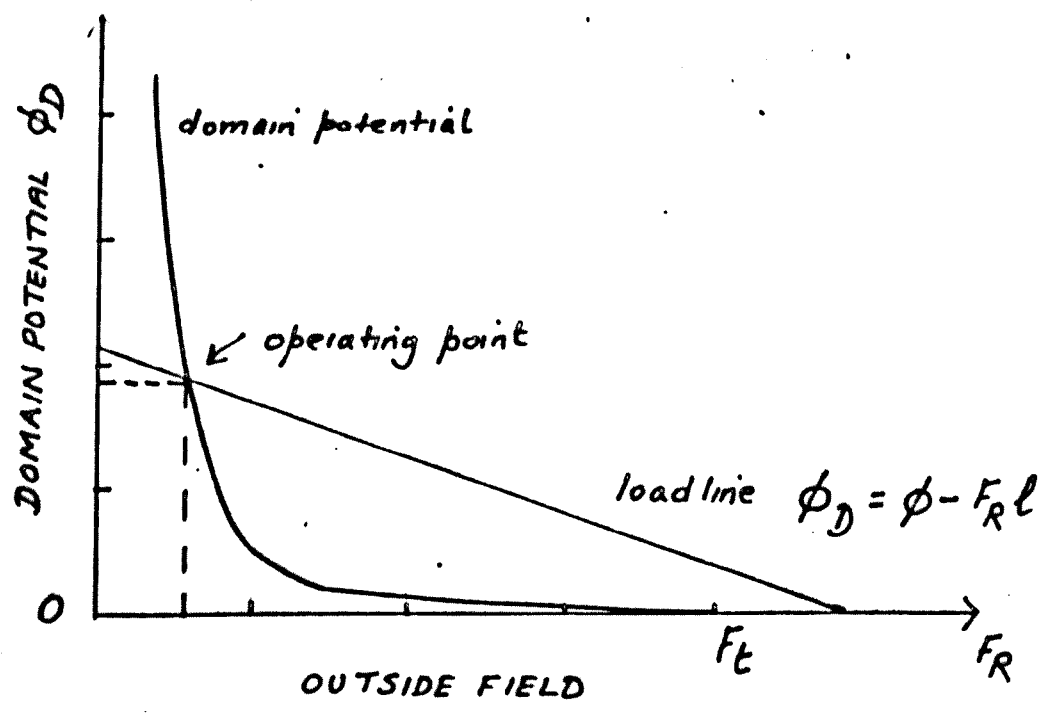
FIG 5.29   EQUAL AREAS RULE

FIG 5.30   DOMAIN POTENTIAL PLOT

These equations are derived from Poisson's equation and the current continuity equation. Since $\partial F/\partial x$ ($\equiv \partial F/\partial y$) is zero at the peak domain field F_D. Poisson's equation shows that $n = n_o$ at $F = F_D$. Substituting $F = F_D$ into (5.7.2) then shows that

$$\int_{F_R}^{F_D} v(F')dF' = v_R(F_D - F_R). \qquad 5.7.3$$

Consequently the two areas shown in Figure 5.29 are equal. For outside fields F_R below a critical field F_M the equal areas rule cannot be satisfied for the non-saturating characteristic and stable domain propagation is impossible. The dotted curve (a) in Figure 5.29 is called the dynamic characteristic and is a plot of F_D against v_R as given by the equal areas rule. The termination of this curve corresponds to $F_R = F_M$ and gives F_S as the maximum peak domain field.

From the domain shape equation (5.7.1) we can calculate ϕ_D the domain potential defined as the area under the domain above the outside field F_R. For a finite sample of length ℓ (no contacts) we have

$$\phi_D = V_o - F_R \ell \qquad \text{(the load-line equation)} \qquad 5.7.4$$

where V_o is the external voltage. The qualitative variation of ϕ_D with F_D for a typical case is shown in Figure 5.30. The working point (F_R, F_D) is given by the intersection of the load line (5.7.4) with the domain potential curve and defines the outside and peak domain field for a given voltage and sample length.

The geometric condition (5.7.3) and the concept of load lines carry over without change to the OPC problem, but the equal areas rule for stable domain type instabilities requires some modification. For peak domain fields less than or equal to F_c the equal areas rule holds but breaks down for higher peak domain fields. The geometric condition is still fulfilled for peak fields in excess of F_c and leads to a generalized areas rule illustrated by Figure 5.31(a). Here
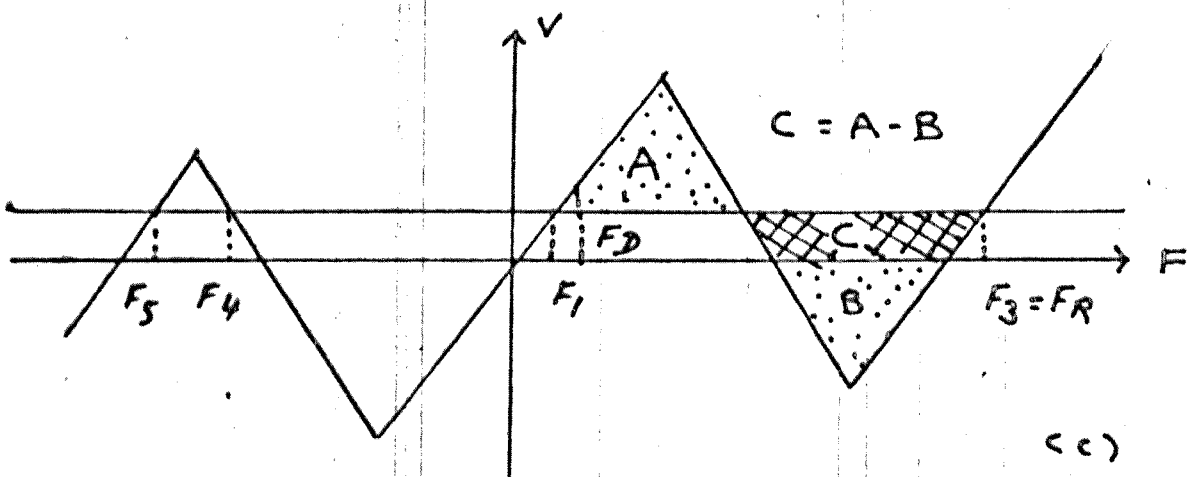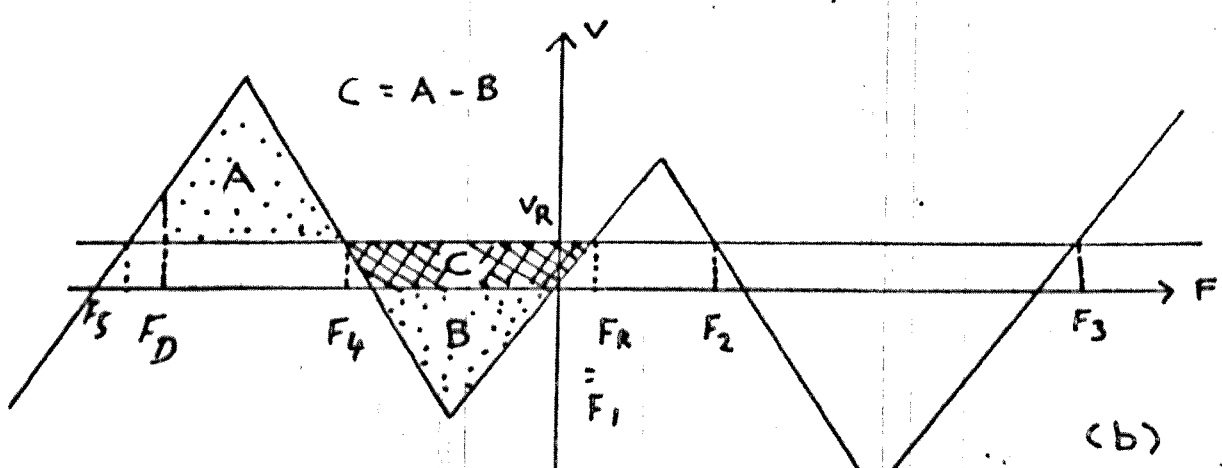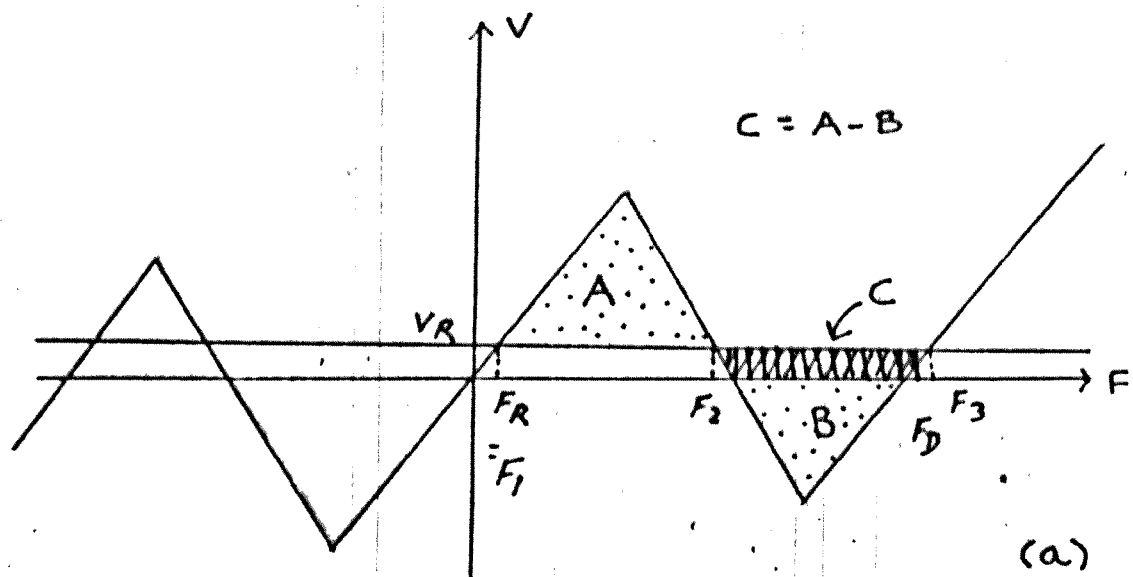
FIG 5.31 GENERALISED EQUAL AREAS RULE

the areas A, B, C are related by C = A-B. All the stable domain solutions found numerically satisfy this rule. All our calculations were based on a velocity-field characteristic in which

$$\int_0^{F_c} v(F)dF \quad - \quad \int_{F_c}^{F_r} v(F)dF.$$

The OPC problem does however admit velocity-field curves in which this inequality is reversed, in which case one might expect negative domains satisfying the geometric condition shown in Figure 5.31(b), where again C = A-B. No numerical calculations were, however, made for this circumstance. The geometric condition (5.7.3) also holds for the inverted domain of Figure 5.17, where in this case the outside field F_R is larger than the domain field F_D. The geometric condition has the form shown in Figure 5.31(c). We note that for the sample length chosen in the OPC numerical experiments the load line condition and equal areas rule leads to peak domain fields in excess of the restoring field F_r. Lower peak fields would require considerably shorter samples.

5.8 Origin of the stable domain solutions

In both the Gunn effect and oscillatory photoconductivity effect we find the possibility of stable uniformly propagating high field domains, where the domain velocity v_D is equal to the drift velocity v_R of electrons in the outside field F_R. During propagation of the domain the total current is positive and constant with a value $en_o v_R$ for an infinite sample (or contactless sample). We may then transform the partial differential equations for the system into ordinary differential equations by setting $y = x - v_D t$. That is we go into the moving frame of reference in which the domain is stationary. Under this transformation we find

$$\frac{\partial F}{\partial t} = - v_D \frac{dF}{dy} \quad , \quad \frac{\partial F}{\partial x} = \frac{dF}{dy} \qquad\qquad 5.8.1$$

and combining Poisson's equation with the total current equation (in the complete ionization limit for the OPC problem) we obtain

$$D \frac{d\psi}{dy} = (g + \psi)(v(F) - v_D); \psi \equiv \frac{dF}{dy} \qquad 5.8.2$$

where as before $g = 4\pi e n_o / \epsilon$. This system is autonomous and is amenable to analysis in the phase plane (F, ψ).

The singular points for the system (5.8.2) occur for the simultaneous conditions $\psi = 0$ and $v(F) = v_D$. Since v_D lies in the range 0 to u there are thus five singular points in the OPC problem which in the notation of section 5.3 are labelled F_i (i = 1 to 5), whilst for the Gunn effect there are three singular points (F_1, F_2, F_3). In order of increasing field they are classified on linear analysis as saddle, centre, saddle, centre, saddle respectively. Higher order analysis suggests that the centres are in fact closely packed unstable foci, and if the diffusion coefficient is field dependent then this is certainly the case. The boundary conditions for the trajectories corresponding to a domain solution are $F = F_R$, $\psi = 0$ at $y = \pm \infty$. The phase planes for the OPC and Gunn effect systems are sketched in Figure 5.32. The zero isoclines are the lines $v(F) = v_D$ and the line $\psi = -g$. We note that in contrast to the phase planes of section 5.3, none of the trajectories in the physical region $(\psi > -g)$ cross into the non-physical (n < 0) region. This is because we have included the time dependence in our basic equations. We also note that $F_1 \equiv F_R$.

In the Gunn effect problem, for a saturating characteristic $F_3 \to \infty$. The domain solution for this case is recognised as the unique re-entrant trajectory leaving the saddle at F_1 (see Figure 5.33). This result was first obtained by Knight and Peterson (1967) in an extensive analysis of the Gunn effect. But this interpretation is true only if F_2 is exactly a centre. If not, the domain solution is most probably a Poincaré limit cycle, (i.e. an isolated closed trajectory such that no trajectory sufficiently near to it is closed; a good discussion of these objects is given by Minorsky, (1962) surrounding F_2
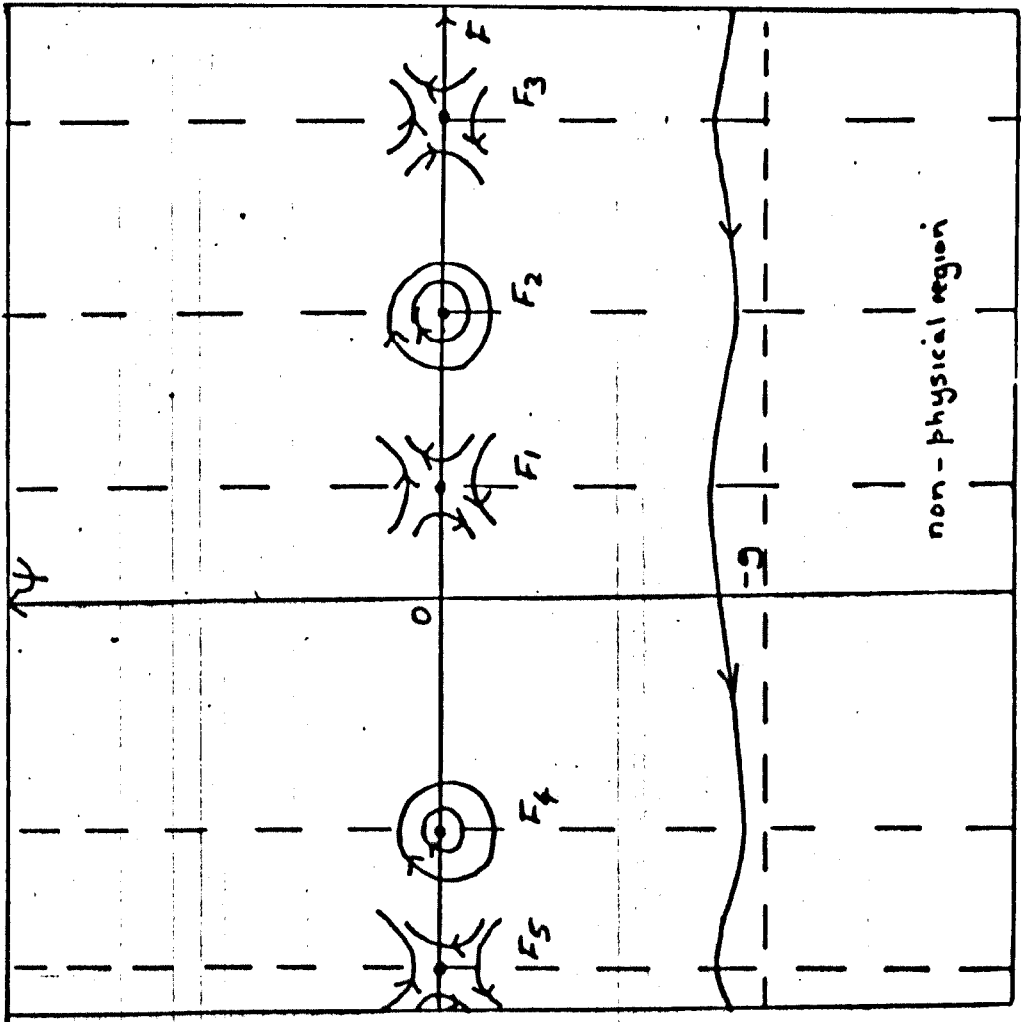
FIG 5.33   TRAJECTORY FOR GUNN DOMAIN

FIG 5.32   PHASE PLANE FOR OPC AND GUNN EFFECT PROBLEMS

with one boundary asymptotic to F_1, the other at F_D the peak domain field. The limit cycle corresponds to a non-linear wave of infinite period (this period would be finite if the locus of the cycle did not touch a singular point). For the non-saturating Gunn characteristic we can also get 'flat topped' domains and this feature may also be found in the phase-plane. In this case the saddle at F_3 distorts the trajectory flow for fields just less than F_3. Trajectories passing close to F_3 involve a very slow variation of F with y, a property of singular points. If the domain trajectory passes close to F_3 the peak domain field changes slowly within the domain and we obtain the flat topped effect. A classification of the possible domain solutions for the Gunn effect is shown in Figure 5.34. The shaded areas illustrate the equal areas rule for the different cases. The total external current decreases in the diagrams in the order (1), (2), (3). The critical case (2) of (5.34) involves separate accumulation and depletion layer solutions where the two saddle points F_1 and F_3 are connected. Case (3) is a possible low field domain, which again satisfies the equal areas rule; this type has not been observed experimentally or in numerical calculations.

Similar remarks apply to the OPC problem, which has an almost identical phase plane. The domain solutions are again interpreted as closed trajectories or limit cycles in analogy with those for the Gunn effect. We remark that various criteria for the non-existence of a limit cycle in this problem, notably the Bendixson theorem (see Minorsky p82, 1962) are not satisfied but an exact proof of the existence of a limit cycle has not been possible (although when F_4 and F_2 are foci we have not been able to construct a consistent phase-plane topology without assuming its existence). A classification of some possible domain like solutions in the OPC problem is given in Figure 5.35 for the two situations in which

$$\int_0^{F_c} v(F)dF > \int_{F_c}^{F_r} |v(F)|dF \qquad \text{(Type I characteristic)}$$

and

$$\int_0^{F_c} v(F)dF < \int_{F_c}^{F_r} |v(F)|dF. \qquad \text{(Type II characteristic)}.$$
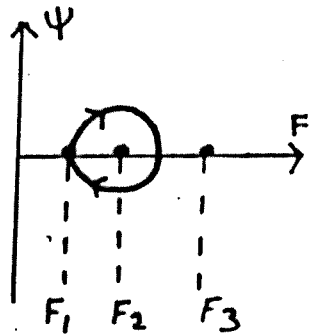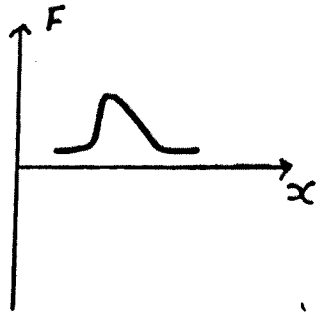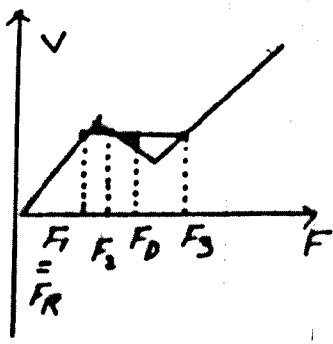
(1) high field domain
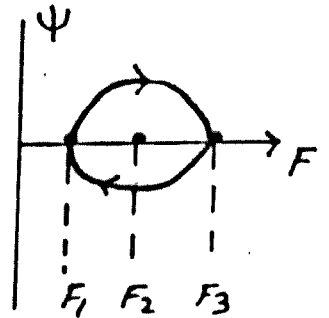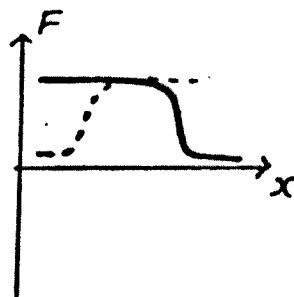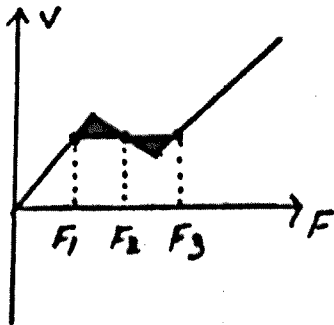
(2) accumulation layer &
      depletion layers
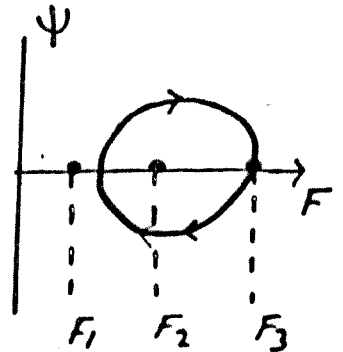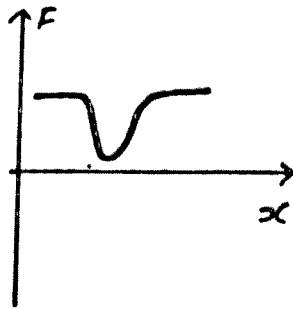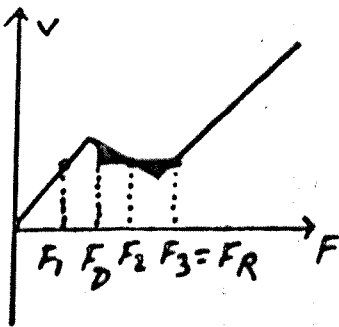
(3) low field domain

FIG 5.34   CLASSIFICATION OF UNIFORMLY PROPAGATING SOLUTIONS
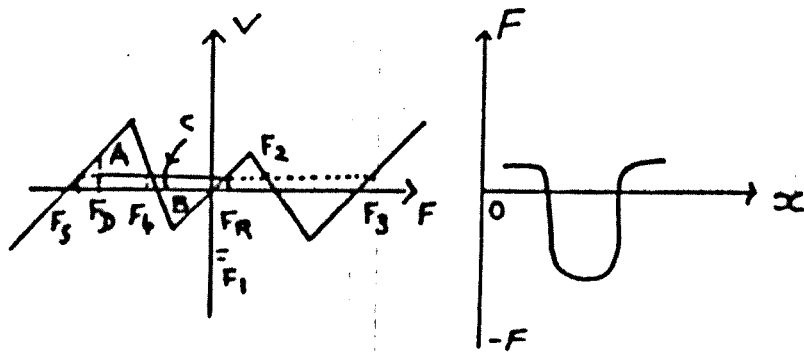
(1)   Type II characteristic
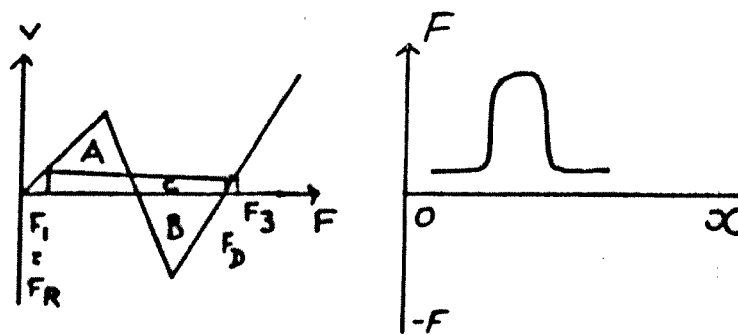
(2)   Type I characteristic
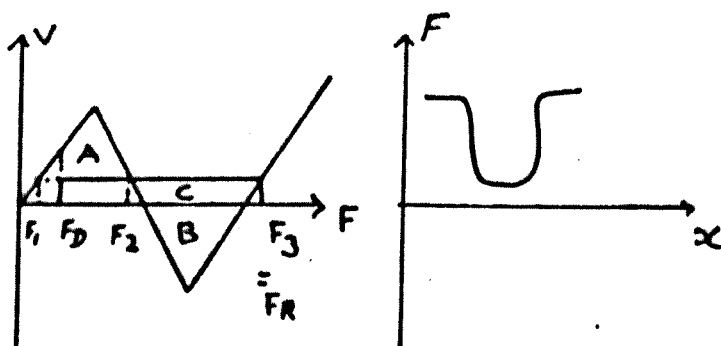
(3)   Type I characteristic

FIG 5.3.5   CLASSIFICATION OF POSSIBLE DOMAIN   SOLUTIONS
          IN THE OPC PROBLEM

The domains observed in the numerical experiments were of the flat topped variety and satisfy the generalised equal areas rule. In the diagram the areas A, B, C are related by C=A-B. Only the solutions (2) and (3) of Figure 5.35 have been found numerically where solution (3) is for the no contacts case and does not arise when contacts are included. As noted previously the complete family of OPC velocity-field characteristics contains characteristics of the non-saturating Gunn type and the Gunn effect analysis is directly applicable to these situations.

5.9 Time development for the general case

The general problem of the nature of the field distribution when the background density of charge p is time dependent is extremely complicated. Only a few calculations have been made for this situation and a complete picture has not emerged. The calculations reported in this section apply to the other extreme to the complete ionization limit in which the characteristic times for the space-charge, electron and hole densities are related by the inequalities

$$\tau_e \gg |\tau_d| \quad ;$$

$$\tau_h \gtrsim |\tau_d| \quad ;$$

$$\tau_e \geq \tau_h \quad .$$

Under these circumstances the assumption that v is a unique function of F is suspect, but the calculations do reflect the main effects of the recombination and generation processes. Four situations have been investigated which we label I, II, III and IV, corresponding to bias fields F_o for four regions of interest on the velocity-field characteristic: these regions are indicated in Table 5.2. Four sets of data are involved which we label A, B, C, D. These correspond to four choices for the generation and recombination parameters S and σ, and lead to different values for n_o, τ_e and τ_h: these values are displayed in Table 5.2. In each case the donor and acceptor densities are chosen as $N_D = 1.1 \times 10^{15}$ cm^{-3},

TABLE 5.2					
BIAS FIELD F_o statvolt/cm	DATA	$\tau_d(F_o)$ seconds	$\delta^{-1} \equiv \tau_e/\tau_d$	τ_h/τ_d	$\gamma^{-1} \equiv \tau_e/\tau_h$
I : 15 $F_t < F_o < F_o$	A	-2.5×10^{-12}	-40	-0.4	100
	B	-0.1×10^{-12}	-30	-30	1
	C	-0.1×10^{-12}	-300	-300	1
	D	-2.5×10^{-12}	-4×10^4	-400	100
II : 42 $F_o < F_o < F_v$	A	-2.5×10^{-12}	-40	-0.4	100
	B	-0.1×10^{-12}	-30	-30	1
III : 52 $F_v < F_o < F_r$	A	1.0×10^{-12}	100	1	100
	B	4.0×10^{-12}	75	75	1
IV : 60 $F_o > F_r$	A	1.0×10^{-12}	100	1	100

A : $n_o = 0.94 \times 10^{15}$ cm^{-3}

B : $n_o = 2.32 \times 10^{14}$ cm^{-3}

C : $n_o = 2.32 \times 10^{14}$ cm^{-3}

D : $n_o = 0.94 \times 10^{15}$ cm^{-3}

$N_A = 0.1 \times 10^{15}$ cm^{-3} respectively so as to correspond to the data used in sections 5.6, 5.7 in the complete ionization limit.

Section I refers to bias fields in the range $F_t < F_o < F_c$. Figure 5.36 shows the calculated field distributions after 10^{-11} seconds for an initial bias field $F_o = 15$ stat volts/cm, corresponding to the parameters given in Table 5.2. These results may be contrasted with the field distribution near the complete ionization limit, ($n_o \approx 10^{15}$ cm^{-3}) illustrated by the dotted line in Figure 5.36. Curve A corresponds most closely to the complete ionization case and involves a 'hole' lifetime τ_h less than the dielectric relaxation time. In case A, a stable flat topped domain analogous to those discussed in section 5.6, is formed and propagates uniformly along the sample. However, the growth rate is considerably smaller than for the complete ionization limit and the space-charge formation around the perturbation notch is retarded. Cases B, C, and D, in which both the electron and hole lifetimes are much longer than the dielectric relaxation time, are characterized by the non-uniform propagation of an accumulation layer instability. In these cases, the perturbation notch has no apparent effect on the system, and domain like solutions do not occur. The linear analysis of section 5.4 allows us to calculate v_1 the velocity of propagation of the space-charge mode in the limit of small signals. We find that v_1 increases in the order IB, IA, IC, ID for the cases given in Table 5.2, where in each case v_1 is just less than $v_o(=v(F_o))$. Inspection of the initial motion of the accumulation layer instabilities shows that this is indeed the case. Similarly the effective diffusion coefficient D_1 for the space-charge mode is found to be enhanced the most for case IB($D_1 \approx 1.5D$) and least for case IC ($D_1 \approx D$). The enhancement of diffusion is seen most clearly as a smearing of the field distribution. The behaviour of the total current is shown in Figure 5.37.

Figure 5.38 shows the field distributions after an elapsed time of 10^{-11} seconds for bias fields in the range $F_c < F_o < F_r$ (cases II, III of Table 5.2).
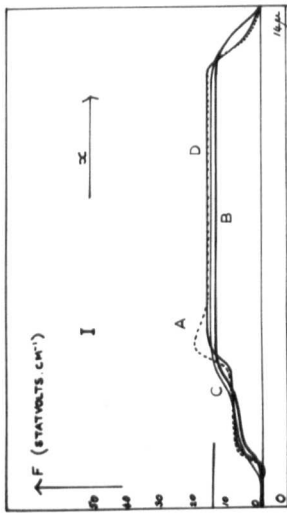
FIG 5.40
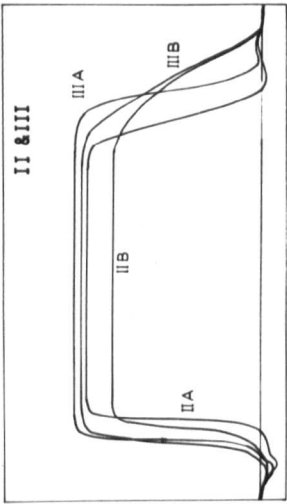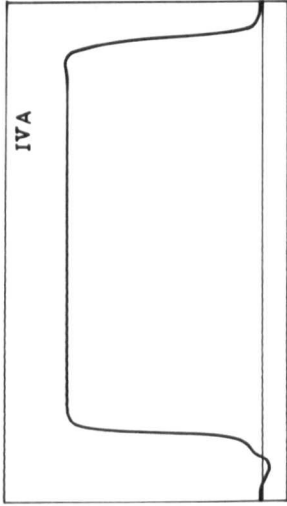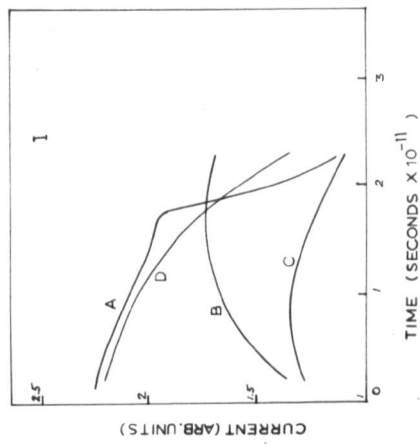
FIG 5.38
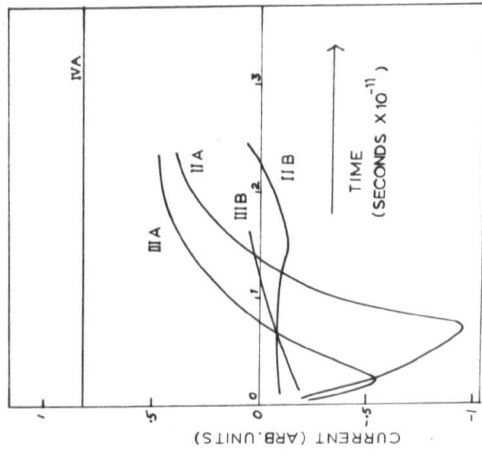
FIG 5.39

FIG 5.36

FIG 5.37

The time evolution of the total current is shown in Figure 5.39. In all three cases shown the initial negative resistance state is rejected and the overall time evolution is similar to the complete ionization limit of section 5.6. The major difference is the lack of space-charge growth in the vicinity of the perturbation notch.

Case IV involves $F_o > F_r$ and we find a stable field distribution analogous to those predicted by the phase-plane analysis in the complete ionization limit. Figure 5.40 shows the steady-state field distribution reached for the bias field $F_o = 60$ stat volts/cm.

The most surprising feature of these general calculations is the lack of influence of the perturbation notch. Apart from case IA, which shows a retardation of space-charge formation not predicted by the growth rate term of the small signal dispersion relation, no space-charge growth is detectable, and domain nucleation does not occur, although if space-charge does form at the notch the small signal analysis predicts that it will grow for bias fields between the threshold and valley fields. On the other hand the accumulation layer instabilities have the general features predicted by the small signal theory. The probable answer to this problem lies with the dispersion relation $\omega(k)$ which controls the linear part of the growth of small perturbations. We first observe that domain nucleation generally requires the presence of a depletion-layer, usually found at the perturbation notch. The form of the perturbation notch makes it impossible for an accumulation layer to form there without an associated depletion layer. We therefore interpret the numerical results by supposing that some process is operative which suppresses the nucleation and growth of a depletion layer at the notch. We have already seen (section 5.4) that the terms in k^o, k^1, k^2 of $\omega(k)$ for the space-charge mode give the growth rate, velocity and spread of a small space-charge perturbation as functions of the electron and 'hole' lifetimes. In the complete ionization limit these three

terms complete the dispersion relation, but in the general case terms in k occur up to infinite order. These higher order terms control the symmetry of the space-charge perturbation. For the short wavelength perturbation at the notch k is large and the higher order terms in k^3 etc. may be important. We suspect then that the higher order terms in $\omega(k)$ act to suppress the growth of large k depletion layers and that space-charge formation at the notch is prohibited. Some evidence for the suppression of the depletion layers may be seen in Figures 5.36, 5.38 where the depletion layers near the anode ($x \simeq \ell$) are considerably smeared out compared with the accumulation layers in the vicinity of the cathode. There is clearly considerable scope for further investigation of the higher order terms in the dispersion relations.

5.10   Conclusions

The calculations described in Chapter IV have demonstrated that the local conductivity can become negative, for a certain range of electric fields, provided that carrier injection occurs close to a multiple optical phonon energy. The phase-plane analysis applied to the problem of the form of static field distributions in a sample with ordinary contacts does not rule out the possibility of bulk negative conductivity under d.c. conditions although the possibility appears doubtful. Such a phenomenon would involve energy flow from the radiation to the field. However, the small signal theory shows that the system is unstable against space-charge formation over the negative slope region of the velocity-field characteristic (for positive and negative velocities) and the recombination does not stabilize the process. Numerical calculations for the time development of the field in a sample showing oscillatory conductivity confirm these findings. Instabilities, analogous to the high field domains in the Gunn effect, occur for bias fields on the negative slope regions of the velocity-field characteristic, and if ordinary contacts are used the negative resistance state is rejected. Small

signal analysis suggests that for uniform bias fields on the positive slope, negative velocity region of the velocity-field characteristic the system is stable agains local space charge formation. However, when contacts are included, the numerical calculations show that the field non uniformity near the contacts, if ordinary contacts are used, leads to a rejection of this negative resistance state. Instead a stable non-uniform field distribution is reached and the sample supports bulk positive resistance.

We conclude that bulk negative conductivity cannot be observed under d.c. conditions if ordinary contacts are used. Instead stable non-uniform fields are set up in the sample which lead to bulk positive resistance, although for small regions in the sample the electronic drift current is negative. In these latter regions the electronic diffusion currents reach sufficient proportions to maintain a total positive current. For a certain range of bias fields, between the threshold and valley vield strengths, the samples do not admit static field distributions and positive current oscillations occur. The oscillations have a frequency which is roughly the reciprocal of the domain transit times when the domain instabilities occur. The transit velocity is of the order of the drift velocity at the threshold field, and for a 1200 micron sample the transit time would be of the order of 10^{-4} to 10^{-5} seconds. The oscillations are therefore expected to be outside the microwave region.

These conclusions are consistent with the experimental observations that bulk negative resistance does not occur in the oscillatory photoconductivity effect. The current oscillations predicted by our analysis are of small amplitude and would be only apparent experimentally as enhanced noise in the 0.01 to 0.1 Megacycles range.

CHAPTER VI
────────

DISCUSSION
─────────

6.1 Introduction
     ────────────

Earlier chapters have outlined some of the origins and consequences of non-
equilibrium distributions of carriers which can arise in semiconductors under photo-
illumination at low temperatures.   In this chapter we discuss some of the problems
raised by our work and make suggestions for future research in these areas.   The
discussion is divided into two parts dealing with the general photoexcited hot
electron phenomena (section 2) and instabilities and non-linear problems
(section 3).   We also include a brief discussion of relevant experimental findings
which were not available during the completion of this work.

6.2 Hot electron phenomena
     ──────────────────────

The major result of this thesis is that hot carrier distributions will occur
in semiconductors provided the mean photoexcitation energy exceeds the mean thermal
equilibrium energy and the carrier lifetime is sufficiently short compared to
the thermalization time.   In the absence of external fields the heated steady-
state distribution function is markedly different from the equilibrium form and
reflects the general form of the excitation spectrum.   A broad excitation spectrum
leads to a dispersed population of carriers over a wide range of momentum states,
generally characterised by an increase in the mean carrier energy from the
equilibrium value.   The dispersed nature of the distribution function in turn
leads to a linear response to weak applied fields.   This Ohmic behaviour means
that the isotropic part of the finite-field distribution function is very nearly
the zero field distribution function.   Transport and trapping parameters deviate
from those expected for closely thermalised carriers: a consequence of averaging

over a non-equilibrium distribution function. Narrow spectrum photoexcitation gives rise to a population of carriers closely localized to a constant energy surface in momentum space under carrier heating conditions. The behaviour with respect to applied electric fields is more complicated here and is critically dependent on the mean carrier energy and the threshold character of the optical phonon scattering. Under appropriate conditions the low field response is highly non-linear and the semiconductor exhibits negative resistance.

The problem of the observed cut-off to the recombination lifetime and capture cross section for carriers in germanium and silicon is re-emphasised by the failure of the hot-electron model to explain all the experimental data. Resolution of this problem is clearly of importance. A discussion of an alternative approach to the problem was given in Chapter II in terms of photo-excitation into more than one valley (for silicon). This behaviour is unlikely for photoexcited holes in germanium, but the sparsity of experimental data does not allow confirmation of the predicted cut-offs due to carrier heating. However, a recent experiment reported by Yariv et al (1968) may be of relevance. The experiment involved measurements of the recombination lifetime of photoexcited holes in compensated germanium (mercury doped with $N_D = 1.9 \times 10^{14}$ cm^{-3}, $N_A = 5.4 \times 10^{15}$ cm^{-3}) as a function of electric field strength (from 2 to 1000 V/cm) at low temperatures (from 5°K to 32°K). Photoexcitation was monoenergetic and effected by a 10.6 micron laser source. The low field recombination lifetimes were deduced from photo-Hall measurements of the carrier concentration, so if heating occurred we might expect a Hall number anomaly. Two results are of interest. The low field (less than 10 V/cm) measurements show an approximately $T^{\frac{1}{2}}$ dependence for the recombination lifetime at low temperatures, with the kinked appearance reminiscent of the Hall number anomaly discussed in Chapter III. Secondly, the Hall mobility and recombination lifetime are field independent up to 10V/cm, beyond which there is strong evidence of electric field induced heating. This

result supports the Monte Carlo calculations of Chapter II which suggests that
field effects are not important up to at least 1 V/cm. It would be useful
if further theoretical calculations on the lines of Chapter II were carried out
for this experiment, taking account of the monoenergetic radiation source.
Certainly the hot carrier model would appear appropriate: the measured
recombination lifetimes are sufficiently short for photo-heating to have
occurred. Further experiments, similar to Yariv et al (1968), would be of
interest, particularly if the mobility as well as the recombination lifetime
can be measured as functions of temperature. This would allow definite observa-
tion of carrier heating if it occurs.

Further theoretical work on the photoexcited hot carrier problem in
germanium and silicon would not be justified until more experimental data on
carrier heating effects is forthcoming. In particular it would be of interest
to see future experimental work specifically aimed at detecting the anomalies in
Hall number and magnetoresistance number. There remains considerable scope for
widening the theoretical investigation of Chapter II to take into account:

(a) non-spherical energy surfaces;

(b) contributions to electron-phonon scattering from both the transverse
    and longitudinal mode phonons (a consequence of (a));

(c) intervalley scattering;

(d) multiple band structure (e.g. the excitation of holes into the heavy and
    light hole bands in germanium);

(e) different excitation spectra;

(f) excitation into more than one valley;

(g) the effects of non-equilibrium phonon distributions;

(h) high electric field effects;

(i) high magnetic field effects;

(j) high light intensities (this would give large electron concentrations and

and lead to consideration of intercarrier scattering and free carrier absorption).

The latter proposition (j) could be usefully extended to the experimental problem of measuring carrier distribution functions by light scattering. This technique was suggested by Mooradian (1968) and a feasibility study was reported recently by Healey and McLean (1969) in connection with distribution functions in gallium arsenide. If this technique proves possible it should be feasible to directly confirm the non-Maxwellian form predicted for the distribution functions in germanium and silicon.

There have been several recent experimental measurements of oscillatory photoconductivity (a list of references in given by Mears et al. 1968). In particular Mears et al report observations of two distinct oscillatory series in n-type cadmium telluride. These are attributed to the presence of two alternative capture processes at shallow donor sites. One series can be accounted for by the mechanism discussed in Chapter IV, the other is accounted for by direct capture into the shallow donors involving optical phonon emission.

Mears and Stradling (private communication 1968) have also found evidence of a non-linear photocurrent-voltage characteristic for monoenergetic excitation in CdTe at 4.2°K at injection energies close to a multiple optical phonon energy. These results are very similar to the current-voltage characteristics expected when the non-linear drift-velocity field characteristic does not show the regions of negative mobility (the current-voltage relation then scales with the velocity-field characteristic). Negative photocurrents were not observed.

Further experimental work involving high intensity strongly monochromatic photoexcitation would be of value in understanding the physics of the oscillatory photoconductivity problem for injection energies close to a multiple number of

optical phonon energies. These experiments would ideally involve accurate measurement of photocurrent-voltage characteristics coupled with noise spectrum analysis to detect the predicted instability phenomena. It is desirable to minimize the number of background thermal carriers in these experiments: this could be achieved by suitable doping and operating at very low temperatures.

The general theory of oscillatory photoconductivity (Chapter IV) is in good agreement with experiment, but several problems remain to be resolved. These include: (a) a determination of the diffusion coefficient as a function of electric field strength. Monte Carlo techniques would be appropriate here;

(b) the influence of background thermalised carriers on the stability of the system;

(c) the effects of non-equilibrium phonon distributions;

(d) the effects of multiple trapping levels;

(e) the influence of magnetic fields on the distribution functions;

(f) the effect of the non-parabolic energy bands in the III-V compounds.

The theoretical discussion given in Chapter VI gives reasons why the spectral response does not show negative photocurrents, although these are predicted by the uniform field analysis of Chapter V. It would be useful if theoretical calculations, based on non-uniform field distributions, could be extended to allow quantitative comparison with experiment in the vicinity of the minima in the spectral response oscillations. A discussion of the theoretical problems to be resolved in this context is given in the following section.

6.3 Non-linear problems and instabilities

One of the most interesting features of the oscillatory photoconductivity calculations is the prediction of highly non-linear drift velocity-field characteristics showing regions of negative mobility under appropriate conditions

at low field strengths. The usual assumption of a uniform electric field distribution in the semiconductor breaks down when the sample is biased into the negative mobility regions. This seriously complicates the microscopic calculations of transport parameters and carrier distribution functions. A complete analysis would necessarily include the spatial dependence of the field and carrier distribution function. The relevant equation is Boltzmann's equation coupled through the field to Poisson's equation. For steady-state calculations the total photoexcitation rate balances the recombination rate so that the spatially dependent background density of positive charge can be eliminated from the equations. However the problem of stability necessitates the introduction of the full time dependent Boltzmann equation and the rate equation for the background density of positive charge. A further complication is the need to specify boundary conditions appropriate to the external circuit conditions and the contacts. Such a theoretical programme would seem impossible at present by analytical or numerical methods. The alternative is the phenomeno-logical approach used in Chapter V. The phenomenological equations involve averaging the Boltzmann equation over momentum space to obtain the continuity equations for electrons and the background density of positive charge. For example the electronic equation is

$$\frac{\partial n}{\partial t} = G - R - \nabla \cdot (n\underline{v})$$

where n is the carrier density, R and G are the net recombination and generation rates and $\underline{v}$ is the average electron velocity. All four quantities are functions of space and time and through Poisson's equation of electric field. It is normal practice to divide the electron velocity into a drift component involving the electric field and an electronic diffusion component which vanishes for uniform fields involving the spatial gradient of the electron density:

$$\underline{v} \equiv \underline{v}_{drift} + \underline{v}_{diffusion}$$

This decomposition is really only meaningful for small departures from local thermal

equilibrium. In the latter case v_{drift} represents the coherent motion of electrons induced by the electric field, whilst $v_{diffusion}$ is related to the random "thermal" motion. Suitable forms for v_{drift} and $v_{diffusion}$, based on separate calculations, must be found before the phenomenological equations can be used. The one dimensional analysis of Chapter V uses the static velocity-field characteristic for v_{drift}, the space and time dependence then entering implicitly through the dependence on field.

The electronic diffusion current $env_{diffusion}$ has an important influence both for the existence and stability of the steady-state field distributions and for the growth and propagation of instabilities. The precise form for this term is unknown for the oscillatory photoconductivity problem. The analysis of Chapter V involves a diffusion current proportional to $D \frac{\partial n}{\partial x} (x,t)$, where D, the diffusion coefficient is a constant independent of field. This constant is unknown for the problem and the numerical calculations of Chapter V are based on a choice of D appropriate to high temperature thermalised electrons. This simple form can be precisely justified for small departures from local equilibrium. In which case D is given by the Einstein relation (Kubo 1965) in terms of the electron temperature and drift mobility. The exact form for the general non-equilibrium problem can only be obtained by averaging over the Boltzmann equation. It would involve knowledge of the detailed form of the spatially dependent carrier distribution function. The strong field dependence of the distribution function suggests a similar strong field dependence in the diffusion current. A reasonable approximation would be to retain the simple form for the diffusion current but allow D to be field dependent. Fawcett and Rees (1969) have recently made Monte Carlo calculations for the field dependence of the diffusion coefficient for electrons in gallium arsenide at high field strengths. Similar calculations appropriate to the oscillatory photoconductivity problem would clearly be of value. There is considerable scope for research into the general problem of diffusion in systems very far from thermal equilibrium.

Classification of the possible steady-state field distributions by analysing the basic non-linear phenomenological equations in the phase-plane $(F, \partial F/\partial x)$ is a useful technique for one-dimensional systems, but does not supply criteria for the stability of such states. Small signal analysis is restricted to uniform field distributions in long samples and does not give stability criteria for the non-uniform field distributions which occur in practice. Only a full time-dependent solution of the basic equations, necessarily by numerical techniques, can explore the problem of stability. There is considerable need for an extension of the phase-plane technique to higher dimensions. For example, it would be useful if the integral curves of the full time dependent problem could be studied in the phase space $(F, \partial F/\partial x, \partial F/\partial t)$. This problem can be made autonomous in the variables x and t if the effects of contacts are replaced by suitable boundary conditions. The resultant topology would ideally indicate the existence or otherwise of stable steady-states asymptotic to points along the $\frac{\partial F}{\partial t} = 0$ axis. However, this extension of non-linear analysis is fraught with difficulties and is at present unexplored. Theoretical research in this area must however be one of the growing points of Physics if the present day difficulties with the wide range of non-linear problems are to be overcome.

It was shown in Chapter V that the phase-plane analysis is also useful in discussing stable uniformly propagating instabilities of the domain or non-linear wave category. The comments there on the interpretation of the stable high field domains can be amplified by a recent analysis of the Gunn effect problem due to Rowlands (private communication 1969). Rowlands has shown by an exact analysis based on a Liapunov function technique (see Minorsky 1962) that the trajectories around the singularity F_2 in the $(F, \partial F/\partial y)$ phase-plane are closed curves. This implies that F_2 is exactly a centre. The result is valid only if the diffusion coefficient is a constant independent of field. The analysis applies equally well to the oscillatory photoconductivity problem and we must

therefore interpret the domain solutions for the two problems as closed trajectories passing through the saddle point singularity at F_1. A further class of solutions is thereby admitted. These are the finite period uniformly propagating non-linear waves, represented by the set of closed trajectories around F_2. These are not observed in the numerical experiments and are probably unstable. Further investigation of the stability of such phenomena is clearly warranted.

As yet no experimental evidence for the occurrence of instabilities in the oscillatory photoconductivity problem has been forthcoming. Detailed work in this area is required. A possible line of attack is through analysis of the current noise measured in the spectral response experiments. This would involve examination of both the a.c. and d.c. components of the photocurrent. Such investigations, coupled with further theoretical work on the lines indicated above, would be of advantage to the general problem of instabilities in semi-conductors. In particular the role of recombination processes in influencing the growth of instabilities in both the linear and non-linear regimes is of considerable interest.

REFERENCES

(1) Alba, de E., and Das, A. ., 1968, Revista Mexicana de Fisica, 17, 235.

(2) Ascarelli, G., and Rodriguez, S., 1961, Phys.Rev., 124, 1321.

(3) Barker, J. R., 1967, M.Sc. dissertation, University of Durham, unpublished.

(4) Barker, J. R., and Hearn, C. J., 1968, Phys.Lett., 26A, 148.

(5) Barker, J. R., and Hearn, C. J., 1969a, Phys.Lett., 29A, 215.

(6) Barker, J. R., and Hearn, C. J., 1969b, J.Phys.C, 2, 2128.

(7) Barker, J. R., and Hearn, C. J., 1969c, Proceedings of Conference on
    Computational Physics, Culham Report, in the press.

(8) Barker, J. R., and Hearn, C. J., 1969, J.Phys.C, in the press.

(9) Betjemann, A. G., 1965, Proc.Phys.Soc., 85, 149.

(10) Blunt, R. F., 1958, Bull.Am.Phys.Soc. 3, 115.

(11) Boardman, A. D., Fawcett, W., and Rees, H. D., 1968, Solid State Comm.,
     6, 305.

(12) Brooks, H., 1955, Advanc.Electron., 7, 87.

(13) Brown, R. A., 1964, Bull.Am.Phys.Soc., 9, 62.

(14) Brown, R. A., 1966, Phys.Rev., 148, 974.

(15) Brown, R. A., and Rodriguez, S., 1967, Phys.Rev., 153, 890.

(16) Butcher, P. N., and Fawcett, W., 1966, Phys.Lett., 21, 489.

(17) Butcher, P. N., 1967, Rep.Prog.Phys., 30, Part 1, 97.

(18) Conwell, E. M., and Vassell, M. O., 1966, Phys.Lett., 21, 612.

(19) Conwell, E. M., 1967, Solid State Physics, Supplement 9, "High Field
     Transport in Semiconductors", Academic Press.

(20) Dyson, F. J., 1949, Phys.Rev., 75, 486.

(21) Ehrenreich, H., 1957, J.Phys.Chem.Solids, 2, 131.

(22) Elesin, V. F., and Manykin, E. A., 1966, Sov.Phys - JETP, 23, 917.

(23) Engeler, W. E., Levinstein, H., and Stannard Jr., C. R., 1961a, J.Phys.
     Chem.Solids, 22, 249.

(24) Engeler, W. E., Levinstein, H., and Stannard Jr., C. R., 1961b, Phys.
     Rev.Lett., 7, 62.

(25) Erginsoy, C., 1950, Phys.Rev., 79, 1013.

(26) Fawcett, W., and Rees, H. D., 1969, Phys.Lett., 29A, 578.

(27) Gaylord, T. K., 1968, IEEE Trans.Elec.Devices, ED-15, 777.

(28) Gunn, J. B., 1963, Sol.State Comm., 1, 88.

(29) Habeggar, M. A., and Fan, H. Y., 1964, Phys.Rev.Lett., 12, 99.

(30) Hamann, D. R., and McWhorter, A. L., 1964, Phys.Rev., 134A, 250.

(31) Harrison, W. A., 1956, Phys.Rev., 104, 1281.

(32) Healey, D., and McLean, T. P., 1969, Phys.Lett., 29A, 607.

(33) Hearn, C. J., Landsberg, P. T., and Beattie, A. R., 1962, Proc.Int.
        Conf. Semiconductor Physics, Exeter, 1962, (London: IPPS), 857.

(34) Hearn, C. J., 1965, Proc.Phys.Soc., 86, 881.

(35) Hearn, C. J., 1966, Phys.Lett., 20, 113.

(36) Hearn, C. J., 1966, Proc.Phys.Soc., 88, 407.

(37) Herring, C., 1955, Advanc.Electron., 7, 87.

(38) Hilsum, C., 1962, Proc.Inst.Radio Engrs., N.Y., 50, 185.

(39) Kane, E. O., (1957), J.Phys.Chem.Solids, 1, 249.

(40) Knight, B. W., and Peterson, G. A., 1967, Phys.Rev., 155, 393.

(41) Koenig, S. N., 1958, Phys.Rev., 110, 988.

(42) Kroemer, H., 1964, Proc.IEEE, 52, 1736.

(43) Kroemer, H., 1966, Trans.IEEE, ED-13, 27.

(44) Kubo, R., (1966), Rep.Prog.Phys.29, Part 1, 255.

(45) Kurosawa, T., 1966, Proc.Int.Conf.Phys.Semiconductors, Kyoto, J.Phys.Soc.
        Japan, (Supplement), 21, 424.

(46) Lawaetz, P., 1968, Phys.Rev., 174, 867.

(47) Lax, M., 1960, Phys.Rev., 119, 1502.

(48) Levitt, R., and Honig, A., 1960, Phys.Rev.Lett. 5, 93.

(49) Levitt, R., and Honig, A., 1961, J.Phys.Chem.Solids, 22, 269.

(50) Loewenstein, M., and Honig, A., 1966, Phys.Rev., 144, 781.

(51) Mattis, D. C., 1960, Phys.Rev., 120, 52.

(52) Meyer, H. J. G., 1958, Phys.Rev., 112, 298.

(53) McCumber, D. E., and Chynoweth, A. G., 1966, Trans.IEEE, ED-13, 4.

(54) Mears, A. L., Spray, A. R. L., and Stradling, R. A., 1968, J.Phys.C, $\underline{1}$, 1412.

(55) Minorsky, N., 1962, "Non linear oscillations", (D. Van Nostrand Company Inc.)

(56) Mooradian, A., 1968, Int.Conf.on Light Scattering in Solids, New York (1968), in the press.

(57) Nasledov, D. N., Popov, Yu. G., and Smetanikova, Yu.S., 1965, Soviet Phys. Solid State $\underline{6}$, 2989.

(58) Paige, E. G. S., 1964, Prog.in Semiconductors, $\underline{8}$.

(59) Pinson, W. E., and Bray, R., 1964, Phys.Rev., $\underline{136A}$, 1449.

(60) Reik, H. G., and Risken, H., 1962, Phys.Rev., $\underline{126}$, 1737.

(61) Ridley, B. K., and Watkins, T. B., 1961, Proc.Phys.Soc., $\underline{78}$, 293.

(62) Rollin, B. V., and Rowell, J. M., 1960, Proc.Phys.Soc., $\underline{76}$, 1001.

(63) Rowlands, G., 1969, private communication.

(64) Shockley, W., 1949, Bell Sys.Tech.J., $\underline{28}$, 435.

(65) Snockley, W., and Bardeen, J., 1950, Phys.Rev., $\underline{80}$, 72.

(66) Shockley, W., 1954, Bell Sys.Tech.J., $\underline{33}$, 799.

(67) Smith, R. A., 1960, "Semiconductors", Cambridge Univ. Press

(68) Stocker, H. J., Stannard, Jr., C. R., Kaplan, H., and Levinstein, H., 1964, Phys.Rev.Lett., $\underline{12}$, 163.

(69) Stocker, H. J., Levinstein, H., and Stannard, Jr., C. R., 1966, Phys.Rev., 150, 613.

(70) Stocker, H. J., and Kaplan, H., 1966, Phys.Rev., $\underline{150}$, 619.

(71) Stocker, H. J., 1967, Phys.Rev. Lett., $\underline{18}$, 1197.

(72) Tyler, W. W., 1959, J.Phys.Chem.Solids, $\underline{8}$, 59.

(73) Von Neumann, J., 1951, Nat.Bureau of Standards App.Maths, Ser., $\underline{12}$, 36.

(74) Weinreich, G., Sanders, Jr., T. M., and White, H. G., Phys.Rev., $\underline{114}$, 33.

(75) Yariv, A., Buczek, C., and Picus, G. S., Proc.Int.Conf.on Phys.Semiconductors, Moscow 1968, Vol 1, 500, (Publishing House Nauka: Leningrad 1968).

(76) Ziman, J. M., 1960, "Electrons and Phonons", (Oxford Univ.Press).

APPENDIX 2.1

THE CARRIER SCATTERING RATE

We give here formulae for the inelastic scattering rate $J(\underline{k})$ appropriate to non-degenerate electron scattering by acoustic and non-polar optical phonons when the distribution function $f(\underline{k})$ is a function of energy only. These scattering processes have been discussed considerably in the literature and for details we refer to recent review articles by Reik and Risken (1962), Paige (1964), Conwell (1967).

The rate of change of $f(\underline{k})$ with time due to scattering may be written

$$\frac{\partial f}{\partial t}(\underline{k}) = -J(\underline{k}) = \sum_{\underline{k}'} \{K(\underline{k}',\underline{k})f(\underline{k}')(1-f(\underline{k}))$$

$$-K(\underline{k},\underline{k}')\,f(\underline{k})(1-f(\underline{k}'))\} \tag{1}$$

where $K(\underline{k},\underline{k}')$ is the transition probability per unit time for an electron in momentum state $|\underline{k}>$ (with probability $f(\underline{k})$) scattering into an empty state $|\underline{k}'>$ (with probability $(1-f(\underline{k}'))$. For a non-degenerate semiconductor we can ignore the restrictions due to the Pauli principle since $f(\underline{k}) \ll 1$ and approximate $(1-f)$ by unity. A similar interpretation holds for $K(\underline{k}',\,\underline{k})$. In thermal equilibrium $f(\underline{k})$ is given by the Maxwell-Boltzmann distribution and is proportional to $\exp(-\varepsilon/k_B T)$, where ε is the carrier energy. Furthermore, in equilibrium the total scattering rate vanishes identically and the principle of detailed balance gives

$$K(\underline{k}',\underline{k})\,\exp(-\varepsilon'/k_B T) = K(\underline{k},\underline{k}')\,\exp(-\varepsilon/k_B T). \tag{2}$$

This result suggests that we define a new kernel $G(\underline{k},\underline{k}')$, symmetric in $\underline{k},\underline{k}'$, by

$$G(\underline{k},\underline{k}') = K(\underline{k},\underline{k}')\,\exp(-\varepsilon/k_B T) \tag{3}$$

The scattering rate (1) has then the symmetric form

$$J(\underline{k}) = - \sum_{\underline{k}'} G(\underline{k},\underline{k}')\{f(\underline{k}')\exp(\epsilon'/k_B T) - f(\underline{k})\exp(\epsilon/k_B T)\}, \qquad (4)$$

from which we immediately deduce the sum rule

$$\sum_{\underline{k}} J(\underline{k}) = 0 \qquad (5)$$

Referrring to acoustic and optical phonons by the suffices 1 and 2 respectively we can decompose J as $J_1 + J_2$ and set

$$K(\underline{k},\underline{k}') \equiv \sum_{p=1}^{2} K_p(\underline{k},\underline{k}') \; ; \; K(\underline{k}',\underline{k}) \equiv \sum_{p=1}^{2} K_p(\underline{k}',\underline{k}) \; . \qquad (6)$$

The transition rates K_p are calculated from the matrix elements of the electron plus phonon states with respect to the electron-phonon interaction Hamiltonian H_p on the basis of first order time dependent perturbation theory (only single phonon processes are considered). For example, we find

$$K_p(\underline{k}',\underline{k}) = \sum_{\underline{q}} \frac{2\pi}{\hbar} \left\{ |<\underline{k}',N_{\underline{q}p}|H_p|\underline{k},N_{\underline{q}p}+1>|^2 \right.$$

$$\times \delta(\epsilon'-\epsilon-\hbar\omega_{\underline{q}p})$$

$$+ |<\underline{k}', N_{\underline{q}p}|H_p|\underline{k}, N_{\underline{q}p} - 1>|^2$$

$$\left. \times \delta(\epsilon'-\epsilon+\hbar\omega_{\underline{q}p}) \right\}, \qquad (7)$$

where $\hbar\omega_{\underline{q}p}$ is the energy of a phonon of type p with wavevector $\underline{q}$.
The state vector $|\underline{k}, N_{\underline{q}p}>$ describes an electron with wavevector $\underline{k}$ and $N_{\underline{q}p}$ phonons with wavevector $\underline{q}$. The first term in (7) represents scattering with the emission of a phonon, whilst the second term involves phonon absorption. A similar expression holds for $K_p(\underline{k},\underline{k}')$. We choose forms for the H_p appropriate to the deformation potential approach to the electron-phonon interaction. For acoustic phonons this involves the approximation that H_1 is locally equivalent to the

energy shift in the band edge produced by a homogeneous strain equal in magnitude to the local strain induced by the lattice vibration (Shockley 1951). A similar concept applies for optical phonons (Shockley 1951, Harrison 1956, Meyer 1958) for which one can define an optical strain in terms of the relative displacement of the sublattices within a unit cell. The matrix elements for both types of scattering can be written in the same form, for example,

$$
\left| \langle \underline{k}', N_{\underline{q}p} | H_p | \underline{k}, N_{\underline{q}p} + 1 \rangle \right|^2
$$

$$
= \frac{D_p^2 \, \hbar \omega_{\underline{q}p}}{2 \rho s^2} \left(N_{\underline{q}p} + 1 \right) \delta_{\underline{k}', \underline{k} + \underline{q}} , \tag{8}
$$

where D_p is the effective deformation potential, ρ is the density of the crystal and s is the longitudinal longwave velocity of sound. We assume here that we have spherical constant energy surfaces for which symmetry considerations eliminate a contribution from the transverse phonon modes. In our approximation the phonons are considered to be in thermal equilibrium for which $N_{\underline{q}p}$ is given by the Bose-Einstein distribution,

$$
N_{\underline{q}p} \equiv \left[\exp(\hbar \omega_{\underline{q}p} / k_B T) - 1 \right]^{-1} \tag{9}
$$

For acoustic phonons, we are largely concerned with long wavelength (small q) phonons which have the linear dispersion relation

$$
\omega_{\underline{q}} 1 = s \, |q|, \tag{10}
$$

whereas for optical phonons we assume the 'flat' dispersion relation (a good approximation for germanium and silicon)

$$
\omega_{\underline{q}} 2 = \omega_o = \text{constant.} \tag{11}
$$

With these considerations in mind we can readily evaluate J_1 and J_2. In terms of the dimensionless variable $K \equiv (\epsilon / k_B T)^{\frac{1}{2}}$ we find for J_1,

$$J_1(K) = -\frac{D_o}{K}\left\{\int_a^b - \int_c^d\right\}\frac{K'(K^2 - K'^2)^2 f(K')dK'}{1 - \exp(K^2 - K'^2)}$$

$$+ f(K)\frac{D_o}{K}\left\{\int_a^b - \int_c^d\right\}\frac{K'(K^2 - K'^2)dK'}{\exp(K'^2 - K^2)-1} \tag{12}$$

where

$$D_o \equiv \frac{2^{-3/2}(k_B T)^{5/2}m^{*\frac{1}{2}} D_1^2}{(\hbar s)^4 \rho} . \tag{13}$$

The ranges of integration are defined as follows,

$$\left.\begin{array}{ll}
a = K & (K \geq K_\alpha/2) \\
\quad = K_\alpha - K & (K \leq K_\alpha/2) \quad ; \\
b = K_\alpha + K & ; \\
c = K & (K \leq K_\alpha/2) \\
\quad = K_\alpha - K & (K_\alpha/2 \leq K \leq K) \\
\quad = K - K_\alpha & (K \geq K_\alpha) \quad ; \\
d = K & ;
\end{array}\right\} \tag{14}$$

where $K_\alpha \equiv (\varepsilon_\alpha/k_B T)^{\frac{1}{2}} \equiv (2m^*s^2/k_B T)^{\frac{1}{2}}$.

The expression for J_2 is

$$J_2(K) = \left(\frac{D_2^2 m^{*3/2} \hbar\omega_o}{2^{\frac{1}{2}}\pi\hbar^4 s^2 \rho}\right)\left(e^M - 1\right)^{-1}(k_B T)^{\frac{1}{2}}\times$$

$$\left(K^+\{e^M f(K^+) - f(K)\} + \theta(K^-)K^-\{f(K^-) - e^M f(K)\}\right) \tag{15}$$

where

$$M \equiv \hbar\omega_o/k_B T, \quad K^\pm \equiv (K^2 \pm M)^{\frac{1}{2}}, \text{ and}$$

$$\theta(K^-) = 0 \text{ for } K^- < 0, = 1 \text{ for } K^- > 0.$$

APPENDIX 2.2

THE MODEL EXCITATION SPECTRUM

We assume that a single electron is excited into the band for each photon absorbed from the applied radiation by the neutral donors. In such a case, the rate of generation of carriers by a flux of photons of energy $\hbar\omega$ is proportional to the concentration of neutral donors, the photoionization cross section (possibly energy dependent) and the intensity of radiation. In our problem the ionization energy E_i for the donors is small, typically $E_i \lesssim 0.05$ eV. We therefore require extrinsic radiation with a significant distribution of photons with energies in excess of E_i. In principle an unlimited set of radiation fields may be devised to satisfy this criterion. For convenience, we adopt a radiation field approximating to black body radiation from a high temperature ($\sim 300^\circ$K) source. For black body radiation the number of photons dn in the energy range ($\hbar\omega$, $\hbar\omega + d\hbar\omega$) is of the Planck form,

$$dn \propto (\hbar\omega)^2 d\hbar\omega \left\{\exp(\hbar\omega/k_B T_r) - 1\right\}^{-1}, \tag{1}$$

where T_r is the radiation temperature. Room temperature radiation corresponds, in the main to infra-red radiation peaked in the wavelength distribution of energy at about 10 microns, or in terms of energy at about 0.13 eV. The maximum number of photons in such radiation occurs for photon energies of about 0.04 eV.

If a photon of energy $\hbar\omega$ excites an electron into the band with energy ε we have from energy conservation:

$$\varepsilon + E_i = \hbar\omega. \tag{2}$$

A strict inequality does not hold since phonons must also participate to conserve crystal momentum. Following absorption of a photon at a donor, the probability per unit time for an electron to make a transition into the band with energy in

the range $(\epsilon, \epsilon + d\epsilon)$ is, from perturbation theory,

$$\frac{2\pi}{\hbar} |M|^2 g(\epsilon) , \tag{3}$$

where $g(\epsilon)$ is the density of final energy states and M is the matrix element for the transition. For the conduction band states $g(\epsilon)$ is proportional to $\epsilon^{\frac{1}{2}}$. Only photons with energies in the range $(\epsilon + E_i, \epsilon + E_i + d\epsilon)$ may excite electrons into the band with energies in the range $(\epsilon, \epsilon + d\epsilon)$. The number of photons in this range, which are absorbed is proportional to dn. The excitation rate into $(\epsilon, \epsilon + d\epsilon)$ is therefore proportional to

$$dn \, |M|^2 \, g(\epsilon) \, \alpha(\hbar\omega) ,$$

where $\alpha(\hbar\omega)$ is the probability that a correct photon is absorbed. But this rate is just equal to

$$W \, \omega_e(\underline{k}) \, g(\epsilon)d\epsilon$$

where W, ω_e are defined in Chapter II. We find therefore

$$W \, \omega_e \, g(\epsilon)d\epsilon \propto \frac{(\hbar\omega)^2 \, |M|^2 \, g(\epsilon) \, \alpha(\hbar\omega) \, d(\hbar\omega)}{\exp(\hbar\omega/k_B T_r) - 1} . \tag{4}$$

From (2) we find $d\epsilon = d(\hbar\omega)$, and substituting for $\hbar\omega$ in (4) we have

$$W \, \omega_e \propto \frac{(\epsilon + E_i)^2 \, |M|^2 \, \alpha(\epsilon + E_i)}{\exp\left[\dfrac{\epsilon + E_i}{k_B T_r}\right] - 1} . \tag{5}$$

For room temperature radiation, $k_B T_r \sim 0.025$ eV and $E_i/k_B T_r \sim 2$, so that we can make the approximation

$$W \, \omega_e \propto (\epsilon + E_i)^2 \, |M|^2 \, \alpha(\epsilon + E_i) \, \exp\left[-\frac{E_i}{k_B T_r}\right] \, \exp\left[-\frac{\epsilon}{k_B T_r}\right] .$$

For this form, most of the carriers enter the band with energies $\epsilon < E_i$ and we approximate $(\epsilon + E_i)^2$ by E_i^2. A complete description of the excitation rate

would demand a knowledge of the donor states and the operative selection rules for donor-conduction band transitions. The general effect, however, is to excite electrons into the band with an energy spectrum peaked at an energy of the order $k_B T_r$. With these considerations in mind we make the approximation that the excitation rate depends only on energy and choose,

$$W \omega_e \propto \varepsilon^{\ell} \exp(-\varepsilon/k_B T_r)$$

where ℓ is essentially determined by the selection rules and the matrix elements for the electron-photon interaction.

APPENDIX 3.1

SCATTERING CHANNELS - GENERAL PROCEDURE

The basic scattering problem is the calculation of the scattered state wavevector $\underline{k}'$ in the frame of reference for the simulation (this frame exploits the cylindrical symmetry of the transport problem by having the polar axis k_z directed parallel (for holes) or antiparallel (for electrons) to the applied electric field). The state $\underline{k}'$ is determined by the initial state $\underline{k}$ and the differential cross section σ for the scattering process involved. We here suppose that the energy ε' of the scattered state (and hence $k' \equiv |\underline{k}'|$) is known, and defer a discussion of the determination of ε' for individual processes to Appendix 3.2.

In our applications the scattering cross section $\sigma(\Theta, \Phi)$ is independent of azimuthal angle Φ, where we consider the scattering in a polar coordinate system with $\underline{k}$, the initial wavevector aligned along the polar axis. The scattering angle Θ is defined by

$$\cos \Theta = \underline{k} \cdot \underline{k}' \Big/ (|\underline{k}| |\underline{k}'|) \tag{1}$$

(see also Figure A3.1.1). Since there is no azimuthal dependence, the total cross section σ_t is given by

$$\sigma_t = 2\pi \int_{-1}^{1} \sigma(\Theta) \, d(\cos \Theta). \tag{2}$$

The probability density for scattering with cosine $\cos \Theta$ follows as

$$p(\cos \Theta) \, d(\cos \Theta) = 2\pi \, \sigma(\cos \Theta) \, d(\cos (\Theta) \, / \, \sigma_t. \tag{3}$$

The corresponding probability distribution function is

$$P(\cos \Theta) = \int_{-1}^{\cos \Theta} p(\cos \Theta') \, d(\cos \Theta'). \tag{4}$$
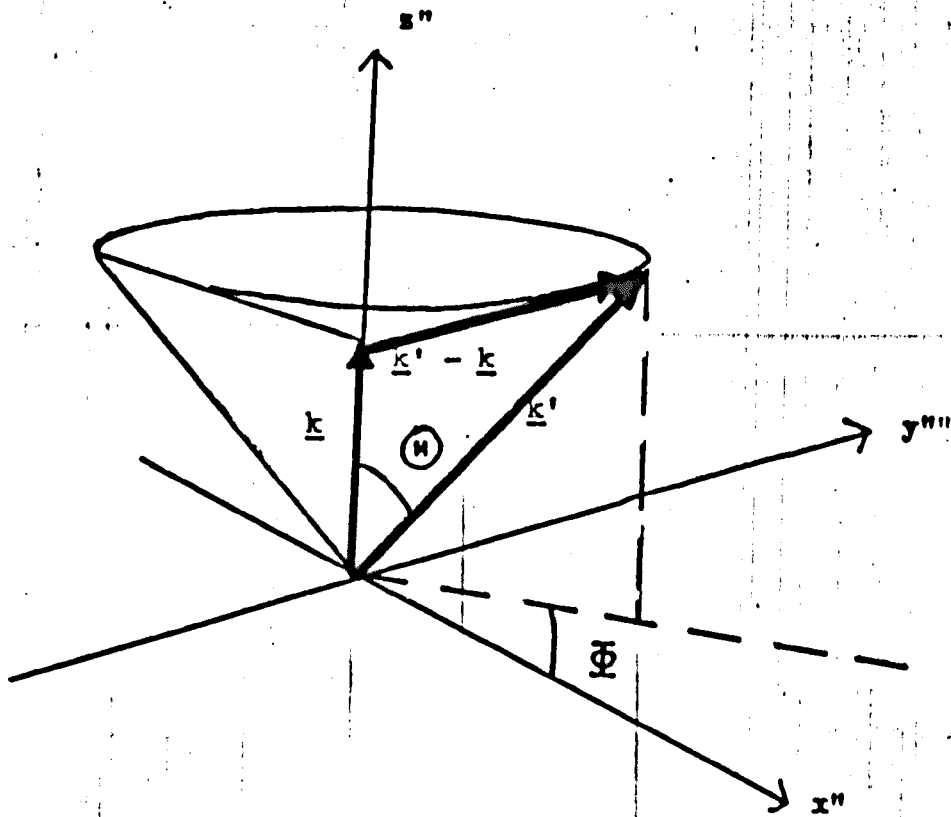
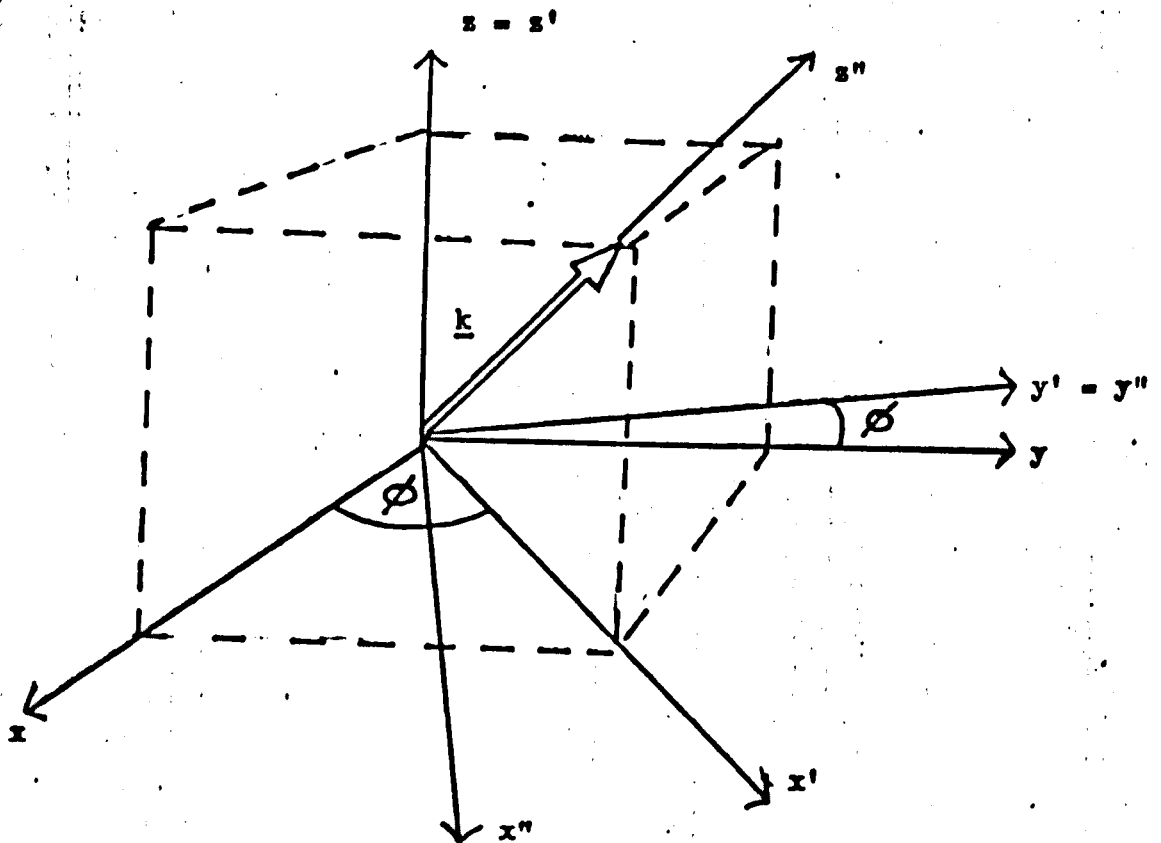**Fig A3.1.1** THE SCATTERING FRAME OF REFERENCE

Fig A3.1.2 TRANSFORMATION FROM THE SCATTERING FRAME
TO THE SIMULATION FRAME

The Monte Carlo procedure generates a random number r on (0,1), and setting r = P(cos Θ), we solve for cos Θ. The azimuthal angle Φ is randomly distributed on (0,2π) with probability density p(Φ) = 1/2π. Monte Carlo yields Φ as Φ = 2πr' where r' is a further random number on (0,1). The wavevector k' is now completely determined in the scattering frame, and the next step is to transform back to the simulation frame.

Let k,k' have spherical polar components (k,θ,φ) and (k',θ',φ') in the simulation frame, or in cartesian coodinates $\underline{k} \equiv (k_x, k_y, k_z)$, $\underline{k}' \equiv (k_x', k_y', k_z')$. The scattering frame is obtained by two successive rotations of the simulation frame of reference (represented by xyz in cartesian coordinates). The first transformation is a rotation by φ about the z-axis, to define an intermediate frame x'y'z' (where z' = z). A second rotation through θ about the y' axis generates the scattering frame x''y''z'' (where y'' = y'), in which k lies along the polar axis z''. The scattering angles Θ,Φ are measured in this frame, where Φ is defined relative to the x'' axis. The transformations are sketched in Figure A3.1.2. The cartesian components of k' in the simulation frame, are then easily calculated as

$$
\begin{pmatrix} k_x' \\ k_y' \\ k_z' \end{pmatrix} = k' \begin{pmatrix} \cos \Phi \sin \Theta \cos \phi \cos \theta - \sin \Phi \sin \Theta \sin \phi + \cos \Theta \cos \phi \sin \theta \\ \cos \Phi \sin \Theta \sin \phi \cos \theta + \sin \Phi \sin \Theta \cos \phi + \cos \Theta \sin \phi \sin \theta \\ \cos \Theta \cos \theta - \cos \Phi \sin \Theta \sin \theta \end{pmatrix}
$$
(5)

This relation is too general for our purposes, and we only require the radial and polar components k_ρ', k_z' of k' in the simulation frame. From (5) these are just

$$
k_z' = k' (\cos \Theta \cos \theta - \cos \Phi \sin \Theta \sin \theta)
$$
$$
= k' \cos \theta' ;
$$

and $k_\rho' = k' \sin \theta' = (k'^2 - k_z'^2)^{\frac{1}{2}}$

(6)

APPENDIX 3.2

SCATTERING CHANNELS - INDIVIDUAL PROCESSES

1. Introduction and notation

We collect here formulae for the calculation of channel probabilities and final state parameters appropriate to the scattering of free carriers by phonons and impurities. The results quoted are valid within the approximation of spherical constant energy surfaces and a parabolic energy-wavevector dispersion relation. Only single phonon processes are considered. In principle the formulae can be adapted to more general situations such as non parabolic bands, no fundamental change in technique is required. Useful reviews of the scattering processes considered here have been given by Smith (1960), Paige (1964) and Conwell (1967).

The following notation is adopted:

(i)   r, r' etc: random numbers, uniformly distributed on (0,1).

(ii) ε_i, ε_f :   carrier energies immediately before and after a collision.

(iii) $\underline{k}_i$, $\underline{k}_f$:   same as (ii) but for carrier wavevectors.

(iv) Γ :   the primary self-scattering parameter.

(v)   All scattering angles Θ, Φ are defined in the
     scattering frame of reference.

2. Ionized Impurity Scattering

This process is highly elastic and the differential scattering cross section $\sigma_1(\Theta)$ is independent of azimuthal angle Φ. The probability per unit time that a carrier in $\underline{k}_i$ scatters via an ionized impurity may be written

$$\lambda_1(\underline{k}_i) = N_I v(k_i) \int_0^{2\pi} d\Phi \int_{-1}^{1} \sigma_1(\Theta) \, d(\cos \Theta), \tag{1}$$

where N_I is the density of ionized impurities, v is the carrier speed. Within the Born approximation for scattering from a hydrogenic model impurity (c.f. Paige 1964),

$$\sigma_1(\Theta) = Z_1^2 \left\{ 2 \, k_i^2 \, (1 - \cos \Theta) + \lambda^{-2} \right\}^{-2} \tag{2}$$

where λ, the Debye screening length is given by

$$\lambda = \left(\frac{\epsilon_r \, k_B T'}{n' e^2} \right)^{\frac{1}{2}}$$

and

$$Z_1 = \frac{2m^* \, Ze^2}{\hbar^2 4\pi\epsilon_r}$$

where ϵ_r is the dielectric constant for the host lattice and Ze is the charge on the impurity. The effective electron concentration n' is given by the Brooks-Herring (1955) expression

$$n' = n + (n + N_A)(1 - \frac{n + N_A}{N_D})$$ where n is the actual carrier density

and N_A, N_D are the acceptor and donor concentrations. For hole scattering, n' has a similar form but with N_A and N_D interchanged. The effective temperature T' is the electron temperature. In highly non equilibrium situations the concept of carrier temperature is ambiguous and in such situations we choose T' as proportional to the mean carrier energy $< \epsilon >$,

$$T' = \frac{2}{3} < \epsilon > / \, k_B$$

This result is true for Maxwellian heating (Das and Alba 1968) but is an approximation otherwise.

The total cross section $\sigma_1 t$ is found from (2) as

$$\sigma_{1t} = 4\pi Z_1^2 / (\lambda^{-4} + 4k_i^2\lambda^{-2})$$

giving the channel probability for ionized impurity scattering as

$$p(1) = \frac{4\pi\hbar N_I Z_1^2}{m^* \Gamma} \frac{\lambda^2 k_i}{\lambda^{-2} + 4 k_i^2} \tag{4}$$

The scattering angle Θ is given by (2) and the general procedure of Appendix 3.1 as

$$\cos\Theta = \frac{2r(\lambda^{-2} + 2k_i^2) - \lambda^{-2}}{4rk_i^2 + \lambda^{-2}} \tag{5}$$

whereas $\phi = 2\pi r'$ $\tag{6}$

Cut off procedure

In general, ionized impurity scattering is characterized by predominant small angle scattering, particularly at high energies. High energy carriers are therefore hardly affected by ionized impurity scattering although the frequency of real collisions may be large. This is wasteful from a computational point of view and we have found it convenient, in some circumstances to introduce a cut off to the differential cross section so as to ignore collisions for which the scattering angle Θ is less than some very small value Θ_o say. Defining $\delta = \cos\Theta_o$ we then find the new channel probability $p^*(1)$ as

$$p^*(1) = p(1) \frac{1}{2} \frac{(1 + \delta)}{(1 + 2k_i^2\lambda^2(1 - \delta))}$$

and the scattering angle Θ as

$$\cos\Theta = \frac{r(1 + \delta)(\lambda^{-2} + 2k_i^2) - (\lambda^{-2} + 2k_i^2(1 - \delta))}{2r(1 + \delta)k^2 + (\lambda^{-2} + 2k^2(1 - \delta))}$$

so that Θ is defined on (Θ_o, π).

3. Neutral Impurity scattering

This channel is highly elastic to a good order of approximation and is characterized by a transition probability per unit time for scattering out of state $\underline{k}_i$ given by,

$$\lambda_2(\underline{k}_i) = N_o \, v(k_i) \int_0^{2\pi} d\phi \int_{-1}^{1} d(\cos\Theta) \, \sigma_2(\Theta) \tag{7}$$

where N_o is the density of neutral impurities and

$$\sigma_2(\Theta) = \frac{.20 \, \hbar \, a_1}{4\pi m^* v(k_i)} \tag{8}$$

Here a_1 is the Bohr radius of the ground state of the impurity on the hydrogenic model (modified by the effective mass m^* and dielectric constant of the host lattice). This result is due to Erginsoy (1950). The channel probability and scattering angles follow immediately as

$$\left. \begin{aligned} p(2) &= \lambda_2(\underline{k}_i) \, /\Gamma = \frac{20 \, N_o \, \hbar \, a_1}{m^* \, \Gamma} \quad ; \\[2mm] \cos\Theta &= 2r - 1 \quad ; \\[2mm] \phi &= 2\pi r' \end{aligned} \right\} \tag{9}$$

4. Inelastic acoustic phonon scattering

We recall from Appendix 2.1 that within the approximation of spherical energy bands only longitudinal phonons (LA phonons) contribute to the intra-valley acoustic phonon-electron interaction. In our applications only the long wavelength phonons are considered. The suffices 3 and 4 are used to denote phonon absorption and emission respectively. From Appendix 2.1 we obtain the following expressions for the channel and final state probabilities. We also include suitable envelope functions for the secondary self-scattering device.

Phonon absorption

The scattering rate is,

$$\lambda_3(\underline{k}_i) = A_o T^3 \epsilon_i^{-\frac{1}{2}} \int_{Z_1}^{Z_2} g_3(Z)dZ \tag{10}$$

where

$$A_o \equiv \frac{m^{*\frac{1}{2}} D^2 k_B^3}{\pi(\hbar s)^4 \rho 2^{2.5}} \quad \text{(in the notation of Appendix 2.1),}$$

$$g_3(Z) \equiv Z^2/(e^Z - 1) \,,$$

$$Z \equiv |(\epsilon_f - \epsilon_i)/k_B T|.$$

The quantity Z is essentially the energy of the scattered phonon expressed in dimensionless form. The permitted range of phonon energies Z_1 to Z_2 is given in Table A3.2.1. The channel probability is given by

$$p(3) = \lambda_3/\Gamma. \tag{11}$$

Assuming a scattering event involving absorption of an LA phonon, the probability density of final state parameter Z is

$$p(Z) = \frac{Z^2}{e^Z - 1} \bigg/ \int_{Z_1}^{Z_2} \frac{t^2 dt}{e^t - 1} \tag{12}$$

and the final state energy ϵ_f is obtained from

$$\epsilon_f = \epsilon_i + k_B T Z. \tag{13}$$

Phonon emission

The scattering rate is

$$\lambda_4(\underline{k}_i) = A_o T^3 \epsilon_i^{-\frac{1}{2}} \int_{Z_1}^{Z_2} g_4(Z)dZ$$

where $g_4(Z) \equiv Z^2/(1 - e^{-Z})$ and the permitted range of Z is given in Table A3.2.1.

RANGE OF FINAL STATES FOR ACOUSTIC PHONON SCATTERING

ABSORPTION	EMISSION
$Z_1 = 0$ for $\varepsilon_i \geq \varepsilon_\alpha / 4$	$Z_1 = 0$ for $\varepsilon_i \leq \varepsilon_\alpha / 4$
$= \left(\varepsilon_\alpha - 2\sqrt{\varepsilon_i \varepsilon_\alpha} \right) / k_B T$	$= \left(-\varepsilon_\alpha + 2\sqrt{\varepsilon_\alpha \varepsilon_i} \right) / k_B T$
for $\varepsilon_i \leq \varepsilon_\alpha / 4$	for $\varepsilon_i \geq \varepsilon_\alpha / 4$
$Z_2 = \left(\varepsilon_\alpha + 2\sqrt{\varepsilon_i \varepsilon_\alpha} \right) / k_B T$	$Z_2 = 0$

where $\varepsilon_\alpha \equiv 2 m^* s^2$

The channel probability is

$$p(4) = \lambda_4/\Gamma, \tag{14}$$

and the probability density for final state parameter Z is

$$p(Z) = \frac{Z^2}{1 - e^{-Z}} \bigg/ \int_{Z_1}^{Z_2} \frac{t^2 dt}{1 - e^{-t}} \tag{15}$$

where the final state energy ε_f is obtained from

$$\varepsilon_f = \varepsilon_i - k_B T \, Z \tag{16}$$

Scattering angles

The scattering angle Θ is determined from ε_f, by applying energy and momentum conservation to the collision. This procedure yields the frequency ω and wavevector q of the participant phonon,

$$\left.\begin{aligned} \hbar\omega &= |\varepsilon_f - \varepsilon_i| \\ \hbar q &= |\underline{k}_f - \underline{k}_i| = |k_f^2 + k_i^2 - 2k_i k_f \cos \Theta|. \end{aligned}\right\} \tag{17}$$

In the long wavelength limit $\omega = sq$, where s is the long wavelength velocity of sound, and using the dispersion relation $\varepsilon = \hbar^2 k^2/2m^*$ we find from (17),

$$\cos \Theta = \frac{1}{2} \left\{ \left(\frac{\varepsilon_f}{\varepsilon_i}\right)^{\frac{1}{2}} \left(1 - \frac{\varepsilon_f}{\varepsilon_\alpha}\right) + \left(\frac{\varepsilon_i}{\varepsilon_f}\right)^{\frac{1}{2}} \left(1 - \frac{\varepsilon_i}{\varepsilon_\alpha}\right) + \frac{2(\varepsilon_i \varepsilon_f)^{\frac{1}{2}}}{\varepsilon_\alpha} \right\} \tag{18}$$

Here $\varepsilon_\alpha = 2m^* s^2$, and equation (18) is valid for emission and absorption processes. Within our approximation the azimuthal angle is isotropically distributed and we find

$$\Phi = 2\pi \, r.$$

Secondary self-scattering

A useful envelope function for $g_3(Z)$ is

$$E_3(Z) \equiv Z(1 + Z)e^{-Z} \qquad (20)$$

with the properties,

(i)
$$\left. g_3(Z), E_3(Z) \right\} \begin{array}{ll} \sim & Z \qquad \text{for } Z \to 0 \\ \sim & Z^2 e^{-Z} \quad \text{for } Z \to \infty \end{array}$$

(ii) $E_3(Z) \gtrsim g_3(Z)$ for all Z (equality holds for $Z \to 0, \infty$)

(iii) $\int E_3(Z)\,dZ = -e^{-Z}(Z^2 + 3Z + 3)$

$$\int_0^\infty E_3(Z)\,dZ = 3 \text{ (whereas } \int_0^\infty g_3(Z)\,dZ = 2.404104)$$

(iv) The new channel probability is

$$p(3) = \frac{A_o T^3 \epsilon_i^{-\frac{1}{2}}}{\Gamma} \left[-e^{-Z}(Z^2 + 3Z + 3) \right]_{Z_1}^{Z_2} .$$

An appropriate envelope function for $g_4(Z)$ is

$$E_4(Z) \equiv Z^2 + E_3(Z) , \qquad (21)$$

with the properties

(i)
$$\left. g_4(Z), E_4(Z) \right| \begin{array}{ll} \sim & Z \text{ for } Z \to 0 \\ \sim & Z^2 \text{ for } Z \to \infty \end{array}$$

(ii) $E_4(Z) \gtrsim g_4(Z)$ for all Z.

(iii) $\int E_4(Z)\,dZ = Z^3/3 - e^{-Z}(Z^2 + 3Z + 3).$

(iv) The new channel probability

$$p(4) = \frac{A_o T^3 \epsilon_i^{-\frac{1}{2}}}{\Gamma} \left[Z^3/3 - e^{-Z}(Z^2 + 3Z + 3) \right]_{Z_1}^{Z_2} .$$

5. Non polar optical phonon scattering

We adopt the deformation potential model for longitudinal non polar optical phonon scattering due to Shockley (1951) and Harrison (1956). Harrison has shown that the matrix elements for the scattering processes may be either of zero or higher order in the wavevector of the phonon or of the carrier. We consider only the zero order situation, which dominates in our applications (a good discussion of this point is given by Conwell 1967). A further approximation is to neglect phonon dispersion and we consider the optical mode frequency to be a constant ω_o independent of phonon wavevector q. As a consequence the scattering is isotropic in the scattering frame of reference and we have

$$\cos \Theta = 1 - 2r, \quad \Phi = 2\pi r' \tag{22}$$

Phonon absorption

The transition probability per unit time for leaving state $\underline{k}_i$ is

$$\lambda_5(\underline{k}_i) = \left(\frac{D_{LO}^2 \, m^{*3/2} \, \omega_o}{2^{\frac{1}{2}} \hbar^3 \pi \rho s^2} \right) \frac{(\epsilon_i + \hbar\omega_o)^{\frac{1}{2}}}{\exp(\hbar\omega_o/k_B T) - 1} \tag{23}$$

with channel probability

$$p(5) = \lambda_5/\Gamma \tag{24}$$

and final state energy

$$\epsilon_f = \epsilon_i + \hbar\omega_o \,. \tag{25}$$

The quantity D_{LO} is the effective deformation potential.

Phonon emission

The transition probability per unit time for leaving state $\underline{k}_i$ is

$$\lambda_6(\underline{k}_i) = 0 \qquad \text{for } \varepsilon_i < \hbar\omega_o$$

(26)

$$= \left(\frac{D_{LO}^2 \, m^{*3/2} \, \omega_o}{2^{\frac{1}{2}}\hbar^3 \pi\rho \, s^2}\right) \frac{(\varepsilon_i - \hbar\omega_o)^{\frac{1}{2}}\exp(\hbar\omega_o/k_B T)}{\exp(\hbar\omega_o/k_B T) - 1} \quad \text{for } \varepsilon_i > \hbar\omega_o.$$

with channel probability

$$p(6) = \lambda_6/\Gamma.$$

(27)

The final state energy, if $\lambda_6 \neq 0$, is

$$\varepsilon_f = \varepsilon_i - \hbar\omega_o$$

(28)

We note that intervalley scattering may be treated in a similar fashion to non-polar optical phonon scattering, with appropirate modifications for the number of valleys involved and the effective mass variations in different valleys (Conwell 1967).

6. Polar optical phonon scattering

This scattering process arises in polar materials from the polarization of the crystal induced by the longitudinal optical mode vibrations of the lattice. We consider the case of a spherical band centred on $\underline{k} = 0$ such that the carriers have s-wave symmetry. The results quoted are based on Ehrenreich's (1957) derivation of the matrix elements for this scattering process. As in non-polar optical phonon scattering we assume a constant phonon frequency ω_o.

Phonon absorption

The transition probability per unit time for scattering out of state $\underline{k}_i$ is

$$\lambda_7(\underline{k}_i) = W_o \, \varepsilon_i^{-\frac{1}{2}} \, (\exp(\hbar\omega_o/k_B T) - 1)^{-1} \int_{y_-}^{y_+} dy/y$$

(29)

where $\quad W_o \equiv \dfrac{e^2 m^* \hbar\omega_o}{2\hbar^2 (2m^*)^{\frac{1}{2}}} \left(\dfrac{1}{\epsilon_\infty} - \dfrac{1}{\epsilon_o}\right)$

$$y^\pm \equiv \left\{(\epsilon_i + \hbar\omega_o)^{\frac{1}{2}} \pm \epsilon_i^{\frac{1}{2}}\right\}^2 ,$$

ϵ_o and ϵ_∞ are the dielectric constants for zero and infinite frequencies respectively. The quantity y is related to the phonon wavevector q involved in the collision by

$y = \hbar^2 q^2 / 2m^*$. Performing the integral in (29) we find the channel probability as

$$p(7) = 4W_o \, \epsilon_i^{-\frac{1}{2}} (\exp(\hbar\omega_o/k_B T) - 1)^{-1} \, \sinh^{-1} \left(\dfrac{\epsilon_i}{\hbar\omega_o}\right)^{\frac{1}{2}} \bigg/ \Gamma \tag{30}$$

The final state energy is given by

$$\epsilon_f = \epsilon_i + \hbar\omega_o . \tag{31}$$

The probability distribution for final state parameter y is readily found from (29) as

$$P(y) = \log_e(y/y^-)/\log_e(y^+/y^-) . \quad \text{Setting } r = P(y) \text{ we find}$$

$$y = y^- (y^+/y^-)^r \tag{32}$$

Applying energy and momentum conservation to the collision then yields the scattering angle Θ as

$$\cos \Theta = \dfrac{-y + (2\epsilon_i + \hbar\omega_o)}{2\left(\epsilon_i(\epsilon_i + \hbar\omega_o)\right)^{\frac{1}{2}}} \tag{33}$$

where y is given by (31). The asimuthal angle Φ is trivially generated as

$$\Phi = 2\pi r' \tag{34}$$

Phonon emission $\quad (\epsilon_i > \hbar\omega_o)$

A similar analysis gives the channel probability as

$$p(8) = 4W_o \epsilon_i^{-\frac{1}{2}} \left\{ 1 + \frac{1}{\exp(\hbar\omega_o/k_BT) - 1} \right\} \sinh^{-1} \left[\frac{\epsilon_i - \hbar\omega_o}{\hbar\omega_o} \right]^{\frac{1}{2}} \qquad (35)$$

The azimuthal angle is given by (34), whilst the scattering angle Θ is found as

$$\cos \Theta = \frac{-y + (2\epsilon_i - \hbar\omega_o)}{2 \left\{ \epsilon_i (\epsilon_i - \hbar\omega_o) \right\}^{\frac{1}{2}}} \qquad (36)$$

where

$$y = y^-(y^+/y^-)^r \qquad (37)$$

and

$$y^{\pm} = \left\{ \epsilon_i^{\frac{1}{2}} \pm (\epsilon_i - \hbar\omega_o)^{\frac{1}{2}} \right\}^2 . \qquad (38)$$

APPENDIX 3.3

VALIDITY OF THE SELF SCATTERING DEVICE

In Monte Carlo simulations of transport problems it is vital to generate times of free flight between real scattering events. The essence of the self-scattering device is the generation of free times from the simple probability density distribution $p_\Gamma(t)$, which describes the probability density for a first real or self-scattering event to occur in the time interval $(t, t + dt)$. The physical free times between real collisions, corresponding to the correct probability density distribution $p_\lambda(t)$, are obtained by summing over all intermediate self-scattering events between two successive real collisions. We now prove that this procedure does indeed generate free times satisfying $p_\lambda(t)$.

Mathematically, the prescription for summing over all intermediate self-scattering events is equivalent to treating $p_\lambda(t)$ as the joint probability,

$$p_\lambda(t) \equiv p_\Gamma(t) \, p_R(t) + \int_0^t dt_1 \, p_\Gamma(t_1) \, p_S(t_1) p_\Gamma(t-t_1) p_R(t) + \cdots$$

$$+ \int_0^t dt_1 \int_0^{t_1} dt_2 \cdots \int_0^{t_{n-1}} dt_n \, p_\Gamma(t_1-t_2) \cdots p_\Gamma(t_{n-1}-t_n) p_\Gamma(t_n)$$

$$\times p_S(t_1) \cdots p_S(t_n) \times p_\Gamma(t-t_1) p_R(t)$$

$$+ \cdots$$
$$(t_n \le t_{n-1} \le \cdots \le t_1 \le t) \tag{1}$$

The probabilities $p_R(t) \equiv \lambda(t)/\Gamma$ and $p_S(t) \equiv 1 - p_R(t)$, are respectively, the probabilities for real or self-scattering to take place if a scattering event occurs. The first term in the series (1) is just the probability density that the carrier evolves freely for a time t and at that time suffers a real collision.

The second term is the probability density, summed over all possible intermediate

times t_1, that the carrier evolves freely to time $t_1 < t$, suffers a self-collision,

evolves freely to time t at which time a real collision occurs. Higher terms

are similarly interpreted. A graphical representation of the series is given

in Figure A3.3.1.

We now prove the identity (1). The series simplifies considerably when

we consider the explicit form of $p_\Gamma(t)$,

$$p_\Gamma(t) = \Gamma \exp(-\Gamma t) \tag{2}$$

which has the group property

$$\frac{p_\Gamma(t-t')}{\Gamma} \cdot \frac{p_\Gamma(t'-t'')}{\Gamma} = \frac{p_\Gamma(t-t'')}{\Gamma} \tag{3}$$

Using (3) we factorize (1) to obtain

$$\frac{p_\Gamma(t)\,\lambda(t)}{\Gamma} \Big\{1 + \int_0^t dt_1 \big(\Gamma - \lambda(t_1)\big) + \cdots$$

$$+ \int_0^t dt_1 \int_0^{t_1} dt_2 \cdots \int_0^{t_{n-1}} dt_n \big(\Gamma - \lambda(t_1)\big) \cdots \big(\Gamma - \lambda(t_n)\big)$$

$$+ \cdots \Big\} \tag{4}$$

Consider now the nth integral in the series (4). We observe that it is essentially

an integral over the entire time interval 0 to t, with the restriction that t_i be

earlier than $t_{i-1}(i \le n)$. We can rewrite this term as

$$\int_0^t dt_1 \int_0^t dt_2 \cdots \int_0^t dt_n\, \theta(t_1 - t_2) \cdots \theta(t_{n-1} - t_n) \times$$

$$\times \big(\Gamma - \lambda(t_1)\big) \cdots \big(\Gamma - \lambda(t_n)\big), \tag{5}$$

where $\theta(t)$ is the step function for which $\theta(t) = 1$ if $t > 0$ and $\theta(t) = 0$ if $t < 0$.

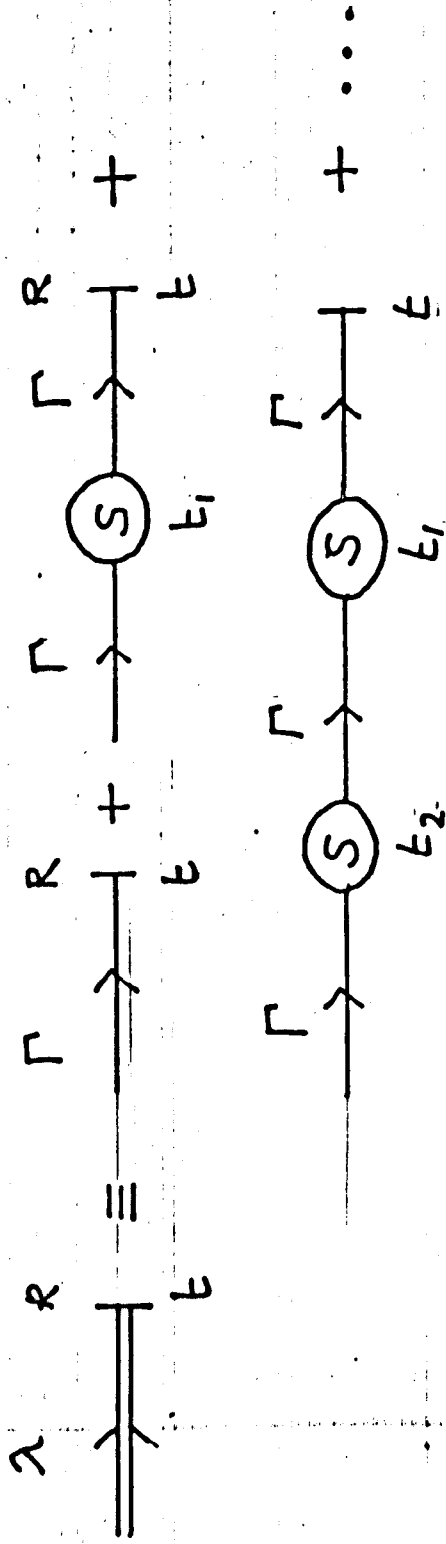Since it is permissible to interchange the order of integration, the nth integral

becomes,

FIG A3.3.1

GRAPHICAL REPRESENTATION OF THE SERIES:

$$p_\lambda(t) = p_\Gamma(t)p_R(t) + \int_0^t dt_1\, p_\Gamma(t_1)\, p_S(t_1)\, p_\Gamma(t-t_1)\, p_R(t) + \cdots$$

$$\frac{1}{n!} \int_o^t dt_1 \cdots \int_o^t dt_n \prod_{j=1}^n \left(\Gamma - \lambda(t_j)\right). \tag{6}$$

We illustrate this equivalence for the case n = 2. Consider the integral

$$\int_o^t dt_1 \int_o^t dt_2 \; V(t_1) \; V(t_2) \tag{7}$$

where $V(t) = \Gamma - \lambda(t)$. This may be written as

$$\int_o^t dt_1 \int_o^{t_1} dt_2 \; V(t_1)V(t_2) + \int_o^t dt_1 \int_{t_1}^t dt_2 \; V(t_1) \; V(t_2) \tag{8}$$

The second term in (8) is rewritten by interchanging the order of integration to give

$$\int_o^t dt_2 \int_o^{t_2} dt_1 \; V(t_1) \; V(t_2) \tag{9}$$

The expression (8) is then, relabelling t_1, t_2 in (9)

$$2 \int_o^t dt_1 \int_o^{t_1} dt_2 \; V(t_1) \; V(t_2)$$

and confirms the result (6). We can extend the argument to any order by induction. The series (4) is now written, with the aid of (6) as the sum

$$\frac{p_\Gamma(t) \; \lambda(t)}{\Gamma} \sum_{n=0}^\infty \frac{1}{n!} \left(\int_o^t dt' \left(\Gamma - \lambda(t')\right)\right)^n \tag{10}$$

and summing the series we obtain

$$\frac{p_\Gamma(t) \; \lambda(t)}{\Gamma} \exp \left(\int_o^t dt' \left(\Gamma - \lambda(t')\right)\right). \tag{11}$$

Using (2), expression (11) reduces to

$$\lambda(t) \exp \left(- \int_o^t dt' \; \lambda(t')\right),$$

which is just $p_\lambda(t)$. The identity (1) is thus proved.

A similar approach was used by Dyson (1949) in deriving the perturbation series for the S-matrix in quantum field theory.

Energy dependent self-scattering may be justified in a similar fashion. Because of the energy dependence Γ becomes a function of time $\Gamma(t)$ and we generalize the probability density for self-scattering to

$$p_\Gamma(t,t_o) \equiv \Gamma(t) \exp\left(- \int_{t_o}^{t} \Gamma(t')dt'\right)$$

$$t_o < t$$

(12)

with the group property,

$$\frac{p_\Gamma(t,t'')}{\Gamma(t)} = \frac{p_\Gamma(t,t')}{\Gamma(t)} \cdot \frac{p_\Gamma(t',t'')}{\Gamma(t')} \quad .$$

The rest of the proof follows as before.

APPENDIX 5.1

PHASE PLANE ANALYSIS

Consider the system of equations,

$$\frac{dF}{dx} = \psi \; ; \quad \frac{d\psi}{dx} = Q(F,\psi) \tag{1}$$

where $Q(F,\psi)$ is a nonlinear function of ψ and F. These equations have the important property of not containing the independent variable x explicitly. That is, they belong to the class of nonlinear autonomous differential equations, for which a variety of useful techniques exist (see for example Minorsky, 1962). It is possible to eliminate the differential dx between these equations to obtain

$$\frac{d\psi}{dF} = \frac{Q(F,\psi)}{\psi} \; ; \quad \psi \neq 0. \tag{2}$$

Equation (2) is a first order differential equation for the integral curves of (1). The introduction of the variable $\psi = \frac{dF}{dx}$ allows investigation of the integral curves in the plane of the variables (F,ψ), called the phase plane. The representation of the integral curves in parametric form $F = F(x); \quad \psi = \psi(x)$, is called a trajectory. We state here a few important definitions and results from the theory of autonomous systems which are relevant to the analysis of Chapter V.

(1) A point (F,ψ) for which ψ, $Q(F,\psi)$ do not vanish simultaneously is called an ordinary point.

(2) A point (F,ψ) for which $\psi = Q = 0$ is called a singular point.

(3) Application of the Cauchy-Lipshitz theorem regarding the existence and uniqueness of a solution of the differential equations has as a consequence that one, and only one, trajectory passes through each ordinary point in the phase plane.

(4) Trajectories only meet at singular points of the phase plane.

(5) Singular points in the phase plane represent stationary points of the 'flow' along trajectories. In our case they correspond to the homogeneous time independent states of the physical system.

(6) If a trajectory passes through an ordinary point it cannot approach a singular point in a finite distance x.

(7) A singular point for which all the trajectories sufficiently close to it tend to it asymptotically as x → ∞ is <u>asymptotically stable</u>. If the trajectories read to the singular point as x → -∞, then the singular point is <u>asymptotically unstable</u>.

(8) The direction of motion of a state point (F,ψ) along a trajectory (i.e. for x increasing) is specified uniquely by equation (2).

(9) An <u>isocline</u> of the system is a curve in the phase plane satisfying the equation

$$d\psi/dF = Q(F,\psi)/\psi = K = \text{constant}, \tag{3}$$

and represents a curve of constant slope for the trajectories.

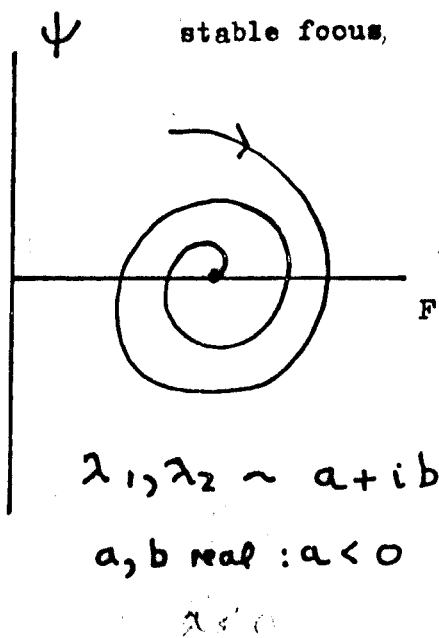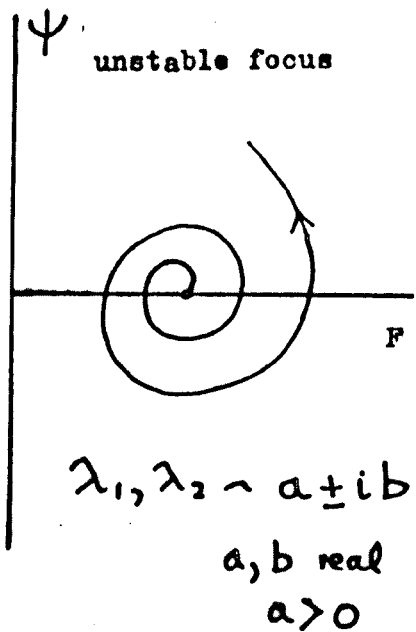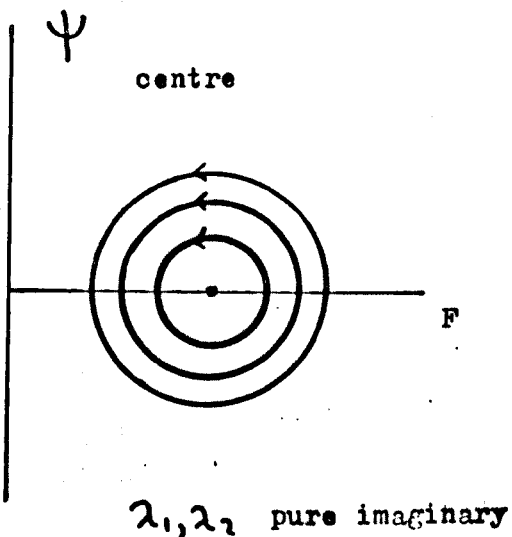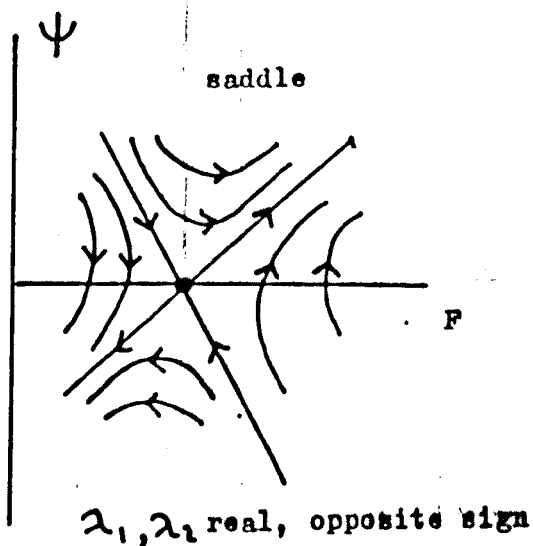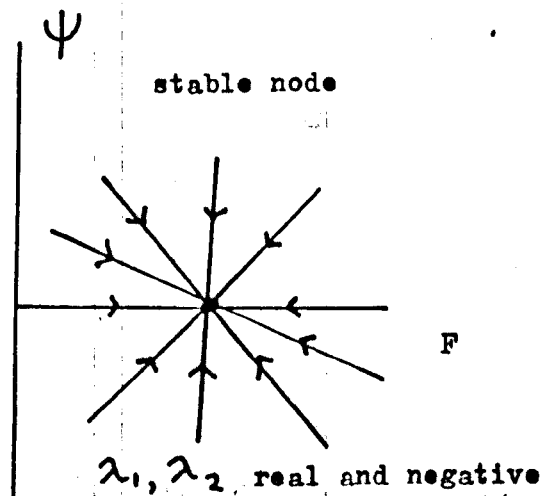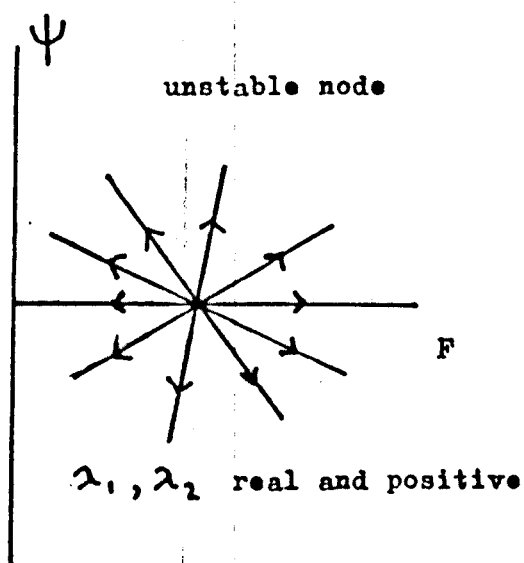Suppose the singular points of the system (1) to be labelled by the integer i and given by

$$\psi = \psi_i = 0 \;\; ; \quad F = F_i \;\; ; \quad i = 1, 2, 3 \text{ etc.} \tag{4}$$

The F_i are clearly the roots of

$$Q(F, \psi = 0) = 0 \tag{5}$$

The nature of the stationary solution in the neighbourhood of a singular point is exhibited by performing a Taylor expansion of ψ and F about the point. We set

FIG A5.1.1   CLASSIFICATION OF SINGULAR POINTS

unstable node

λ_1, λ_2 real and positive

stable node

λ_1, λ_2 real and negative

saddle

λ_1, λ_2 real, opposite sign

centre

λ_1, λ_2 pure imaginary

unstable focus

$\lambda_1, \lambda_2 \sim a \pm ib$

a, b real

$a > 0$

stable focus,

$\lambda_1, \lambda_2 \sim a + ib$

a, b real : $a < 0$

$$\left.\begin{array}{l} \psi = \psi_i + \delta\psi = \delta\psi, \\[2mm] F = F_i + \delta F , \end{array}\right\} \tag{6}$$

where δF, $\delta\psi$ are 'small'. Equation (2) is then linearized to give

$$a \frac{d^2}{dx^2}\delta F + 2b \frac{d}{dx}\delta F + c \delta F = 0, \tag{7}$$

where the coefficients a, b, c are functions of F_i. Solutions of this linear equation have the form $\exp(\lambda x)$. Substituting this into equation (7) gives the so-called <u>characteristic equation</u>,

$$a\lambda^2 + 2b\lambda + c = 0, \tag{8}$$

with roots

$$\lambda = \left\{- b \pm (b^2 - ac)^{\frac{1}{2}}\right\}/a . \tag{9}$$

The form of the trajectories around an isolated singular point depends then entirely on the values of the roots, λ_1, λ_2 of the characteristic equation. Figure 5.1 shows the classification of singular points according to the roots λ_1, λ_2 and also illustrates the form of the corresponding trajectories. Arrows denote the direction of motion of a state point along a trajectory as x increases.

APPENDIX 5.2

DISPERSION RELATIONS FOR THE STEADY-STATE

Let F_o, n_o, $p_o(=n_o)$ denote the steady-state values of field, carrier density and ionized donor density. For small departures from the steady-state we may write $n(x,t) = n_o + \delta n(x,t)$, $p(x,t) = n_o + \delta p(x,t)$, $F(x,t) = F_o + \delta F(x,t)$. Constant current density conditions are assumed, that is $\delta J = 0$. The small fluctuations satisfy the linearised versions of Poisson's equation and the continuity equations (equations 5.4.1 of Chapter V), which after some rearrangement take the form,

$$\frac{\partial}{\partial x} \delta F = \frac{4\pi e}{\varepsilon} (\delta n - \delta p) \tag{1}$$

$$\left\{ \tau_e \frac{\partial}{\partial t} + \frac{\tau_e}{\tau_h} \right\} \delta p = - \delta n \tag{2}$$

$$\frac{\partial}{\partial t} \{\delta n - \delta p\} + n_o \left. \frac{dv}{dF} \right|_{F_o} \frac{\partial}{\partial x} \delta F + v_o \frac{\partial}{\partial x} \delta n - D \frac{\partial^2}{\partial x^2} \delta n = 0. \tag{3}$$

In these equations $v_o = v(F_o)$ the steady state drift velocity, and we assume that the velocity fluctuations $\delta v(x,t)$ are instantaneously related to the local electric field fluctuations by

$$\delta v(x,t) = \left. \frac{dv}{dF} \right|_{F_o} \delta F(x,t). \tag{4}$$

The variables τ_e, τ_h have the dimensions of time and are defined by

$$\frac{1}{\tau_e} \equiv \omega_e = \sigma(N_A + n_o); \quad \frac{1}{\tau_h} \equiv \omega_h = S + n_o \sigma. \tag{5}$$

The diffusion coefficient D and capture coefficient σ are taken to be constant and independent of field.

Equations (1), (2) and (3) are readily manipulated to eliminate the variable δF and give two simultaneous differential equations for δn and δp. We represent these equations in matrix form as,

$$
\begin{bmatrix} F_1(D_x, D_t) & F_2(D_x, D_t) \\ F_3(D_x, D_t) & F_4(D_x, D_t) \end{bmatrix} \begin{bmatrix} \delta p \\ \delta n \end{bmatrix} = \begin{bmatrix} 0 \\ 0 \end{bmatrix}
\tag{6}
$$

where the operators F_1, etc., are defined by

$$
\left.
\begin{aligned}
F_1 &\equiv -D_t - \frac{1}{\tau_d} \quad ; \quad F_2 \equiv D_t + \frac{1}{\tau_d} + v_o D_x - D\,D_x^2 \quad ; \\
F_3 &\equiv D_t + \frac{1}{\tau_h} \quad ; \quad F_4 \equiv \frac{1}{\tau_e} \quad .
\end{aligned}
\right\}
\tag{7}
$$

Here $D_x \equiv \partial/\partial x$, $D_t \equiv \partial/\partial t$; the differential dielectric relaxation time is defined as $\tau_d \equiv \omega_d^{-1} = \left(\frac{4\pi e n_o}{\varepsilon} \frac{dv}{dF} \right)^{-1}$.

Consider a travelling wave perturbation to the steady state solution of the form $\delta n = \overline{\delta n} \exp\left(i(kx - \omega t)\right)$. In general such a perturbation may be Fourier analysed as

$$
\delta n = \frac{1}{2\pi} \int_{-\infty}^{\infty} d\omega\, \overline{\delta n}\,(\omega)\, \exp\left(i(kx - \omega t)\right).
$$

The fluctuation in ionized donor density must have a similar form for equation (6) to be satisfied for all space and time, i.e.

$$
\delta p = \overline{\delta p} \exp\left(i(kx - \omega t)\right).
$$

Substituting these forms into the matrix equation, the necessary and sufficient conditon for the system to have a non-trivial solution for $\overline{\delta p}$ and $\overline{\delta n}$ is

$$\det \begin{pmatrix} \dfrac{1}{\delta p} \ F_1 \ \delta p & \dfrac{1}{\delta n} \ F_2 \ \delta n \\[3mm] \dfrac{1}{\delta p} \ F_3 \ \delta p & \dfrac{1}{\delta n} \ F_4 \ \delta n \end{pmatrix} = 0 \tag{8}$$

This yields the dispersion relation

$$\omega^2 + \omega \left(i(\omega_d + \omega_e + \omega_h) - kv_o + iDk^2 \right)$$

$$- \omega_d(\omega_e + \omega_h) - i(kv_o - iDk^2)\omega_h = 0. \tag{9}$$

There are two branches to the dispersion relation. The relation between δp and δn for the separate branches may be obtained by inserting the roots of (9) into the matrix equation (6). In the limit $\dfrac{S}{\sigma} \to \infty$ we obtain the single branched relation

$$\omega = kv_o - i \left(\frac{1}{\tau_d} + Dk^2 \right) \tag{10}$$